CONTRACT NUMBER MASG-R/ER-13
GRANT NUMBER NA81AA-D-00050

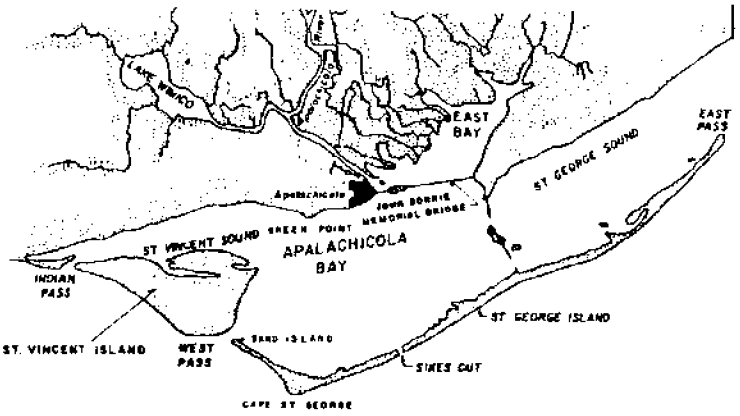

A HYDRODYNAMIC AND SALINITY MODEL FOR APALACHICOLA BAY, FLORIDA

by

DONALD C. RANEY
PROFESSOR OF ENGINEERING MECHANICS

I. HUANG
POST DOCTORAL FELLOW

and

HASAN URGUN
GRADUATE RESEARCH ASSISTANT

November 1985
BER REPORT NO. 339-183
MASGP-84-020

The University of Alabama
College of Engineering
Bureau of Engineering Research
P.O. Box 1968
University, Alabama 35486
Telephone (205) 348-1591

Prepared for the U. S. Army Corps of Engineers, Mobile District in accordance with an interagency agreement with the National Sea Grant College Program, National Oceanic and Atmospheric Administration and Mississippi - Alabama Sea Grant Consortium.

THE UNIVERSITY OF ALABAMA
COLLEGE OF ENGINEERING

The College of Engineering at The University of Alabama has an undergraduate enrollment of more than 2,300 students and a graduate enrollment exceeding 180. There are approximately 100 faculty members, a significant number of whom conduct research in addition to teaching.

Research is an integral part of the educational program, and research interests of the faculty parallel academic specialities. A wide variety of projects are included in the overall research effort of the College, and these projects form a solid base for the graduate program which offers fourteen different master's and five different doctor of philosophy degrees.

Other organizations on the University campus that contribute to particular research needs of the College of Engineering are the Charles L. Seebeck Computer Center, Geological Survey of Alabama, Marine Environmental Sciences Consortium, Mineral Resources Institute—State Mine Experiment Station, Mineral Resources Research Institute, Natural Resources Center, School of Mines and Energy Development, Tuscaloosa Metallurgy Research Center of the U.S. Bureau of Mines, and the Research Grants Committee.

This University community provides opportunities for interdisciplinary work in pursuit of the basic goals of teaching, research, and public service.

BUREAU OF ENGINEERING RESEARCH

The Bureau of Engineering Research (BER) is an integral part of the College of Engineering of The University of Alabama. The primary functions of the BER include: 1) identifying sources of funds and other outside support bases to encourage and promote the research and educational activities within the College of Engineering; 2) organizing and promoting the research interests and accomplishments of the engineering faculty and students; 3) assisting in the preparation, coordination, and execution of proposals, including research, equipment, and instructional proposals; 4) providing engineering faculty, students, and staff with services such as graphics and audiovisual support and typing and editing of proposals and scholarly works; 5) promoting faculty and staff development through travel and seed project support, incentive stipends, and publicity related to engineering faculty, students, and programs; 6) developing innovative methods by which the College of Engineering can increase its effectiveness in providing high quality educational opportunities for those with whom it has contact; and 7) providing a source of timely and accurate data that reflect the variety and depth of contributions made by the faculty, students, and staff of the College of Engineering to the overall success of the University in meeting its mission.

Through these activities, the BER serves as a unit dedicated to assisting the College of Engineering faculty by providing significant and quality service activities.

Contract Number MASG-R/ER-13
Grant Number NA81AA-D-00050

A HYDRODYNAMIC AND SALINITY MODEL FOR APALACHICOLA BAY, FLORIDA

by

Donald C. Raney
Professor of Engineering Mechanics

I. Huang
Post-Doctoral Fellow

and

Hasan Urgun
Graduate Research Assistant

Prepared for the U. S. Army Corps of Engineers, Mobile District in accordance with an interagency agreement with the National Sea Grant College Program, National Oceanic and Atmospheric Administration and Mississippi - Alabama Sea Grant Consortium.

November 1985

BER Report No. 339-183
MASGP-84-020

TABLE OF CONTENTS

I. SUMMARY

A hydrodynamic and salinity model has been developed for the Apalachicola Bay System, Florida shown in Figure I.1. The numerical model is based upon an implicit finite difference formulation of the governing equations. A variable size finite difference cell is used in the model to allow a more efficient resolution of physical details of the bay.

The bay system is assumed to be well mixed and a two-dimensional depth averaged formulation of the governing equations is used. Boundary conditions are satisfied at the bottom and top of the water column but vertical components of velocity are neglected. Horizontal components of velocity, and the surface elevation and salinity level are calculated for each finite difference cell in the model.

The model has been calibrated and verified using prototype data collected in September 1983 and March 1984, respectively. Sufficient prototype data are available to demonstrate that the numerical model reproduces the behavior of the bay system when subjected to variations in tidal elevation, salinity, river inflow and wind boundary conditions.

Model results indicate that the hydrodynamics of the bay, velocities and surface elevations, are generally dominated by astronomical tides, although at times, the wind can significantly affect water surface elevations. Freshwater inflow and wind conditions both contribute to the velocities but are relatively minor, for the estuary as a whole, compared with tidal elevations. Astronomical tides, however, are not the sole major factor affecting the distribution of water quality parameters in the bay. Salinity values and contours are very dependent upon the level of fresh water inflow. Large river inflows significantly

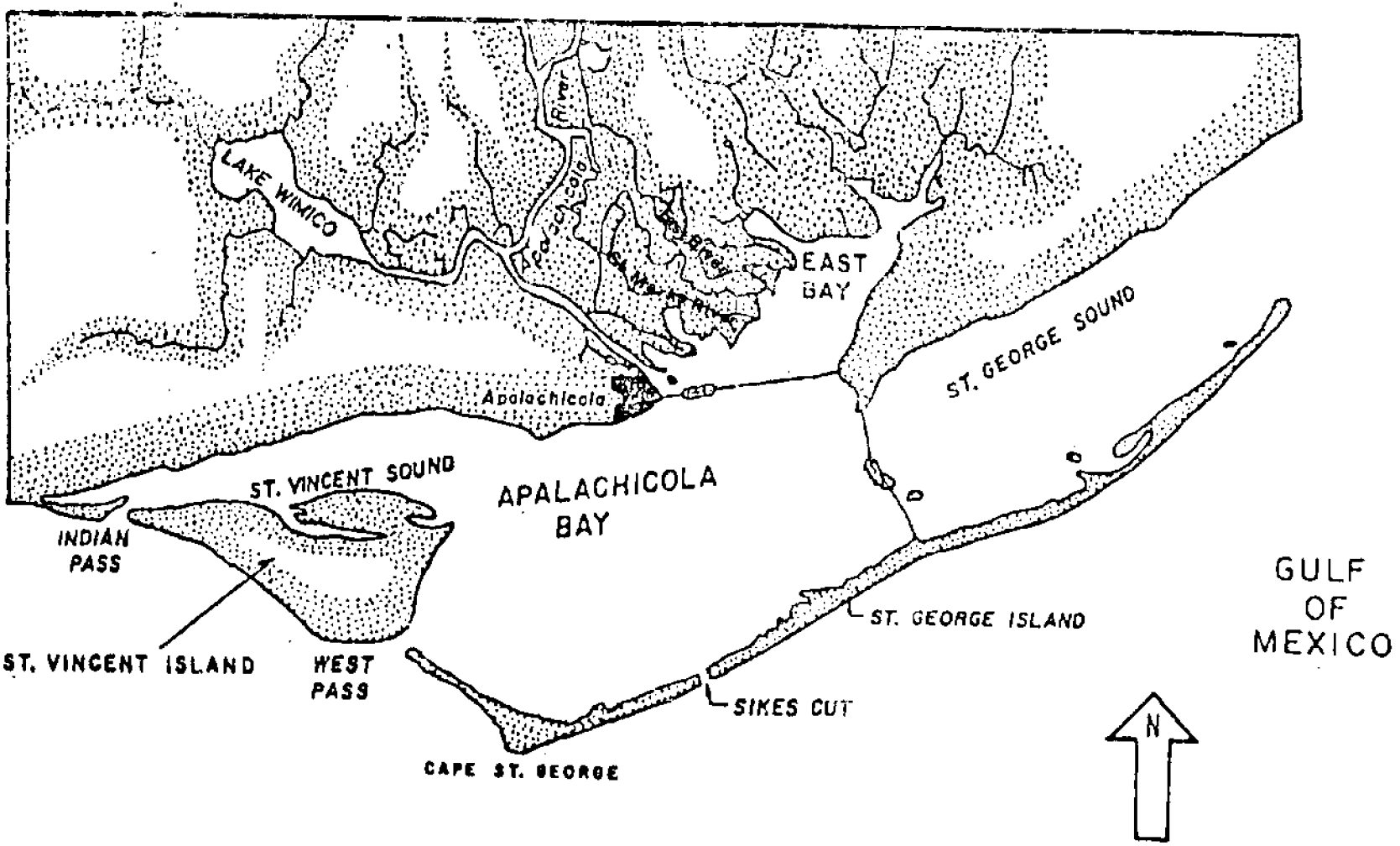

Figure I.1. Apalachicola Bay System

lower the salinity levels in the bay system, especially in East Bay, Apalachicola Bay and St. Vincent Sound. Since the overall flow in the bay system is from east to west, salinity values in St. George Sound are not as affected by fresh water inflows entering the bay system.

Sikes Cut is observed to have a measurable effect upon the circulation velocities and salinity contours in the bay system. The extent of the effect of Sikes Cut on Apalachicola Bay was not a part of this study.

In addition, the model appears to be capable of being used as a predictive tool for most conditions in the bay despite the fact that areas near passes and fresh water inflow may be stratified at least for certain times in the tidal cycle.

II. OBJECTIVE

There are currently a number of existing Federal projects within Apalachicola Bay. The most extensive of these is a portion of the Gulf Intracoastal Waterway (GIWW) which extends from the mouth of the Apalachicola River through Apalachicola Bay proper and continues eastward through St. George Sound. The GIWW project is the current focus of this investigation.

In response to a permitting condition imposed on the Corps of Engineers by the Florida Department of Environmental Regulations, a hydrodynamic and salinity model of the Apalachicola Bay was developed, calibrated and verified. The model was required to be capable of simulating a wide range of boundary forcing functions (tidal elevations and salinities, wind speed and direction and river discharge). The purpose of the modeling effort is to provide information on the current and salinity patterns within the bay so that, together with other environmental data, an assessment of the impacts that result from channel maintenance may be made.

The Apalachicola coastal zone is experiencing increased developmental interest. Future development could threaten the productive capacity of the estuary and the area's large traditional fishing industry if adequate environmental safeguards are not employed. One tool available to planners and environmental agencies to evaluate proposed developments and the associated environmental affects is the numerical model. Also, in addition to the modeling of the proposed action, modifications of the original plans can be modeled to determine the least adverse impact that would result from new construction.

Therefore, in addition to satisfying the immediate need to evaluate the environmental impacts associated with GIWW maintenance operations, the existing model can also serve to aid in the assessment of impacts that may result from proposed construction within the Apalachicola coastal zone.

III. THE NUMERICAL MODEL

The basic numerical model used is a version of WIFM developed by the U. S. Army Corps of Engineers at the Waterways Experiment Station (WES) in Vicksburg, Mississippi [3,4,5,6,7]. The model allows simulation of the hydrodynamics and salinity distribution in an estuarine environment [20,21]. In this version of the model the fluid is considered as incompressible. The density is not considered to vary with salinity and the hydrodynamic and salinity calculations are uncoupled. In the following sections, the hydrodynamic and salinity equations are presented as separate entities.

3.1 Governing Hydrodynamic Equations

The hydrodynamic equations used in WIFM are derived from the classical Navier-Stokes equations and the continuity equation in a Cartesian coordinate system [19]. For turbulent flow in a Cartesian coordinate system as indicated in Figure III.1, these equations take the form:

$$\rho\left(u\frac{\partial u}{\partial x} + v\frac{\partial u}{\partial y} + w\frac{\partial u}{\partial z} + \frac{\partial u}{\partial t}\right) - \rho f v = -\frac{\partial p}{\partial x} + \varepsilon\left(\frac{\partial^2 u}{\partial x^2} + \frac{\partial^2 u}{\partial y^2} + \frac{\partial^2 u}{\partial z^2}\right) \tag{3.1}$$

$$\rho\left(u\frac{\partial v}{\partial x} + v\frac{\partial v}{\partial y} + w\frac{\partial v}{\partial z} + \frac{\partial v}{\partial t}\right) + \rho f u = -\frac{\partial p}{\partial y} + \varepsilon\left(\frac{\partial^2 v}{\partial x^2} + \frac{\partial^2 v}{\partial y^2} + \frac{\partial^2 v}{\partial z^2}\right) \tag{3.2}$$

$$\rho\left(u\frac{\partial w}{\partial x} + v\frac{\partial w}{\partial y} + w\frac{\partial w}{\partial z} + \frac{\partial w}{\partial t}\right) = \rho g - \frac{\partial p}{\partial z} + \varepsilon\left(\frac{\partial^2 w}{\partial x^2} + \frac{\partial^2 w}{\partial y^2} + \frac{\partial^2 w}{\partial z^2}\right) \tag{3.3}$$

$$\frac{\partial \rho}{\partial t} + \frac{\partial}{\partial x}(\rho u) + \frac{\partial}{\partial y}(\rho v) + \frac{\partial}{\partial z}(\rho w) = 0 \tag{3.4}$$

The usual two-dimensional depth averaged equations are obtained by assuming: that the fluid is incompressible and homogeneous; that vertical accelerations of the fluid are negligible; and that the horizontal flow is reasonably uniform over the fluid depth. The three-dimensional equations are then integrated over the fluid depth from bottom to water surface and forced to satisfy the appropriate boundary conditions [16].

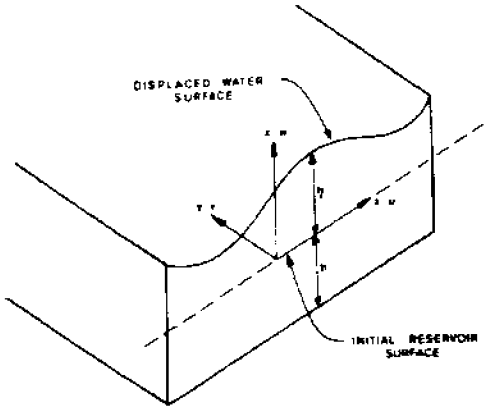

Figure III.1. Cartesian Coordinate System for Problem Formulation

With reference to Figure III.1, the model differential equations become:

Momentum Equations

$$\frac{\partial u}{\partial t} + u\frac{\partial u}{\partial x} + v\frac{\partial u}{\partial y} - fv + g\frac{\partial}{\partial x}(\eta - \eta_a)$$

$$+ \frac{gu}{C^2 d}(u^2 + v^2)^{\frac{1}{2}} - \varepsilon\left(\frac{\partial^2 u}{\partial x^2} + \frac{\partial^2 u}{\partial y^2}\right) + F_x = 0 \qquad (3.5)$$

$$\frac{\partial v}{\partial t} + u\frac{\partial v}{\partial x} + v\frac{\partial v}{\partial y} + fu + g\frac{\partial}{\partial y}(\eta - \eta_a)$$

$$+ \frac{gv}{C^2 d}(u^2 + v^2)^{\frac{1}{2}} - \varepsilon\left(\frac{\partial^2 v}{\partial x^2} + \frac{\partial^2 v}{\partial y^2}\right) + F_y = 0 \qquad (3.6)$$

Continuity Equation

$$\frac{\partial \eta}{\partial t} + \frac{\partial}{\partial x}(ud) + \frac{\partial}{\partial y}(vd) = \hat{R} \qquad (3.7)$$

The surface elevation (η) and the depth averaged velocity components (u,v) are the three unknowns in the model equations.

3.2 Stretched Coordinates

A major advantage of WIFM is the capability of applying a smoothly varying grid as shown in Figure III.2 to the given study region permitting simulation of a complex landscape by locally increasing grid resolution and/or aligning coordinates along physical boundaries. Independently for each direction, a piecewise reversible transformation [24] is used to map prototype or real space (x,y) into computational space (α_1,α_2). The transformation takes the form

$$x = a_1 + b_1\alpha_1^{c_1} \qquad (3.8)$$
$$y = a_2 + b_2\alpha_2^{c_2}$$

where a, b, and c are arbitrary constants. The transformation is such that all derivatives are centered in α-space. Many stability problems commonly associated with variable grid schemes are eliminated via the continuity of the transformation procedure.

Introducing the transformation indicated in equation (3.8) the governing equations in α-space can be written as

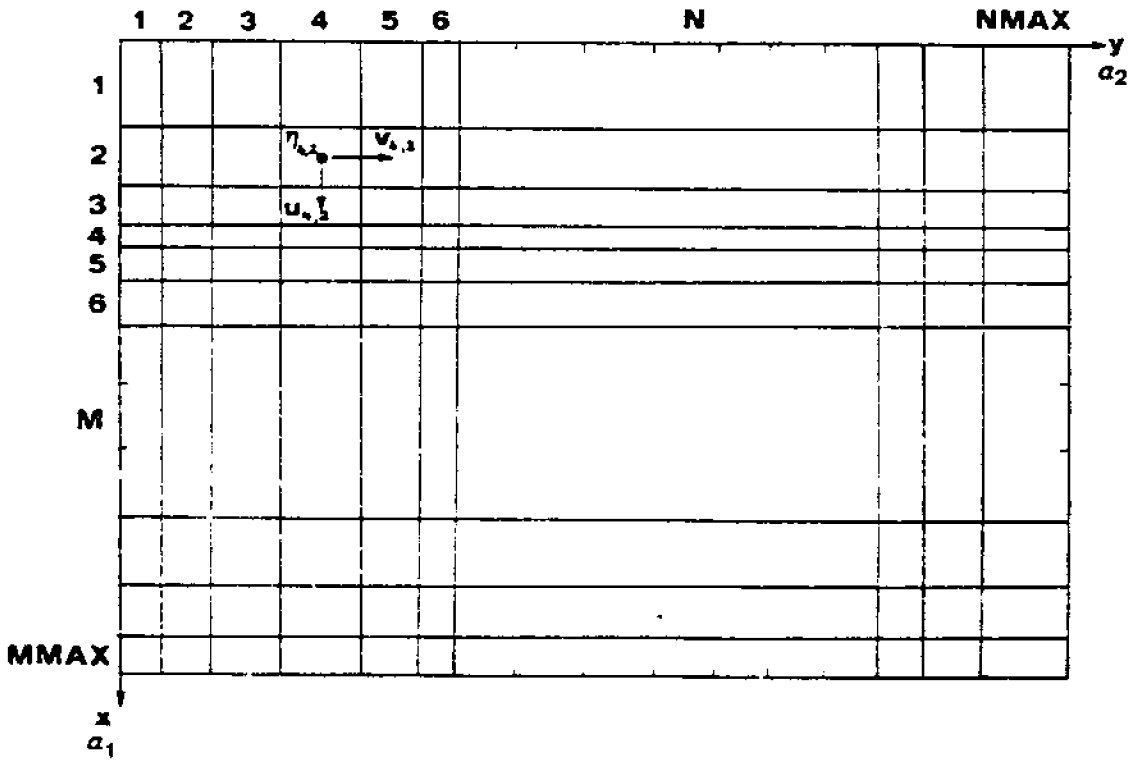

Figure III.2. Computational Grid Index Coordinates

Momentum Equations

$$u_t + \frac{1}{\mu_1} uu_{\alpha_1} + \frac{1}{\mu_2} vu_{\alpha_2} - fv$$

$$+ \frac{g}{\mu_1}(\eta - \eta_a)_{\alpha_1} + \frac{gu}{C^2 d}(u^2 + v^2)^{\frac{1}{2}}$$

$$- \varepsilon\Big[(\frac{1}{\mu_1})^2 u_{\alpha_1\alpha_1} + \frac{1}{\mu_1}(\frac{1}{\mu_1})_{\alpha_1} u_{\alpha_1} + (\frac{1}{\mu_2})^2 u_{\alpha_2\alpha_2}$$

$$+ \frac{1}{\mu_2}(\frac{1}{\mu_2})_{\alpha_2} u_{\alpha_2}\Big] + F_{\alpha_1} = 0 \qquad (3.9)$$

$$v_t + \frac{1}{\mu_1} uv_{\alpha_1} + \frac{1}{\mu_2} vv_{\alpha_2} + fu + \frac{g}{\mu_2}(\eta - \eta_a)_{\alpha_2}$$

$$+ \frac{gv}{C^2 d}(u^2 + v^2)^{\frac{1}{2}} - \varepsilon\Big[(\frac{1}{\mu_1})^2 v_{\alpha_1\alpha_1} + \frac{1}{\mu_1}(\frac{1}{\mu_1})_{\alpha_1} v_{\alpha_1}$$

$$+ (\frac{1}{\mu_2})^2 v_{\alpha_2\alpha_2} + \frac{1}{\mu_2}(\frac{1}{\mu_2})_{\alpha_2} v_{\alpha_2}\Big] + F_{\alpha_2} = 0 \qquad (3.10)$$

Continuity Equation

$$\eta_t + \frac{1}{\mu_1}(du)_{\alpha_1} + \frac{1}{\mu_2}(dv)_{\alpha_2} = \hat{R} \qquad (3.11)$$

where

$$u_t = \frac{\partial u}{\partial t} \quad , \quad uu_{\alpha_1} = u\frac{\partial u}{\partial \alpha_1} \quad , \quad \text{etc.}$$

$$\mu_1 = \frac{\partial x}{\partial \alpha_1} = b_1 c_1 \alpha^{c_1 - 1} \qquad (3.12)$$

$$\mu_2 = \frac{\partial y}{\partial \alpha_2} = b_2 c_2 \alpha^{c_2 - 1} \qquad (3.13)$$

Quantities μ_1 and μ_2 define the stretching of the regular-spaced computational grid in α-space to approximate a study region in real space (directions α_1 and α_2 correspond to x and y, respectively).

Many numerical modelers have found it difficult to obtain meaningful solutions to equations (3.9-3.11) when advective terms (single bar

underlined terms of equations (3.9 and 3.10)) are included. These terms are included in WIFM using a formulation by Weare [25]. The double bar underlined last terms in the momentum equations are representative of equivalent internal stress resultants due to turbulent and dispersive momentum flux [23]. They provide a mechanism for dissipating wave energy of wavelength on the order of twice the spatial step by smoothing curvatures developing in the solution. Although the finite difference formulations used for these terms alleviate most problems encountered when including such effects, appropriate grid parameters (time and spatial step- sizes) for the phenomena being modeled must be chosen.

3.3 Model Formulation Schemes

The model partial differential equations are to be approximated by finite difference equations. There are many computational techniques that can be used as a solution scheme. Basically, solution schemes can be classified as explicit or implicit.

Explicit solutions are formulated such that each difference equation has only one unknown. To advance the solution through time it is necessary only to cycle through the equations solving for the new variables at each finite difference cell. The solution scheme is simple; however, such solution procedures generally have stability problems which severely restrict the allowable computational time step.

Implicit solution schemes are formulated such that each individual finite difference equation may have many unknowns. For the complete finite difference grid, N equations in N unknowns will be obtained. The implicit scheme thus requires solution of a system of simultaneous equations. The implicit methods have more desirable stability characteristics; however, they are more difficult to formulate and may present

computational problems. This is especially true as the number of simultaneous equations increases.

Alternating Direction Implicit (ADI) methods [11,12,13] represent an attempt to retain the desirable stability characteristics of the implicit scheme while utilizing a relatively simple solution algorithm. ADI schemes restrict the number of unknowns in each finite difference equation to three. In addition, the coefficient matrix must be tri-diagonal, only the coefficient on the diagonal and on either side of the diagonal may be present. This general procedure leads to a two part solution scheme in which the finite difference grid is traversed in the x-direction followed by a traverse in the y-direction to complete the calculation procedure for one time step. This model formulation, while implicit, is relatively easy to formulate and has an efficient solution procedure. A large number of hydrodynamic and water quality models are based upon ADI formulations.

3.4 WIFM Model

The partial differential equations (3.9-3.11) derived from physical laws are to be approximated by finite difference equations. In the program WIFM, a special form of the ADI method is used. This method is known as the Stabilizing Correction (SC) scheme.

To illustrate the SC scheme consider the simplified linearized matrix equation

$$U_t + AU_x + BU_y = 0 \tag{3.14}$$

where

$$U = \begin{pmatrix} \eta \\ u \\ v \end{pmatrix}, \quad A = \begin{pmatrix} 0 & d & 0 \\ g & 0 & 0 \\ 0 & 0 & 0 \end{pmatrix}, \text{ and } B = \begin{pmatrix} 0 & 0 & d \\ 0 & 0 & 0 \\ g & 0 & 0 \end{pmatrix}$$

Applying a standard Crank-Nickolson technique [1,8,9,10] to equation (3.14) yields

$$\frac{1}{\Delta t}(U^{k+1} - U^{k}) + \frac{1}{2}\left(\frac{A}{\Delta x}\delta x + \frac{B}{\Delta y}\delta y\right)(U^{k+1} + U^{k}) = 0 \qquad (3.15)$$

where δ_x and δ_y are centered difference operators and the superscript k indicates time levels.

This equation can be written in a simpler form

$$(1 + \lambda_x + \lambda_y)\, U^{k+1} = (1 - \lambda_x - \lambda_y)\, U^{k} \qquad (3.16)$$

where

$$\lambda_x = \frac{1}{2}\frac{\Delta t}{\Delta x} A\delta_x$$

$$\lambda_y = \frac{1}{2}\frac{\Delta t}{\Delta y} b\delta_y.$$

By adding the quantity $\lambda_x\lambda_y(U^{k+1} - U^{k})$ of order $(\Delta x^2, \Delta t^2)$, the equation can be factorized as

$$(1 + \lambda_x)(1 + \lambda_y)U^{k+1} = (1 - \lambda_x)(1 - \lambda_y)U^{k} \qquad (3.17)$$

Introducing an intermediate value, U*, and splitting the equation into a two-step operation results in the basic equations for the Stabilizing Correction (SC) scheme,

$$(1 + \lambda_x)U^{*} = (1 - \lambda_x - 2\lambda_y)U^{k} \qquad (3.18)$$

$$(1 + \lambda_y)U^{k+1} = U^{*} + \lambda_y U^{k} \qquad (3.19)$$

The first step is to compute intermediate U* values during the first ½ time step by sweeping the grid in the x-direction, and the second step is to compute corrected values (U^{k+1}) during the second ½ time step by sweeping the grid in the y-direction. Completing both sweeps constitutes a full time step, and advances the solution to the next time step. The stabilizing correction (SC) scheme has been found

to be more satisfactory than other ADI calculation procedures. The quantity $\lambda_x\lambda_y(U^{k+1}-U^k)$ added to the equations for factoring purposes is of order $(\Delta x^2,\Delta t^2)$ and introduces no significant error into the calculations.

In the WIFM model, a three time level, leapfrog version of the SC scheme is used. This allows all derivatives to be approximated as centered derivatives. Under these conditions Equation 3.15 will take the form

$$\frac{1}{2\Delta t}(U^{k+1} - U^{k-1}) + \frac{1}{2}(\frac{A}{\Delta x}\delta x + \frac{B}{\Delta y}\delta y)(U^{k+1} - U^{k-1}) = 0.$$

After some simplifications which reduce the number of equations from three to two in both the x and y sweep, the difference equations for the x-sweep become

$$\frac{1}{2\Delta t}(\eta^* - \eta^{k-1}) + \frac{1}{2\Delta x}\,\delta_x(u^{k+1}{}_d + u^{k-1}{}_d) + \frac{1}{\Delta y}\,\delta_y(v^{k-1}{}_d) = 0 \tag{3.20}$$

$$\frac{1}{2\Delta t}(u^{k+1} - u^{k-1}) + \frac{g}{2\Delta x}\,\delta_x(\eta^* + \eta^{k-1}) = 0 \tag{3.21}$$

and for the y-sweep

$$\frac{1}{2\Delta t}(\eta^{k+1} - \eta^*) + \frac{1}{2\Delta y}\,\delta_y(v^{k+1}{}_d - v^{k-1}{}_d) = 0 \tag{3.22}$$

$$\frac{1}{2\Delta t}(v^{k+1} - v^{k-1}) + \frac{g}{2\Delta y}\,\delta_y(\eta^{k+1} + \eta^{k-1}) = 0 \tag{3.23}$$

Observe that during the x-sweep a correct value of the x component of velocity (U^{k+1}) and an approximate value for the surface elevation (η^*) is calculated. During the y-sweep the approximate value of η is replaced by the corrected value, η^{k+1}, and a correct value of the y component of velocity (V^{k+1}) is calculated.

The SC scheme can be expanded to the full model equations. Appropriate variables on each grid cell in a space-staggered fashion are defined as shown in Figure III.3. Note that because of the space staggered definition of variables the finite difference equations are written for various locations in the finite difference cell, these locations being consistent with where variables are actually defined. The difference equations for the x-sweep are

$$\frac{1}{2\Delta t}\,(\eta^{*} - \eta^{k-1}) + \frac{1}{2\mu_1\Delta\alpha_1}\,[\delta_{\alpha_1}(u^{k+1}\,\bar{d}^{k} + u^{k-1}\,\bar{d}^{k})]$$

$$+ \frac{1}{\mu_2\Delta\alpha_2}\,\delta_{\alpha_2}(v^{k-1}\,\bar{d}^{k}) = R \qquad \text{at } (n,m) \tag{3.24}$$

and

$$\frac{1}{2\Delta t}\,(u^{k+1} - u^{k-1}) + \frac{1}{2\mu_1\Delta\alpha_1}\,u^{k}\delta_{2\alpha_1}(u^{k})$$

$$+ \frac{1}{2\mu_2\Delta\alpha_2}\,\bar{\bar{v}}^{k}\delta_{2\alpha_2}(u^{k}) - f\bar{\bar{v}}^{k}$$

$$+ \frac{g}{2\mu_1\Delta\alpha_1}\,[\delta_{\alpha_1}(\eta^{*} + \eta^{k-1} - 2\eta_a^{k})]$$

$$+ \frac{g}{(\bar{C}^{2}\bar{d})^{k}}\,u^{k+1}\,[(u^{k-1})^{2} + (\bar{\bar{v}}^{k-1})^{2}]^{\frac{1}{2}}$$

$$- \varepsilon\,\Big[\frac{1}{(\mu_1\Delta\alpha_1)^{2}}\,\delta_{\alpha_1\alpha_1}(u^{k})$$

$$+ \frac{1}{(\mu_2\Delta\alpha_2)^{2}}\,\delta_{\alpha_2\alpha_2}(u^{k}) + \frac{1}{2\mu_1\Delta\alpha_1^{2}}\,\delta_{\alpha_1}\Big(\frac{1}{\mu_1}\Big)\,\delta_{2\alpha_1}(u^{k})$$

$$+ \frac{1}{2\mu_2\Delta\alpha_2^{2}}\,\delta_{\alpha_2}\Big(\frac{1}{\mu_2}\Big)\delta_{2\alpha_2}(u^{k})\Big] + F_{\alpha_1}^{k} = 0 \text{ at } (n,m+\tfrac{1}{2}) \tag{3.25}$$

The difference operators are defined as

$$\delta_{\alpha}(Z) = Z_{\alpha+\frac{1}{2}} - Z_{\alpha-\frac{1}{2}} \qquad \text{for any variable Z.}$$

$$\delta_{2\alpha}(Z) = Z_{\alpha+1} - Z_{\alpha-1}$$

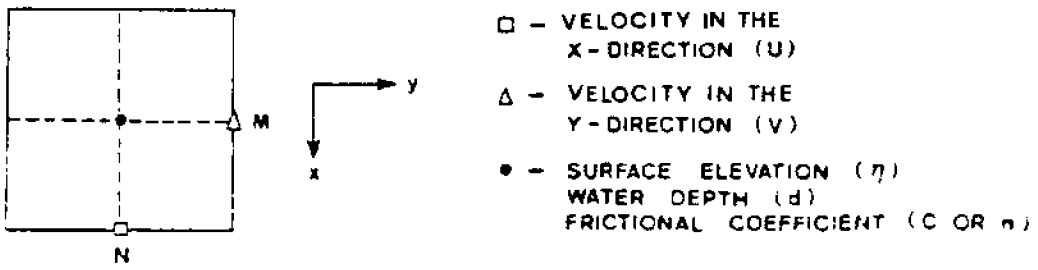

Figure III.3. Grid Cell Definition

In addition a single bar over a variable (such as $\bar{d}$) represents a two point average and a double bar over a variable (such as $\bar{\bar{v}}$) represents a four-point average.

Applying these equations at each grid cell in a given direction results in a system of linear algebraic equations whose coefficient matrix is tridiagonal. It should be noted that the entire grid of finite difference equations is not solved simultaneously. The numerical procedure allows calculations of one row (or column) at a time. In fact, if there are more than two boundary conditions to be applied on the row (or column) then the row will be broken into separate computational segments. A computational segment is defined by a lower and upper boundary condition to be applied on the row (column). The numerical procedure actually solves each computational segment independently.

Gathering the terms to be computed along the x-direction at time level $(k+1)\Delta t$, equations 3.24 and 3.25 can be written as follows

$$-a_m \eta^*_{n,m} + \bar{a}_{m+\frac{1}{2}} u^{k+1}_{n,m+\frac{1}{2}} + a_{m+1} \eta^*_{n,m+\frac{1}{2}} = B_{m+\frac{1}{2}} \text{ at } (n,m+\tfrac{1}{2}) \qquad (3.26)$$

and

$$-a_{m-\frac{1}{2}} u^{k+1}_{m-\frac{1}{2}} + \eta^{*}_{n,m} + a_{m+\frac{1}{2}} u^{k+1}_{n,m+\frac{1}{2}} = A_m \quad \text{at } (n,m) \tag{3.27}$$

where

$$A_m = \eta^{k-1}_{n,m} - \frac{\Delta t}{(\mu_1)_m \Delta\alpha_1} \delta_{\alpha_1}(u^{k-1}\,\bar{\bar{d}}^{k}) - \frac{2\Delta t}{(\mu_2)_n \Delta\alpha_2} \delta_{\alpha_2}(v^{k-1}\,\bar{\bar{d}}^{k}) + 2\Delta t\, R^{k}_{n,m} \tag{3.28}$$

$$B_{m+\frac{1}{2}} = u^{k-1}_{n,m+\frac{1}{2}} + \Delta t \left\{ \bar{\bar{v}}^{k}_{n,m+\frac{1}{2}} \left(2f - \frac{\delta_{2\alpha_2}(u^{k})}{(\mu_2)_n \Delta\alpha_2}\right) - \frac{u^{k}_{n,m+\frac{1}{2}} \delta_{2\alpha_1}(u^{k})}{(\mu_1)_{m+\frac{1}{2}} \Delta\alpha_1} - \frac{g}{(\mu_1)_{m+\frac{1}{2}} \Delta\alpha_1} \delta_{\alpha_1}(\eta^{k-1} - 2\eta^{k}_{a}) \right.$$

$$+ 2\varepsilon \left[\frac{\delta_{\alpha_1\alpha_1}(u^{k})}{((\mu_1)_{m+\frac{1}{2}} \Delta\alpha_1)^2} + \frac{\delta_{\alpha_2\alpha_2}(u^{k})}{((\mu_2)_n \Delta\alpha_2)^2} \right.$$

$$\left. + \frac{1}{2(\mu_1)_{m+\frac{1}{2}} \Delta\alpha_1^{\,2}} \delta_{\alpha_1}\left(\frac{1}{\mu_1}\right) \delta_{2\alpha_1}(u^{k}) \right.$$

$$\left. \left. + \frac{1}{2(\mu_2)_n \Delta\alpha_2^{\,2}} \delta_{\alpha_2}\left(\frac{1}{\mu_2}\right) \delta_{2\alpha_2}(u^{k}) \right] + 2F^{k}_{\alpha_1} \right\} \tag{3.29}$$

and

$$\bar{\bar{v}}^{k}_{n,m+\frac{1}{2}} = \frac{1}{4}\left(v^{k}_{n+\frac{1}{2},m} + v^{k}_{n-\frac{1}{2},m} + v^{k}_{n+\frac{1}{2},m+1} + v^{k}_{n-\frac{1}{2},m+1}\right) \tag{3.30}$$

The coefficients are defined as

$$a_{m\pm\frac{1}{2}} = \frac{\Delta t}{(\mu_1)_m \Delta\alpha_1} \bar{d}_{n,m\pm\frac{1}{2}} \tag{3.31}$$

$$a_m = a_{m+1} = \frac{(\Delta t) g}{(\mu_1)_{m+\frac{1}{2}} \Delta\alpha_1} \tag{3.32}$$

$$\bar{a}_{m+\frac{1}{2}} = 1 + \frac{2g(\Delta t)}{(\bar{\bar{C}}^2 \bar{\bar{d}})^{k}_{n,m+\frac{1}{2}}} \left[(u^{k-1}_{n,m+\frac{1}{2}})^2 + (\bar{\bar{v}}^{k-1}_{n,m+\frac{1}{2}})^2 \right]^{\frac{1}{2}} \tag{3.33}$$

For a finite difference cell adjacent to the model boundary, certain boundary conditions on velocity or surface elevation will be specified.

For example, at a land boundary the velocity normal to the boundary is zero. At a river boundary, the velocity will be a specified function of time. At a tidal boundary, the surface elevation will be a prescribed function of time. For example, assuming that η_m is a specified water elevation at the lower boundary and that $u^{k+1}_{n,L+\frac{1}{2}}$ is a given velocity at the upper boundary, the equations for line n can be written in matrix form.

$$\begin{vmatrix} \bar{a}_{M+\frac{1}{2}} & a_{M+1} & & & \cdots & 0 \\ -a_{M+\frac{1}{2}} & 1 & a_{M+3/2} & 0 & \cdots & 0 \\ 0 & -a_{M+1} & \bar{a}_{M+3/2} & a_{M+2} & \cdots & 0 \\ & & & & \cdots & \\ & & & & \cdots & \\ & & & & \cdots & \\ 0 & 0 & 0 & \cdots -a_{L-\frac{1}{2}} & & 1 \end{vmatrix} \begin{vmatrix} u^{k+1}_{M+\frac{1}{2}} \\ \eta^*_{M+1} \\ u^{k+1}_{M+3/2} \\ 0 \\ 0 \\ 0 \\ \eta^*_L \end{vmatrix} = \begin{vmatrix} \hat{B}_{M+\frac{1}{2}} \\ A_{M+1} \\ B_{M+3/2} \\ 0 \\ 0 \\ 0 \\ \hat{A}_L \end{vmatrix} \quad k \tag{3.34}$$

By defining the process of elimination as a set of recursive formulas, the above tridiagonal equations can be solved with a minimum number of operations [11]. Starting with equation (3.26)

$$u^{k+1}_{m+\frac{1}{2}} = -R_m \eta^*_{m+1} + S_m \tag{3.35}$$

where

$$R_m = \frac{a_{m+1}}{\bar{a}_{m+\frac{1}{2}}} \quad ; \quad S_m = \frac{\hat{B}_{m+\frac{1}{2}}}{\bar{a}_{m+\frac{1}{2}}} \tag{3.36}$$

and

$$\hat{B}_{m+\frac{1}{2}} = B_{m+\frac{1}{2}} + a_m \eta^*_M \tag{3.37}$$

By substituting equation (3.35) into equation (3.27) (evaluated at M+1), we obtain

$$-a_{m+\frac{1}{2}}(-R_m \eta^*_{m+1} + S_m) + \eta^*_{m+1} + a_{m+3/2}\, u^{k+1}_{m+3/2} = A_{m+1} \tag{3.38}$$

or

$$\eta^*_{m+1} = -P_{m+1} u^{k+1}_{m+3/2} + Q_{m+1} \tag{3.39}$$

where

$$P_{m+1} = \frac{a_{m+3/2}}{1 + a_{m+\frac{1}{2}} R_m} \quad ; \quad Q_{m+1} = \frac{A_{m+1} + a_{m+\frac{1}{2}} S_m}{1 + a_{m+\frac{1}{2}} R_m} \tag{3.40}$$

Also the velocity can be expressed as a function of the next water level

$$u^{k+1}_{m+3/2} = -R_{m+1} \eta^*_{m+2} + S_{m+1} \tag{3.41}$$

where

$$R_{m+1} = \frac{a_{m+2}}{\bar{a}_{m+3/2} + a_{m+1} R_{m+1}} \quad ; \quad S_{m+1} = \frac{B_{m+3/2} + a_{m+1} Q_{m+1}}{\bar{a}_{m+3/2} + a_{m+1} R_{m+1}} \tag{3.42}$$

The recursion formulas, in general, can be written as

$$\eta^*_m = -P_m u^{k+1}_{m+\frac{1}{2}} + Q_m \tag{3.43}$$

$$u^{k+1}_{m-\frac{1}{2}} = -R_{m-1} \eta^*_m + S_{m-1} \tag{3.44}$$

where

$$T1 = 1 + a_{m-\frac{1}{2}} R_{m-1} \qquad T2 = \bar{a}_{m+\frac{1}{2}} + a_m P_m$$

$$P_m = \frac{a_{m+\frac{1}{2}}}{T1} \qquad Q_m = \frac{A_m + a_{m-\frac{1}{2}} S_{m-1}}{T1} \tag{3.45}$$

$$R_m = \frac{a_{m+1}}{T2} \qquad S_m = \frac{B_{m+\frac{1}{2}} + a_m Q_m}{T2}$$

In the Fortran code fractional subscripts are not permitted. The variables as defined in Figure III.3 are represented by the same coordinate index (N,M). Using this notation, the expanded form of the recursion formulas for the x-sweep can be expressed as:

Coefficient Equations

$$P_M = \frac{\Delta t\ \bar{d}^k_{N,M}}{(\mu_1)_{2M-1}\Delta\alpha_1} \Big/ \left[1 + \frac{\Delta t\ \bar{d}^k_{N,M-1}}{(\mu_1)_{2M-1}\Delta\alpha_1} R_{M-1}\right] \tag{3.46}$$

$$Q_M = \left[A_M + \frac{\Delta t\ \bar{d}^k_{N,M-1}}{(\mu_1)_{2M-1}\Delta\alpha_1} S_{M-1}\right] \Big/ \left[1 + \frac{\Delta t\ \bar{d}^k_{N,M-1}}{(\mu_1)_{2M-1}\Delta\alpha_1} R_{M-1}\right] \tag{3.47}$$

$$D1 = 1 + \frac{2\Delta t}{\bar{d}^k_{N,M}\ (C_{N,M+1} + C_{N,M})^2} \cdot \left[(u^{k-1}_{N,M})^2 + (\bar{v}^{k-1}_{N,M})^2\right]^{\frac{1}{2}}$$

$$+ \frac{g\Delta t}{(\mu_1)_{2M}\Delta\alpha_1} P_M \tag{3.48}$$

$$R_M = \frac{g\Delta t}{(\mu_1)_{2M}\Delta\alpha_1} \Big/ D1 \tag{3.49}$$

$$S_M = \left[B_M + \frac{g\Delta t}{(\mu_1)_{2M}\Delta\alpha_1} Q_m\right] / D1 \tag{3.50}$$

The solution for each computational segment in the x-direction can be expressed as:

$$\eta^*_{N,M} = -P_M\ u^{k+1}_{N,M} + Q_M \tag{3.51}$$

$$u^{k+1}_{N,M-1} = -R_{M-1}\ \eta^*_{N,M} + S_{M-1} \tag{3.52}$$

The recursion coefficients, P, Q, R, and S, can be computed in succession between boundaries on column N. Depending upon the types of boundary conditions (solid boundary, tidal elevation, flow conditions, etc.) that are applied, various approximations of these coefficients are required. Having calculated the set of coefficients, the solution equations can be solved for the approximate surface elevations, η^*, and the x velocity components (k+1) in descending order within the computational segment.

The second portion of the computation scheme is a similar operation, but this time solving for a corrected value of the surface elevations, η^{k+1}, and the y velocity components, v^{k+1}.

For the y-sweep:

Coefficient Equations

$$P_N = \frac{\Delta t\ \bar{d}_{N,M}}{(\mu_2)_{2N-1}\Delta\alpha_2} \Big/ \left[1 + \frac{\Delta t\ \bar{d}_{N-1,M}}{(\mu_2)_{2N-1}\Delta\alpha_2} R_{N-1}\right] \tag{3.53}$$

$$Q_N = \left[A_N + \frac{\Delta t\ \bar{d}_{N-1,M}}{(\mu_2)_{2N-1}\Delta\alpha_2} S_{N-1}\right] \Big/ \left[1 + \frac{\Delta t\ \bar{d}_{N-1,M}}{(\mu_2)_{2N-1}\Delta\alpha_2} R_{N-1}\right] \tag{3.54}$$

$$D2 = 1 + \frac{2g\Delta t}{\bar{d}^k_{N,M}\ (C_{N+1,M} + C_{N,M})^2} \cdot \left[(\bar{u}^{k-1}_{N,M})^2 + (v^{k-1}_{N,M})^2\right]^{\frac{1}{2}} + \frac{g\Delta t}{(\mu_2)_{2N}\Delta\alpha_2} P_N \tag{3.55}$$

$$R_N = \frac{g\Delta t}{(\mu_2)_{2N}\Delta\alpha_2} \Big/ D2 \tag{3.56}$$

$$S_N = \left[B_N + \frac{g\Delta t}{(\mu_2)_{2N}\Delta\alpha_2} Q_W\right] \Big/ D2 \tag{3.57}$$

The solution for each computational segment in the y-direction can be expressed as:

$$\eta^{k+1}_{N,M} = -P_M\ v^{k+1}_{N,M} + Q_N \tag{3.58}$$

$$v^{k+1}_{N-1,M} = -R_{N-1}\ \eta^{k+1}_{N,M} + S_{N-1} \tag{3.59}$$

3.5 Boundary Conditions

The program WIFM is formulated to handle three different general types of boundary conditions. These boundary types are: open boundaries, water-land boundaries, and subgrid barriers.

3.5.1 Open Boundaries

These boundaries define the computational cell rows or columns exiting the grid. At these boundaries water levels or flow rates are prescribed as functions of location and time. This is usually in the form of a tidal gage output or a river hydrograph. The open boundaries are shown on the grid for Biloxi Bay in Figure III.4.

3.5.2 Water-Land Boundaries

The assumption made at these boundaries is that of "no-flow" normal to the boundary. This condition is satisfied by setting u=0 or v=0 at the appropriate cell face.

Since the program WIFM has a flooding capability, low-lying areas may dry and flood alternately several times within a tidal cycle depending on the flow conditions. Flooding and drying of a cell is controlled by checking the water levels in adjacent cells. The initial movement of water onto a dry cell is computed by a formula [17] given as

$$Q_n = \pm C_0 d_H \sqrt{d_H} \quad . \tag{3.60}$$

The closed boundary face is treated as open after the water level on the dry cell exceeds some small prescribed value (ε^*). Computations for water elevation (η), and velocities (u,v) are made for that cell as soon as the water level exceeds the value of ε^*. In equation (3.60), the admittance coefficient is taken less than 5.0 for controlling movement of water onto a dry cell. The drying of cells is inversely the same procedure as flooding. Figure III.5 shows the graphic representation of flood cell treatment.

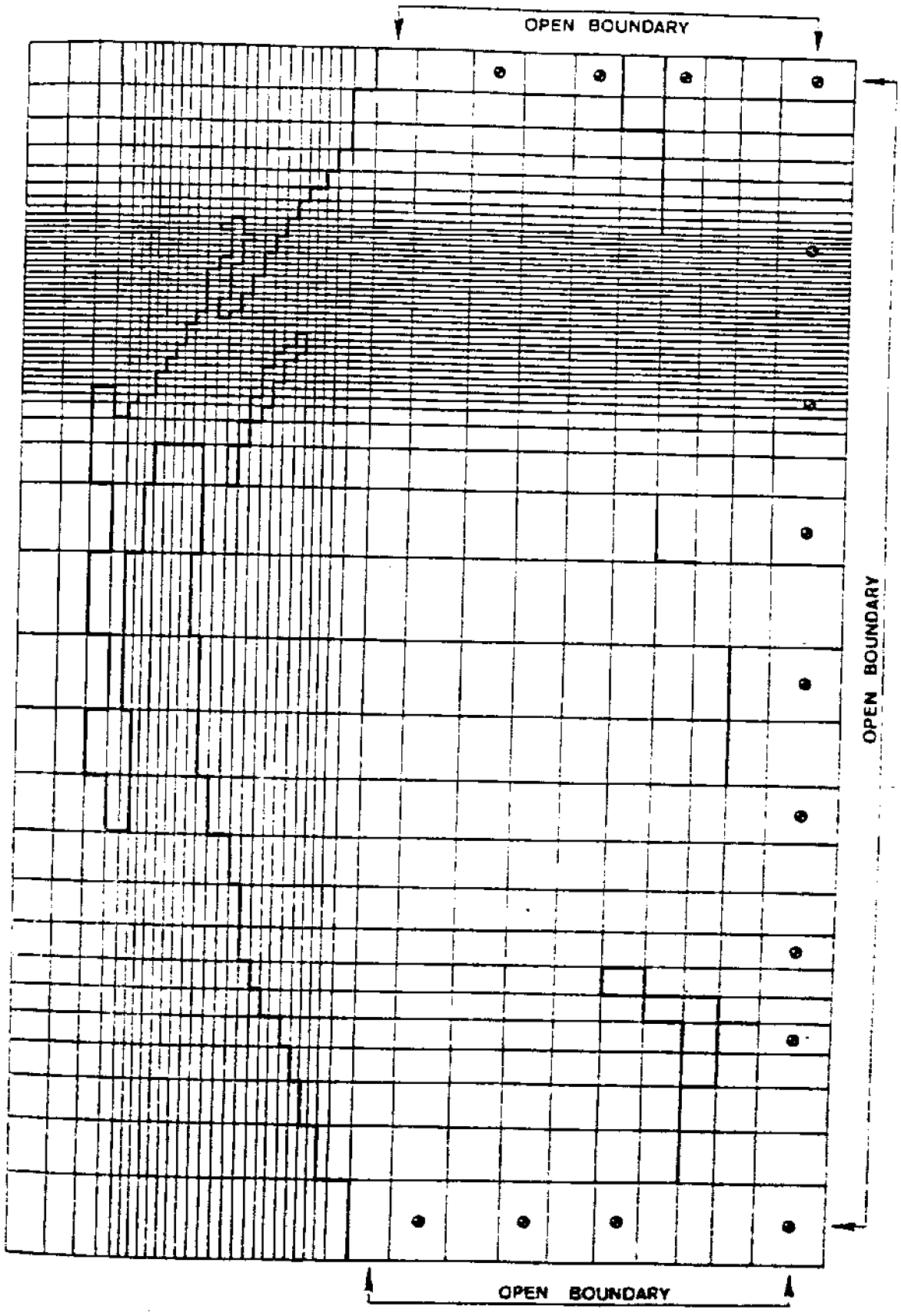
OPEN BOUNDARY
OPEN BOUNDARY
OPEN BOUNDARY

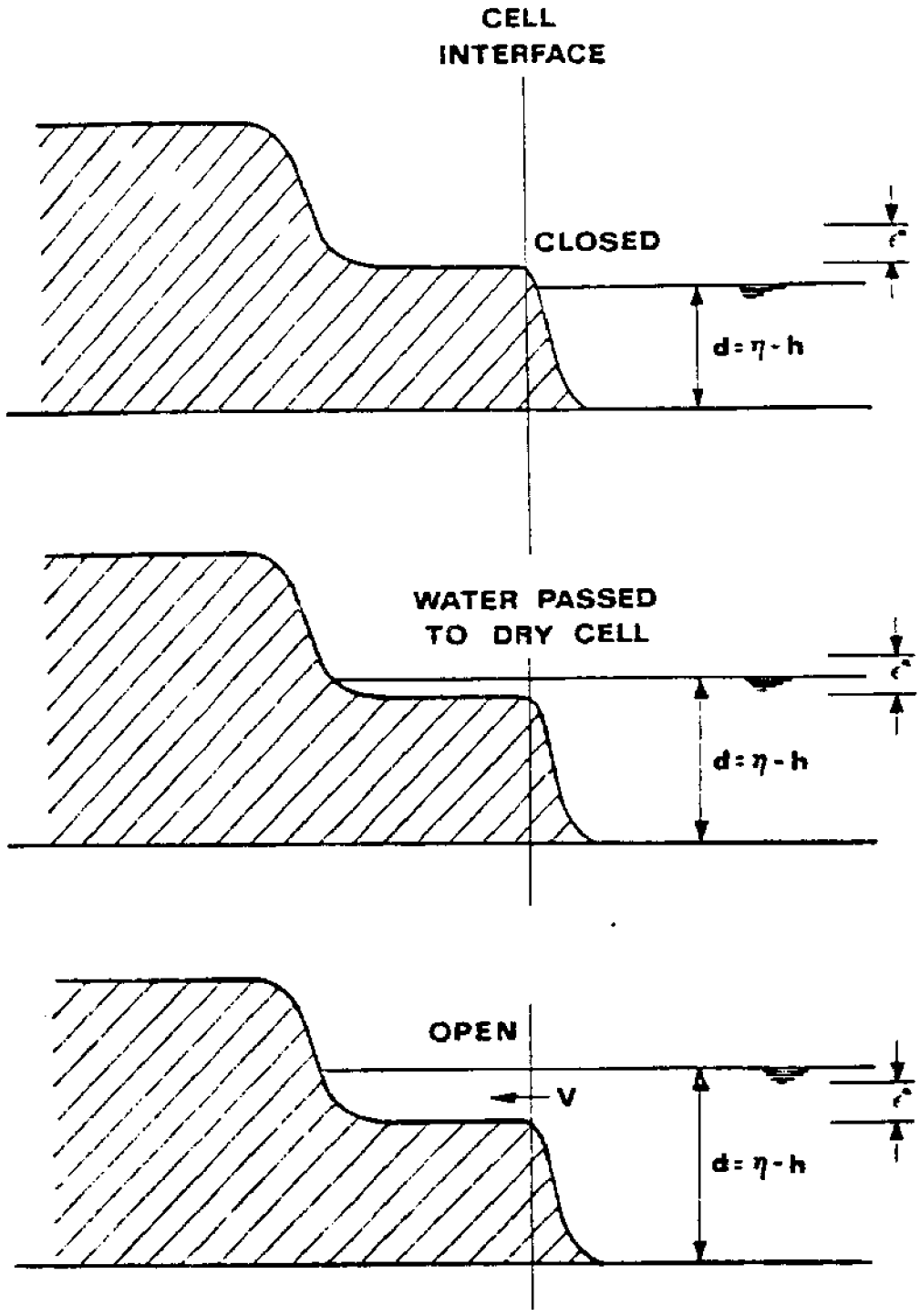

Figure III.5. Flood Cell Treatment

3.5.3 Subgrid Barriers

Subgrid barriers are defined along cell interfaces. The three types of subgrid barriers are shown in Figure III.6.

The first type, namely exposed barrier, does not permit fluid flow across the appropriate flagged cell faces. As the water level increases the exposed barrier becomes an overtopping or submerged barrier. Overtopping barriers can be submerged during one segment of the simulation and totally exposed in another.

For submerged and overtopping barriers the flow rate across the barrier is again computed by using the transport formula, equation (3.60). The admittance coefficient (C_0) for the submerged and overtapping barriers will differ from that governing the initial movement of water onto a dry cell.

3.6 An Introduction to the Salinity Equation

As an introduction to the salinity computations consider an approach similar to that of Schmaltz [20,21]. The simplified equation

$$\frac{\partial c}{\partial t} + \frac{\partial (uc)}{\partial x} + \frac{\partial (vc)}{\partial y} = 0 \tag{3.61}$$

will be analyzed.

The following finite difference form of (3.61) is considered.

$$c_{i,k}^{n+1} = c_{i,k}^{n} - \frac{\Delta t}{\Delta x \Delta y} (f_R - f_L + g_T - g_B) \tag{3.62}$$

where

$f_R \equiv$ right flux for grid cell surrounding $c_{i,k}$

$f_L \equiv$ left flux for grid cell surrounding $c_{i,k}$

$g_T \equiv$ top flux for grid cell surrounding $c_{i,k}$

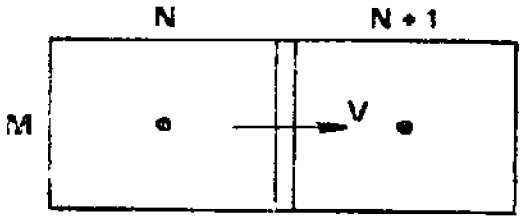

BARRIER AT CELL INTERFACE (HEIGHT b)

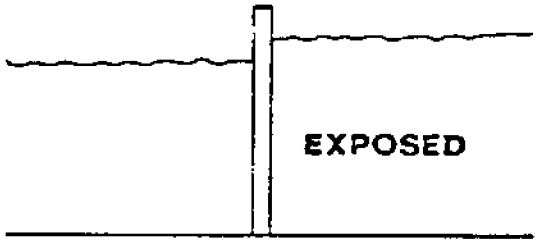

$V = 0$

$\eta_N < b + \epsilon^*$

$\eta_{N+1} < b + \epsilon^*$

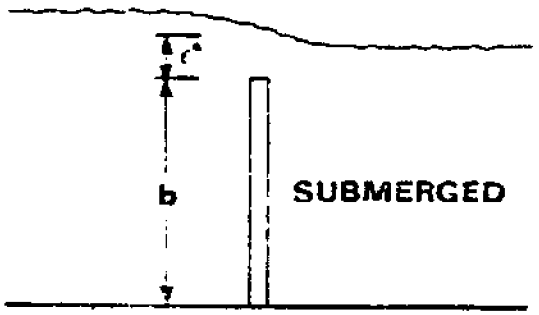

$\eta_N > b + \epsilon^*$

$\eta_{N+1} > b + \epsilon^*$

V CONTROLLED BY

SPECIAL CHEZY COEFFICIENT

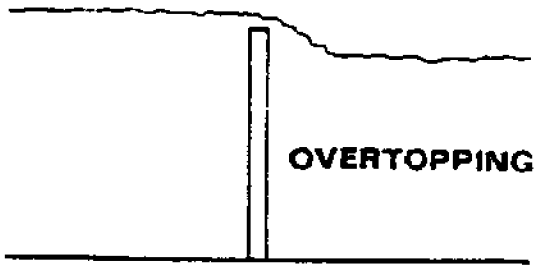

$\eta_N > b + \epsilon^*$

$\eta_{N+1} < b + \epsilon^*$

$V = C_D d_u \sqrt{d_u}$

WATER IS PASSED TO LOW SIDE

ACCORDING TO FLOW RATE V

Figure III.6. Barrier Conditions Treated by WIFM

$g_B \equiv$ bottom flux for grid cell surrounding $c_{i,k}$

The quantities in Equation 3.62 are indicated in Figure III.7. Several

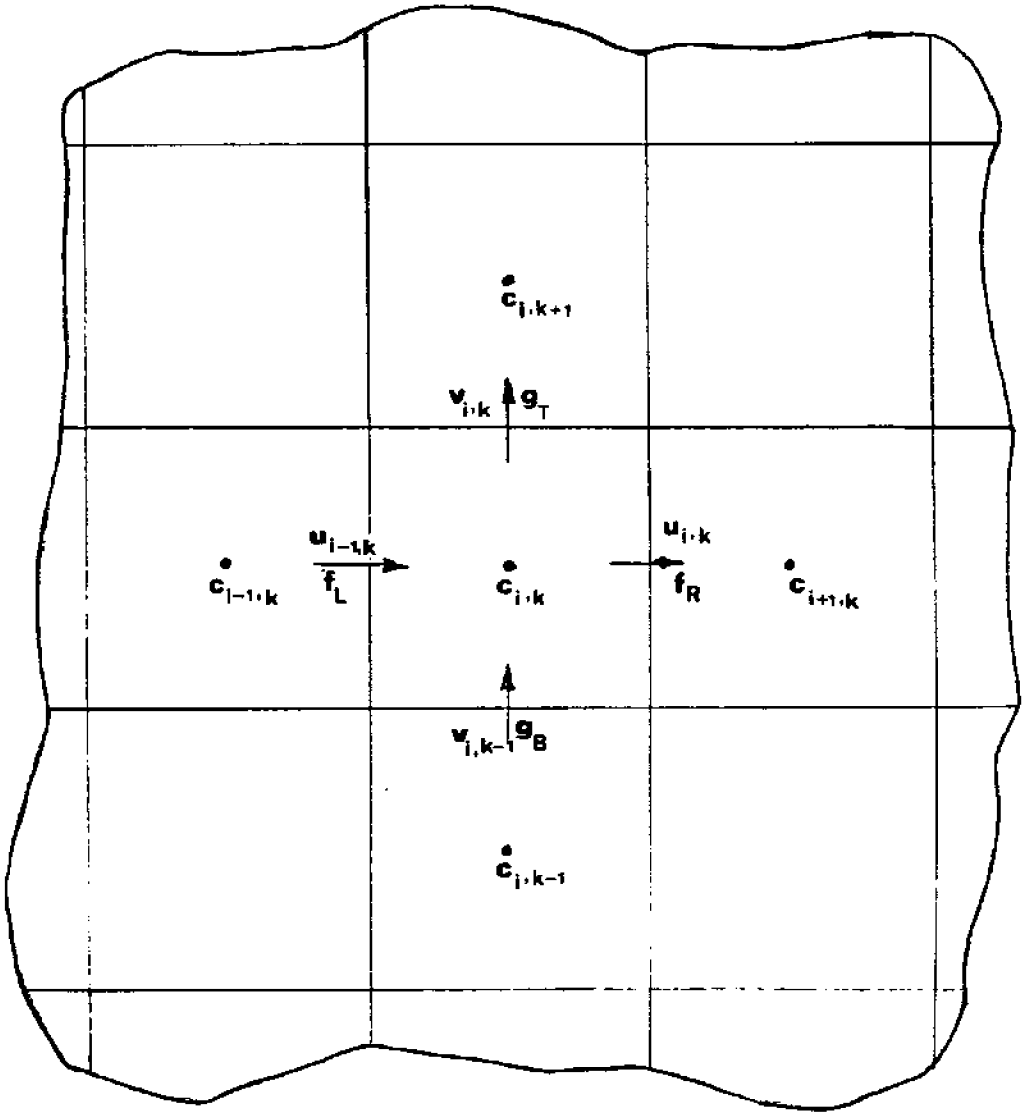

Figure III.7 Notation for Simplified Salinity Equation

approximations may be obtained for f_R, f_L, g_T, and g_B based upon alternative finite difference schemes. The solution scheme used in this work (flux corrected transport) will make use of two finite difference approximations for the terms in equation 3.62; the upwind difference and the central difference approximations.

3.6.1 Upwind Solution Scheme

The upwind solution scheme insures that changes in salinity for a cell are consistent with the direction of the fluid velocity. The finite difference approximations differ depending on the direction of the fluid velocity at each cell face.

$$f_R = \begin{cases} u_{i,k} \cdot c_{i+1,k}(\Delta y) & u_{i,k} < 0 \\ u_{i,k} \cdot c_{i,k}(\Delta y) & u_{i,k} > 0 \end{cases} \qquad (3.63)$$

$$f_L = \begin{cases} u_{i-1,k} \cdot c_{i,k}(\Delta y) & u_{i-1,k} < 0 \\ u_{i-1,k} \cdot c_{i-1,k}(\Delta y) & u_{i-1,k} > 0 \end{cases} \qquad (3.64)$$

$$g_T = \begin{cases} v_{i,k} \cdot c_{i,k+1}(\Delta x) & v_{i,k} < 0 \\ v_{i,k} \cdot c_{i,k}(\Delta x) & v_{i,k} > 0 \end{cases} \qquad (3.65)$$

$$g_B = \begin{cases} v_{i,k-1} \cdot c_{i,k}(\Delta x) & v_{i,k-1} < 0 \\ v_{i,k-1} \cdot c_{i,k-1}(\Delta x) & v_{i,k-1} > 0 \end{cases} \qquad (3.66)$$

Let us consider the case $u_{i,k} > 0$, $u_{i-1,k} > 0$ and $v_{i,k} \cdot v_{i,k-1} > 0$ to illustrate the final form by substituting the above relations under these conditions into Equation 3.62:

$$\frac{c_{i,k}^{n+1} - c_{i,k}^{n}}{\Delta t} = - \frac{(u_{i,k}c_{i,k} - u_{i-1,k}c_{i-1,k})}{\Delta x}$$

$$- \frac{(v_{i,k}c_{i,k} - v_{i,k-1}c_{i,k-1})}{\Delta y} \qquad (3.67)$$

If $u_{i,k} = u_{i-1,k}$ and $v_{i,k} = v_{i-1,k}$, then the above equation reduces to the following form:

$$\frac{c_{i,k}^{n+1} - c_{i,k}^{n}}{\Delta t} = - \frac{u_{i,k}}{\Delta x} (c_{i,k} - c_{i-1,k}) - \frac{v_{i,k}}{\Delta y} (c_{i,k} - c_{i,k-1}) \qquad (3.68)$$

and the space differences are only first order accurate. In computation, an artificial (numerical) dispersion is introduced by this scheme.

3.6.2 Central Difference Solution Scheme

A more accurate mathematical representation (2nd order accuracy) but less accurate representation from a physical viewpoint is obtained by representing f_R, f_L, g_T and g_B as central finite differences.

$$f_R = u_{i,k} \frac{(c_{i+1,k} + c_{i,k})}{2} (\Delta y) \qquad (3.69)$$

$$f_L = u_{i-1,k} \frac{(c_{i-1,k} + c_{i,k})}{2} (\Delta y) \qquad (3.70)$$

$$g_T = v_{i,k} \frac{(c_{i,k} + c_{i,k+1})}{2} (\Delta x) \qquad (3.71)$$

$$g_B = v_{i,k-1} \frac{(c_{i,k} + c_{i,k-1})}{2} (\Delta x) \qquad (3.72)$$

Substitute the above relations in Equation 3.62 to obtain:

$$c_{i,k}^{n+1} = c_{i,k}^{n} - \frac{\Delta t}{\Delta x} \left[u_{i,k} \frac{(c_{i+1,k} + c_{i,k})}{2} - u_{i-1,k} \frac{(c_{i,k} + c_{i-1,k})}{2} \right] \qquad (3.73)$$

$$- \frac{\Delta t}{\Delta y} \left[v_{i,k} \frac{(c_{i,k} + c_{i,k+1})}{2} - v_{i,k-1} \frac{(c_{i,k} + c_{i,k-1})}{2} \right]$$

Note if $u_{i,k} = u_{i-1,k}$ and $v_{i,k} = v_{i,k-1}$, then the equation reduces to

$$\frac{c_{i,k}^{n+1} - c_{i,k}^{n}}{\Delta t} = - u_{i,k} \frac{(c_{i+1,k} - c_{i-1,k})}{2\Delta x} - v_{i,k} \frac{(c_{i,k+1} - c_{i,k-1})}{2\Delta y} \tag{3.74}$$

Observe that the spatial differences are centered in the x and z directions and are thus second order accurate. Although these forms are more accurate than upwind differencing, an oscillatory behavior has been observed when they are applied in regions where large salinity gradients exist. From a physical viewpoint, this method can permit salinity transport opposite in direction to the fluid velocity at a cell face. Negative salinity values for a cell may be obtained using this difference scheme.

3.6.3 Combined Upwind and Central Difference Solution Scheme

In order to avoid negative concentrations but reduce the smearing effect, the following combined scheme has been suggested.

$$f_R = \begin{cases} u_{i,k} c_{i,k} (\Delta y) & u_{i,k} > 0 \quad c_{i,k} < c_{i+1,k} \\ u_{i,k} \dfrac{(c_{i,k} + c_{i+1,k})}{2} (\Delta y) & u_{i,k} > 0 \quad c_{i,k} > c_{i+1,k} \\ u_{i,k} c_{i+1,k} (\Delta y) & u_{i,k} < 0 \quad c_{i,k} > c_{i+1,k} \\ u_{i,k} \dfrac{(c_{i,k} + c_{i+1,k})}{2} (\Delta y) & u_{i,k} < 0 \quad c_{i,k} < c_{i+1,k} \end{cases} \tag{3.75}$$

$$f_L = \begin{cases} u_{i-1,k} c_{i-1,k} (\Delta y) & u_{i-1,k} > 0 \quad c_{i-1,k} < c_{i,k} \\ u_{i-1,k} \dfrac{(c_{i-1,k} + c_{i,k})}{2} (\Delta y) & u_{i-1,k} > 0 \quad c_{i-1,k} > c_{i,k} \\ u_{i-1,k} c_{i,k} (\Delta y) & u_{i-1,k} < 0 \quad c_{i-1,k} > c_{i,k} \\ u_{i-1,k} \dfrac{(c_{i,k} + c_{i-1,k})}{2} (\Delta y) & u_{i-1,k} < 0 \quad c_{i-1,k} < c_{i,k} \end{cases} \tag{3.76}$$

Analogous expressions hold for g_T and g_B. This scheme is similar to second upwind differencing and uses the central difference approximations as often as possible. Lower order differencing (first upwind) is employed as necessary to eliminate negative salinity values. The effective advective concentration employed in an outgoing flux is always less than or equal to the concentration of the cell providing the flux.

3.6.4 Flux-Corrected-Transport (FCT) Solution Scheme

This method was originally developed by Boris and Book [2]. It was subsequently improved, and generalized by Zalesak [26]. It is a two step method, first involving a lower order calculation and a correction to a higher order solution. The upwind solution scheme as given by Equations 3.63 to 3.66 is used to compute the first order result

$$c_{i,k}^{td} = c_{i,k}^{n} - \frac{\Delta t}{\Delta x \Delta y} (f_R^1 - f_L^1 + g_T^1 - g_B^1) \tag{3.77}$$

where $c_{i,k}^{td}$ is the first order (transported and diffused) concentration. A higher order scheme, e.g., the central difference scheme as given by equations 3.69 to 3.72, can be applied to compute higher order fluxes f_R^2, f_L^2, g_T^2, and g_B^2.

Antidiffusive fluxes are defined as

$$\begin{aligned} A_R &= f_R^2 - f_R^1 \\ A_L &= f_L^2 - f_L^1 \\ A_T &= g_T^2 - g_T^1 \\ A_B &= g_B^2 - g_B^1 \end{aligned} \tag{3.78}$$

It is these antidiffusive fluxes which are limited in the Zalesak procedure such that

$$A_R^c = A_R \cdot D_{i+\frac{1}{2},k} \qquad 0 \leq D_{i+\frac{1}{2},k} \leq 1$$

$$A_L^c = A_L \cdot D_{i-\frac{1}{2},k} \qquad 0 \leq D_{i-\frac{1}{2},k} \leq 1$$

$$A_T^c = A_T \cdot D_{i,k+\frac{1}{2}} \qquad 0 \leq D_{i,k+\frac{1}{2}} \leq 1 \tag{3.79}$$

$$A_B^c = A_B \cdot D_{i,k-\frac{1}{2}} \qquad 0 \leq D_{i,k-\frac{1}{2}} \leq 1$$

Finally

$$c_{i,k}^{n+1} = c_{i,k}^{td} - \frac{\Delta t}{\Delta x \Delta z}\left(A_R^c - A_L^c + A_T^c - A_B^c\right) \tag{3.80}$$

3.7 Fully Multidimensional Flux-Corrected Transport Algorithms for Fluids

Consider the simplified two-dimensional salinity equation in the following fashion. Two solutions are introduced:

$$c_{i,j}^{Ltd} = c_{i,j}^{n} - (\Delta x_{ij}\Delta y_{ij})^{-1}(\Delta t)(F_{i+\frac{1}{2},j}^{L} - F_{i-\frac{1}{2},j}^{L} + F_{i,j+\frac{1}{2}}^{L} - F_{i,j-\frac{1}{2}}^{L}) \tag{3.81}$$

and

$$c_{i,j}^{Htd} = c_{i,j}^{n} - (\Delta x_{ij}\Delta y_{ij})^{-1}(\Delta t)(F_{i+\frac{1}{2},j}^{H} - F_{i-\frac{1}{2},j}^{H} + F_{i,j+\frac{1}{2}}^{H} - F_{i,j-\frac{1}{2}}^{H}) \tag{3.82}$$

where $c_{i,j}^{Ltd}$ represents the lower order transported and diffused solution and $c_{i,j}^{Htd}$ represents $w_{i,j}^{Htd}$ the higher order solution. We observe that the difference between the solutions may be written as

$$c^{Htd}_{i,j} - c^{Ltd}_{i,j} = -(\Delta x_{i,j}\Delta y_{i,j})^{-1}(\Delta t)[(F^{H}_{i+\frac{1}{2},j} - F^{L}_{i+\frac{1}{2},j}) - (F^{H}_{i-\frac{1}{2},j} - F^{L}_{i-\frac{1}{2},j}) + (F^{H}_{i,j+\frac{1}{2}} - F^{L}_{i,j+\frac{1}{2}}) - (F^{H}_{i,j-\frac{1}{2}} - F^{L}_{i,j-\frac{1}{2}})] \tag{3.83}$$

Note this difference is written as an array of fluxes between different grid points and is the condition required to implement the flux corrected transport scheme.

Flux-corrected transport is implemented in the following fashion for implicit difference schemes for $w^{Ltd}_{i,j}$ and $w^{Htd}_{i,j}$:

1. Compute a lower order solution $c^{Ltd}_{i,j}$ for all cells.
2. Calculate the flux rate through each face of each cell ($F^{L}_{i+\frac{1}{2},j}$, $F^{L}_{i-\frac{1}{2},j}$, $F^{L}_{i,j+\frac{1}{2}}$, $F^{L}_{i,j-\frac{1}{2}}$)
3. Compute a higher order solution $c^{Htd}_{i,j}$ for all cells
4. Calculate the flux rate through each face of each cell ($F^{H}_{i+\frac{1}{2},j}$, $F^{H}_{i-\frac{1}{2},j}$, $F^{H}_{i,j+\frac{1}{2}}$, $F^{H}_{i,j-\frac{1}{2}}$)
5. Determine the antidiffusive fluxes $(F^{H}-F^{L}) = (A)$ for each face of each cell.
6. Limit these antidiffusive fluxes (A) as follows:

$$A^{c}_{i+\frac{1}{2},j} = A_{i+\frac{1}{2},j}D_{i+\frac{1}{2},j} \qquad 0 \le D_{i+\frac{1}{2},j} \le 1 \tag{3.84}$$

$$A^{c}_{i,j+\frac{1}{2}} = A_{i,j+\frac{1}{2}}D_{i,j+\frac{1}{2}} \qquad 0 \le D_{i,j+\frac{1}{2}} \le 1$$

etc.

The determination of the coefficients (D) will be discussed subsequently.

7. Apply the limited antidiffusive fluxes to determine the solution for the new time step.

$$c_{i,j}^{n+1} = c_{i,j}^{Ltd} - (\Delta x_{ij}\Delta y_{ij})^{-1}\,(\Delta t)(A_{i+\frac{1}{2},j}^{c} - A_{i-\frac{1}{2},j}^{c} + A_{i,j+\frac{1}{2}}^{c} - A_{i,j-\frac{1}{2}}^{c}) \tag{3.85}$$

The crucial step in the above process is Step 6, the flux-limiting stage. The following quantities are computed to allow determination of the flux limiting coefficients (D).

$P_{i,j}^{+}$ = the sum of all antidiffusive fluxes <u>into</u> grid point (i,j)

$$= \max(0, A_{i-\frac{1}{2},j}) - \min(0, A_{i+\frac{1}{2},j}) + \max(0, A_{i,j-\frac{1}{2}}) - \min(0, A_{i,j+\frac{1}{2}}) \tag{3.86}$$

$$Q_{i,j}^{+} = (c_{i,j}^{max} - c_{i,j}^{Ltd})(\Delta x_{ij}\Delta y_{ij}) \tag{3.87}$$

$$R_{i,j}^{+} = \begin{cases} \min(1, Q_{i,j}^{+}/P_{i,j}^{+}) & P_{i,j}^{+} > 0 \\ 0 & P_{i,j}^{+} = 0 \end{cases} . \tag{3.88}$$

$P_{i,j}^{-}$ = the sum of all antidiffusive fluxes <u>out</u> of grid point (i,j)

$$= \max(0, A_{i+\frac{1}{2},j}) - \min(0, A_{i-\frac{1}{2},j}) + \max(0, A_{i,j+\frac{1}{2}}) - \min(0, A_{i,j-\frac{1}{2}}) \tag{3.89}$$

$$Q_{i,j}^{-} = (c_{i,j}^{Ltd} - c_{i,j}^{min})(\Delta x_{i,j}\Delta y_{i,j}) \tag{3.90}$$

$$R_{i,j}^{-} = \begin{cases} \min(1, Q_{i,j}^{-}/P_{i,j}^{-}) & P_{i,j}^{-} > 0 \\ 0 & P_{i,j} = 0 \end{cases} \tag{3.91}$$

The limiting coefficients are then given by

$$D_{i+\frac{1}{2},j} = \begin{cases} \min\,(R^{+}_{i+1,j},\ R^{-}_{i,j}) & A_{i+\frac{1}{2},j} \geq 0 \\ \min\,(R^{+}_{i,j},\ R^{-}_{i+1,j}) & A_{i+\frac{1}{2},j} < 0 \end{cases} \tag{3.92}$$

$$D_{i,j+\frac{1}{2}} = \begin{cases} \min\,(R^{+}_{i,j+1},\ R^{-}_{i,j}) & A_{i,j+\frac{1}{2}} \geq 0 \\ \min\,(R^{+}_{i,j},\ R^{-}_{i,j+1}) & A_{i,j+\frac{1}{2}} < 0 \end{cases} \tag{3.93}$$

Prior to the application of equations 3.86 thru 3.93 the following calculations are necessary.

$$A_{i+\frac{1}{2},j} = 0 \quad \text{for} \quad A_{i+\frac{1}{2},j}(c^{Ltd}_{i+1,j} - c^{Ltd}_{i,j}) < 0$$

$$\text{or} \quad A_{i+\frac{1}{2},j}(c^{Ltd}_{i+2,j} - c^{Ltd}_{i+1,j}) < 0 \tag{3.94}$$

$$\text{or} \quad A_{i+\frac{1}{2},j}(c^{Ltd}_{i,j} - c^{Ltd}_{i-1,j}) < 0$$

$$A_{i,j+\frac{1}{2}} = 0 \quad \text{for} \quad A_{i,j+\frac{1}{2}}(c^{Ltd}_{i,j+1} - c^{Ltd}_{i,j}) < 0$$

$$A_{i,j+\frac{1}{2}}(c^{Ltd}_{i,j+2} - c^{Ltd}_{i,j+1}) < 0 \tag{3.95}$$

$$A_{i,j+\frac{1}{2}}(c^{Ltd}_{i,j} - c^{Ltd}_{i,j-1}) < 0$$

$$c^{a}_{i,j} = \max\,(c^{n}_{i,j},\ c^{Ltd}_{i,j}) \tag{3.96}$$

$$c^{b}_{i,j} = \min\,(c^{n}_{i,j},\ c^{Ltd}_{i,j}) \tag{3.97}$$

$$c^{max}_{i,j} = \max\,(c^{a}_{i-1,j},\ c^{a}_{i,j},\ c^{a}_{i+1,j},\ c^{a}_{i,j-1},\ c^{a}_{i,j+1}) \tag{3.98}$$

$$c^{min}_{i,j} = \min\,(c^{b}_{i-1,j},\ c^{b}_{i,j},\ c^{b}_{i+1,j},\ c^{b}_{i,j-1},\ c^{b}_{i,j+1}) \tag{3.99}$$

Zalesak notes that while the solution will be kept between c^{min} and c^{max}, monotonicity may in rare cases be violated.

3.8 The Complete Salinity Equation

Consider application to the general one constituent water quality equation

$$\frac{\partial(HP)}{\partial t} + \frac{\partial(HuP)}{\partial x} + \frac{\partial(HvP)}{\partial y} - \frac{\partial}{\partial x}\left(HD_x \frac{\partial P}{\partial x}\right) - \frac{\partial\left(HD_y \frac{\partial P}{\partial y}\right)}{\partial y} - \underset{\text{source}}{HS_A} = 0 \tag{3.100}$$

In our use of the equation, P is the salinity; however, the equation can be used to consider an arbitrary pollutant, not affected by the fluid density.

The finite difference scheme is the ADI implicit formulation with the time step Δt being split in half to advance the solution from t to t + Δt. Variables are defined as shown in Figure III.8. In the first sweep from t → t + $\Delta t/2$ the following finite difference equations are employed in an x sweep of the grid.

$$\begin{aligned}
&\frac{P^{n+\frac{1}{2}}_{j,k} D^{n+\frac{1}{2}}_{j,k} - P^{n}_{j,k} D^{n}_{j,k}}{\frac{\Delta t}{2}} - \left[sx^{n}_{j-\frac{1}{2},k}\, u^{n+\frac{1}{2}}_{j-\frac{1}{2},k}\left(P^{n+\frac{1}{2}}_{j-\frac{1}{2},k} + P^{n+\frac{1}{2}}_{j,k}\right)\right.\\
&\left. - sx^{n}_{j+\frac{1}{2},k}\, u^{n+\frac{1}{2}}_{j+\frac{1}{2},k}\left(P^{n+\frac{1}{2}}_{j,k} + P^{n+\frac{1}{2}}_{j+1,k}\right)\right]\frac{1}{4\Delta x} - \left[sy^{n}_{j,k-\frac{1}{2}}\, v^{n}_{j,k-\frac{1}{2}}\right.\\
&\left. \times \left(P^{n}_{j,k-1} + P^{n}_{j,k}\right) - sy^{n}_{j,k+\frac{1}{2}}\, v^{n}_{j,k+\frac{1}{2}}\left(P^{n}_{j,k+1} + P^{n}_{j,k}\right)\right]\frac{1}{4\Delta y}\\
&+ \frac{1}{2(\Delta x)^2}\left[sx^{n+\frac{1}{2}}_{j-\frac{1}{2},k}\, D^{n+\frac{1}{2}}_{x_{j-\frac{1}{2},k}}\left(P^{n+\frac{1}{2}}_{j,k} - P^{n+\frac{1}{2}}_{j-1,k}\right) - sx^{n+\frac{1}{2}}_{j+\frac{1}{2},k}\right.\\
&\left. \times D^{n+\frac{1}{2}}_{x_{j+\frac{1}{2},k}}\left(P^{n+\frac{1}{2}}_{j+1,k} - P^{n+\frac{1}{2}}_{j,k}\right)\right] + \frac{1}{2(\Delta y)^2}\left[sy^{n}_{j,k-\frac{1}{2}}\, D^{n}_{y_{j,k-\frac{1}{2}}}\right.\\
&\left. \times \left(P^{n}_{j,k} - P^{n}_{j,k-1}\right) - sy^{n}_{j,k+\frac{1}{2}}\, D^{n}_{y_{j,k+\frac{1}{2}}}\left(P^{n}_{j,k+1} - P^{n}_{j,k}\right)\right] = 0
\end{aligned} \tag{3.101}$$

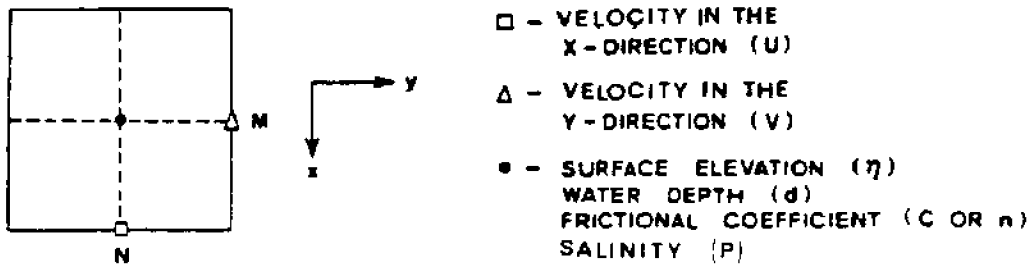

Figure III.8. Space Staggered Grid System

where

$$sx^{n}_{j\pm\frac{1}{2},k} = (\eta^{n}_{j\pm1,k} + \eta^{n}_{j,k} + h_{j\pm\frac{1}{2},k-\frac{1}{2}} + h_{j\pm\frac{1}{2},k+\frac{1}{2}})$$

$$sy^{n}_{j,k\pm\frac{1}{2}} = (\eta^{n}_{j,k\pm1} + \eta^{n}_{j,k} + h_{j-\frac{1}{2},k\pm\frac{1}{2}} + h_{j+\frac{1}{2},k\pm\frac{1}{2}})$$

The equation for the x sweep is then written in the following general form:

$$a_j\, P^{n+\frac{1}{2}}_{j-1,k} + b_j\, P^{n+\frac{1}{2}}_{j,k} + c_j\, P^{n+\frac{1}{2}}_{j+1,k} = D_j \qquad (3.102)$$

Let us now consider the y sweep in which the solution is advanced from time level $n+\frac{1}{2} \rightarrow n$ or $t + \Delta t/2 \rightarrow t + \Delta t$. The constituent equation for the y sweep is expressed as:

$$\delta_{+t/2}[P(\bar{\bar{h}} + \eta)] + \delta_x[(\bar{h}^y + \bar{\eta}^x)uP^{-x}] + \delta_y[(\bar{h}^x + \bar{\eta}^y)\, v_t\, \bar{P}^y_t]$$

$$- \delta_x[(\bar{h}^y + \bar{\eta}^x)\, D_x\, \delta_x\, P] - \delta_y[(\bar{h}^x + \bar{\eta}^y)\, D_{y_t}\, \delta_y\, P_t] = 0 \quad \text{at} \quad j,k,n+\tfrac{1}{2}$$

where

$$\delta_{+t/2}[P(\bar{\bar{h}} + \eta)] = \frac{P^{n+1}_{j,k}(\bar{\bar{h}} + \eta^{n+1}_{j,k}) - P^{n}_{j,k}(\bar{\bar{h}} + \eta^{n+\frac{1}{2}}_{j,k})}{\frac{\Delta t}{2}}$$

with

$$4\bar{\bar{h}} = h_{j+\frac{1}{2},k+\frac{1}{2}} + h_{j+\frac{1}{2},k-\frac{1}{2}} + h_{j-\frac{1}{2},k+\frac{1}{2}} + h_{j-\frac{1}{2},k-\frac{1}{2}}$$

$$\delta_x[(\bar{h}^y + \bar{\eta}^x)\ u\bar{P}^x] = \delta_x[\frac{(h_{j,k+\frac{1}{2}} + h_{j,k-\frac{1}{2}} + \eta^{n+\frac{1}{2}}_{j+\frac{1}{2},k} + \eta^{n+\frac{1}{2}}_{j-\frac{1}{2},k})}{2}\ u$$

$$x\ \frac{(P^{n+\frac{1}{2}}_{j+\frac{1}{2},k} + P^{n+\frac{1}{2}}_{j-\frac{1}{2},k})}{2}] = [(h_{j+\frac{1}{2},k+\frac{1}{2}}$$

$$+ h_{j+\frac{1}{2},k-\frac{1}{2}} + \eta^{n+\frac{1}{2}}_{j+1,k} + \eta^{n+\frac{1}{2}}_{j,k})\ u^{n+\frac{1}{2}}_{j+\frac{1}{2},k}\ (P^{n+\frac{1}{2}}_{j+1,k}$$

$$+ P^{n+\frac{1}{2}}_{j,k})/4\Delta x] - [(h_{j-\frac{1}{2},k+\frac{1}{2}} + h_{j-\frac{1}{2},k-\frac{1}{2}}$$

$$+ \eta^{n+\frac{1}{2}}_{j,k} + \eta^{n+\frac{1}{2}}_{j-1,k})\ u^{n+\frac{1}{2}}_{j-\frac{1}{2},k}\ (P^{n+\frac{1}{2}}_{j,k} + P^{n+\frac{1}{2}}_{j-1,k})/4\Delta x]$$

$$\delta_y[(\bar{h}^x + \bar{\eta}^y)v_t\bar{P}^y_t] = \delta_y[\frac{(h_{j+\frac{1}{2},k} + h_{j-\frac{1}{2},k} + \eta^{n+\frac{1}{2}}_{j,k+\frac{1}{2}} + \eta^{n+\frac{1}{2}}_{j,k-\frac{1}{2}})}{2}\ v_t$$

$$x\ \frac{(P^{n+1}_{j,k+\frac{1}{2}} + P^{n+1}_{j,k-\frac{1}{2}})}{2}] = [(h_{j+\frac{1}{2},k+\frac{1}{2}}$$

$$+ h_{j-\frac{1}{2},k+\frac{1}{2}} + \eta^{n+\frac{1}{2}}_{j,k+1} + \eta^{n+\frac{1}{2}}_{j,k})\ v^{n+1}_{j,k+\frac{1}{2}}\ (\ P^{n+1}_{j,k+1}$$

$$+ P^{n+1}_{j,k}\ )/4\Delta y] - [(h_{j+\frac{1}{2},k-\frac{1}{2}} + h_{j-\frac{1}{2},k-\frac{1}{2}}$$

$$+ \eta^{n+\frac{1}{2}}_{j,k} + \eta^{n+\frac{1}{2}}_{j,k-1})\ v^{n+1}_{j,k-\frac{1}{2}}\ (\ P^{n+1}_{j,k} + P^{n+1}_{j,k-1}\ )/4\Delta y]$$

$$\delta_x[(\bar{h}^y + \bar{\eta}^x)D_x\delta_x P] = \delta_x[\frac{(h_{j,k+\frac{1}{2}} + h_{j,k-\frac{1}{2}} + \eta^{n+\frac{1}{2}}_{j+\frac{1}{2},k} + \eta^{n+\frac{1}{2}}_{j-\frac{1}{2},k})}{2}\ D_x$$

$$x\ \frac{(P^{n+\frac{1}{2}}_{j+\frac{1}{2},k} - P^{n+\frac{1}{2}}_{j-\frac{1}{2},k})}{\Delta x}] = [(h_{j+\frac{1}{2},k+\frac{1}{2}}$$

$$+ h_{j+\frac{1}{2},k-\frac{1}{2}} + \eta^{n+\frac{1}{2}}_{j+1,k} + \eta^{n+\frac{1}{2}}_{j,k})\ D^{n+\frac{1}{2}}_{x_{j+\frac{1}{2},k}}(P^{n+\frac{1}{2}}_{j+1,k}$$

$$- P^{n+\frac{1}{2}}_{j,k}\ )/2\Delta x^2] - [(h_{j-\frac{1}{2},k+\frac{1}{2}} + h_{j-\frac{1}{2},k-\frac{1}{2}}$$

$$+ \eta^{n+\frac{1}{2}}_{j,k} + \eta^{n+\frac{1}{2}}_{j-1,k})\ D^{n+\frac{1}{2}}_{x_{j-\frac{1}{2},k}}(P^{n+\frac{1}{2}}_{j,k} + P^{n+\frac{1}{2}}_{j-1,k})/2\Delta x^2]$$

$$\delta_y[(\bar{h}^x + \bar{\eta}^y)D_{y_t}\delta_y P_t] = \delta_y\{\frac{(h_{j+\frac{1}{2},k} + h_{j-\frac{1}{2},k} + \eta^{n+\frac{1}{2}}_{j,k+\frac{1}{2}} + \eta^{n+\frac{1}{2}}_{j,k-\frac{1}{2}})}{2} D_{y_t}$$

$$x \frac{(P^{n+1}_{j,k+\frac{1}{2}} - P^{n+1}_{j,k-\frac{1}{2}})}{\Delta y}] = [(h_{j+\frac{1}{2},k+\frac{1}{2}}$$

$$+ h_{j-\frac{1}{2},k+\frac{1}{2}} + \eta^{n+\frac{1}{2}}_{j,k+1} + \eta^{n+\frac{1}{2}}_{j,k}) D^{n+1}_{y_{j,k+\frac{1}{2}}}$$

$$x (P^{n+1}_{j,k+1} - P^{n+1}_{j,k})/2\Delta y^2] - [(h_{j+\frac{1}{2},k-\frac{1}{2}}$$

$$+ h_{j-\frac{1}{2},k-\frac{1}{2}} + \eta^{n+\frac{1}{2}}_{j,k} + \eta^{n+\frac{1}{2}}_{j,k-1}) D^{n+1}_{y_{j,k-\frac{1}{2}}}$$

$$x (P^{n+1}_{j,k} - P^{n+1}_{j,k-1})/2\Delta y^2]$$

The equation for the y sweep can be simplified to the form:

$$a_{k-1} P^{n+1}_{j,k-1} + b_k P^{n+1}_{j,k} + C_{k+1} P^{n+1}_{j,k+1} = D_k \qquad (3.103)$$

Transforming Equation (3.100) from x-y space to α_1 - α_2 space yields the following result.

$$(ds)_t + \frac{(dus)_{\alpha_1}}{\mu_1} + \frac{(dvs)_{\alpha_2}}{\mu_2} = \frac{1}{\mu_1}[dK_{\alpha_1}\frac{(s)_{\alpha_1}}{\mu_1}]_{\alpha_1} + \frac{1}{\mu_2}[dK_{\alpha_2}\frac{(s)_{\alpha_2}}{\mu_2}]_{\alpha_2} \qquad (3.104)$$

where d is introduced as the depth in place of H

$$( )_t = \partial/\partial t$$

$$( )_{\alpha_1} = \partial/\partial\alpha_1$$

$$( )_{\alpha_2} = \partial/\partial\alpha_2$$

Equation (3.104) is the actual equation that is the subject of numerical approximation in the WIFM model. Consider the space staggered grid shown in Figure III.9 and the datum convention illustrated in Figure III.10.

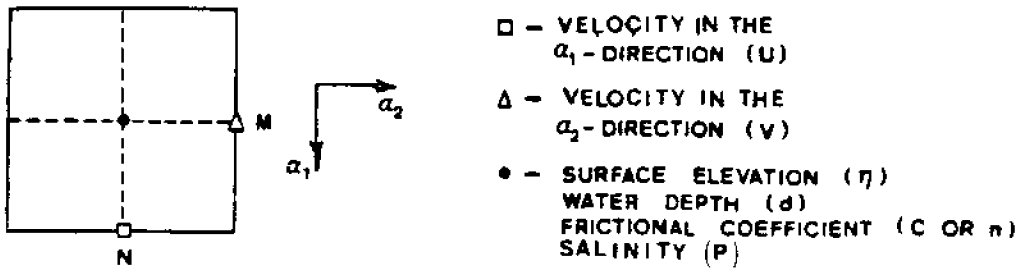

Figure III.9. Space Staggered Finite Difference Grid in Transformed Coordinates

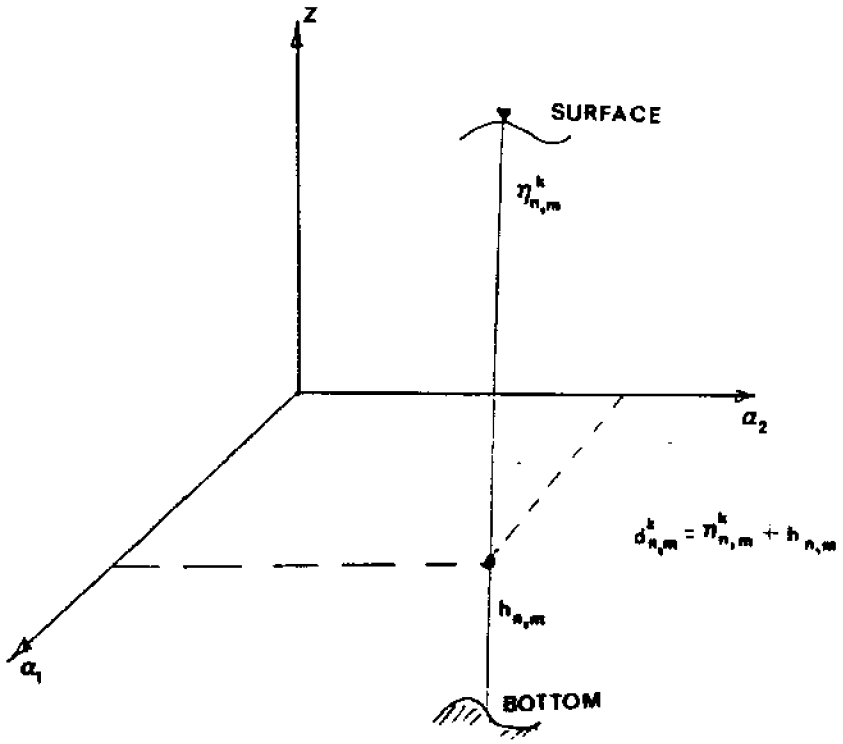

Figure III.10. Datum Convention Employed within the Space Staggered Grid System

Introduce the following notation as a prelude to formulating the numerical approximations. Define for an arbitrary variable $F^k_{n,m}$, where $t = k\Delta t$, $y = n\Delta y$, $x = m\Delta x$:

$$\delta^k_t(F^k_{n,m}) = F^{k+\frac{1}{2}}_{n,m} - F^k_{n,m} \tag{3.105}$$

$$\delta_{\alpha_1}(F^k_{n,m}) = F^k_{n,m+\frac{1}{2}} - F^k_{n,m-\frac{1}{2}} \tag{3.106}$$

$$\delta_{\alpha_2}(F^k_{n,m}) = F^k_{n+\frac{1}{2},m} - F^k_{n-\frac{1}{2},m} \tag{3.107}$$

$$\frac{\alpha_1}{F_{n,m}} = \frac{(F^k_{n,m+\frac{1}{2}} + F^k_{n,m-\frac{1}{2}})}{2} \tag{3.108}$$

$$\frac{\alpha_2}{F_{n,m}} = \frac{(F^k_{n+\frac{1}{2},m} + F^k_{n-\frac{1}{2},m})}{2} \tag{3.109}$$

3.8.1 Leendertse FTCS Multioperational Scheme

The approximations for the x-sweep using a forward time-centered space scheme may now be written as follows

$$\begin{aligned}
&{}^k\delta_t(ds) + \frac{\Delta t\ \delta_{\alpha_1}}{2\Delta\alpha_1(\mu_1)_m}\left(\frac{\alpha_1}{d^{k+\frac{1}{2}*}\ s^{k+\frac{1}{2}*}\ u^{k+\frac{1}{2}*}}\right) \\
&- \frac{\Delta t\ \delta_{\alpha_1}}{2\Delta\alpha_1^2(\mu_1)_m}\left[\frac{\alpha_1}{d^{k+\frac{1}{2}*}}\ K^{k+\frac{1}{2}*}_{\alpha_1}\ \frac{\delta_{\alpha_1}(s)^{k+\frac{1}{2}*}}{(\mu_2)_m}\right] \\
&+ \frac{\Delta t}{2(\mu_2)_n\Delta\alpha_2}\ \delta_{\alpha_2}\left(\frac{\alpha_2}{d^k s^k v^k}\right) \\
&- \frac{\Delta t\ \delta_{\alpha_2}}{2\Delta\alpha_2^2(\mu_2)_n}\left[\frac{\alpha_1}{d^k}\ K^k_{\alpha_2}\ \frac{\delta_{\alpha_2}(s^k)}{(\mu_2)_n}\right] = 0 \quad \text{at } (n,m)
\end{aligned} \tag{3.110}$$

If we place all terms at time level $k+\frac{1}{2}*$ on the left-hand side of the equation and expand

$$(ds)^{k+\frac{1}{2}*}_{n,m} + \frac{\Delta t}{2\Delta\alpha_1(\mu_1)_m}\left[\frac{(\eta^{k+\frac{1}{2}*}_{n,m+1} - h_{n,m+1} + \eta^{k+\frac{1}{2}*}_{n,m} - h_{n,m})}{2} u^{k+\frac{1}{2}*}_{n,m+\frac{1}{2}}\right.$$

$$\frac{(s^{k+\frac{1}{2}*}_{n,m+1} + s^{k+\frac{1}{2}*}_{n,m})}{2} - \frac{(\eta^{k+\frac{1}{2}*}_{n,m-1} - h_{n,m-1} + \eta^{k+\frac{1}{2}*}_{n,m} - h_{n,m})}{2} u^{k+\frac{1}{2}*}_{n,m-\frac{1}{2}}$$

$$\left.\frac{(s^{k+\frac{1}{2}*}_{n,m-1} + s^{k+\frac{1}{2}*}_{n,m})}{2}\right] - \frac{\Delta t}{2\Delta\alpha_1^2(\mu_1)_m}$$

(3.111)

$$\left[\frac{(\eta^{k+\frac{1}{2}*}_{n,m+1} - h_{n,m+1} + \eta^{k+\frac{1}{2}*}_{n,m} - h_{n,m})}{2} \frac{(s^{k+\frac{1}{2}*}_{n,m+1} - s^{k+\frac{1}{2}*}_{n,m})}{(\mu_1)_{m+\frac{1}{2}}} K^{k+\frac{1}{2}*}_{x_{n,m+\frac{1}{2}}}\right.$$

$$\left. - \frac{(\eta^{k+\frac{1}{2}*}_{n,m-1} - h_{n,m-1} + \eta^{k+\frac{1}{2}*}_{n,m} - h_{n,m})}{2} \frac{(s^{k+\frac{1}{2}*}_{n,m} - s^{k+\frac{1}{2}*}_{n,m-1})}{(\mu_1)_{m-\frac{1}{2}}} K^{k+\frac{1}{2}*}_{x_{n,m-\frac{1}{2}}}\right]$$

Placing all terms in (3.110) at time level k on the right-hand side, denoting the result as B_n, we obtain

$$B_m = (ds)^k_{n,m} - \frac{\Delta t}{2\Delta\alpha_2(\mu_2)_n}\left[\frac{(\eta^k_{n+1,m} + h_{n+1,m} + \eta^k_{n,m} + h_{n,m})}{2} v^k_{n+\frac{1}{2},m}\right.$$

$$\left.\frac{(s^k_{n+1,m} + s^k_{n,m})}{2} - \frac{(\eta^k_{n-1,m} + h_{n-1,m} + \eta^k_{n,m} + h_{n,m})}{2} v^k_{n-\frac{1}{2},m} \frac{(s^k_{n-1,m} + s^k_{n,m})}{2}\right]$$

(3.112)

$$+ \frac{\Delta t}{2(\mu_2)_n(\Delta\alpha_2)^2}\left[\frac{(\eta^k_{n+1,m} + h_{n+1,m} + \eta^k_{n,m} + h_{n,m})}{2} \frac{(s^k_{n+1,m} - s^k_{n,m})}{(\mu_2)_{n+\frac{1}{2}}} K^k_{y_{n+\frac{1}{2},m}}\right.$$

$$\left. - \frac{(\eta^k_{n-1,m} + h_{n-1,m} + \eta^k_{n,m} + h_{n,m})}{2} \frac{(s^k_{n,m} - s^k_{n-1,m})}{(\mu_2)_{n-\frac{1}{2}}} K^k_{y_{n-\frac{1}{2},m}}\right]$$

Collecting all results we obtain the following interior equation. For the x-sweep the equations may now be written as:

$$- a_{n,m-1}\, s^{k+\frac{1}{2}*}_{n,m-1} + a_{n,m}\, s^{k+\frac{1}{2}*}_{n,m} + a_{n,m+1}\, s^{k+\frac{1}{2}*}_{n,m+1} = B_m \qquad (3.113)$$

where

$$- a_{n,m-1} = \frac{\Delta t\left(\frac{\alpha_1}{d^{k+\frac{1}{2}*}}\right)_{n,m-\frac{1}{2}}}{2\Delta\alpha_1(\mu_1)_m}\left[\frac{u^{k+\frac{1}{2}*}_{n,m-\frac{1}{2}}}{2} + \frac{(K_x)^{k+\frac{1}{2}*}_{n,m-\frac{1}{2}}}{\Delta\alpha_1(\mu_1)_{m-\frac{1}{2}}}\right] \qquad (3.114)$$

$$a_{n,m+1} = \frac{\Delta t\left(\frac{\alpha_1}{d^{k+\frac{1}{2}*}}\right)_{n,m+\frac{1}{2}}}{2\Delta\alpha_1(\mu_1)_m}\left[\frac{u^{k+\frac{1}{2}*}_{n,m+\frac{1}{2}}}{2} + \frac{(K_x)^{k+\frac{1}{2}*}_{n,m+\frac{1}{2}}}{\Delta\alpha_1(\mu_1)_{m+\frac{1}{2}}}\right] \qquad (3.115)$$

$$a_{n,m} = d^{k+\frac{1}{2}*}_{n,m} + \frac{\Delta t}{2\Delta\alpha_1(\mu_1)_m}\left[\frac{\left(\frac{\alpha_1}{du}\right)^{k+\frac{1}{2}*}_{n,m+\frac{1}{2}}}{2} - \frac{\left(\frac{\alpha_1}{du}\right)^{k+\frac{1}{2}*}_{n,m-\frac{1}{2}}}{2}\right]$$

$$+ \frac{\Delta t}{2\Delta\alpha_1^2(\mu_1)_m}\left[\frac{\left(\frac{\alpha_1}{dK}\right)^{k+\frac{1}{2}*}_{n,m+\frac{1}{2}}}{(\mu_1)_{m+\frac{1}{2}}} + \frac{\left(\frac{\alpha_1}{dK}\right)^{k+\frac{1}{2}*}_{n,m-\frac{1}{2}}}{(\mu_1)_{m-\frac{1}{2}}}\right] \qquad (3.116)$$

The approximations for the y-sweep may now be written as follows:

$$\delta_t^{k+\frac{1}{2}*}(ds) + \frac{\Delta t\ \delta_{\alpha_2}}{2\Delta\alpha_2(\mu_2)_n}\left(\frac{\alpha_2}{d^{k+1}s^{k+1}v^{k+1}}\right) - \frac{\Delta t\ \delta_{\alpha_2}}{2\Delta\alpha_2^2(\mu_2)_n}\left[\frac{\alpha_2}{d^{k+1}}\ K^{k+1}_{\alpha_2}\ \frac{\delta_{\alpha_2}(s^{k+1})}{(\mu_2)_n}\right] \qquad (3.117)$$

$$+ \frac{\Delta t\ \delta_{\alpha_1}}{2\Delta\alpha_1(\mu_1)_m}\left(\frac{\alpha_1}{d^{k+\frac{1}{2}*}s^{k+\frac{1}{2}*}u^{k+\frac{1}{2}*}}\right) + \frac{\Delta t\ \delta_{\alpha_1}}{2\Delta\alpha_1^2(\mu_1)_m}\left[\left(\frac{\alpha_1}{d^{k+\frac{1}{2}*}}\right)K^{k+\frac{1}{2}*}_{\alpha_1}\ \frac{\delta_{\alpha_1}(s^{k+\frac{1}{2}*})}{(\mu_1)_m}\right] = 0 \text{ at } (n,m)$$

Expanding (3.117) by employing (3.105-3.109) and collecting terms at time level k+1 on the left-hand side and leaving terms at time level $k+\frac{1}{2}*$ on the right-hand side the equation for the y-sweep is obtained.

$$- a_{n-1,m}\, s^{k+1}_{n-1,m} + a_{n,m}\, s^{k+1}_{n,m} + a_{n+1,m}\, s^{k+1}_{n+1,m} = B_n \qquad (3.118)$$

where

$$- a_{n-1,m} = \frac{\Delta t\left(\frac{\alpha_2}{d^{k+1}}\right)_{n-\frac{1}{2},m}}{2\Delta\alpha_2(\mu_2)_n}\left[\frac{v^{k+1}_{n-\frac{1}{2},m}}{2} + \frac{(K_y)^{k+1}_{n-\frac{1}{2},m}}{\Delta\alpha_2(\mu_2)_{n-\frac{1}{2}}}\right] \qquad (3.119)$$

$$a_{n+1,m} = \frac{\Delta t\left(\frac{\alpha_2}{d^{k+1}}\right)_{n+\frac{1}{2},m}}{2\Delta\alpha_2(\mu_2)_n}\left[\frac{v^{k+1}_{n+\frac{1}{2},m}}{2} + \frac{(K_y)^{k+1}_{n+\frac{1}{2},m}}{\Delta\alpha_2(\mu_2)_{n+\frac{1}{2}}}\right] \qquad (3.120)$$

$$a_{n,m} = d^{k+1}_{n,m} + \frac{\Delta t}{2\Delta\alpha_2(\mu_2)_n}\left[\frac{\left(\frac{\alpha_2}{(dv)^{k+1}}\right)_{n+\frac{1}{2},m}}{2} - \frac{\left(\frac{\alpha_2}{(dv)^{k+1}}\right)_{n-\frac{1}{2},m}}{2}\right] \qquad (3.121)$$

$$+ \frac{\Delta t}{2\Delta\alpha_2^2(\mu_2)_n}\left[\frac{\left(\frac{\alpha_2}{(dK_y)^{K+1}}\right)_{n+\frac{1}{2},m}}{(\mu_2)_{n+\frac{1}{2}}} + \frac{\left(\frac{\alpha_2}{(dK_y)^{k+1}}\right)_{n-\frac{1}{2},m}}{(\mu_2)_{n-\frac{1}{2}}}\right]$$

$$B_n = (ds)^{k+\frac{1}{2}*}_{n,m} - \frac{\Delta t}{2(\mu_1)_m\Delta\alpha_1}\left[\left(\frac{\alpha_1}{(ds)^{k+\frac{1}{2}*}_{n,m+\frac{1}{2}}}\right)u^{k+\frac{1}{2}*}_{n,m+\frac{1}{2}} - \left(\frac{\alpha_1}{(ds)^{k+\frac{1}{2}*}_{n,m-\frac{1}{2}}}\right)u^{k+\frac{1}{2}*}_{n,m-\frac{1}{2}}\right]$$

$$+ \frac{\Delta t}{2(\mu_1)_m(\Delta\alpha_1)^2}\left[\left(\frac{\alpha_1}{(dK_x)^{k+\frac{1}{2}*}_{n,m+\frac{1}{2}}}\right)\frac{(s^{k+\frac{1}{2}*}_{n,m+1} - s^{k+\frac{1}{2}*}_{n,m})}{(\mu_1)_{m+\frac{1}{2}}}\right.$$

$$\left. - \left(\frac{\alpha_1}{(dK_x)^{k+\frac{1}{2}*}_{n,m-\frac{1}{2}}}\right)\frac{(s^{k+\frac{1}{2}*}_{n,m} - s^{k+\frac{1}{2}*}_{n,m-1})}{(\mu_1)_{m-\frac{1}{2}}}\right] \qquad (3.122)$$

3.8.2 Leendertse FTUS Multioperational Scheme

This scheme is similar to the Leendertse FTCS technique except that upwind differencing is employed for the advective terms. The necessary

modifications for the x-sweep are shown in Table 3.1 while those employed for the y-sweep are given in Table 3.2.

The FTUS scheme may be obtained from the FTCS scheme programming with only modest programming modification.

3.9 Flux Corrector Scheme for Salinity

The Flux Corrector (FC) scheme described earlier is utilized for the salinity calculations. The FTCS scheme of Leendertse is used as the lower order solution and the FTUS scheme as the higher order solution. This solution scheme requires more computer time than most other schemes since the system of equations is solved twice; i.e., the lower order solution and the higher order solution. The increased accuracy of the results especially in areas of large salinity gradient justify the increased computational requirements.

Table 3.1. X-Sweep Modifications FTUS

EQUATION	FTCS	FTUS
3.112	$\frac{(s^k_{n+1,m} + s^k_{n,m})}{2}$	$s^k_{n,m} \quad v^k_{n+\frac{1}{2},m} \geq 0$
		$s^k_{n+1,m} \quad v^k_{n+\frac{1}{2},m} < 0$
3.112	$\frac{(s^k_{n-1,m} + s^k_{n,m})}{2}$	$s^k_{n-1,m} \quad v^k_{n-\frac{1}{2},m} \geq 0$
3.113	$\frac{u^{k+\frac{1}{2}*}_{n,m-\frac{1}{2}}}{2}$	$\max\ (0.,\ u^{k+\frac{1}{2}*}_{n,m-\frac{1}{2}})$
3.114	$\frac{u^{k+\frac{1}{2}*}_{n,m+\frac{1}{2}}}{2}$	$\min\ (0.,\ u^{k+\frac{1}{2}*}_{n,m+\frac{1}{2}})$
3.115	$\frac{(\frac{\alpha_1}{(du)^{k+\frac{1}{2}*}_{n,m+\frac{1}{2}}})}{2}$	$\max\ [0.,\ (\frac{\alpha_1}{(du)^{k+\frac{1}{2}*}_{n,m+\frac{1}{2}}})\ ]$
3.115	$\frac{(\frac{\alpha_1}{(du)^{k+\frac{1}{2}*}_{n,m-\frac{1}{2}}})}{2}$	$\max\ [0.,\ (\frac{\alpha_1}{(du)^{k+\frac{1}{2}*}_{n,m-\frac{1}{2}}})\ ]$

Table 3.2. Y-Sweep Modifications FTUS

EQUATION	FTCS	FTUS		
3.119	$\frac{v^{k+1}_{n-\frac{1}{2},m}}{2}$	$\max\ (0.,\ v^{k+1}_{n-\frac{1}{2},m})$		
3.120	$\frac{v^{k+1}_{n+\frac{1}{2},m}}{2}$	$\min\ (0.,\ v^{k+1}_{n+\frac{1}{2},m})$		
3.121	$\frac{(\frac{\alpha_2}{(dv)^{k+1}_{n+\frac{1}{2},m}})}{2}$	$\max\ [0.,\ (\frac{\alpha_2}{(dv)^{k+1}_{n+\frac{1}{2},m}})]$		
3.121	$\frac{(\frac{\alpha_2}{(dv)^{k+1}_{n-\frac{1}{2},m}})}{2}$	$\min\ [0.,\ (\frac{\alpha_2}{(dv)^{k+1}_{n-\frac{1}{2},m}})]$		
3.122	$(\frac{\alpha_1}{(ds)^{k+\frac{1}{2}*}_{n,m+\frac{1}{2}}})$	$(\frac{\alpha_1}{d^{k+\frac{1}{2}*}_{n,m+\frac{1}{2}}})\ s^{k+\frac{1}{2}*}_{n,m}$	$u^{k+\frac{1}{2}*}_{n,m+\frac{1}{2}} \geq 0$	
		$(\frac{\alpha_1}{d^{k+\frac{1}{2}*}_{n,m+\frac{1}{2}}})\ s^{k+\frac{1}{2}*}_{n,m+1}$	$u^{k+\frac{1}{2}*}_{n,m+\frac{1}{2}} < 0$	
3.122	$(\frac{\alpha_1}{(ds)^{k+\frac{1}{2}*}_{n,m-\frac{1}{2}}})$	$(\frac{\alpha_1}{d^{k+\frac{1}{2}*}_{n,m-\frac{1}{2}}})\ s^{k+\frac{1}{2}*}_{n,m-1}$	$u^{k+\frac{1}{2}*}_{n,m-\frac{1}{2}} \geq 0$	
		$(\frac{\alpha_1}{d^{k+\frac{1}{2}*}_{n,m-\frac{1}{2}}})\ s^{k+\frac{1}{2}*}_{n,m}$	$u^{k+\frac{1}{2}*}_{n,m-\frac{1}{2}} < 0$	

IV. APALACHICOLA BAY SYSTEM

4.1 Physical Description

The Apalachicola Bay System, Figure I.1, is a barrier island contained estuary on the Florida Panhandle. Apalachicola Bay is the principal embayment with St. Vincent Sound to the west, East Bay to the north and St. George Sound to the east. These waters comprise an integral estuarine system and are identified as Apalachicola Bay in this report. St. Vincent Sound is about 9 miles long and 2 miles wide with a surface area of about 18 square miles. East Bay is the smallest water body being about 5 miles long and over 3 miles wide at its mouth. Its' area is just over 17 square miles. St. George Sound is approximately 11 miles long, averages about 4 miles wide and covers an area of about 48 square miles. Apalachicola Bay is approximately 12 miles long and is about 6 miles wide. The bay covers an area of 77 square miles. Barrier islands separating the embayment from the Gulf of Mexico are: St. Vincent, St. George and Dog Islands. Access to the Gulf is afforded by Indian Pass, West Pass, Sikes Cut, and openings on each end of Dog Island. All of the openings are natural except Sikes Cut which was originally dredged across St. George Sound in 1954. The bay system is shallow, the average depth being only about 10 feet.

The Apalachicola River originates from the drainage of the 37,500-acre Lake Seminole formed by the Jim Woodruff Dam, the source of the reservoir being the Flint and Chattahoochee Rivers. The Apalachicola River, together with the Chipola River which joins the Apalachicola about 35 miles north of the mouth, is the major source of nutrients supplied to the Apalachicola Bay estuary. This river system drains approximately 13,400 square miles of Georgia, 3,200 square miles of

Alabama and 3,400 square miles of Florida. The mean discharge into Apalachicola Bay is approximately 23,300 cfs. The actual river discharge into Apalachicola Bay is through an involved mesh of marshy channels, as indicated in Figure IV.1. The major inflow sources into the bay are East River, Marks River and Apalachicola River. East River and Marks River are branches of Apalachicola River. The observed relationship between flow rates in Apalachicola River, East River and Marks River are shown in Figure IV.2.

The Apalachicola, Florida area is served by several small craft channels and ports. Eastpoint, Florida, Two Mile, Florida, and Apalachicola, Florida are served by Federally maintained channels from deep water in the bay into the ports. The Gulf Intracoastal Waterway with project dimensions of 12 by 125 feet traverses the lower six miles of the Apalachicola River and continues through Apalachicola Bay and St. George Sound to Carrabelle. Direct passage to the Gulf from Apalachicola is provided by the St. George Island Channel (Sikes Cut). A natural channel, suitable only for very small boats, provides a somewhat protected route from the Eastpoint channel to the processing houses at Apalachicola. The projects are shown on Figure IV.3.

4.2 Climate

The climate of this locality is typical of that experienced on the northern Gulf of Mexico. Because of the moderating effect of the surrounding Gulf, temperatures are usually mild and subtropical in nature. Southerly winds produce frequent afternoon thundershowers in the summer while winter storms are of the frontal type in which showers generally last the duration of the storm.

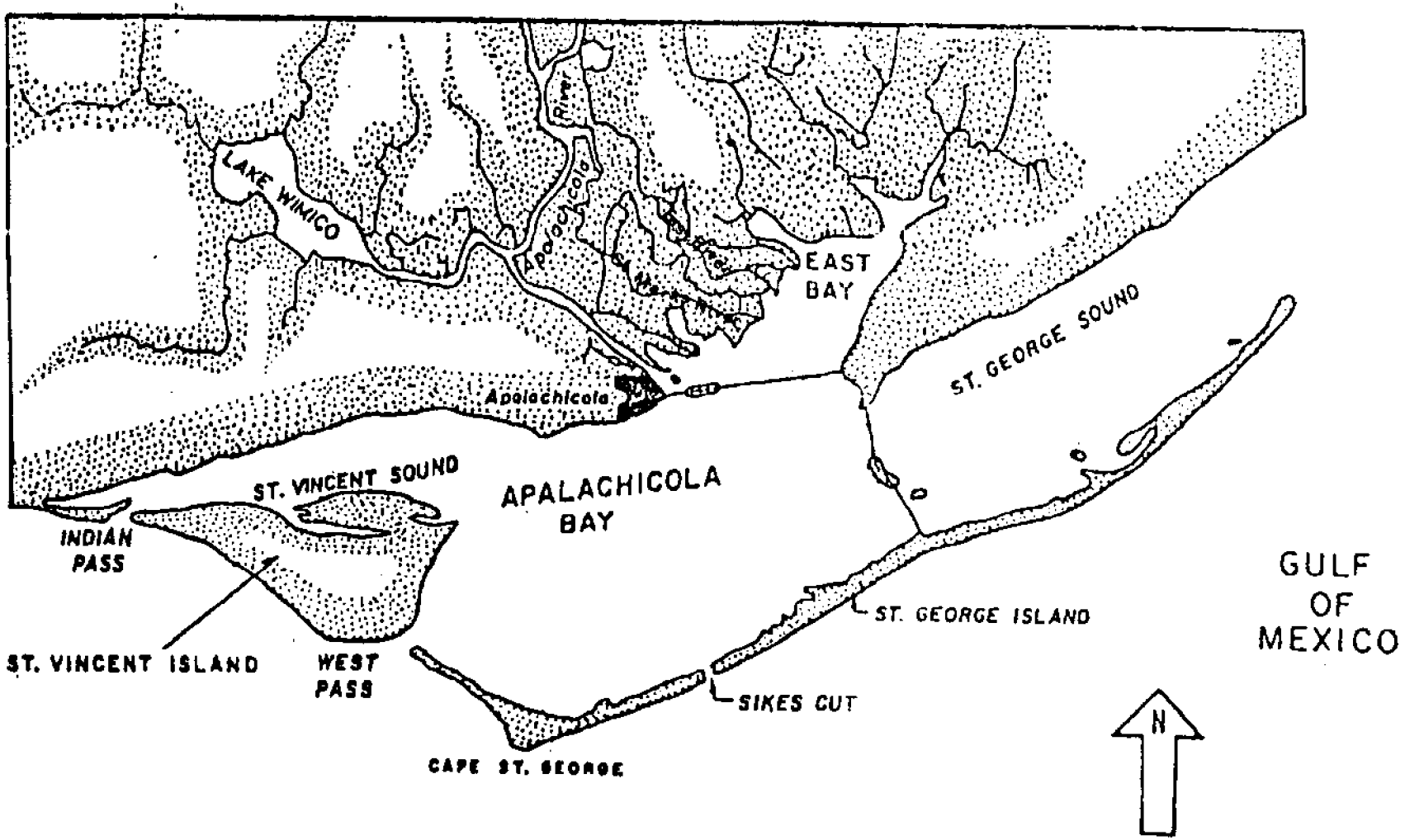

Figure IV.1. Freshwater Inflow Sources for Apalachicola Bay

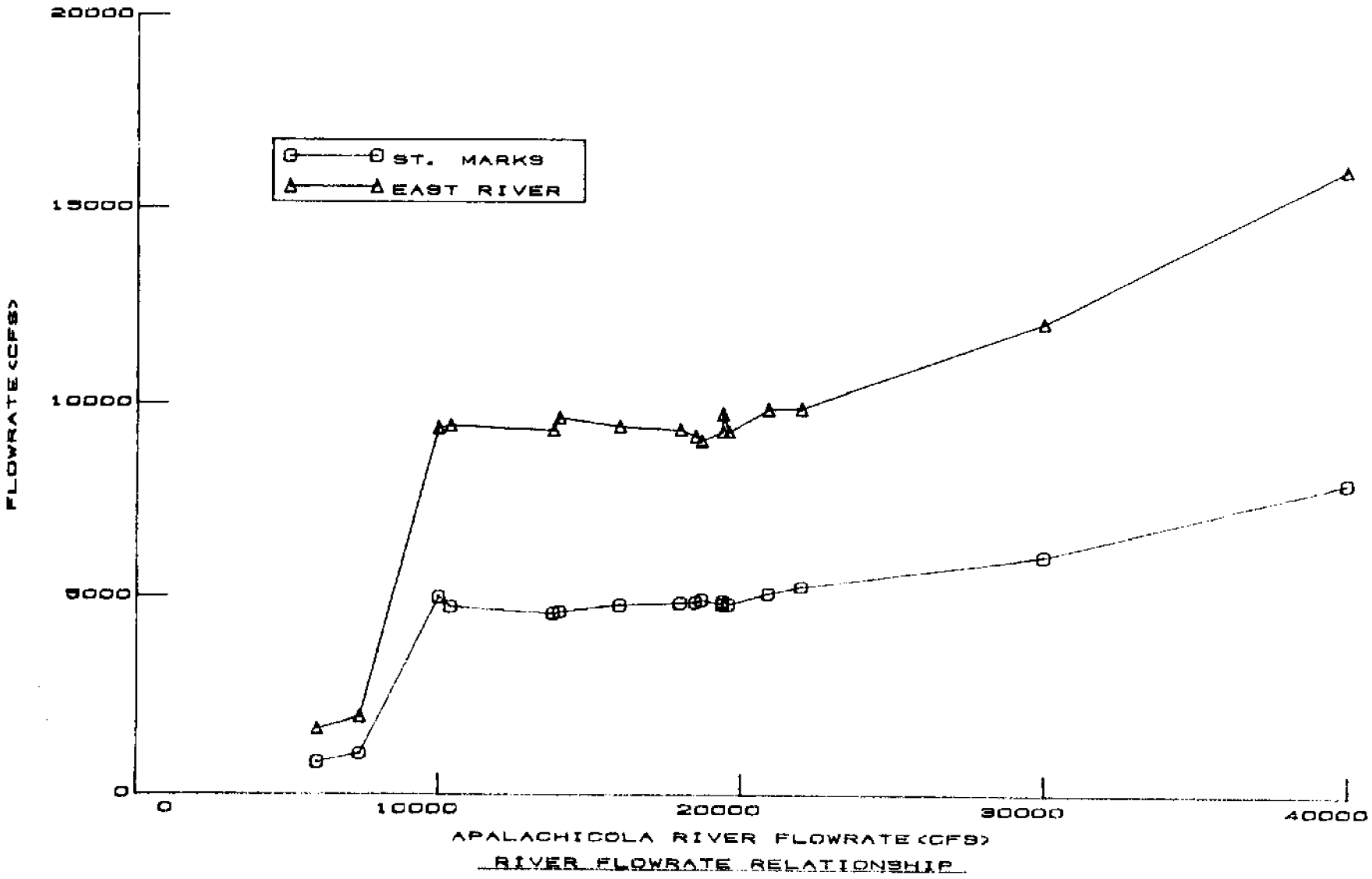

Figure IV.2. Relationship between Major Sources of Freshwater Inflow into Apalachicola Bay

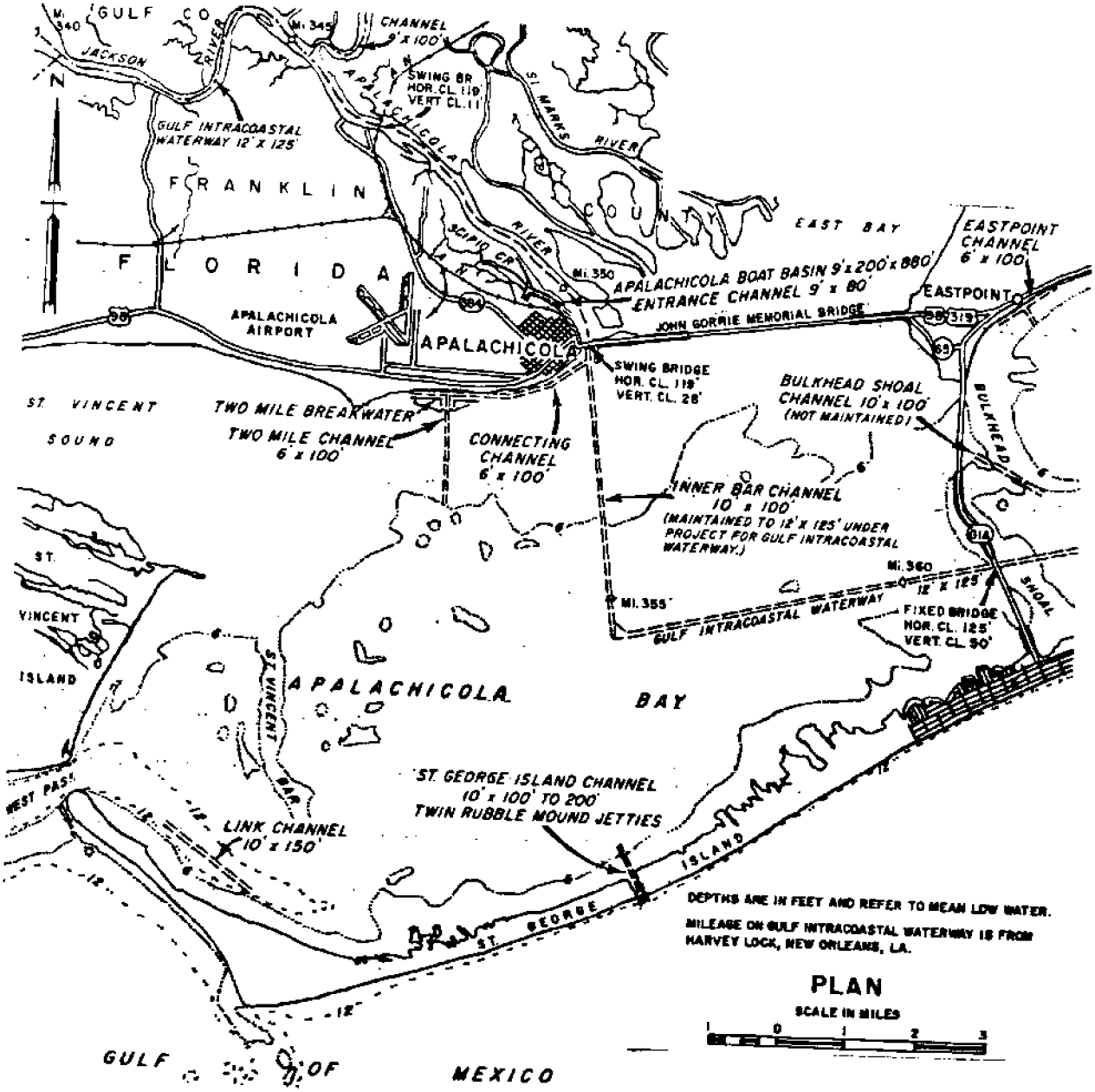

Figure IV.3. Federal Projects in Apalachicola Bay, Florida

The average mean monthly rainfall for the Apalachicola Bay area is 4.7 inches with a mean annual rainfall of 56.1 inches. Maximum rainfall occurs during the summer months, September being the wettest month. The mean rainfall from June to September is 28.6 inches, which accounts for approximately 55 percent of the annual rainfall. Convection type storms are the predominate source of rainfall in the summer months.

Ambient daily temperatures for the summer months average between 73°F and 86°F with the higher daily temperatures occurring in August. The mean monthly temperature varies from a low of 54.4°F in January to a high of 81.4°F in July and August. Periods of cold weather generally do not last more than a few days, and the temperature rarely falls below freezing for more than an entire day.

The surface wind is influenced by the Bermuda High throughout the year. Easterly component winds prevail for all months, varying from northeast to southeast. Winds become more variable in both speed and direction on approaching the coast and continental influences. The wind effects of the Bermuda High are greatest during spring and summer. Although these winds have a high constancy, they are relatively light and are responsible for summer minimums in mean wind speeds. The record highest winds are likely to occur during the summer or early fall, during the season of tropical cyclones. In the fall, the continental influences increase, becoming greatest in February and March, the months having the highest mean wind speeds. Mean wind speed varies from a low of 6.6 miles per hour to 9.1 miles per hour in March.

Tides in the area are semi-diurnal. The mean diurnal range is 1.6 feet and the extreme, except during storms, is 3 feet. Abnormal lows, often for protracted periods, frequently occur during the winter when

northerly winds predominate. The maximum tide measured in recent years occurred during the hurricane of August 1950 when the water level rose to 6.8 feet above mean sea level.

4.3 Features

The thousands of acres of protected waters within Apalachicola Bay furnish some of the better small-boat, salt-water fishing to be found along the South Atlantic and Gulf coasts. Numerous scattered oyster reefs and grassy flats are the preferred habitat of game fish such as spotted seatrout, redfish, and flounder. Most of these areas are accessible only by boat and offer fishing opportunities in nearly pristine surroundings. While spotted seatrout is the most popular sportfish, redfish is a close second. Additionally, pompano, jacks, bluefish, and spanish mackerel are taken in the vicinity of Indian Pass and the outer beaches.

Water temperatures in Apalachicola Bay range from 37°F to 93°F, with low temperatures occurring during the winter months (December - February) and high temperatures occurring in July, August, or September. Salinities range from 0 parts per thousand (ppt) to approximately 34 ppt. Most of the bay appears to behave as a well mixed system much of the time; however, significant stratification can occur. Turbidity levels vary widely and appear to be directly related to river discharge and wind speed.

In general, the environmental characteristics of Apalachicola Bay reflect the undeveloped and relatively unpolluted nature of the area. However, high coliform bacteria levels preclude the harvest of oysters in certain areas with Apalachicola Bay. Waters are permanently closed to shellfish harvesting within a triangle formed by Green Point,

Apalachicola, and the 90 degree turn in the GIWW in the middle of Apalachicola Bay and within a two-mile radius of John Gorrie Memorial Bridge. The other waters of East Bay and that portion of Apalachicola Bay north of the GIWW and west of the bridge to St. George Island are conditionally approved for shellfish harvesting.

V. THE FINITE DIFFERENCE GRID

The Apalachicola Bay system is represented in the numerical model using a variable cell size finite difference grid. Due to the large number of cells the grid is presented in four parts; St. Vincent Sound, Apalachicola Bay, East Bay and St. George Sound. A high resolution numerical model was desired with particular emphasis on areas near passes, channels, and other critical features.

The finite difference grid was developed using a 1:48,000 scale nautical chart developed by Raytheon Service Company based upon a bathymetric survey during September 1983 and March 1984. Bathymetric data from the survey were digitized and the best average depth for each finite difference cell was calculated. Manning n friction values for bottom material (mud, sand, weeds, etc.) was also digitized in a similar manner.

The dimensions of the resulting finite difference grid was 99 by 79 cells or a total of 7821 cells. The geometry for the finite difference cells is indicated in Figures V.1 thru V.4. Smaller cells were used in areas near passes opening to the Gulf of Mexico, the Gulf Intracoastal Waterway Channel, the inner bar channel and other critical features or in areas where the bay geometry or depths were changing rapidly. Larger cells were used in East Bay and other areas of the bay where geometry and bathymetry were reasonably simple or constant. The smallest cell dimension was approximately 110 feet. A half time step of 60 seconds was used to obtain a reasonable Courant number for the calculations.

A time dependent tidal and salinity boundary condition was specified at all computational boundary openings to the Gulf of Mexico; Indian Pass, West Pass, Sikes Cut and the northeast end of St. George

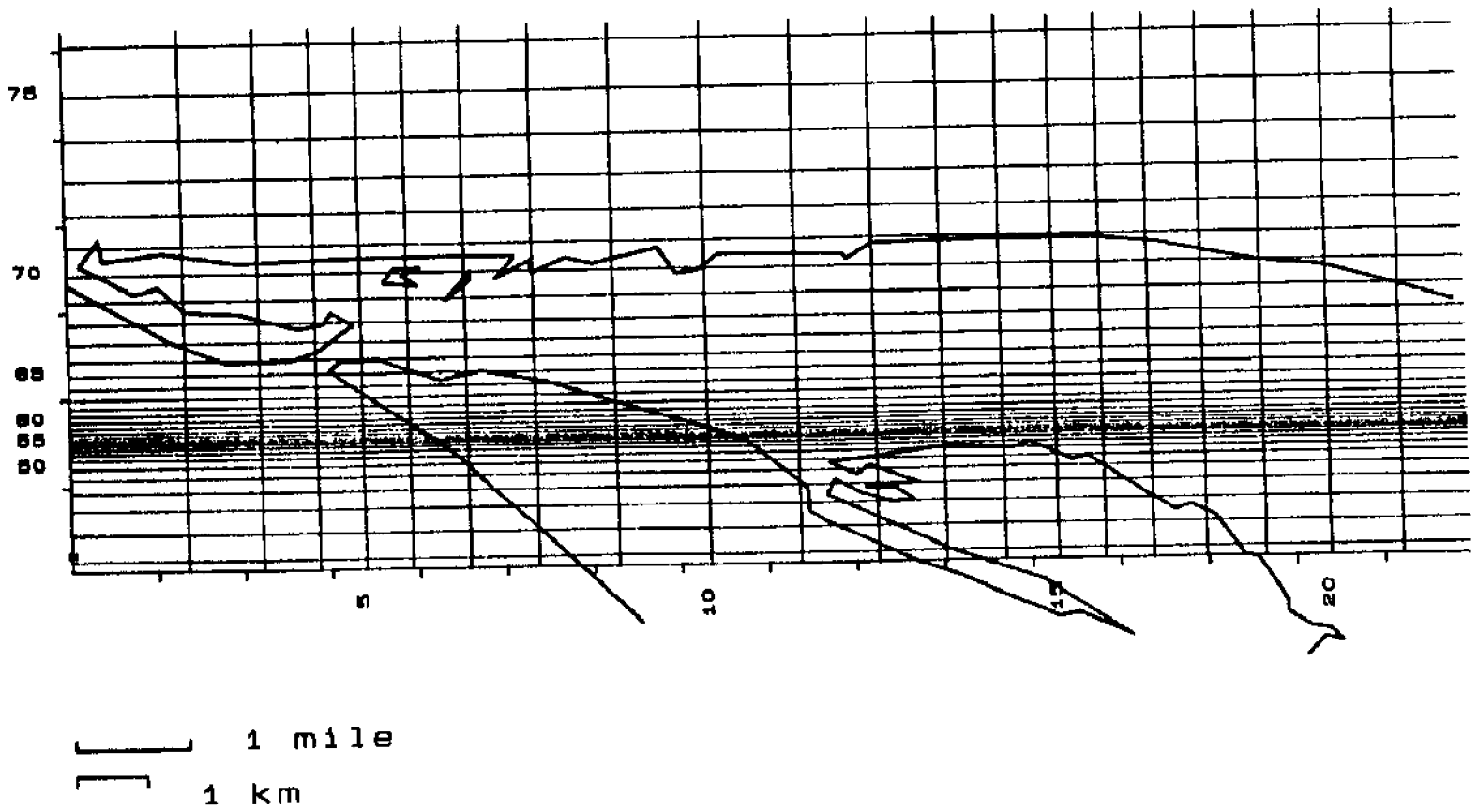

Figure V.1. Finite Difference Grid in St. Vincent Sound

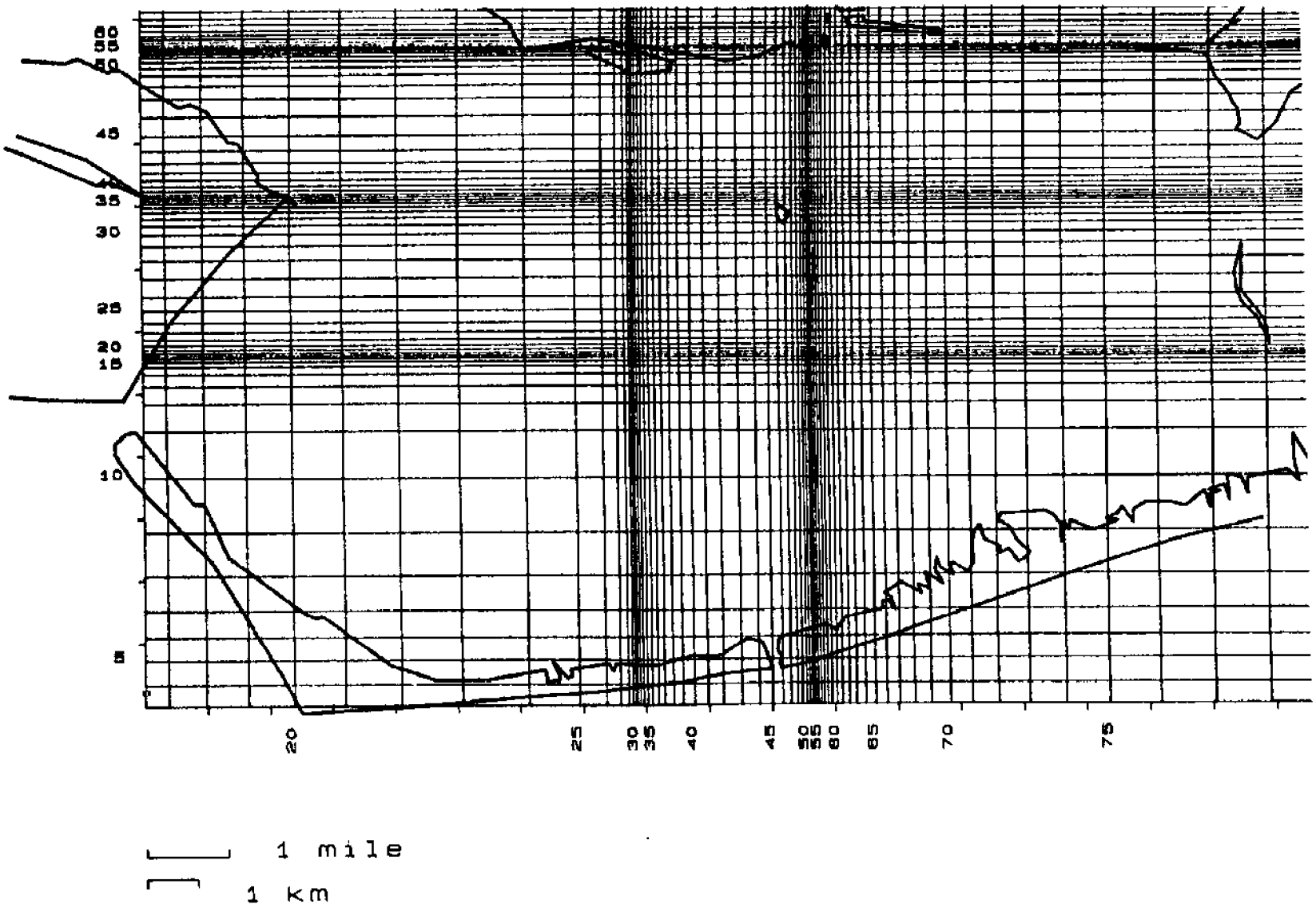

Figure V.2. Finite Difference Grid in Apalachicola Bay

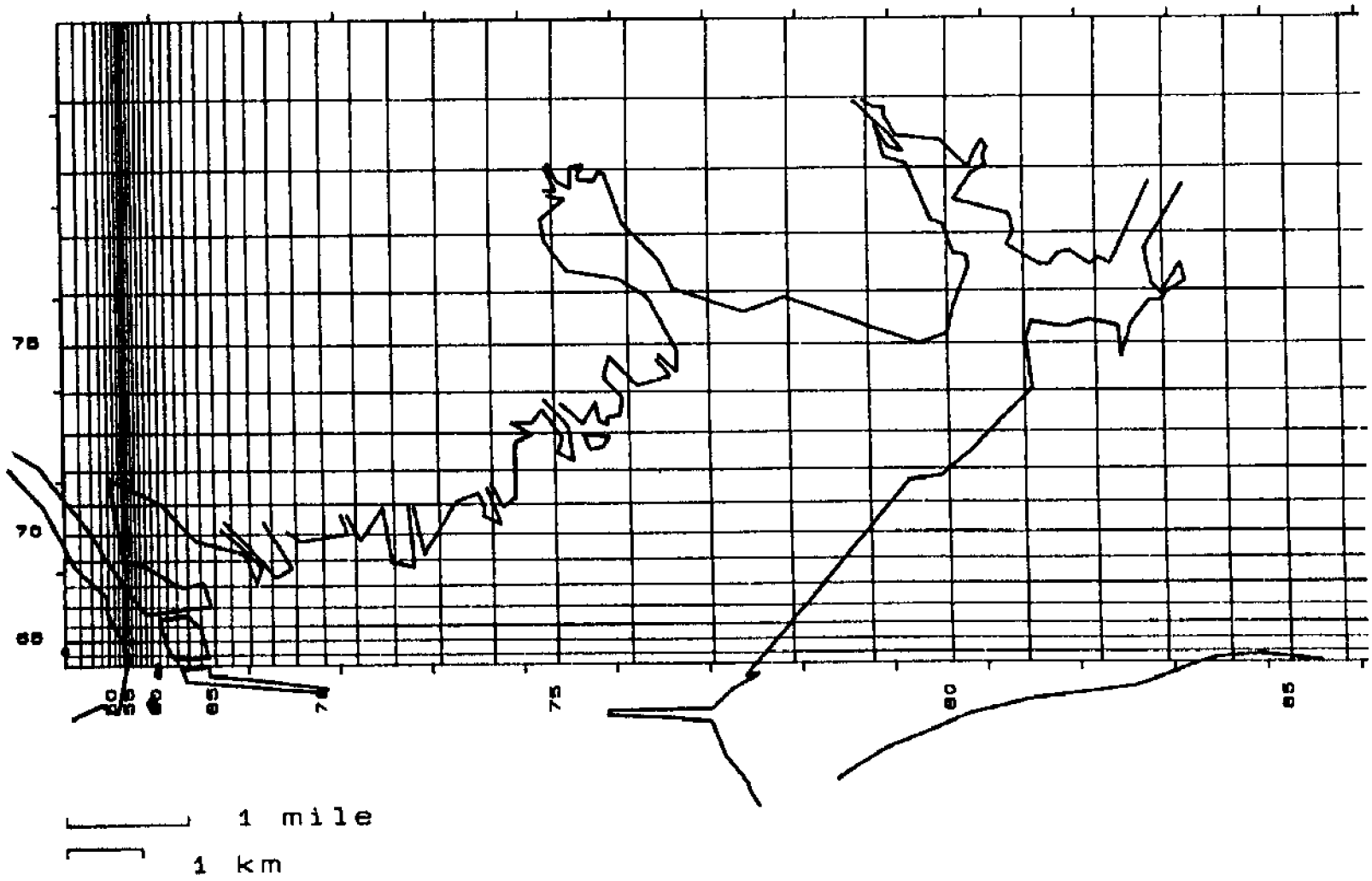

Figure V.3. Finite Difference Grid in East Bay

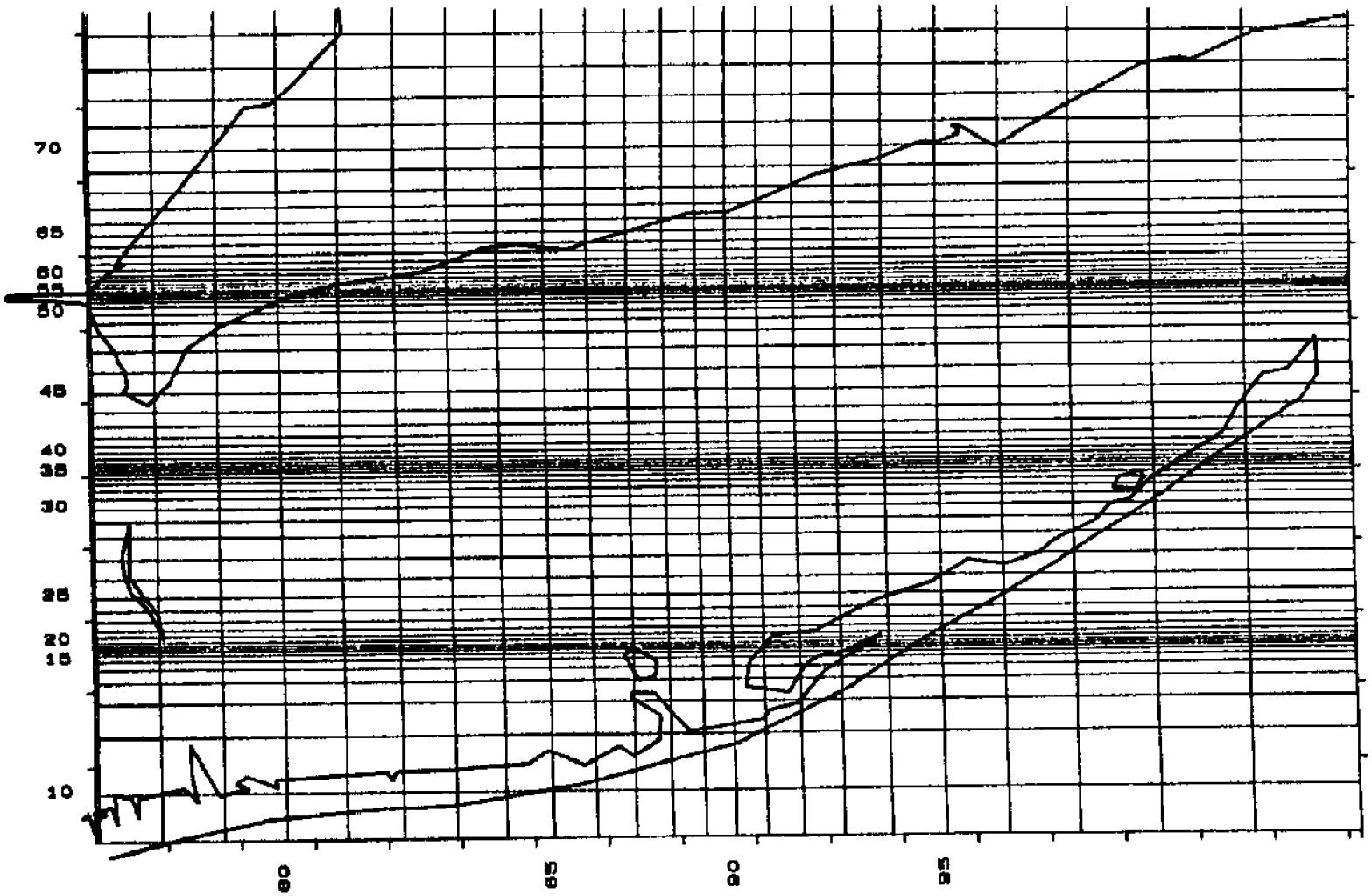

Figure V.4. Finite Difference Grid in St. George Sound

Island. Volumetric flow rate and salinity boundary conditions were specified for river inflows. The time dependent freshwater input to the bay was represented by three river inflows representing Apalachicola River, St. Marks River and East River. An appropriate wind shear stress based upon the time varying wind velocity, measured from the station installed on St. George Island during the two study months, was applied to each finite difference cell.

VI. MODEL CALIBRATION AND VERIFICATION

6.1 Available Data

Prototype data were collected for two 30-day periods for calibration and verification of the numerical model. Data were collected on magnetic tape at locations indicated as SG1, SG2...SG10 in Figure VI.1, a total of nine locations where velocity and salinity data were collected and seven locations where water surface elevation was measured. Wind data was collected on St. George Island at a station installed as a part of the data collection effort. In addition, a bathymetric survey was conducted in the bay. Data were collected in September 1983 and with supplemental data collected during March 1984. The velocity, salinity and bathymetric data were collected by Continental Shelf Associates, Inc. while the National Oceanic and Atmospheric Administration, National Ocean Service (NOS) provided the wind and tidal data. Data on fresh water inflow into the bay for the time period of interest were obtained from the U. S. Department of Interior, Geological Survey.

In addition to the 30 days of meter data, the U. S. Army Corps of Engineers, Mobile District (USCEM) with the assistance of the U.S.G.S. and the Florida Department of Environmental Regulation, manually collected hourly data for 24-hour periods during September 14-15, 1983 and March 8-9, 1984. A variety of data (salinity, dissolved oxygen, turbidity, temperature, etc.) were collected at 9 supplemental locations. The USCEM et. al. data collection locations are also indicated as G1, G2...G9 in Figure VI.1. The salinity data collected at these locations provided valuable additional data for model calibration and verification.

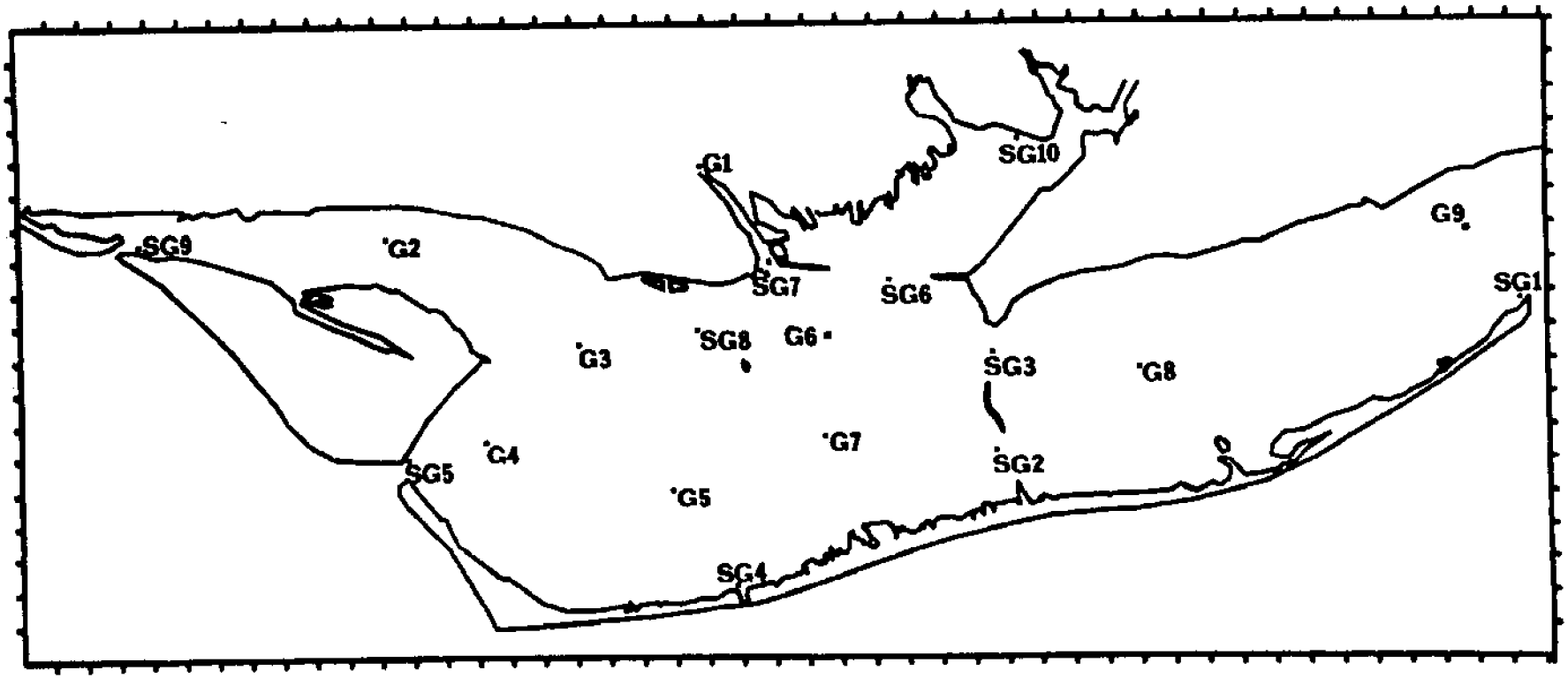

Note:
Tide gages SG1, SG3, SG4, SG5, SG7, SG9, SG10
Velocity gages SG1-SG9
Salinity gages SG1-SG9
Manual velocity G5-G9
Manual salinity, etc. G1-G9

Figure VI.1. Prototype Data Collection Stations

After review of all the prototype data it was decided to use the September 14-15, 1983 data period for calibrating the model. This period coincided with the September manual data collection period by USCEM et. al. so additional salinity data were available. In addition, the river inflow during this period was fairly representative of the yearly average river flow rate. The winds during the period were typical of those occurring during September.

The March 8-9, 1984 time period when USCEM et. al. conducted its spring manual data collection occurred during a period of high river inflow and was selected as the verification time period. In addition to the different river inflow conditions, average wind magnitudes were higher and the average wind direction was about 90° different than for the calibration period. The tidal range was slightly lower than for the calibration period.

6.2 Calibration

As indicated previously, the time period September 14-15, 1983 was used as the calibration condition. Appropriate bathymetric and bottom friction data were determined for each finite difference cell of the model. Prototype surface elevation and salinity data were applied as boundary conditions at each computational boundary of the model opening to the Gulf of Mexico. These boundary conditions are summarized in Figures VI.2 and VI.3. The river inflows for Apalachicola River, St. Marks River and East River are indicated in Figure VI.4. The wind magnitude and direction applied to the model are represented in Figures VI.5 and VI.6.

Initial conditions were established for the model and the model was allowed to "warm-up" for a period of time prior to the actual period of

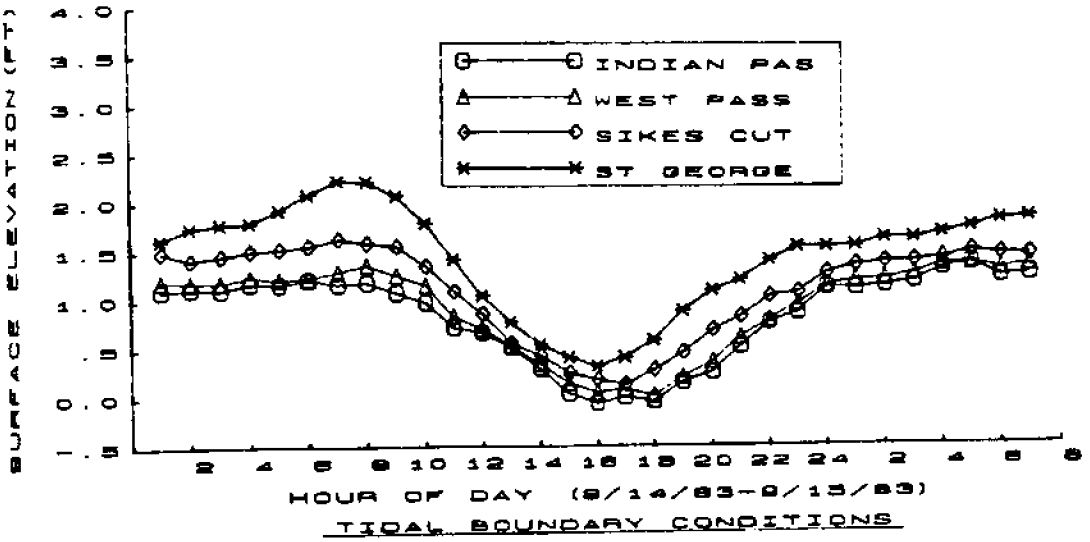

Figure VI.2. Tidal Boundary Conditions for Calibration Period

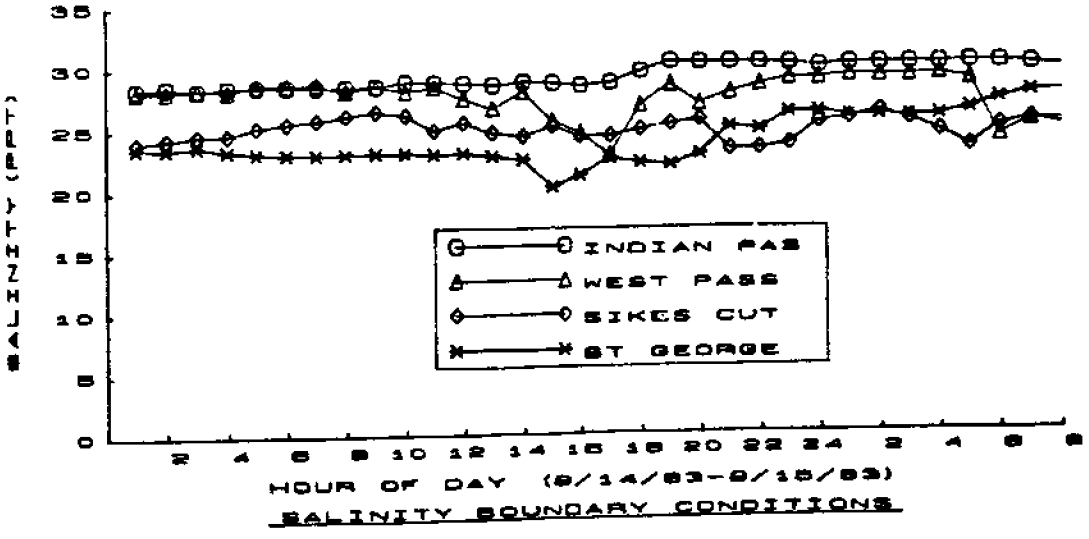

Figure VI.3. Salinity Boundary Conditions for Calibration Period

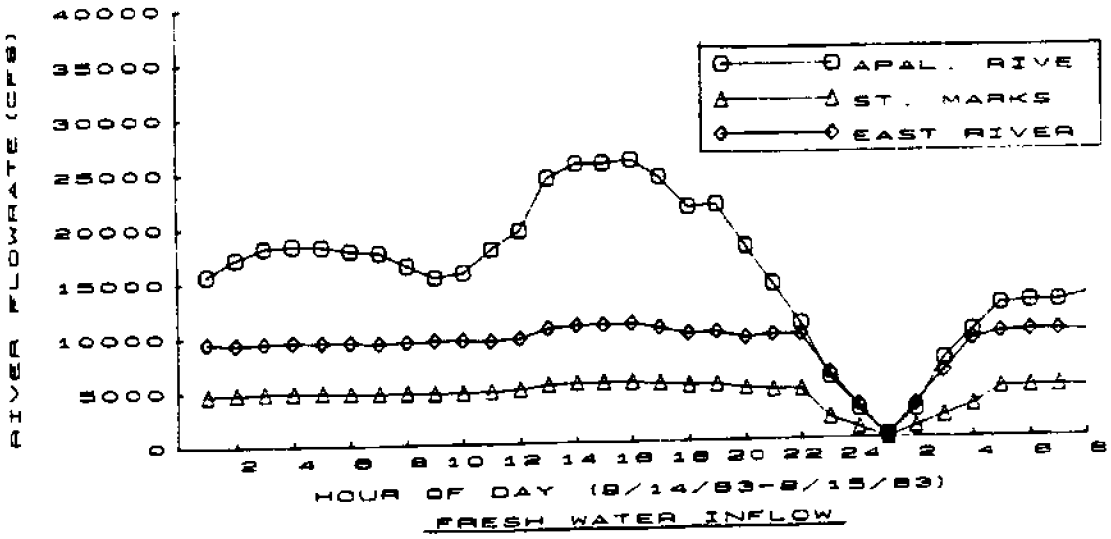

Figure VI.4. River Boundary Conditions for Calibration Period

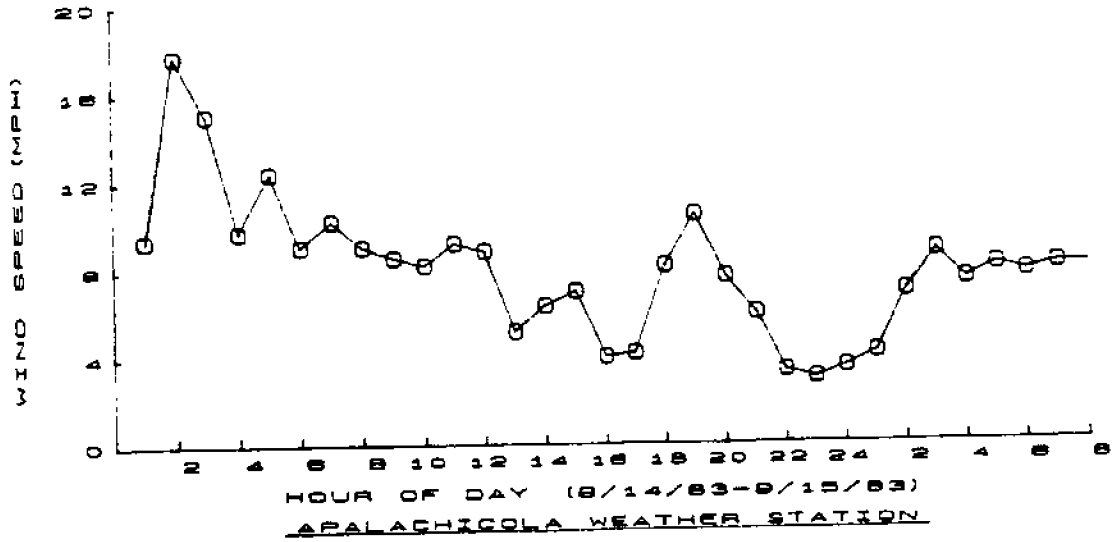

Figure VI.5. Wind Magnitude Boundary Condition for Calibration Period

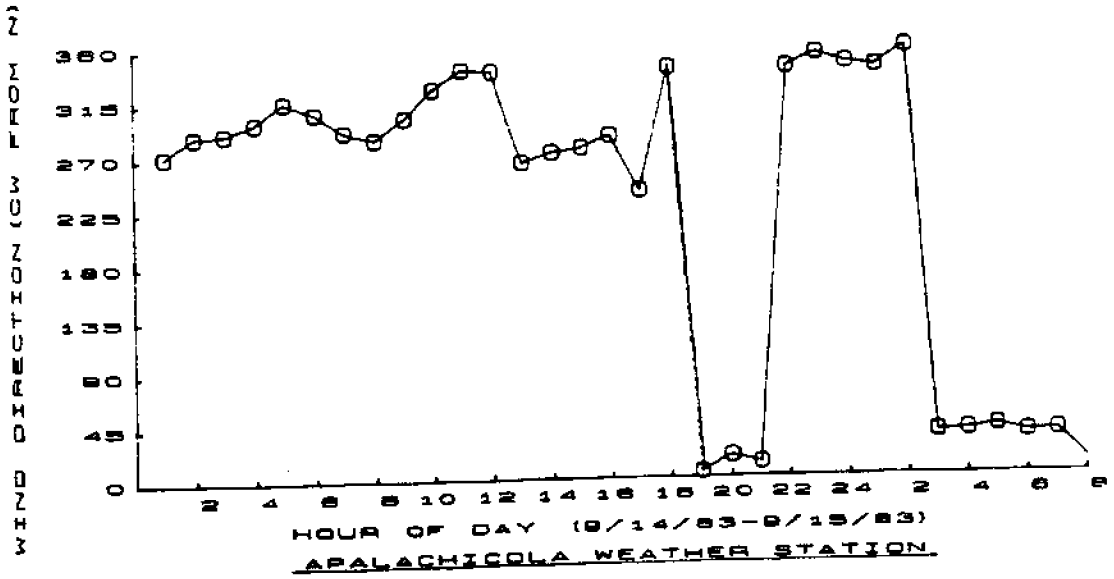

Figure VI.6. Wind Direction Boundary Condition for Calibration Period

calibration. The warm-up period is necessary to allow time for the model to minimize errors associated with incorrect starting conditions. After allowing the model to run for the calibration period, model results were compared with prototype data. Model parameters (friction, depths, diffusivity, etc.) and initial conditions were adjusted appropriately and the model was rerun. This process was continued until the model produced results which agreed with prototype data within an acceptable degree of accuracy.

Results at gage point locations for the calibration run are presented in Appendix A. Figures A-1 thru A-3 present the surface elevation; velocities are presented in Figures A-4 thru A-11 and salinity results are presented in Figures A-12 thru A-24. Surface elevation, salinity and velocity results are not presented at gage point locations where they represent applied boundary conditions to the model. At these locations these variables in the model are set identically equal to the prototype value. This is true of surface elevation and salinity at all openings of the bay to the Gulf of Mexico and for velocity and salinity values at river inflow locations.

Overall, the calibration results are extremely good. At most gage locations the numerical model results are in excellent agreement with prototype data. There are, however, a few points of disagreement which require some discussion.

The surface elevation prototype data at gage SG7 (Figure A-2) is not consistent with other surface elevation gages. This gage appears to indicate values that are 0.1 to 0.2 feet lower then what would appear to be consistent with the other tide gages.

The velocity meters at gage locations SG6 (Figure A-9) and SG8 (Figure A-10) do not appear to have been operational during the calibration period. Both gages indicated basically zero velocity for the entire calibration period.

Of the 13 salinity gage points, only two gages indicate significant differences between the model results and prototype data. Gage SG6 (Figure A-14) is in a very dynamic area due to its location relative to the main river inflow. In the region around this gage large salinity gradients exist and salinity is changing appreciably over relatively short distances. Gage SG8 (Figure A-16) in St. George Sound shows a tendency for the model to predict a lower salinity value than was indicated by the prototype data. The model salinity results at other gages in St. George Sound are in much closer agreement with prototype data than are the results at SG8.

Salinity contours, based on model results, are presented in Figures A-25 thru A-37 at 2-hour intervals for the calibration period. The movement of the salinity contours over the calibration period appear consistent with the primary driving forces; the tidal elevations and river inflow. Initially, for the calibration period, there is a flood tidal condition and the total river inflow (Apalachicola River, East River, St. Marks River) is around 33,000 cfs. The bay system has a relatively high salinity level with 10 to 15 ppt water extending up into some areas of East Bay. For the next eight hours as the tide ebbs, the total river flow increased to over 40,000 cfs and the higher salinity levels are pushed away from the fresh water inflow locations. Observe that the 10-15 ppt water was pushed completely out of East Bay. The tide now begins another flood period which lasts for the remainder of

the calibration period. The surface elevations in the bay are increasing and river flows decrease very significantly, falling to almost zero at 0100 on September 15. The salinity contours reflect the movement of the higher salinity water back into areas near the fresh water inflow. Observe that the 10-15 ppt water has returned to East Bay by the end of the calibration period.

There is also significant movement of the 20 ppt contour in St. George Sound and in Apalachicola Bay during the calibration period. The 25 ppt contour line in St. Vincent Sound is also observed to migrate during the calibration period although its movement is not as significant as is the change in other areas.

Observe that the salinity curves are not extremely regular curves. There are bulges and undulations created by the primary velocity patterns in the bay. The average river flow rate during the calibration period is similar to the yearly average. The tidal range and wind conditions are also reasonably close to average conditions, thus, the salinity contours for the calibration condition should represent conditions that are relatively close to average salinity patterns in the bay system.

Representative velocity vector plots are presented in Figures A-38 thru A-61. The direction of the velocity for each finite difference is indicated by the direction of the arrow and the length of the arrow represents the magnitude of the velocity. A velocity vector scale is shown on each vector plot. It was necessary to divide the study region into four sub-regions to present these data at a reasonable resolution level. St. Vincent Sound, Apalachicola Bay, East Bay and St. George Sound are presented on separate plots. These plots are presented at six

times during the calibration period. Because of the extremely small finite difference cell size in some areas the velocity vectors coalesce and individual finite difference cell velocities cannot be distinguished, however, the overall velocity patterns are apparent.

There is an overall flow from east to west in the bay system. Most of the fresh water inflow is discharged through West Pass or Indian Pass. The salinity level range in St. George Sound is smaller than in other areas of the bay as a result of the generally east to west flow.

6.3 Verification for Large River Inflow

The time period March 8-9, 1984 was used as the verification condition. The basic model parameters established in the calibration process were fixed and only tide, wind and river boundary conditions were changed for the verification run. The boundary conditions are indicated in Figures VI.7 thru VI.11.

After the initial "warm-up" period, the model was run for the verification period and model results were compared with prototype data. Results at gage point locations are presented in Appendix B. Figures B-1 and B-2 present surface elevation, Figures B-3 thru B-11 present velocities and Figures B-12 thru B-22 present salinity results.

Overall, while not as good as the calibration results, the numerical model clearly does a reasonably good job of representing the behavior of the system. At first inspection some of the salinity results differ more than might be desirable, however, as will be, apparent from inspection of the salinity contours, very large salinity gradients exist in several regions of the bay. In many cases the salinity changes from 2 ppt to 10 or 15 ppt within a few thousand yards. The numerical model presents a good overall salinity pattern for the bay

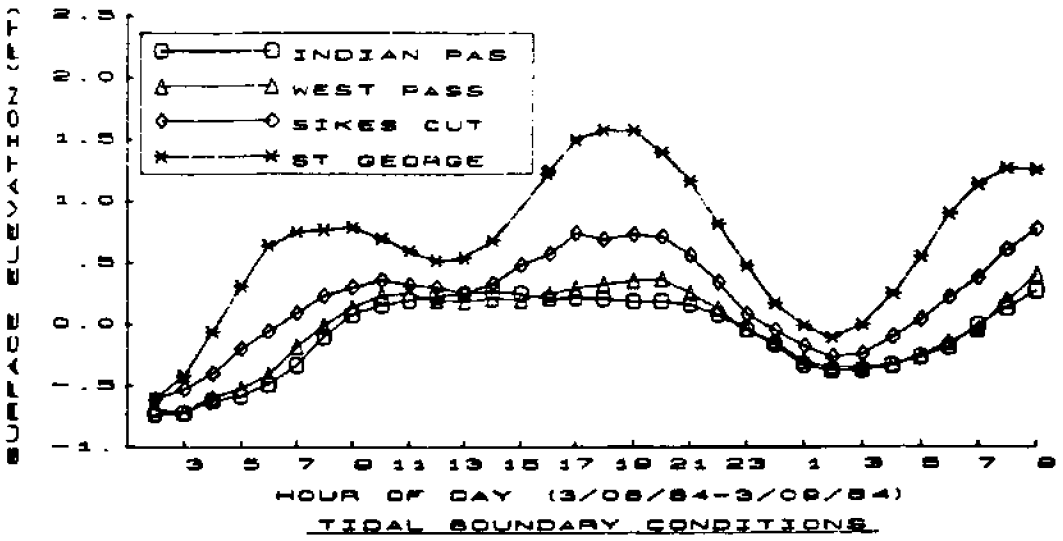

Figure VI.7. Tidal Boundary Conditions for Verification Period

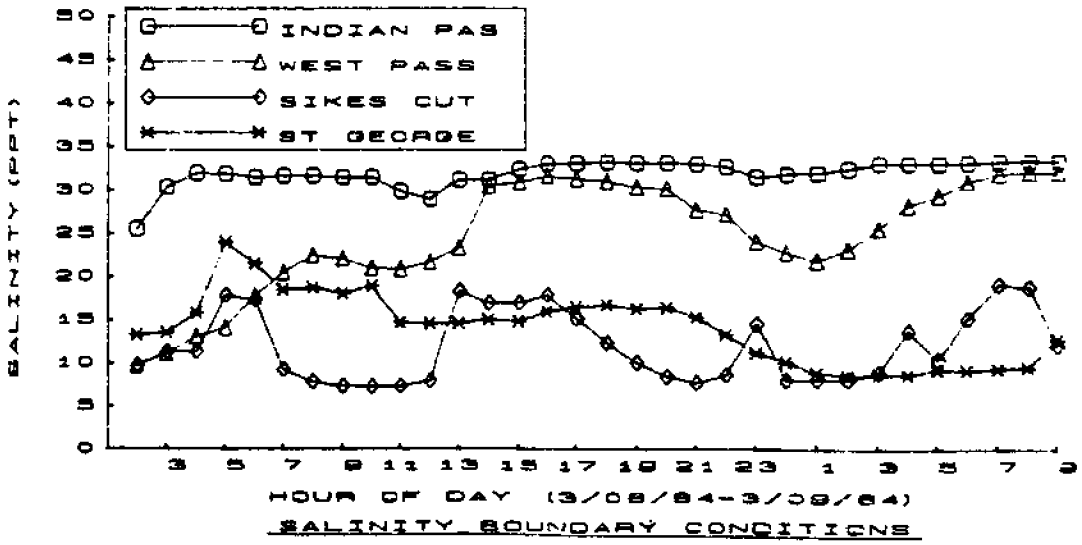

Figure VI.8. Salinity Boundary Conditions for Verification Period

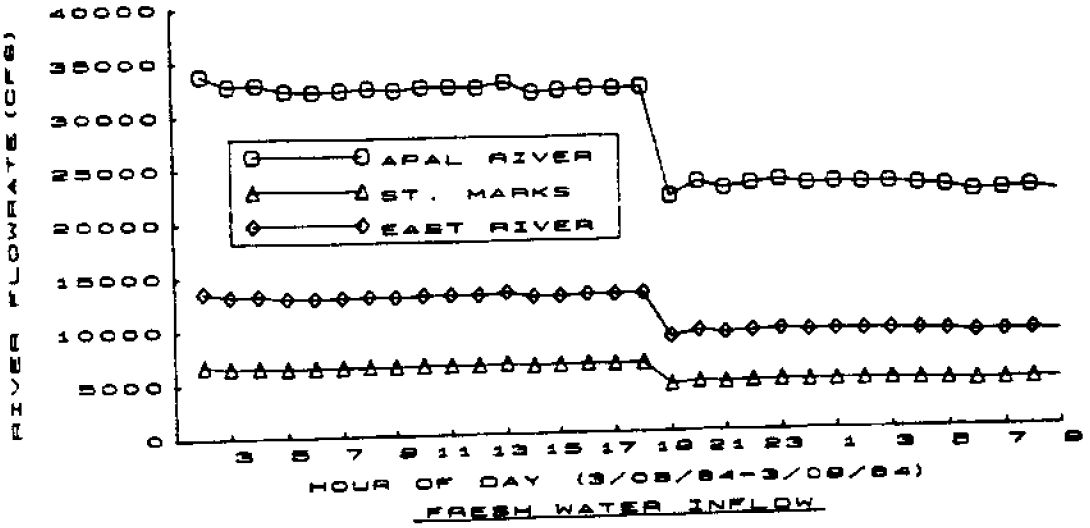

Figure VI.9. River Boundary Conditions for Verification Period

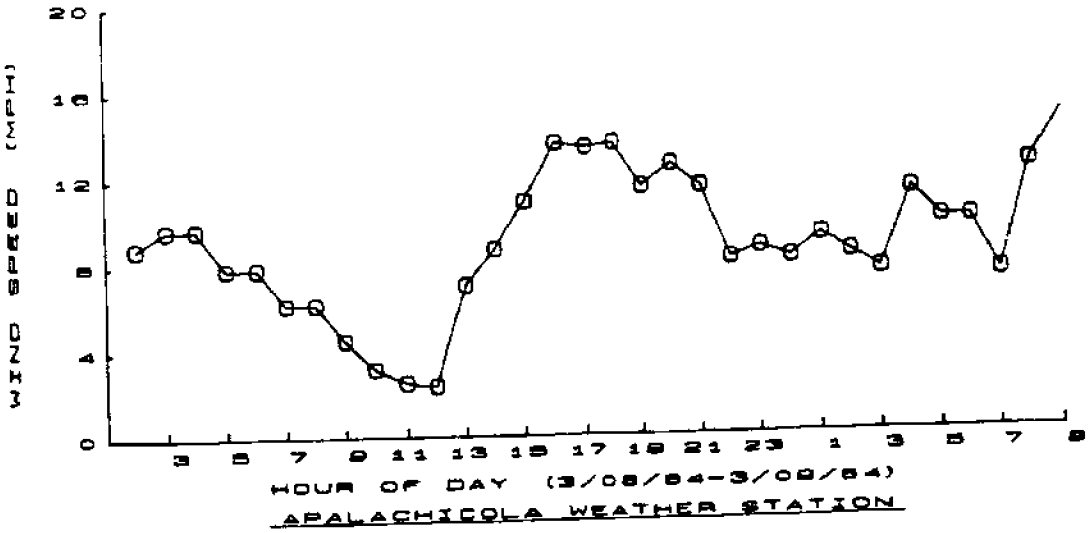

Figure VI.10. Wind Magnitude Boundary Condition for Verification Period

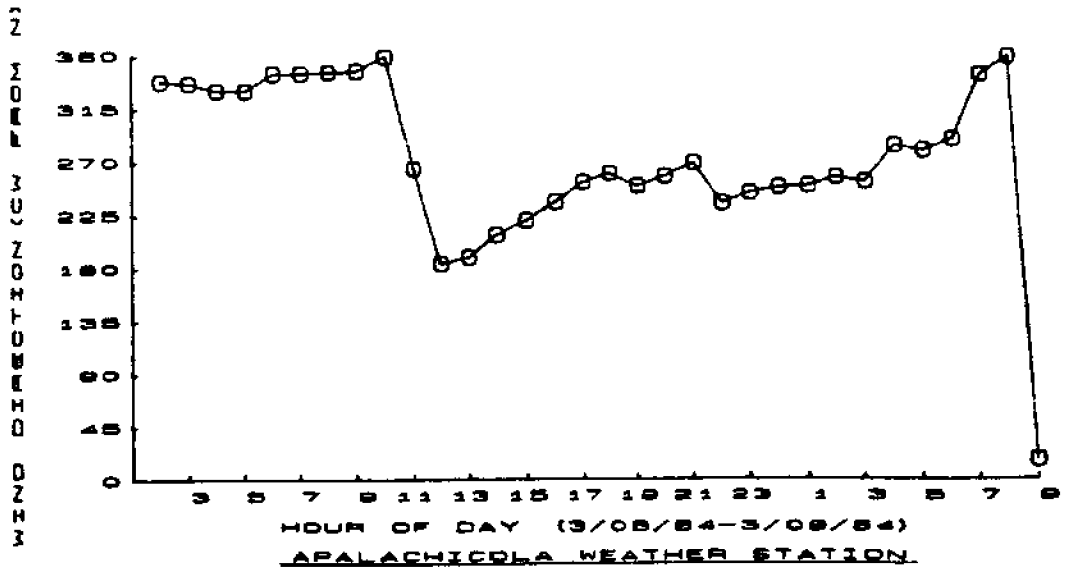

Figure VI.11. Wind Direction Boundary Condition for Verification Period

although at some locations the specific value predicted by the model may differ somewhat from the measured value.

Salinity contours are presented in Figures B-23 thru B-35. At the beginning of the calibration period a low tide condition exists and the total river inflow is high (approximately 51,000 cfs). Low salinity water is observed in a major portion of Apalachicola Bay. The 15 ppt salinity contour has been pushed into St. George Sound, St. Vincent Sound and the region near West Pass. Over the next seven hours the river inflow remains essentially constant and the low salinity water region expands with 10 ppt water extending into St. George Sound and St. Vincent Sound. At about 1800 on March 8, 1984 the bay is approaching a high tide condition and the total river inflows decrease significantly, to around 37,000 cfs, and remains near this value for the remainder of the verification period. During this period there is a very significant tidal elevation difference between St. George Sound and West Pass and Indian Pass producing a strong flow to the west. The low salinity water moves out of St. George Sound and is pushed towards West Pass and Indian Pass. At the end of the verification period almost all of St. George Sound contains water of 20 ppt or higher.

Representative velocity vector plots are presented in Figures B-36 thru B-59. The vector plots represent flow conditions at six times during the verification process for St. Vincent Sound, Apalachicola Bay, East Bay and St. George Sound.

VII. CONCLUSIONS

One of the problems with which numerical modelers must normally contend is the lack of sufficient prototype data for model calibration and verification. Fortunately, in this study of Apalachicola Bay, sufficient prototype data were available. The 30 days of prototype data in September 1983 and April 1984 combined with 24-hour manual collection periods during these same time periods and at other locations in Apalachicola Bay provide an excellent database for model calibration and verification. Data were available to establish all tidal, river and wind boundary conditions. In addition, there were as many as three other locations where surface elevation was known, eight other locations where velocity data were available and 13 other locations where salinity data were available for at least a continuous 24-hour period.

The model calibration process was successful with numerical model results showing very good agreement with prototype data. Of course, the model formulation assumes that conditions are constant across the water column. However, even in regions where prototype data indicated some degree of flow stratification, numerical model results appear to accurately represent average conditions over the water depth.

The prototype data used to calibrate the numerical model are very similar to average conditions found in Apalachicola Bay; i.e., the tidal range, river inflows, wind conditions, etc., are similar to yearly average conditions. The numerical model results for the calibration condition thus represent somewhat average conditions for Apalachicola Bay. This is of particular interest with regard to salinity contours in Apalachicola Bay and how the salinity contours change over the tidal cycle.

The prototype conditions used to verify the numerical model are more typical of early spring conditions than average conditions for the bay. Here again, the numerical model results demonstrate the model's ability to predict the overall behavior of Apalachicola Bay when subjected to specific forcing functions (tidal elevations, river inflows, wind).

For both calibration and verification conditions, model results indicate that the hydrodynamics of the bay (velocities and surface elevations) are dominated by astronomical tides. There is a net west flow in the bay system. River inflow contributes measurably to the bay hydrodynamics but the effects are relatively small compared with the astronomical tide effects. The river inflow level does, however, very significantly affect the salinity contours in the bay and their variation over the tidal cycle. Under low to average river inflow conditions, significant amount of 10-15 ppt salinity water may enter the lower reaches of East Bay. Under large river flow conditions, East Bay and significant portions of the main body of Apalachicola Bay will contain essentially fresh water. Salinity level in St. George Sound are not as affected by fresh water inflows as are other portions of the bay because of the net east to west flow within the bay.

The numerical model of Apalachicola Bay has been calibrated and verified to an extent where it appears capable of being used as a predictive tool. The current finite difference grid may provide sufficient resolution for a particular study or the current grid can be used in conjunction with a sub-grid if smaller resolution in the study area is required.

VIII. REFERENCES

1. Ames, William F., "Numerical Methods for Partial Differential Equations," Academic Press, 2nd Edition, 1977.

2. Boris, J. P. and Book, D. L., 1973 (Jan), "Flux-Corrected Transport I: SHASTA, A Fluid Transport Algorithm That Works," Journal of

3. Butler, H. L. and Raney, D. C., "Finite Difference Schemes for Simulating Flow in an Inlet-Wetlands System," Proceedings of the Army Numerical Analysis and Computers Conference, The Army Mathematics Steering Committee, Durham, NC, March 1976.

4. Butler, H. Lee, "Coastal Flood Simulation in Stretched Coordinates," 16th International Conference on Coastal Engineering, proc. to be published, Hamburg, Germany, 27 August-1 September, 1978c.

5. Butler, H. Lee, "Evolution of a Numerical Model for Simulating Long-Period Wave Behavior in Ocean-Estuarine Systems," Estuarine and Wetland Processes with Emphasis on Modeling, Marine Science Series, Vol. 11, Plenum Press, New York, 1980.

6. Butler, H. Lee, "Finite Difference Numerical Model for Long-Period Wave Behavior: With Emphasis on Storm Surge Modeling," Proceedings of a Two-Dimensional Flow Modeling Seminar, Hydrologic Engineering Center, CE, Davis, CA, 7-9 July 1981a, proc. to be published.

7. Butler, H. Lee, "Lake Pontchartrain and Vicinity Hurricane Protection Plan, Report 3, Technical Report, U. S. Army Engineer Waterways Experiment Station, CE, Vicksburg, MS, 1981b, in publication.

8. Carnahan, Brice, Luther, H. A., and Wilkes, James O., "Applied Numerical Methods," John Wiley and Sons, Inc., 1969.

9. Ferziger, Joel H., "Numerical Methods for Engineering Application," John Wiley and Sons, 1981.

10. Greenspan, Donald, "Discrete Numerical Methods in Physics and Engineering," Vol. 107 in Mathematics in Science and Engineering Series, Academic Press, Inc., 1974.

11. Leendertse, J. J., "Aspects of Computational Model for Long-Period Water-Wave Propagation," RM-5294-PR, Rand Corporation, Santa Monica, CA, 1967.

12. Leendertse, J. J., "A Water-Quality Simulation Model for Well-Mixed Estuaries and Coastal Seas., Vol. 1, Principals of Computation," RM-6230-RC, Rand Corporation, Santa Monica, CA, February 1970.

13. Leendertse, J. J. and Gritton, E. C., "A Water-Quality Simulation Model for Well-Mixed Estuaries and Coastal Seas., Vol. 2, Computational Procedures," RM-708-NYC, Rand Institute, New York, NY, April 1971.

14. Leonard, B. P., Dec., "A Consistency Check for Estimating Truncation Error due to Upstream Differencing," Applied Math. Modelling, Vol. 2, pp. 239-244.

15. Mitchell, A. R. and Griffiths, D. F., 1980. The Finite Difference Method in Partial Differential Equations, John Wiley & Sons, New York.

16. Raney, D. C., Durham, D. L., and Butler, H. L., "Lake Erie International Jetport Model Feasibility Investigation; Numerical Model Feasibility Study," Technical Report H-74-6, Report 17-4, U. S. Army Engineer Waterways Experiment Station, CE, Vicksburg, MS, April 1977.

17. Reid, R. O. and Bodine, B. R., "Numerical Model for Storm Surges in Galveston Bay," Journal of Waterways and Harbors Division, ASCE, Vol. 94, No. WW 1, February 1968, Proc. Paper 5805, pp. 33-57.

18. Roache, P. J., 1976, Computational Fluid Dynamics, Hermosa Publishers, Albuquerque, New Mexico.

19. Shames, Irving H., "Mechanics of Fluids," McGraw-Hill Book Company, Inc., 2nd Edition, 1982.

20. Schmalz, R. A., "The Development of a Numerical Solution to the Transport Equation: Methodology," Miscellaneous Paper in publication, U. S. Army Engineer Waterways Experiment Station, Vicksburg, MS, 1981a.

21. Schmalz, R. A., "The Development of a Numerical Solution to the Transport Equation: Computational Procedures," Miscellaneous Paper in publication, U. S. Army Engineer Waterways Experiment Station, CE, Vicksburg, MS, 1981b.

22. van Leer, B., 1977, "Towards the Ultimate Conservative Difference Scheme III, Upstream-Centered Finite-Difference Schemes for Ideal Compressible Flow," Journal of Computational Physics, 23, pp. 263-275.

23. Vreugdenhil, C. B., "Secondary-Flow Computations," Delft Hydraulics Laboratory, Publication No. 114, November 1973.

24. Wanstrath, J. J., Whitaker, R. E., Reid, R. O., and Vastano, A. C., "Storm Surge Simulation in Transformed Coordinates, Vol. I - Theory and Application," Technical Report 76-3, U. S. Army Coastal Engineering Research Center, CE, Fort Belvoir, VA, November 1976.

25. Weare, T. John, "Errors Arising from Irregular Boundaries in ADI Solutions of the Shallow-Water Equations," International Journal for Numerical Methods in Engineering, Vol. 14, pp. 921-931, 1980.

26. Zalesak, S. T., 1979, "Fully Multi-Dimensional Flux-Corrected Transport Algorithms for Fluids," Journal of Computational Physics, 31, pp. 335-362.

IX. LIST OF FIGURES

LIST OF FIGURES (continued)

LIST OF FIGURES (continued)

LIST OF FIGURES (continued)

LIST OF FIGURES (continued)

APPENDIX A

Calibration Results

(0800 on September 14, 1983 to 0800 on September 15, 1983)

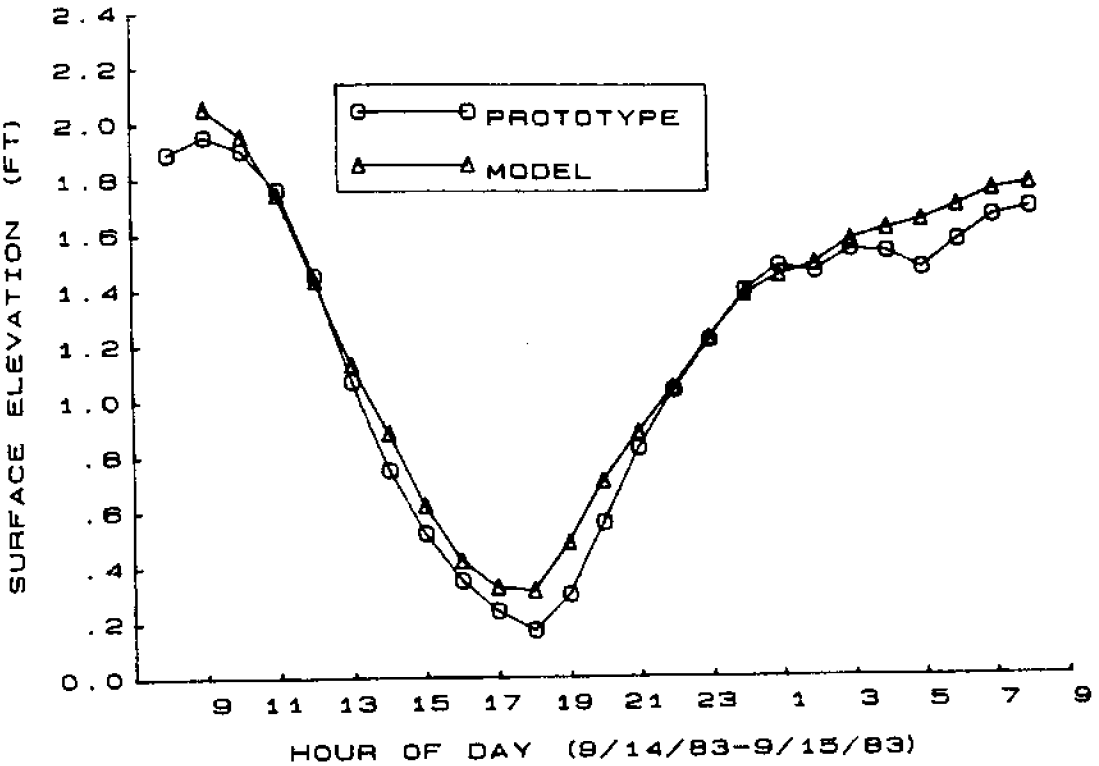

Figure A-1. Surface Elevation at Station SG3 for Calibration Condition

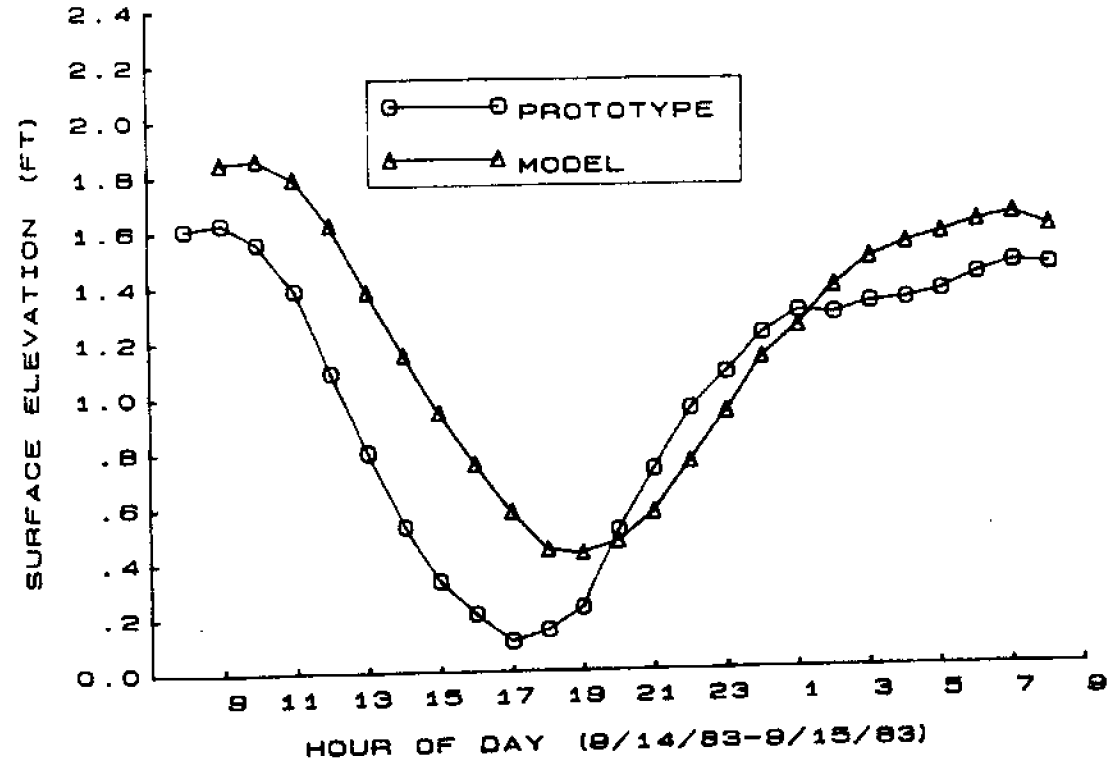

Figure A-2. Surface Elevation at Station SG7 for Calibration Condition

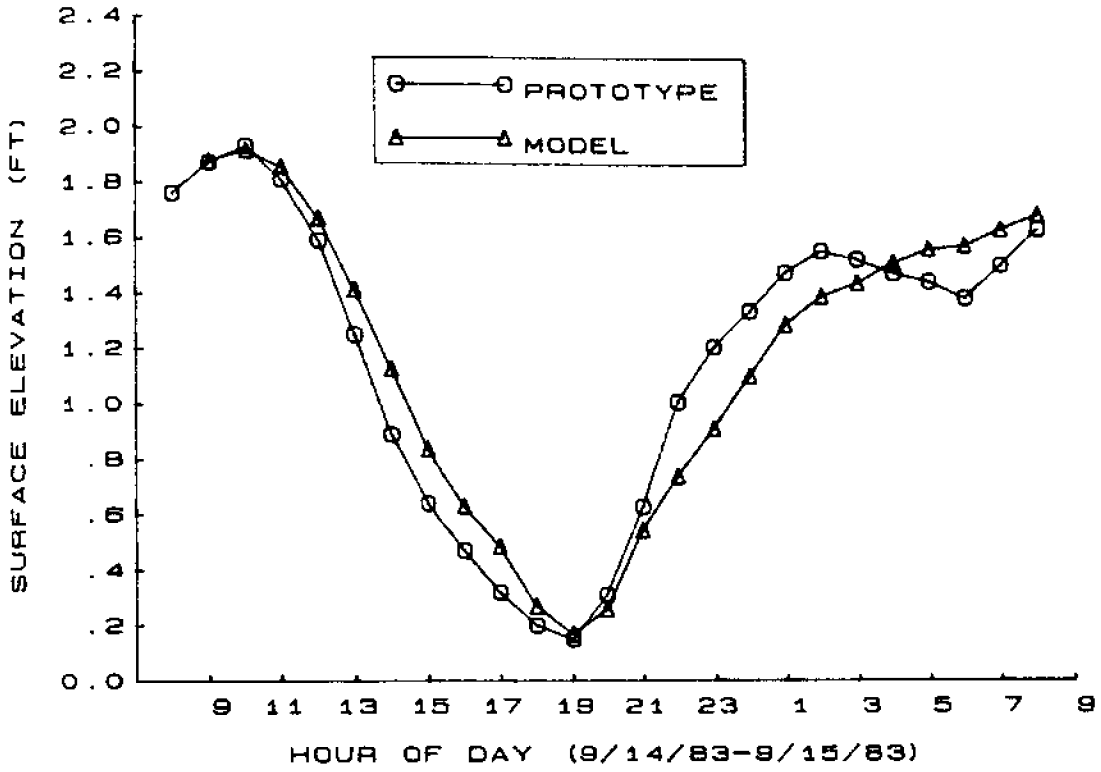

Figure A-3. Surface Elevation at Station SG10 for Calibration Condition

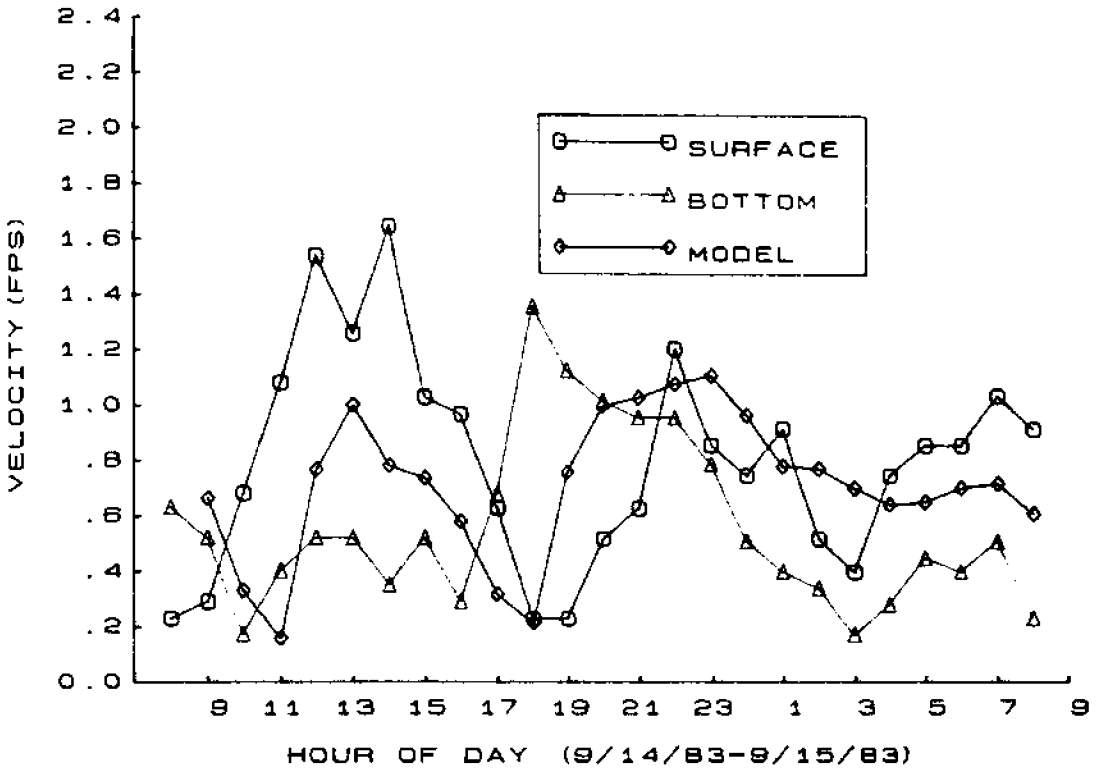

Figure A-4. Velocity at Station SG1 for Calibration Condition

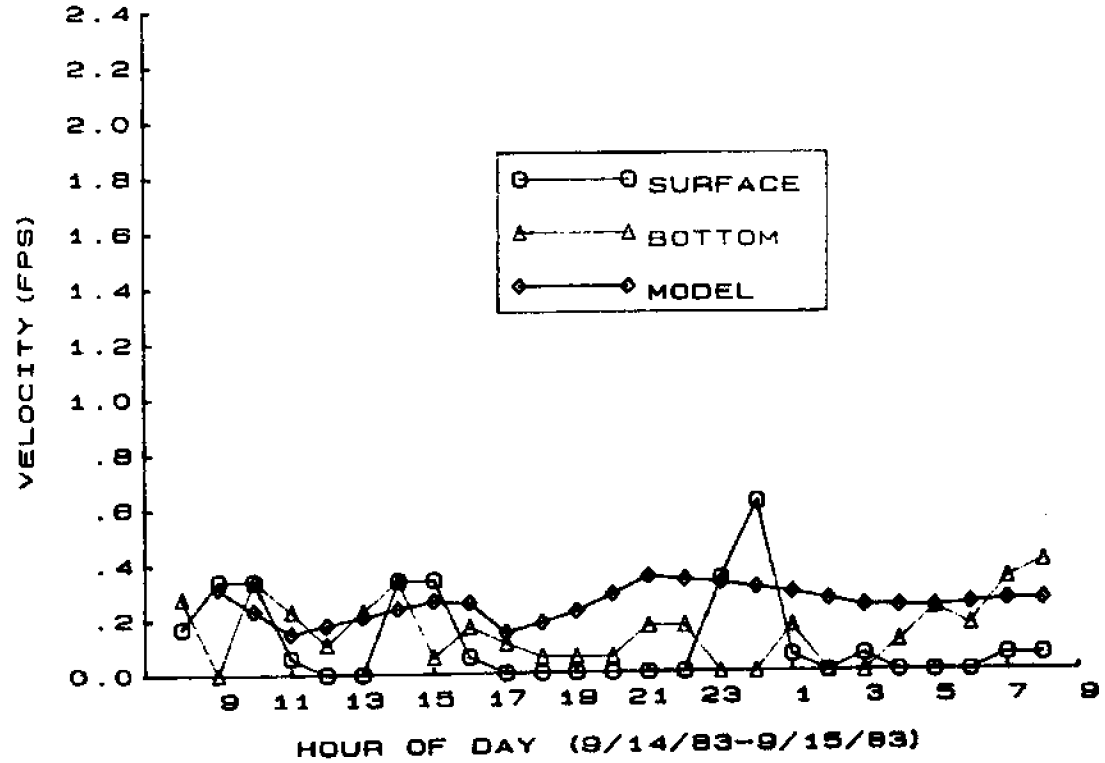

Figure A-5. Velocity at Station SG2 for Calibration Condition

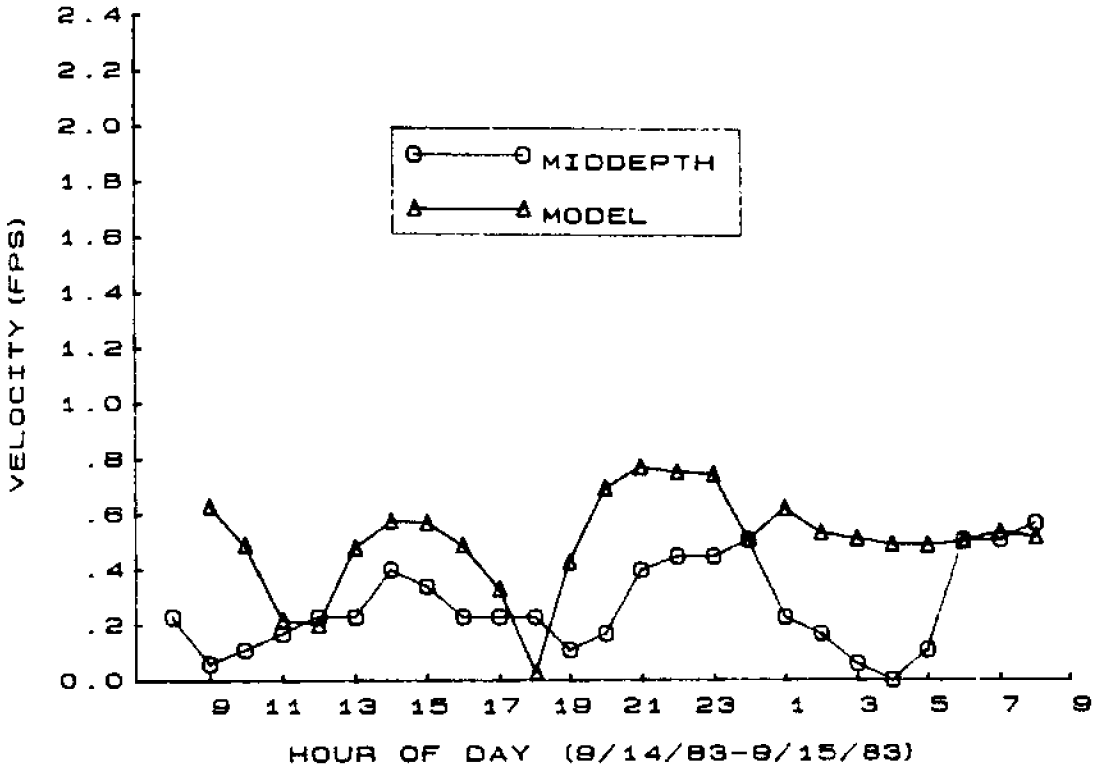

Figure A-6. Velocity at Station SG3 for Calibration Condition

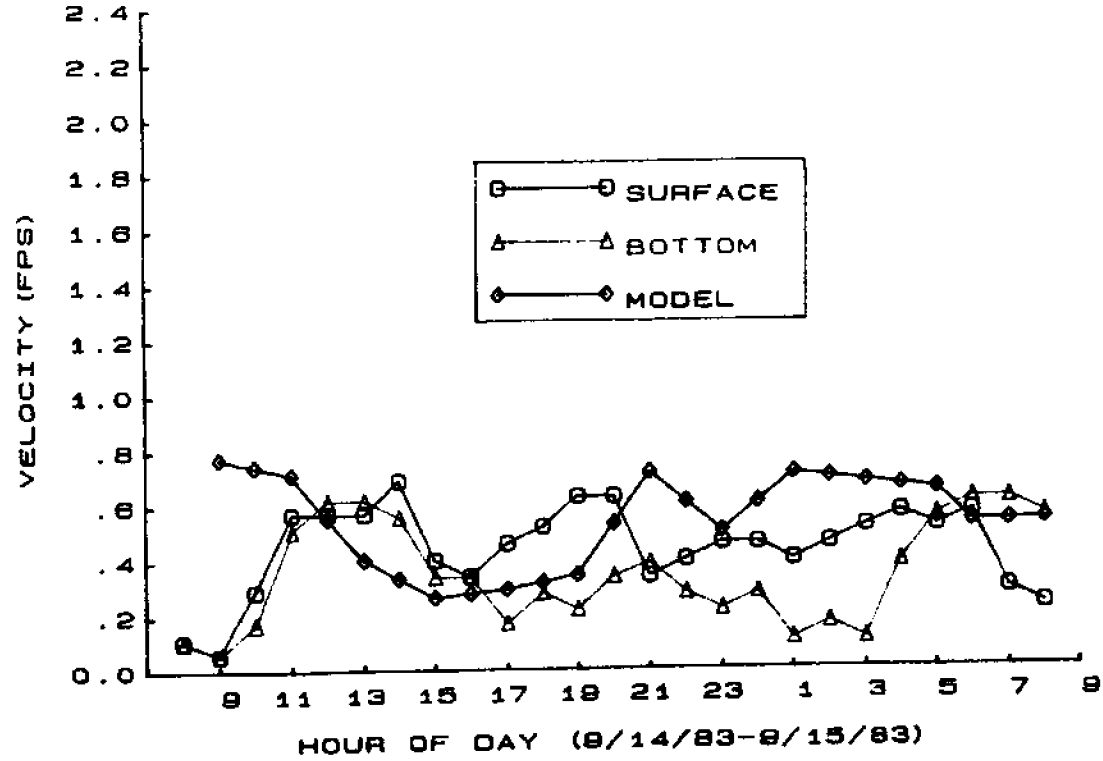

Figure A-7. Velocity at Station SG4 for Calibration Condition

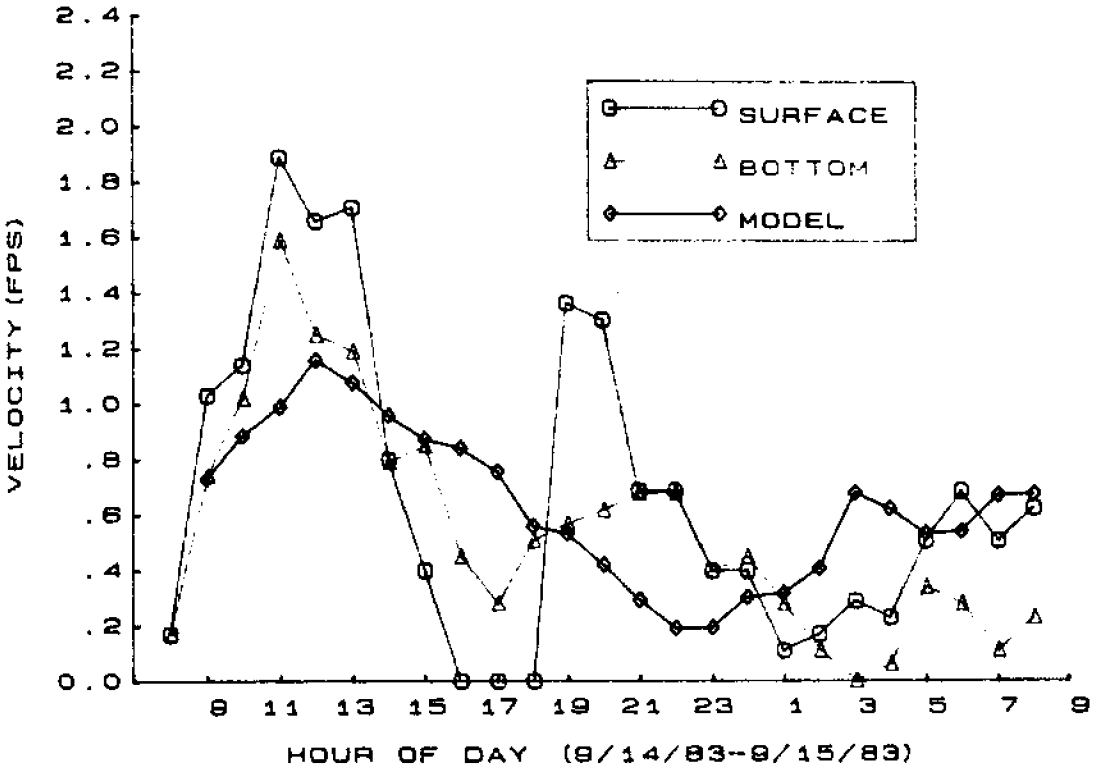

Figure A-8. Velocity at Station SG5 for Calibration Condition

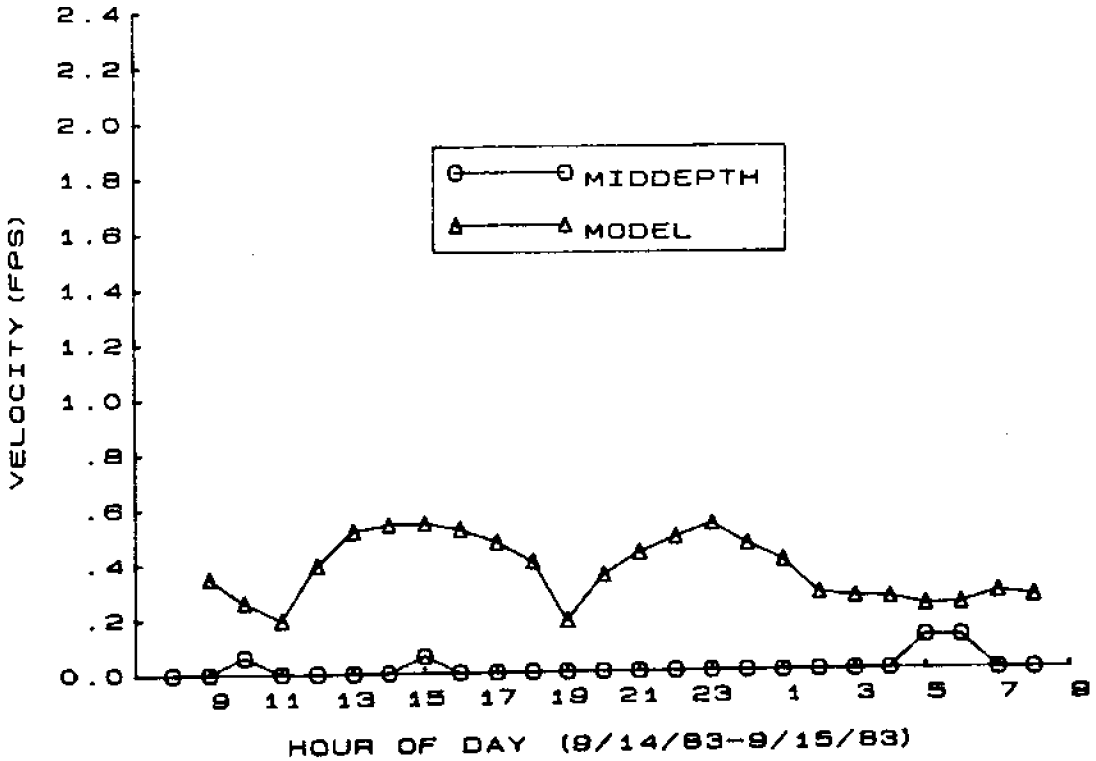

Figure A-9. Velocity at Station SG6 for Calibration Condition

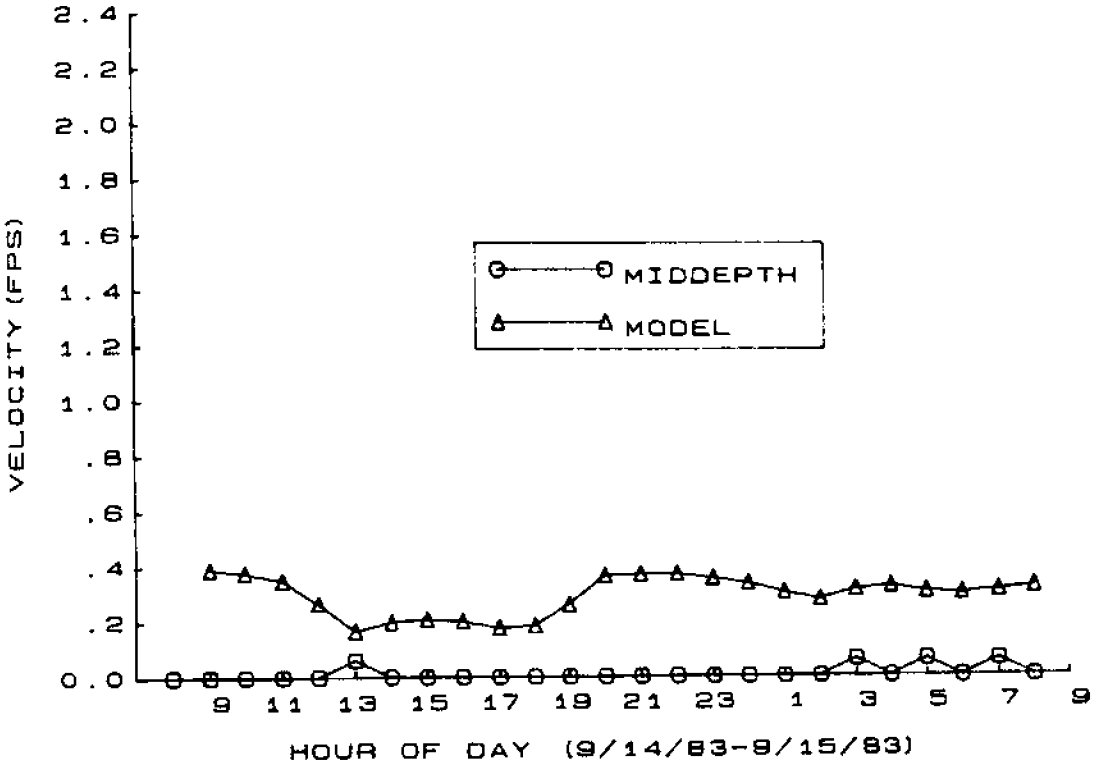

Figure A-10. Velocity at Station SG8 for Calibration Condition

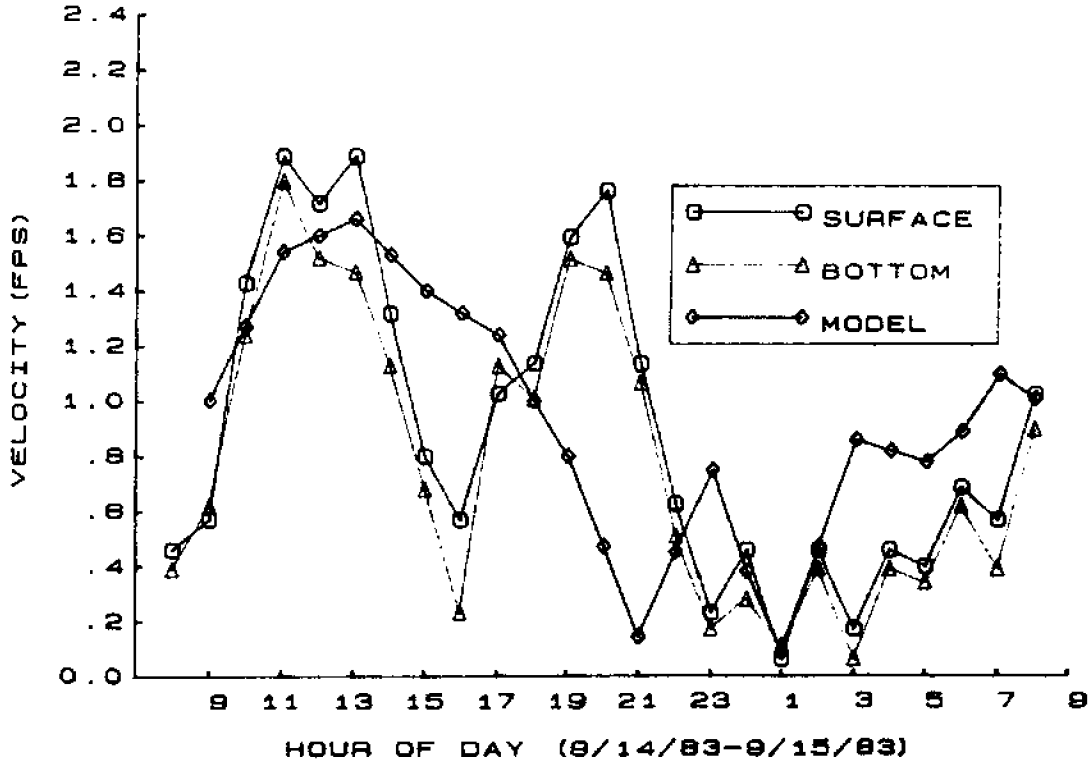

Figure A-11. Velocity at Station SG9 for Calibration Condition

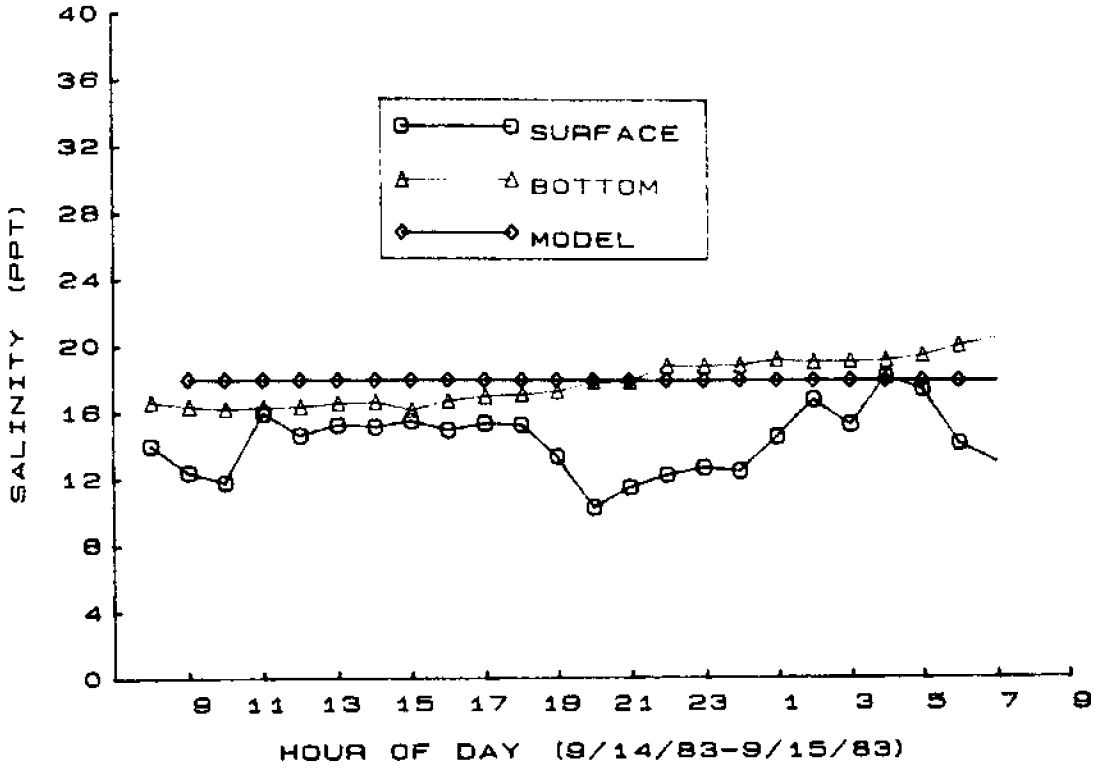

Figure A-12. Salinity at Station SG2 for Calibration Condition

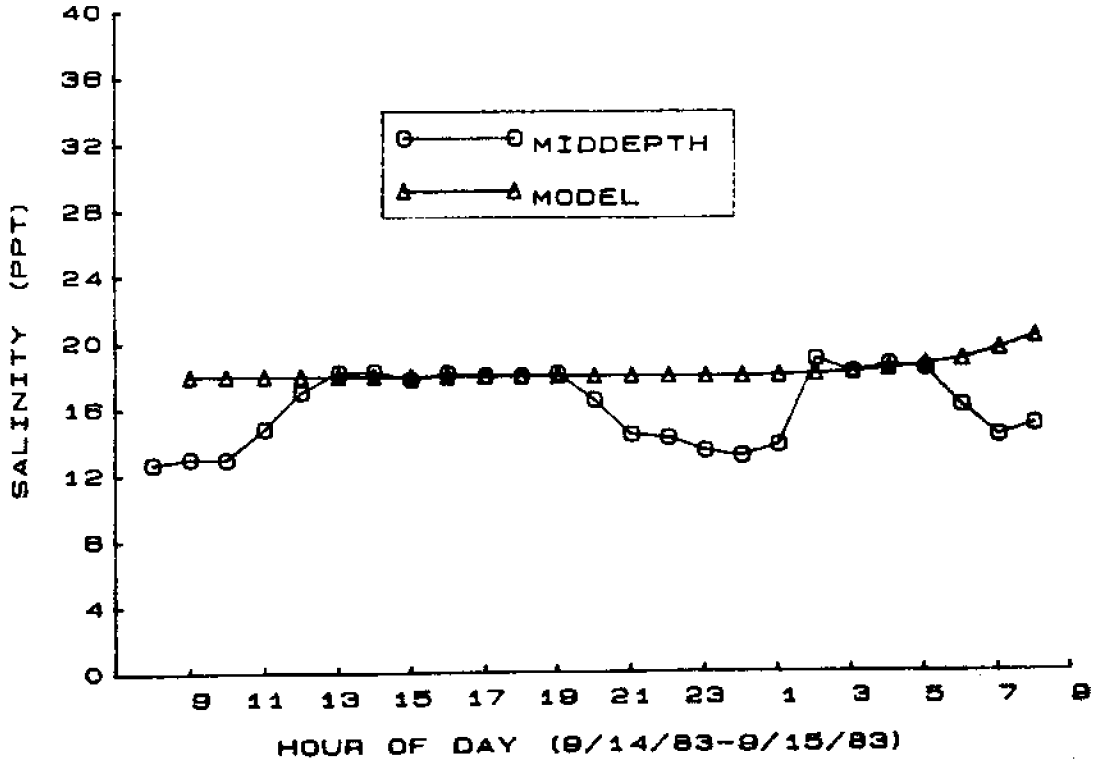

Figure A-13. Salinity at Station SG3 for Calibration Condition

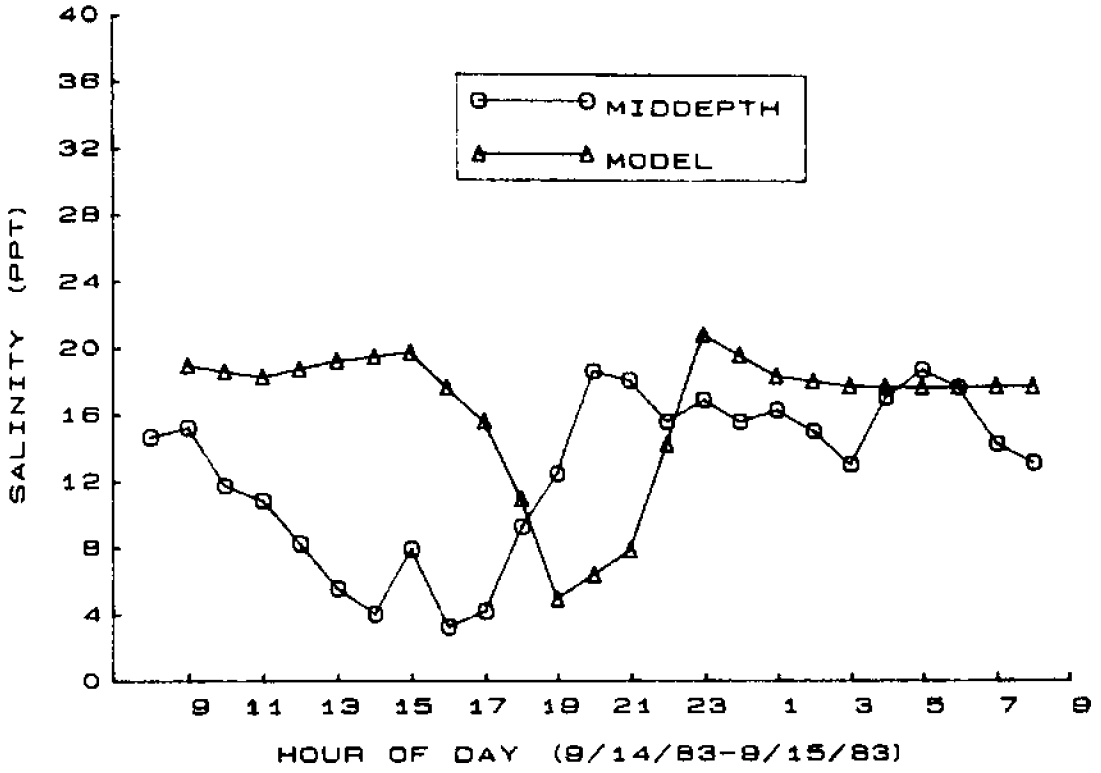

Figure A-14. Salinity at Station SG6 for Calibration Condition

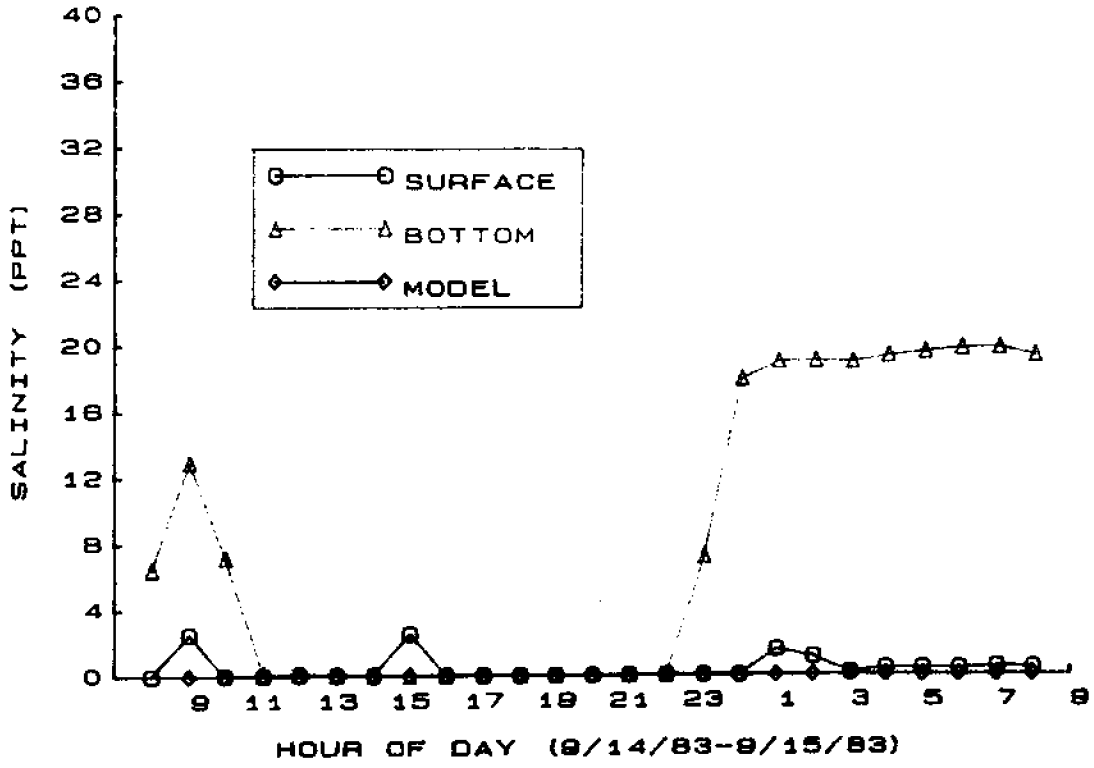

Figure A-15. Salinity at Station SG7 for Calibration Condition

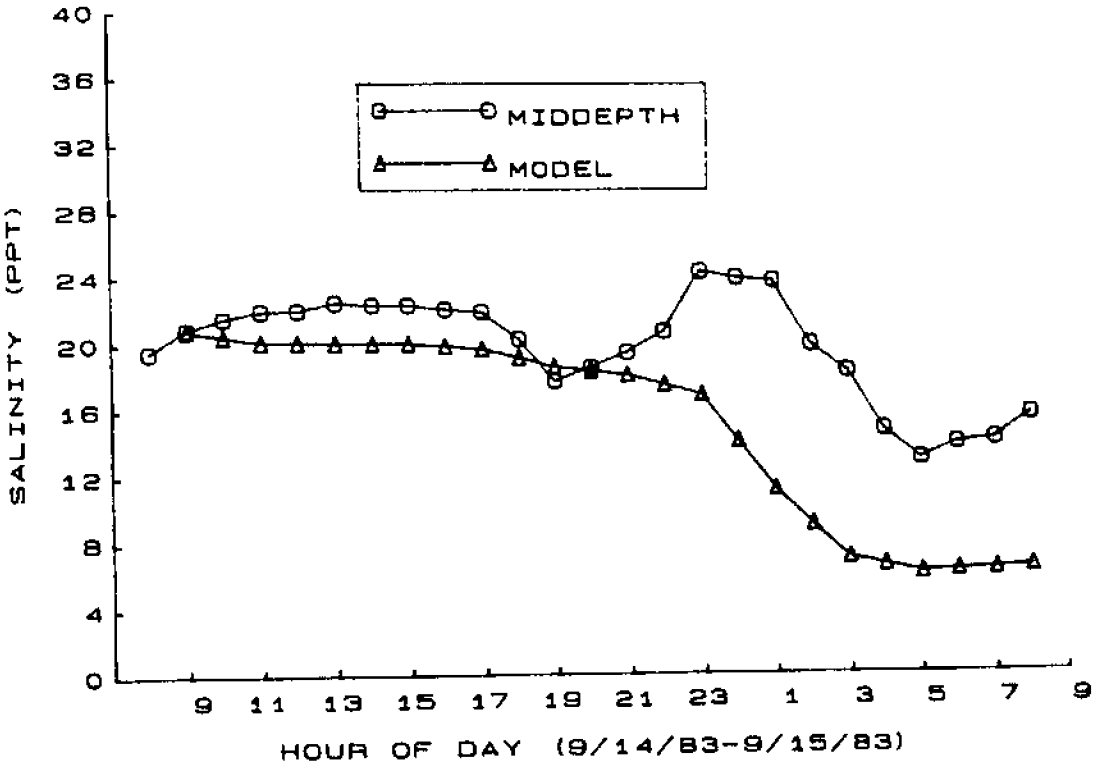

Figure A-16. Salinity at Station SG8 for Calibration Condition

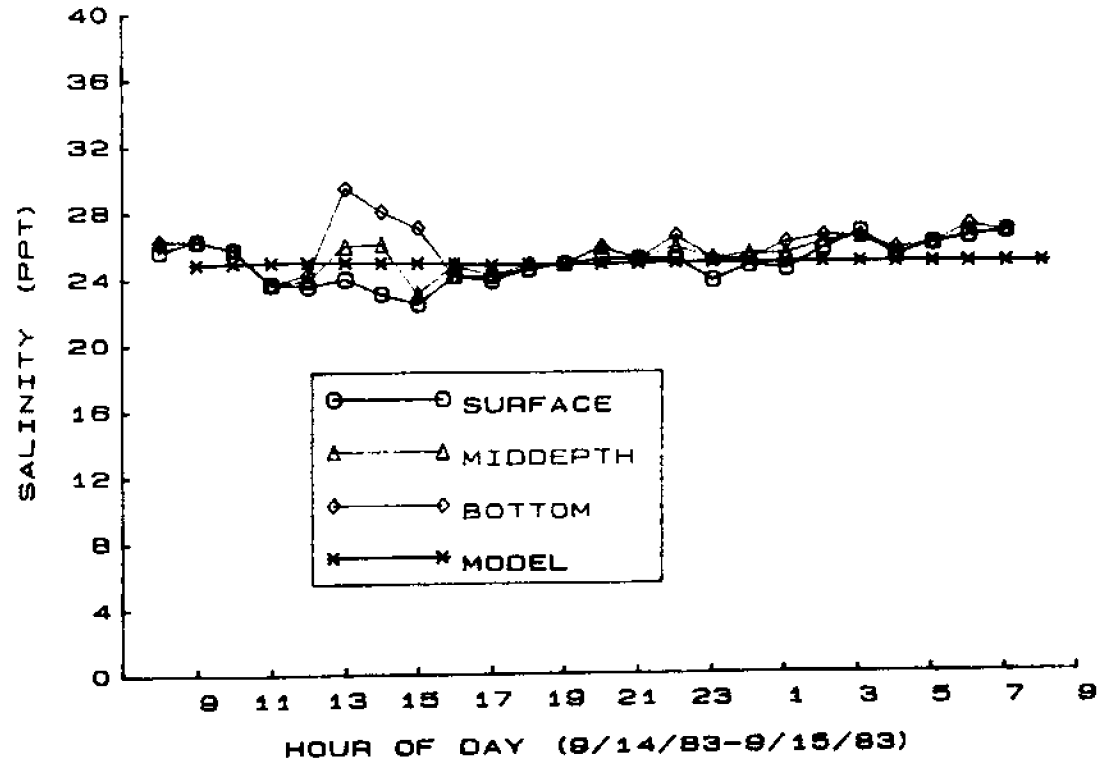

Figure A-17. Salinity at Station G2 for Calibration Condition

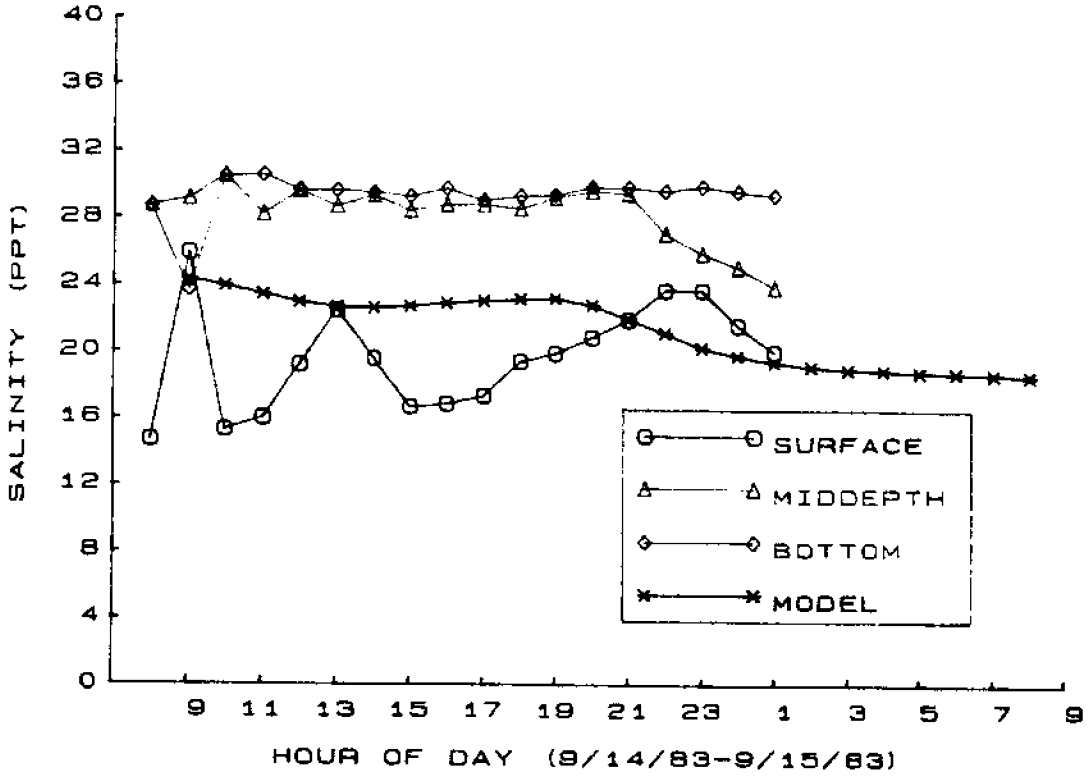

Figure A-18. Salinity at Station G3 for Calibration Condition

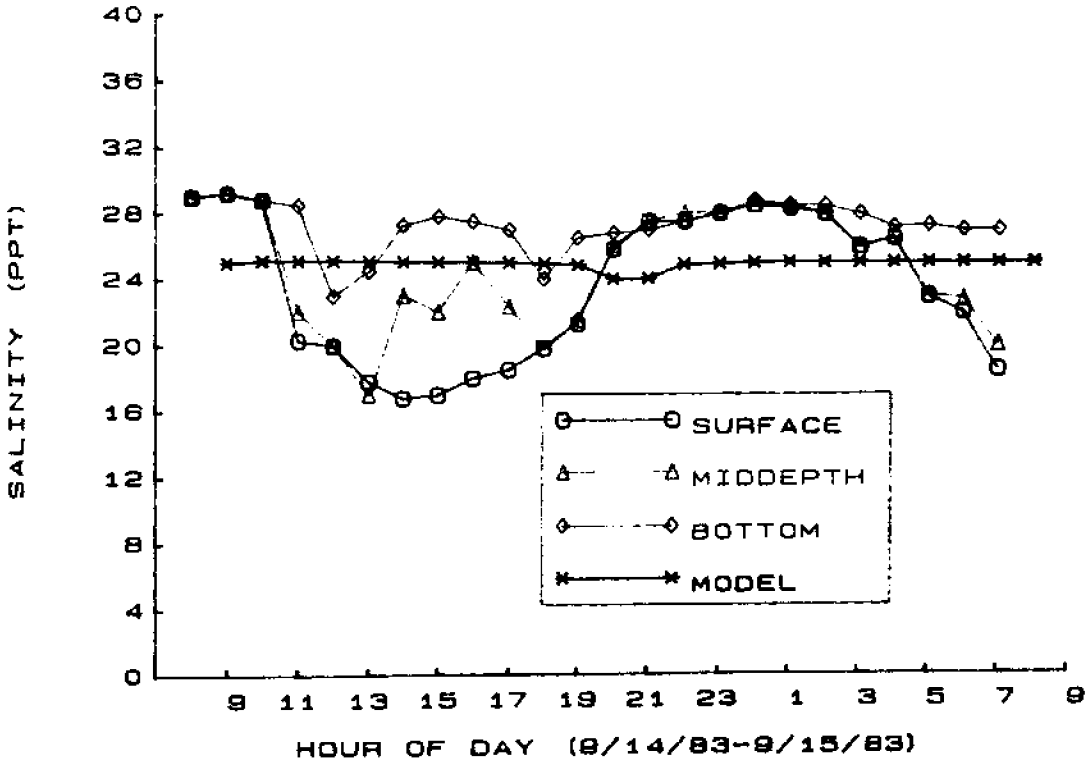

Figure A-19. Salinity at Station G4 for Calibration Condition

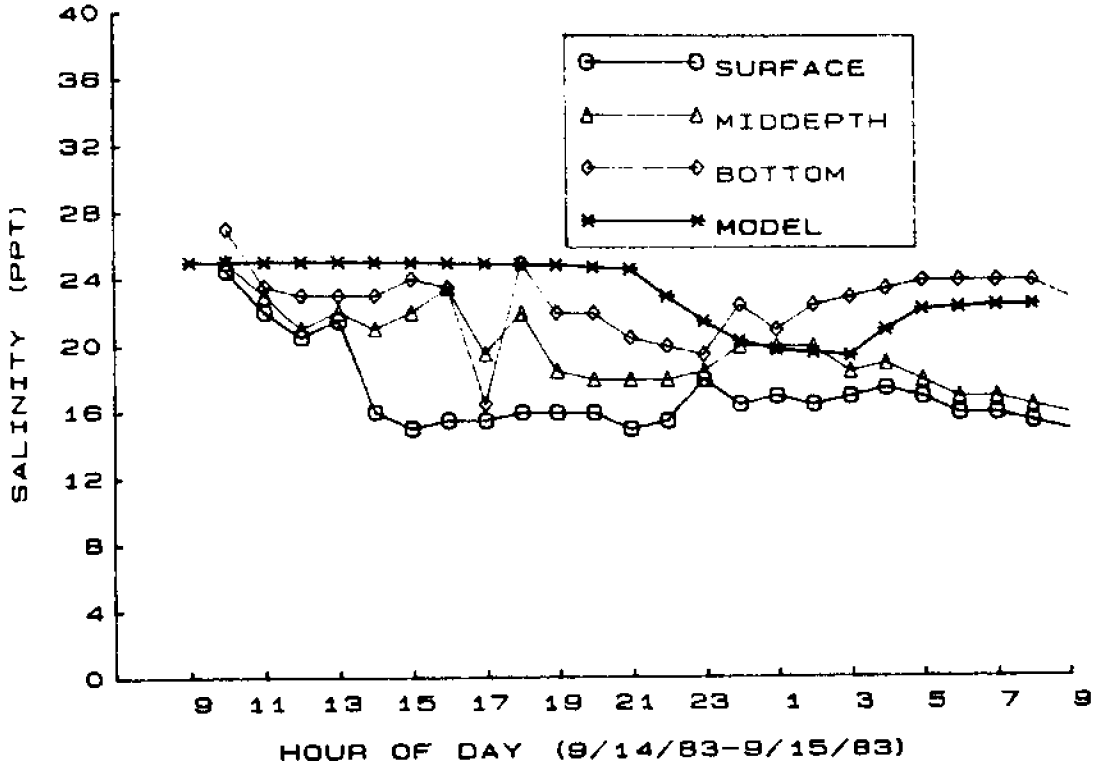

Figure A-20. Salinity at Station G5 for Calibration Condition

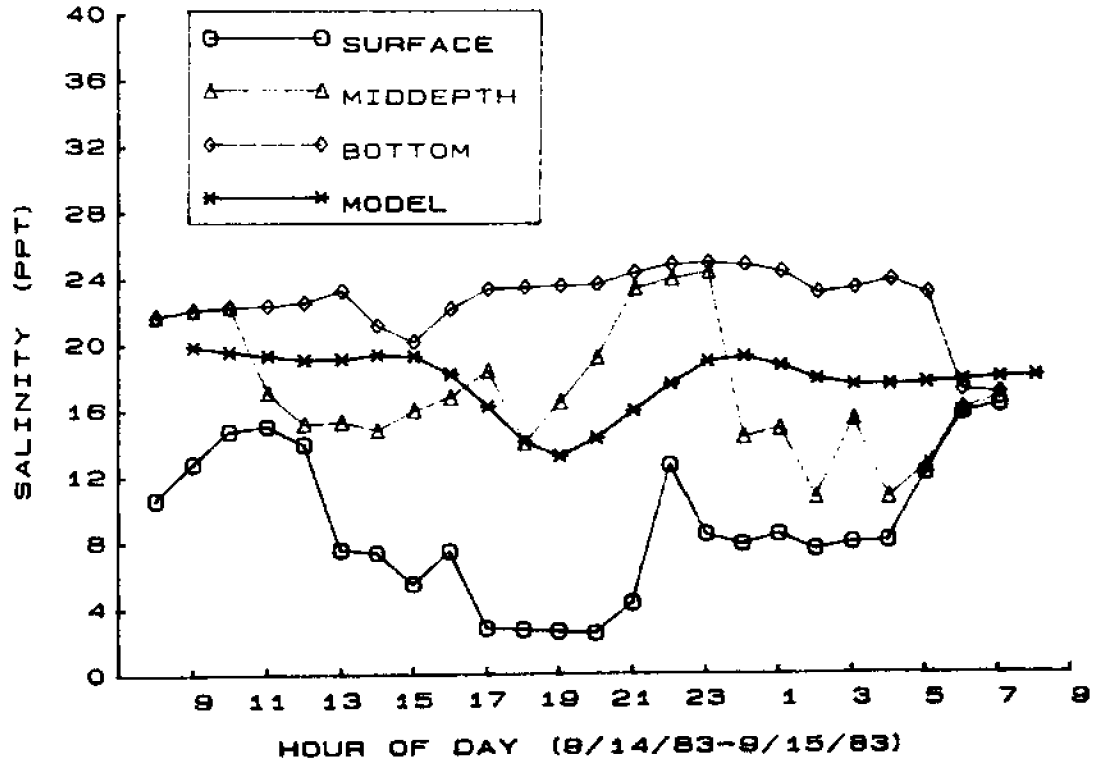

Figure A-21. Salinity at Station G6 for Calibration Condition

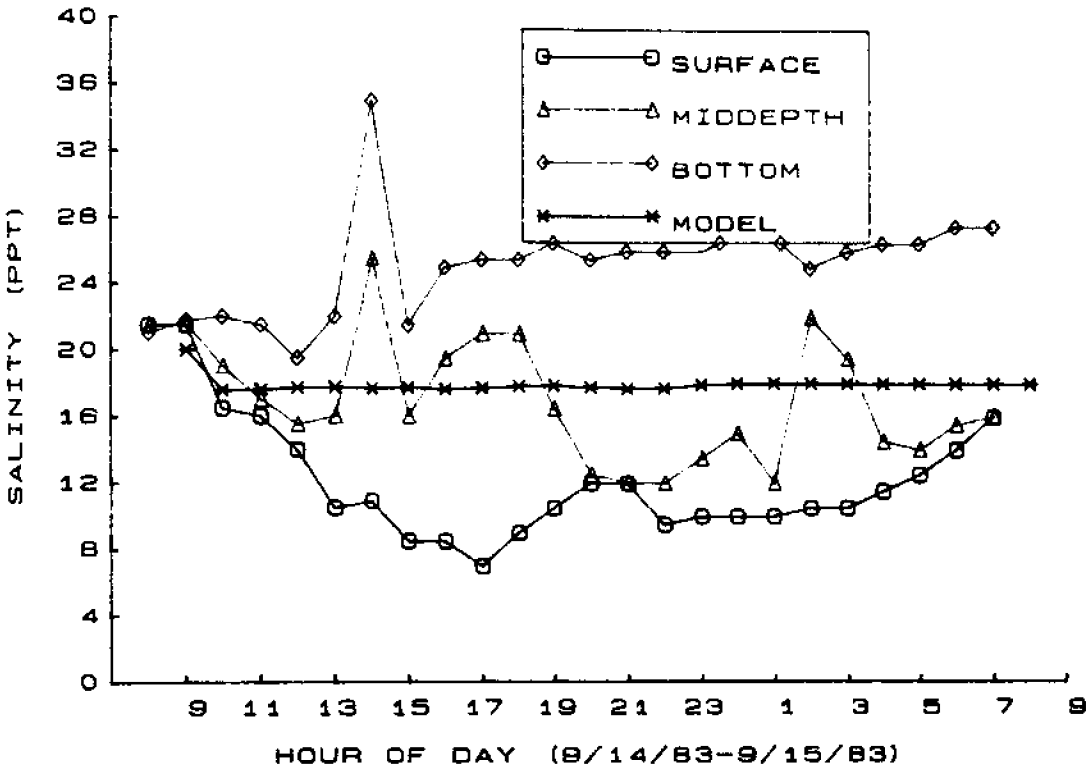

Figure A-22. Salinity at Station G7 for Calibration Condition

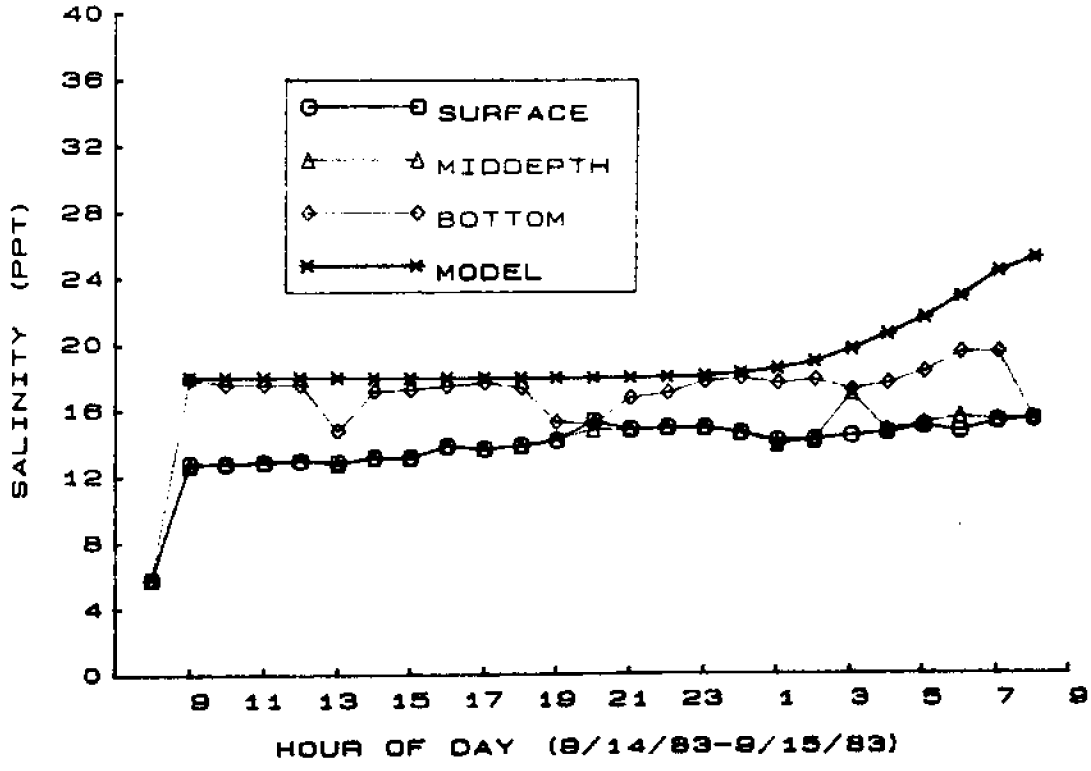

Figure A-23. Salinity at Station G8 for Calibration Condition

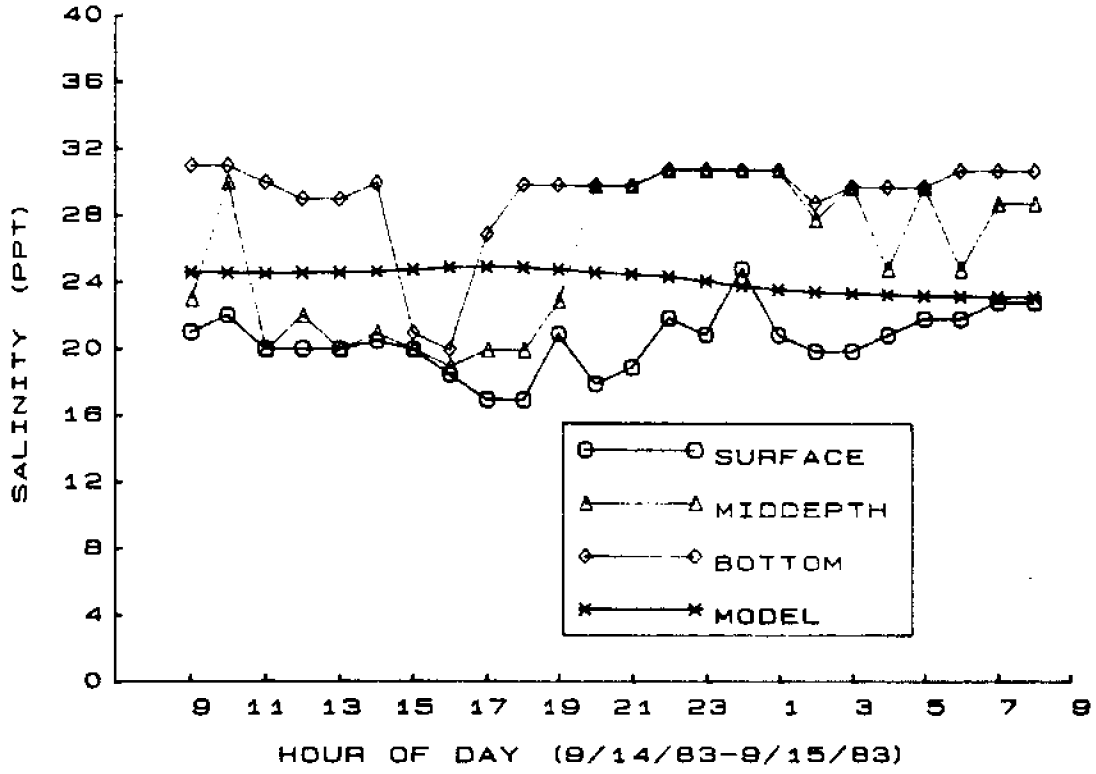

Figure A-24. Salinity at Station G9 for Calibration Condition

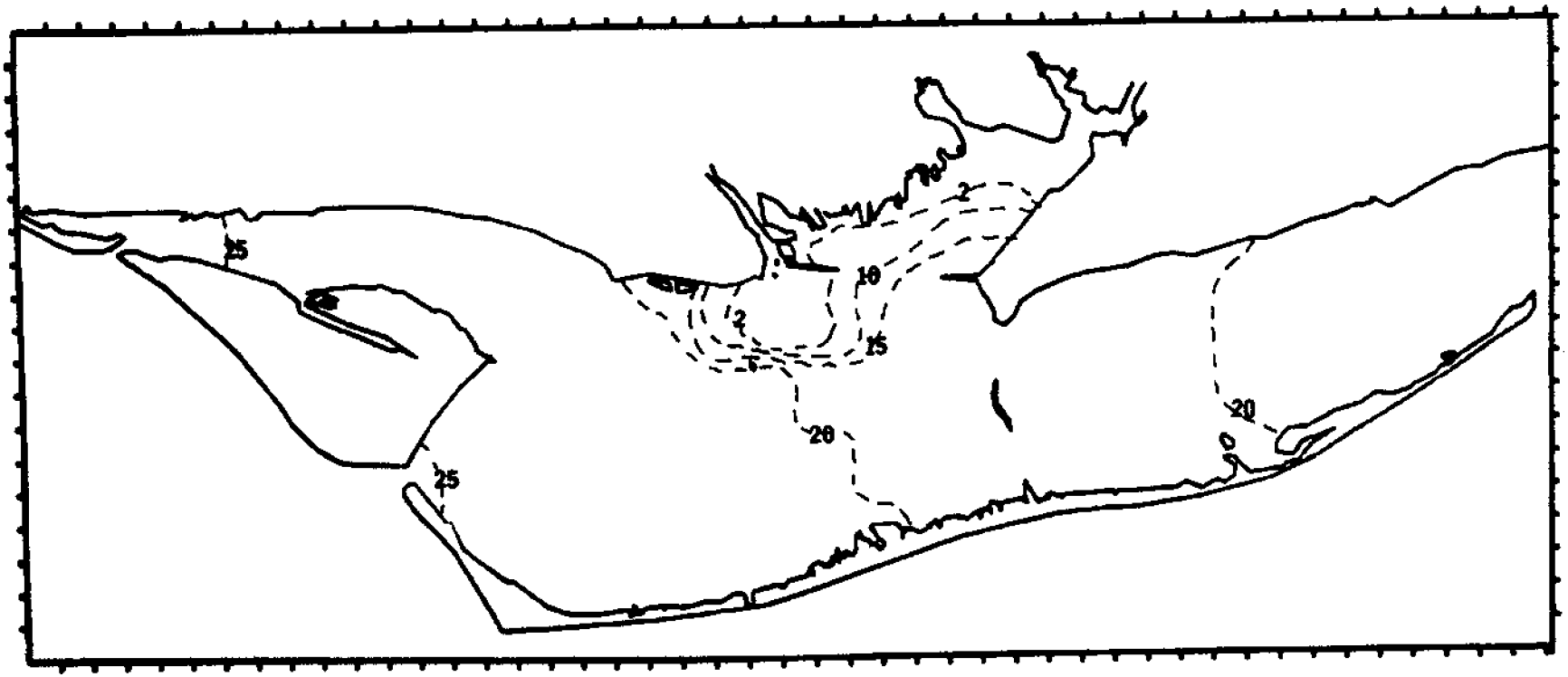

Figure A-25. Salinity Contours at 0900 on September 14, 1983

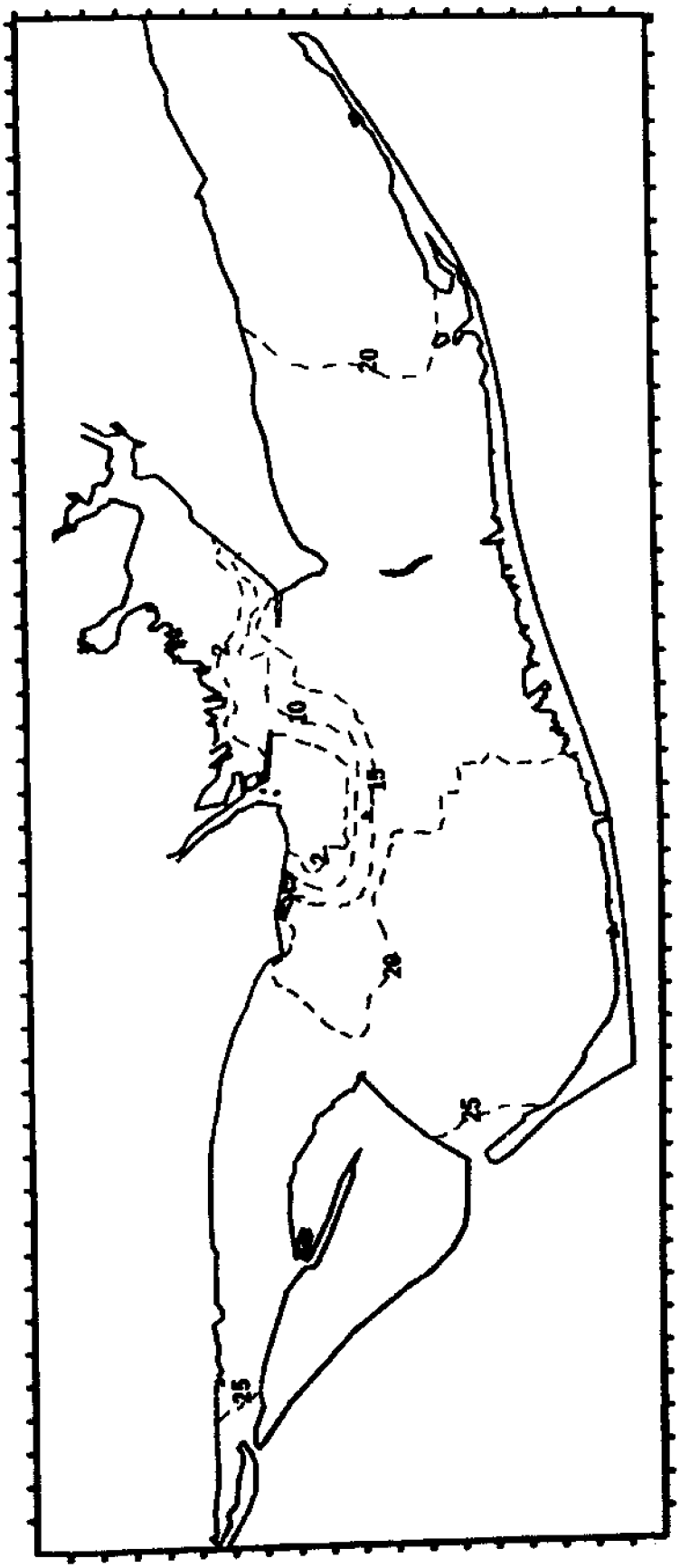

Figure A-26. Salinity Contours at 1100 on September 14, 1983

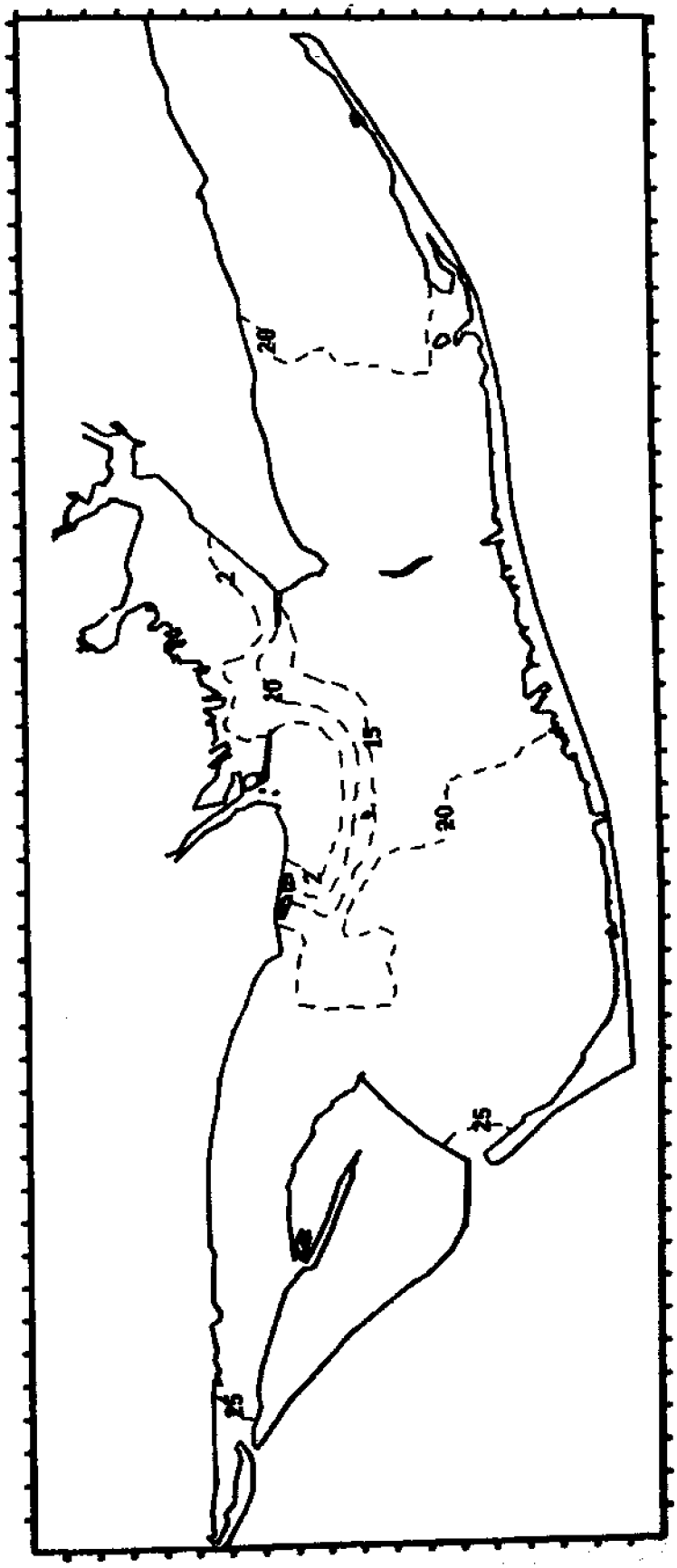

Figure A-27. Salinity Contours at 1300 on September 14, 1983

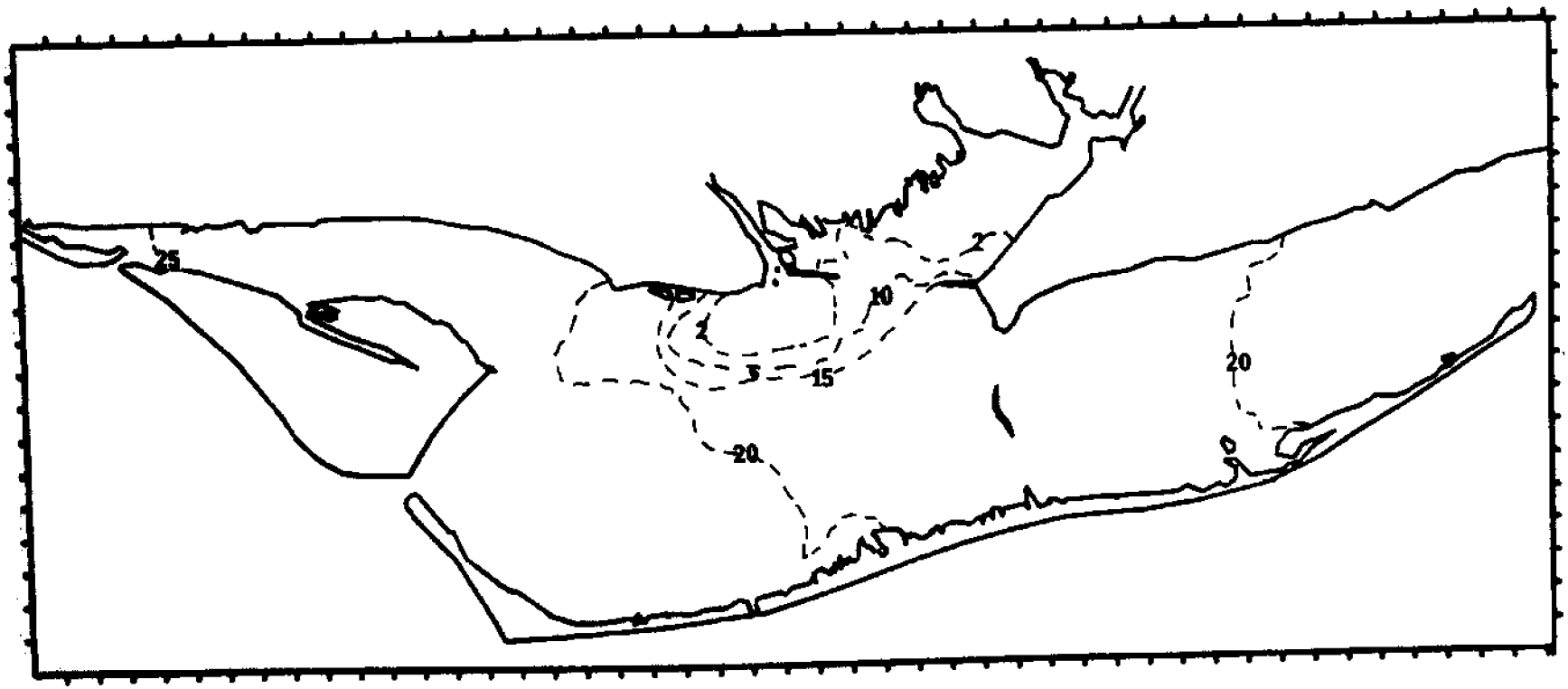

Figure A-28. Salinity Contours at 1500 on September 14, 1983

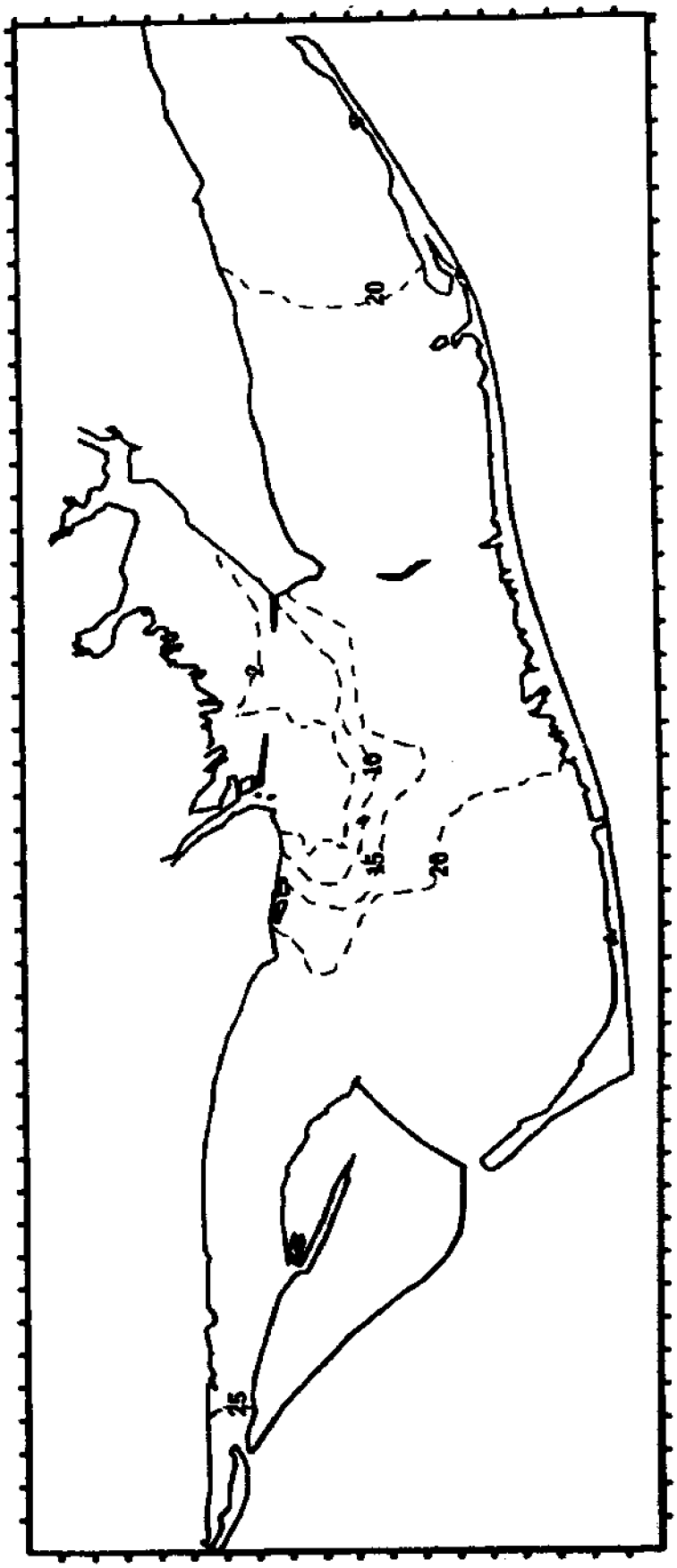

Figure A-29. Salinity Contours at 1700 on September 14, 1983

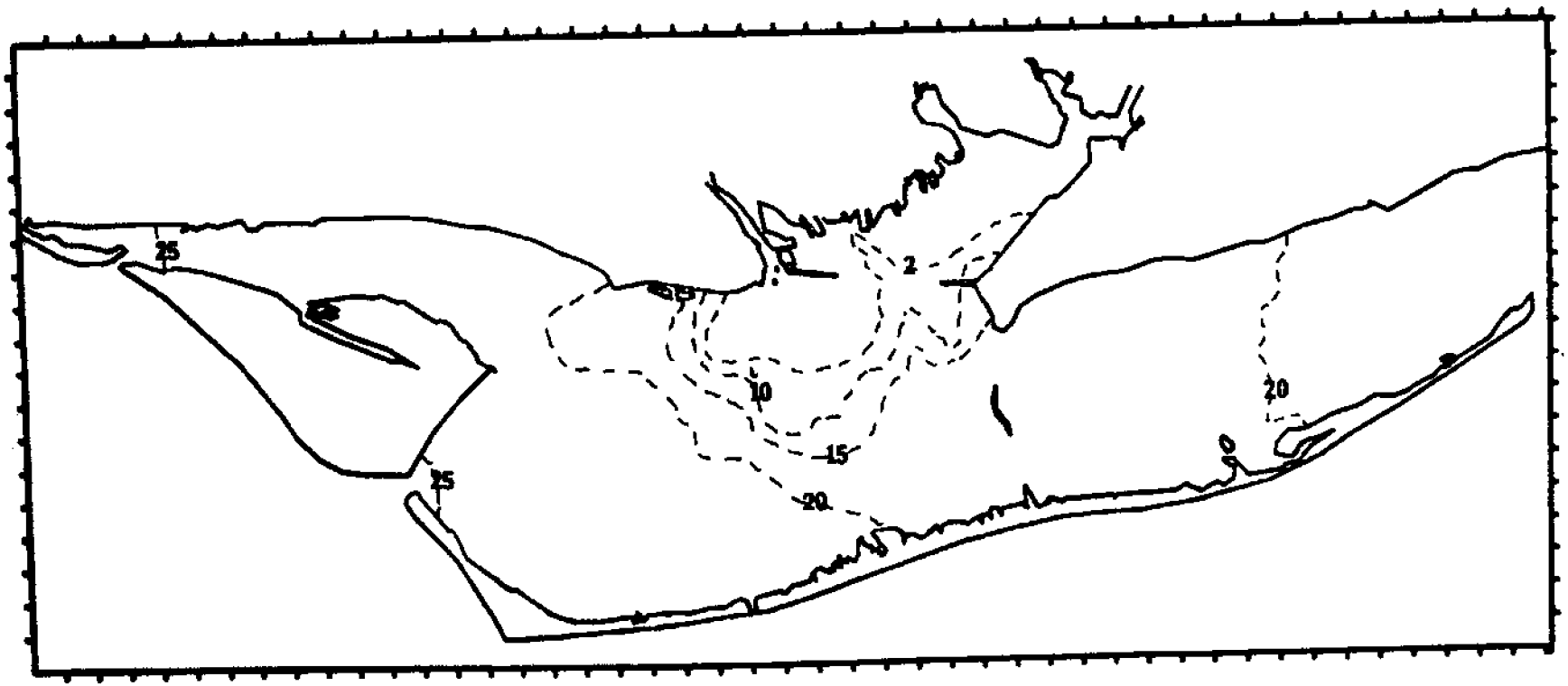

Figure A-30. Salinity Contours at 1900 on September 14, 1983

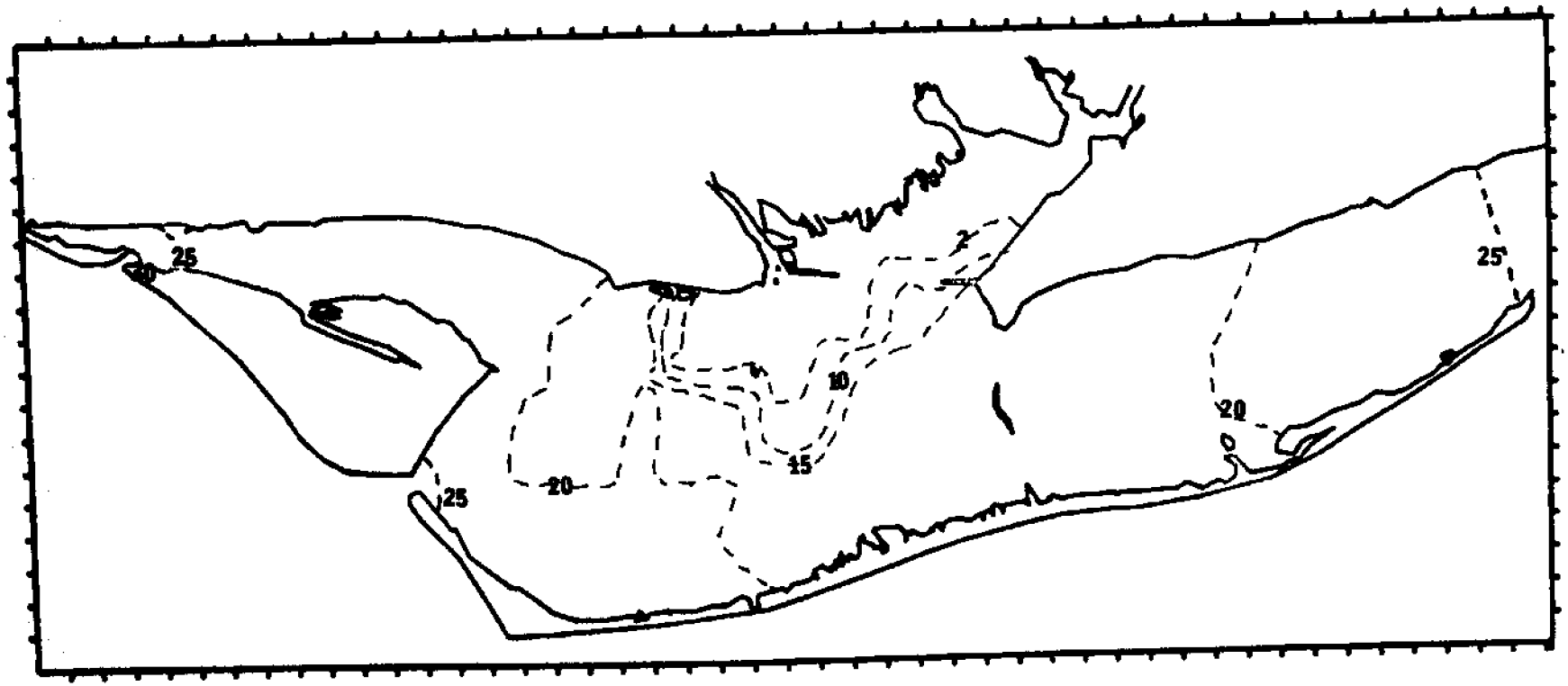

Figure A-31. Salinity Contours at 2100 on September 14, 1983

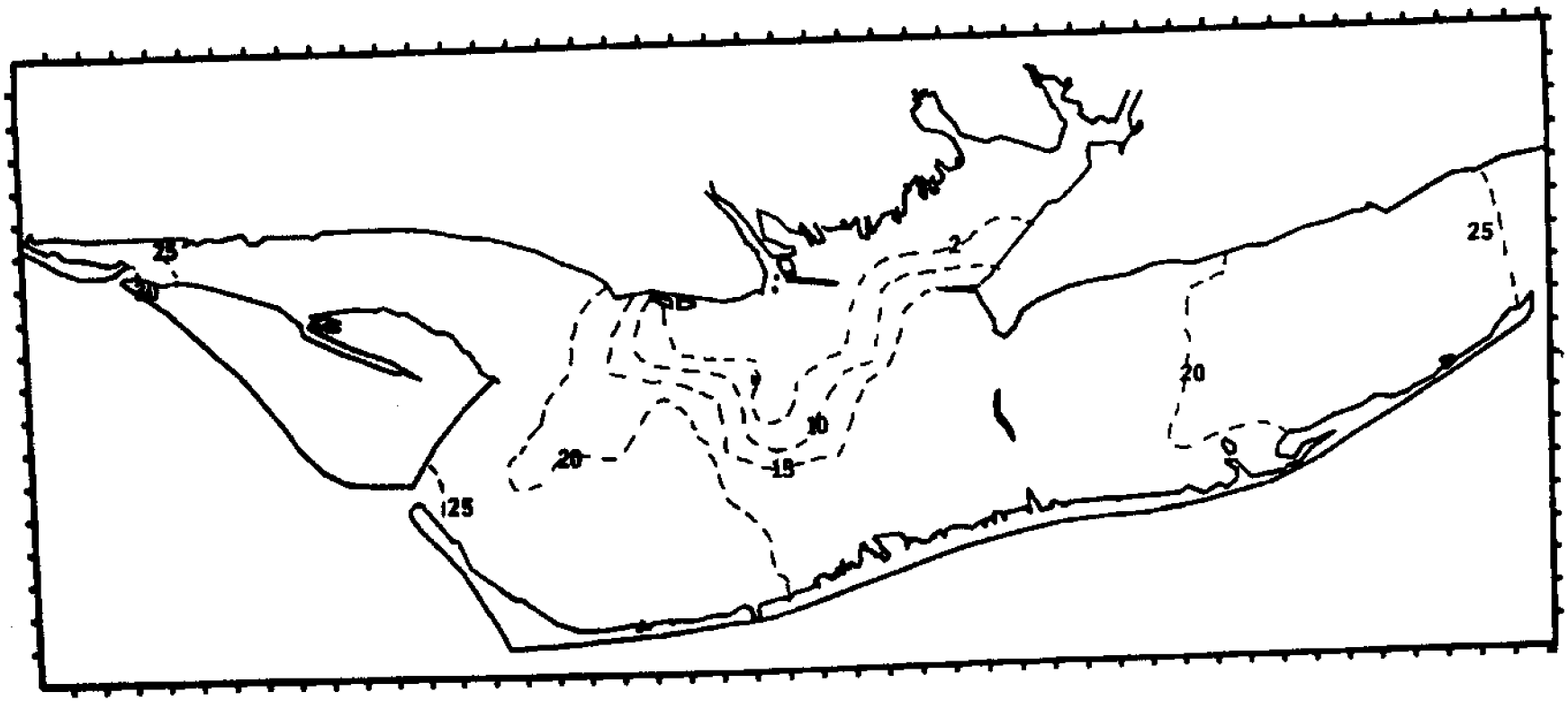

Figure A-32. Salinity Contours at 2300 on September 14, 1983

Figure A-33. Salinity Contours at 0100 on September 15, 1983

Figure A-34. Salinity Contours at 0300 on September 15, 1983

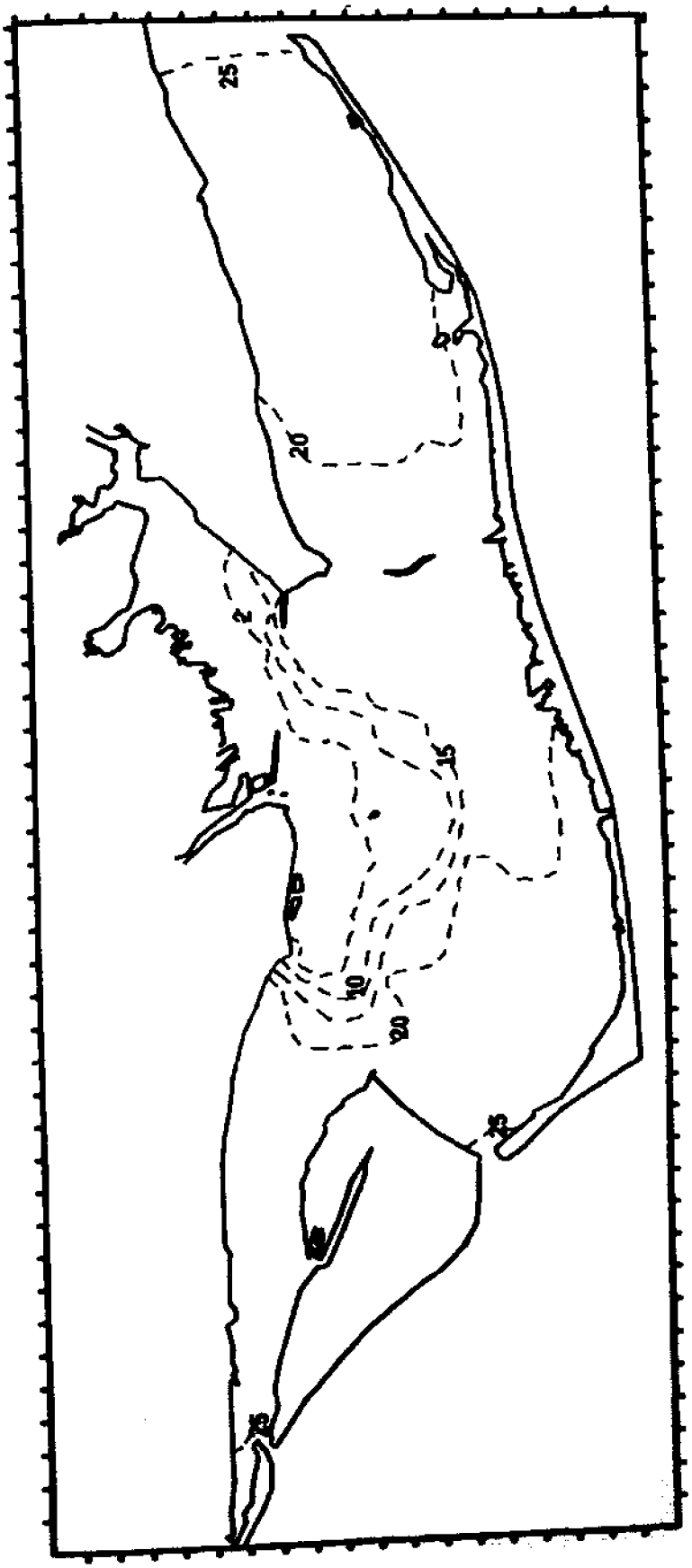

Figure A-35. Salinity Contours at 0500 on September 15, 1983

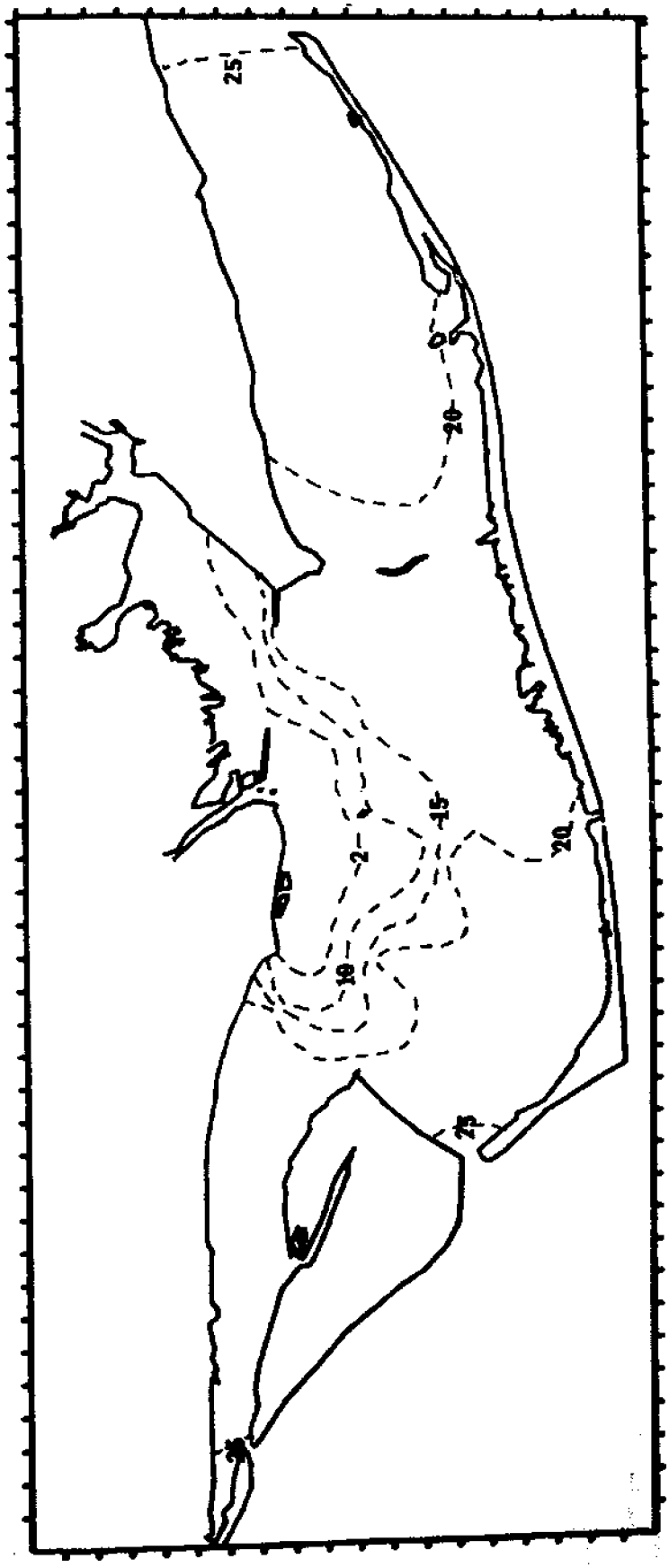

Figure A-36. Salinity Contours at 0700 on September 15, 1983

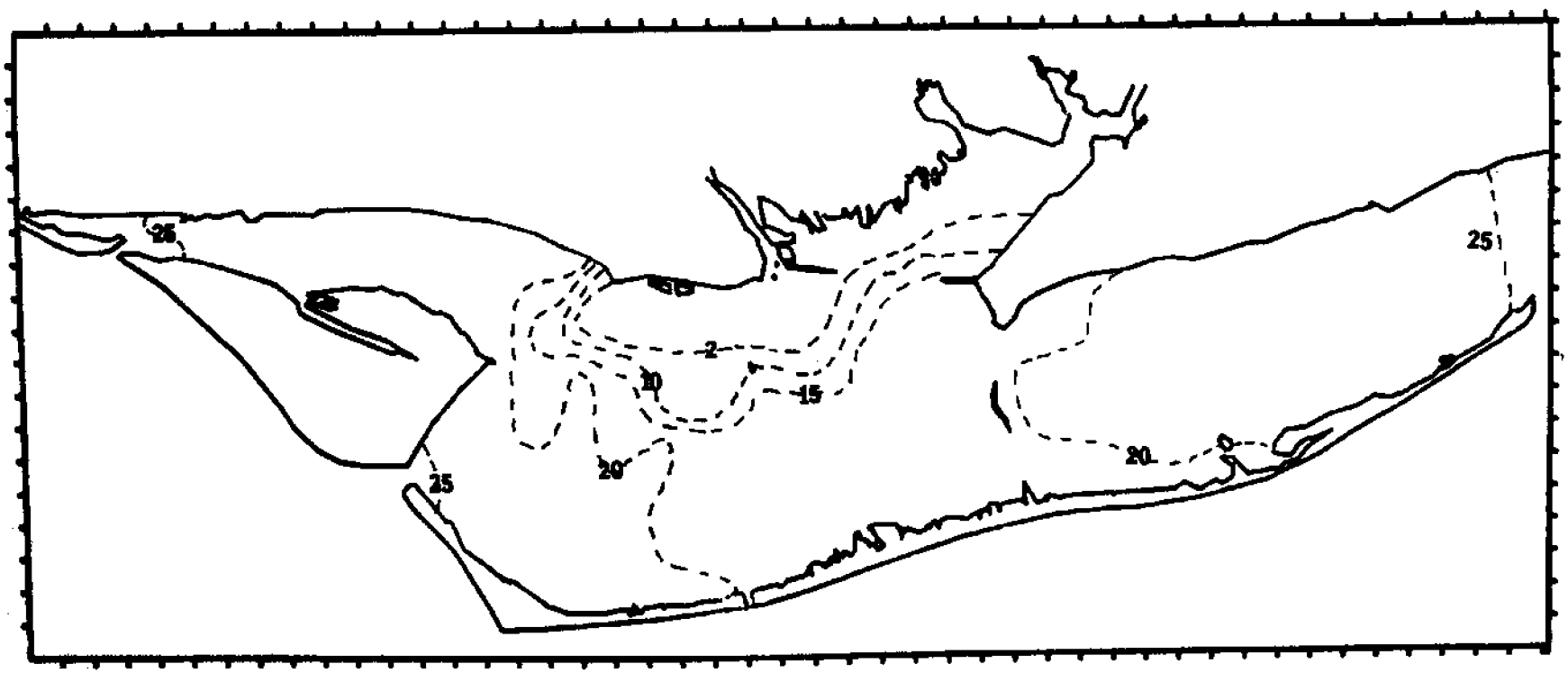

Figure A-37. Salinity Contours at 0900 on September 15, 1983

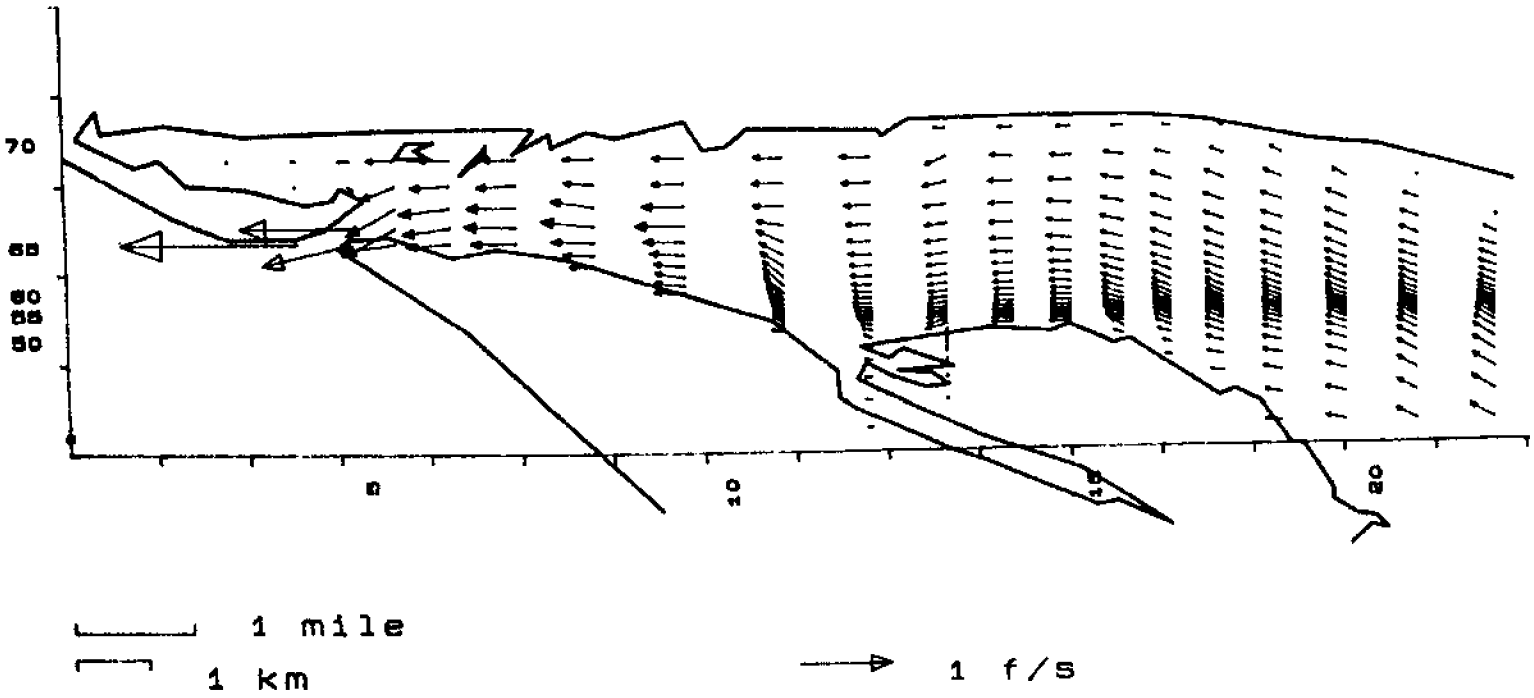

Figure A-38. Velocity Plot for St. Vincent Sound at 0900 on September 14, 1983

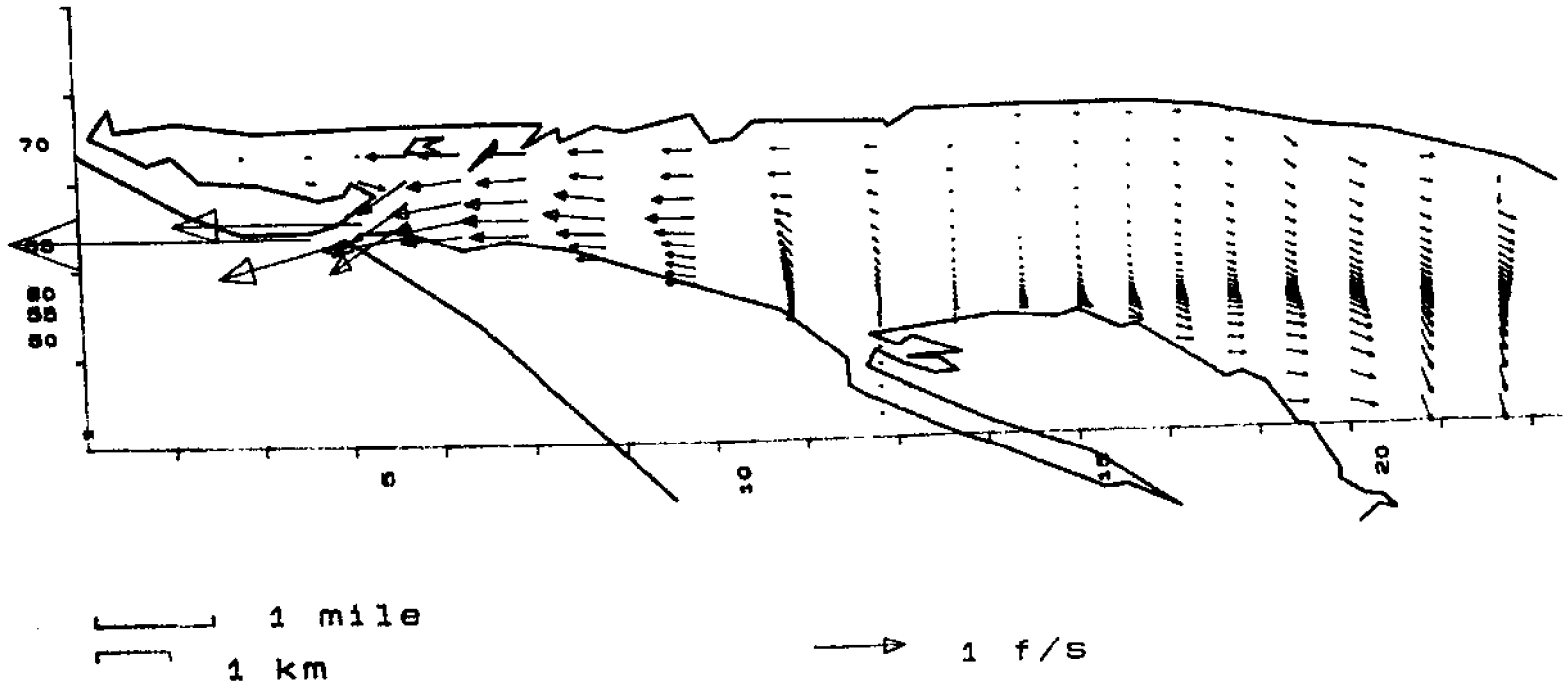

Figure A-39. Velocity Plot for St. Vincent Sound at 1300 on September 14, 1983

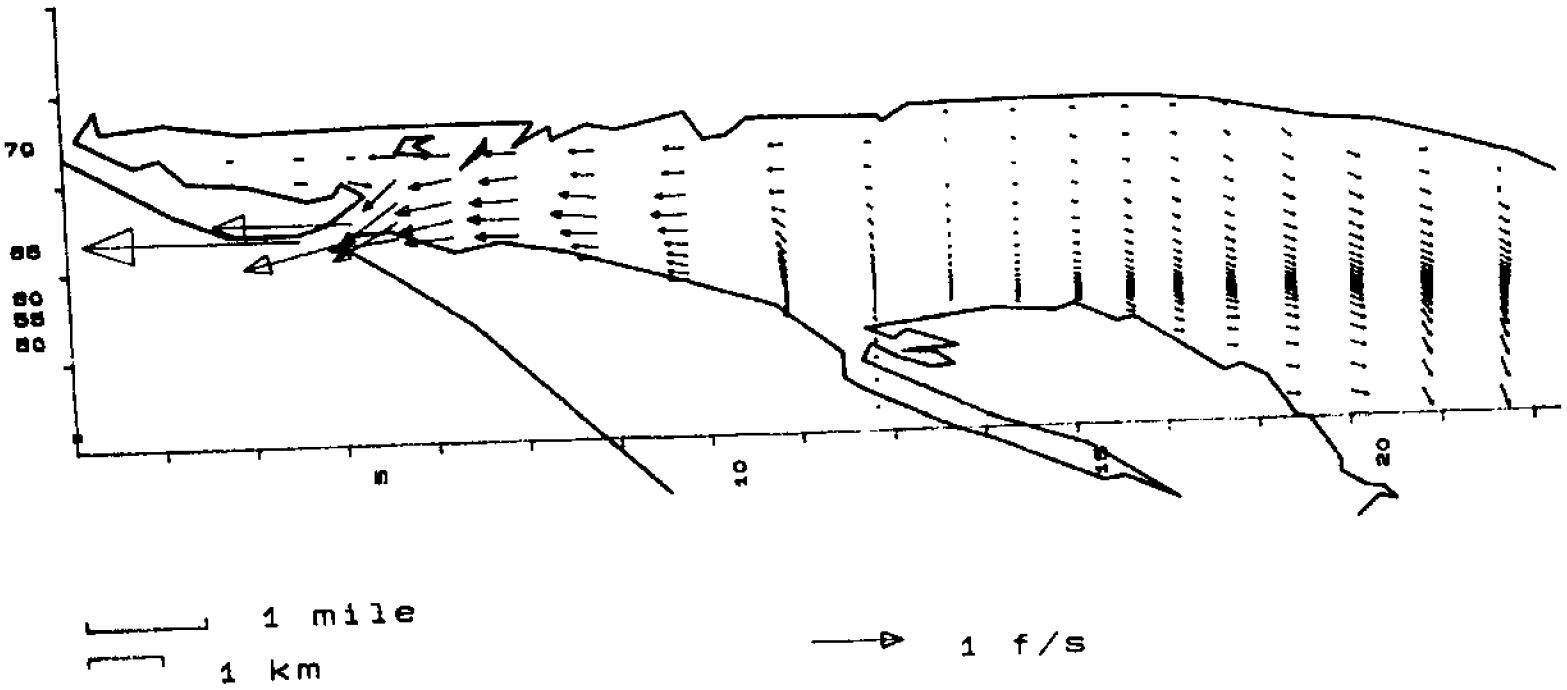

Figure A-40. Velocity Plot for St. Vincent Sound at 1700 on September 14, 1983

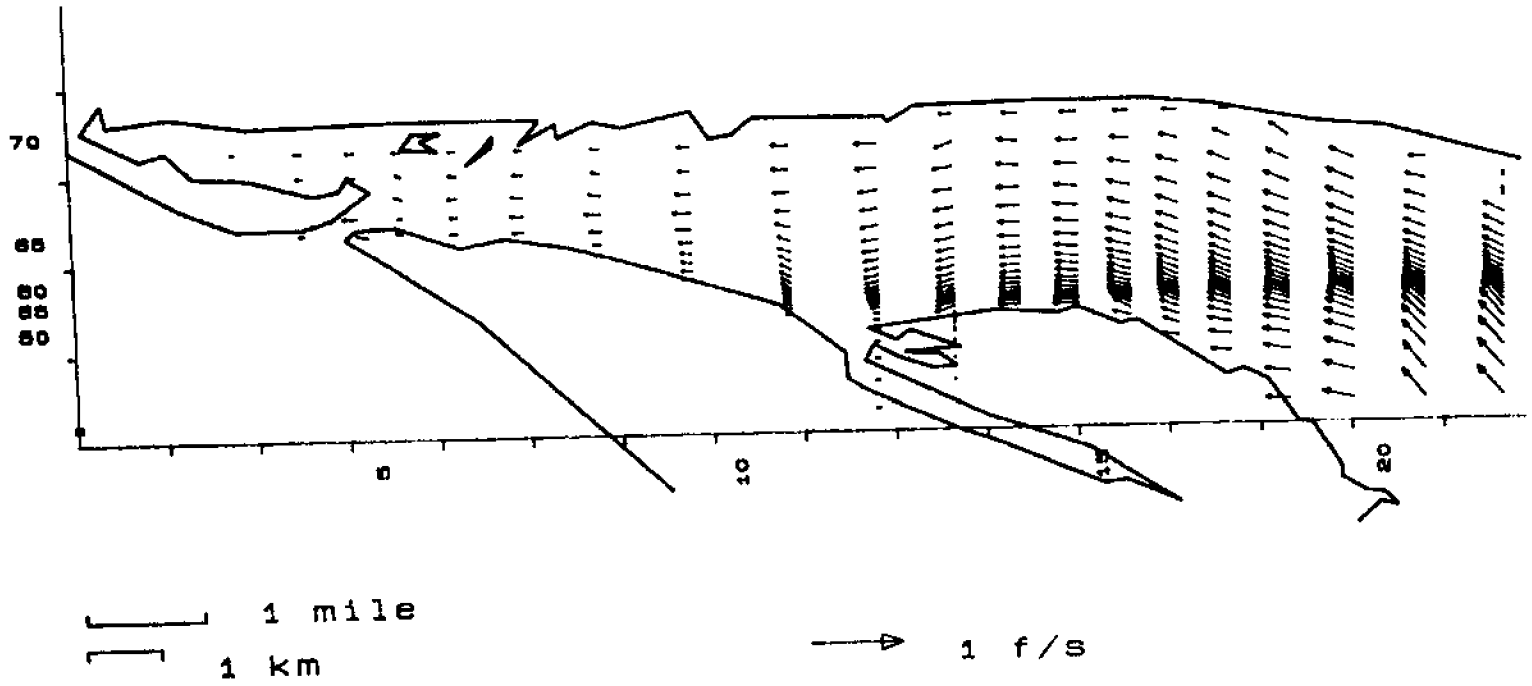

Figure A-41. Velocity Plot for St. Vincent Sound at 2100 on September 14, 1983

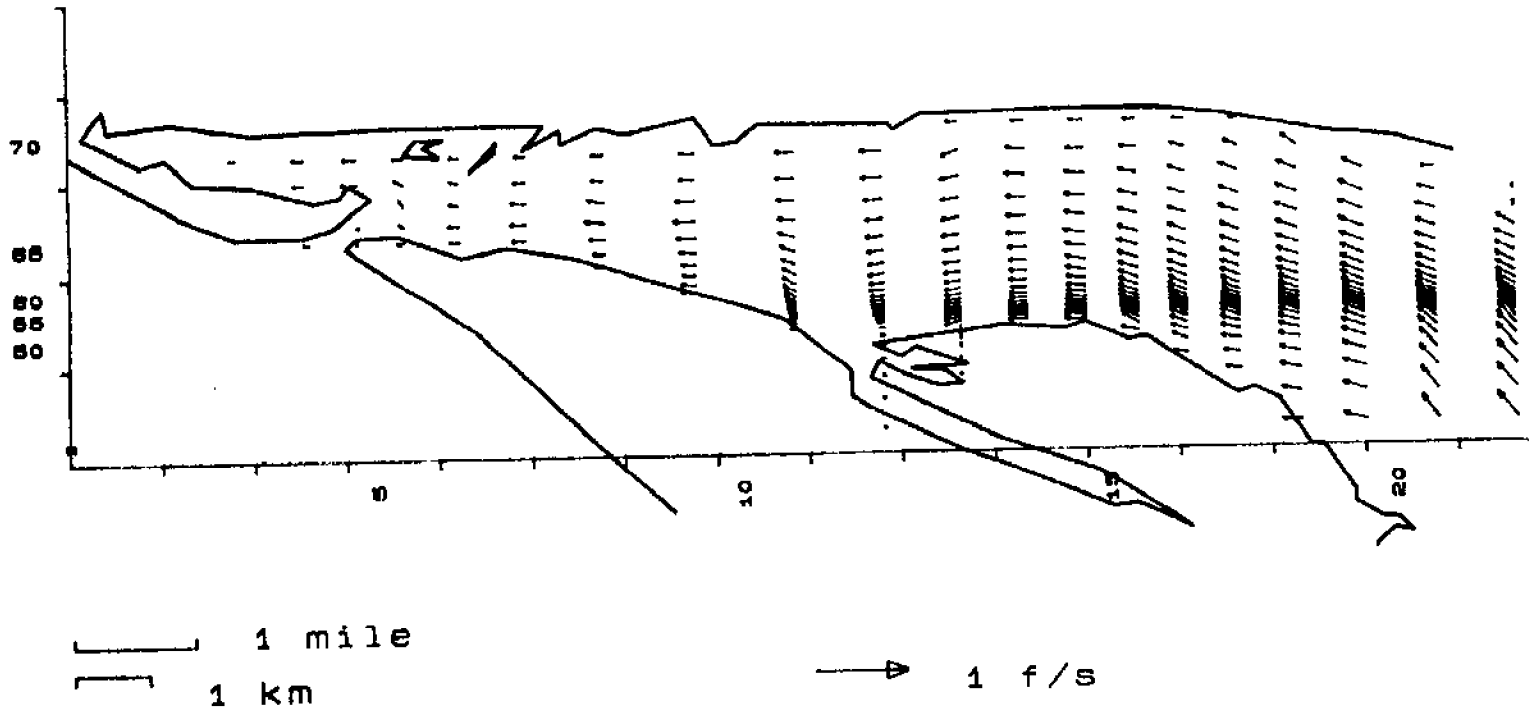

Figure A-42. Velocity Plot for St. Vincent Sound at 0100 on September 15, 1983

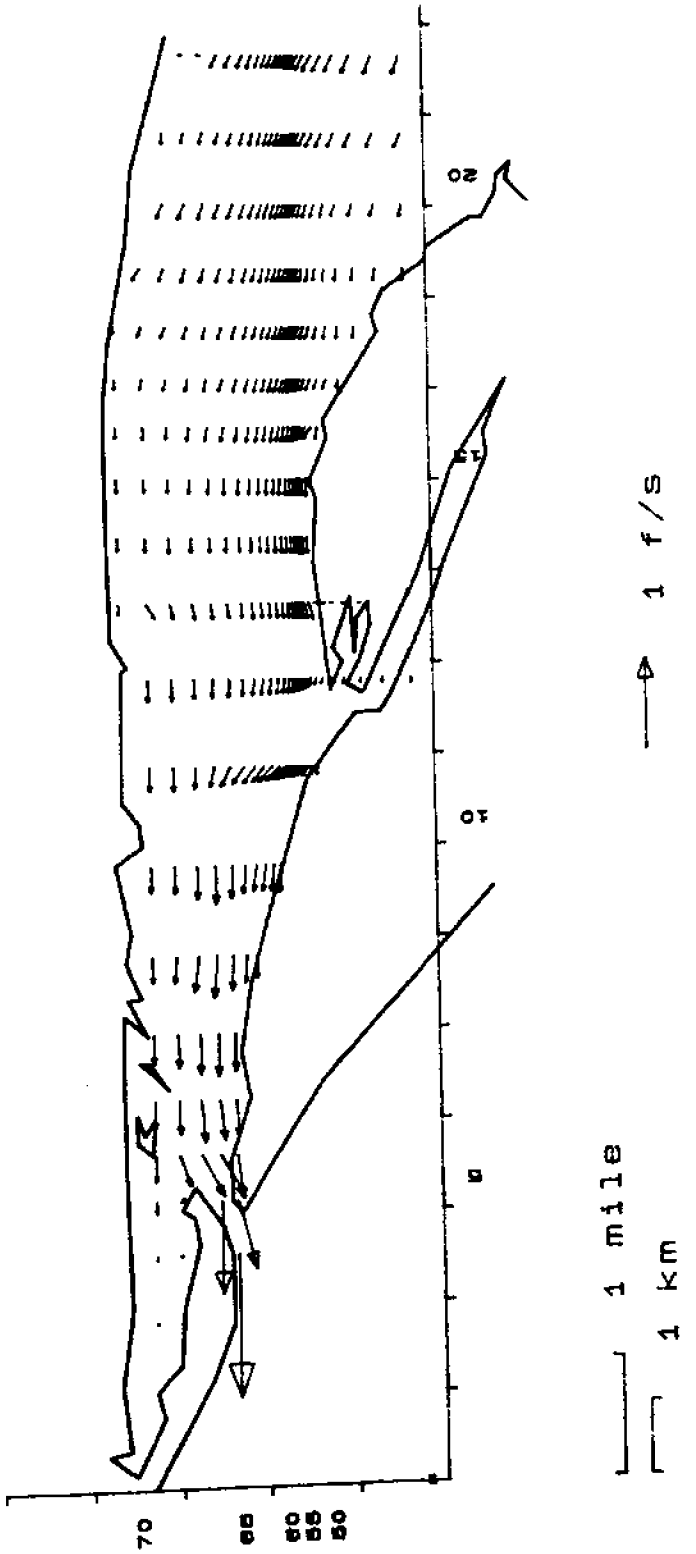

Figure A-43. Velocity Plot for St. Vincent Sound at 0500 on September 15, 1983

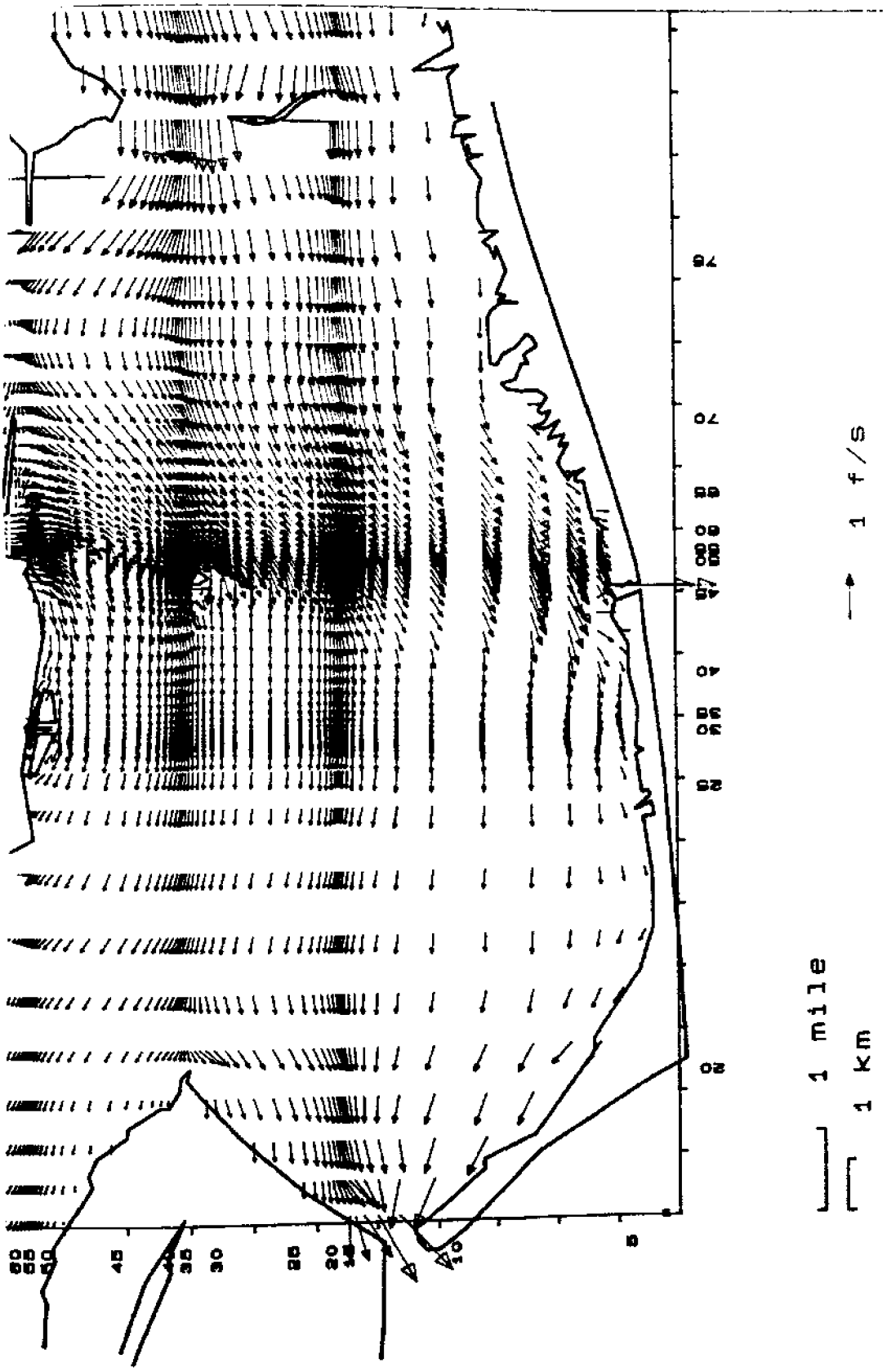

Figure A-44. Velocity Plot for Apalachicola Bay at 0900 on September 14, 1983

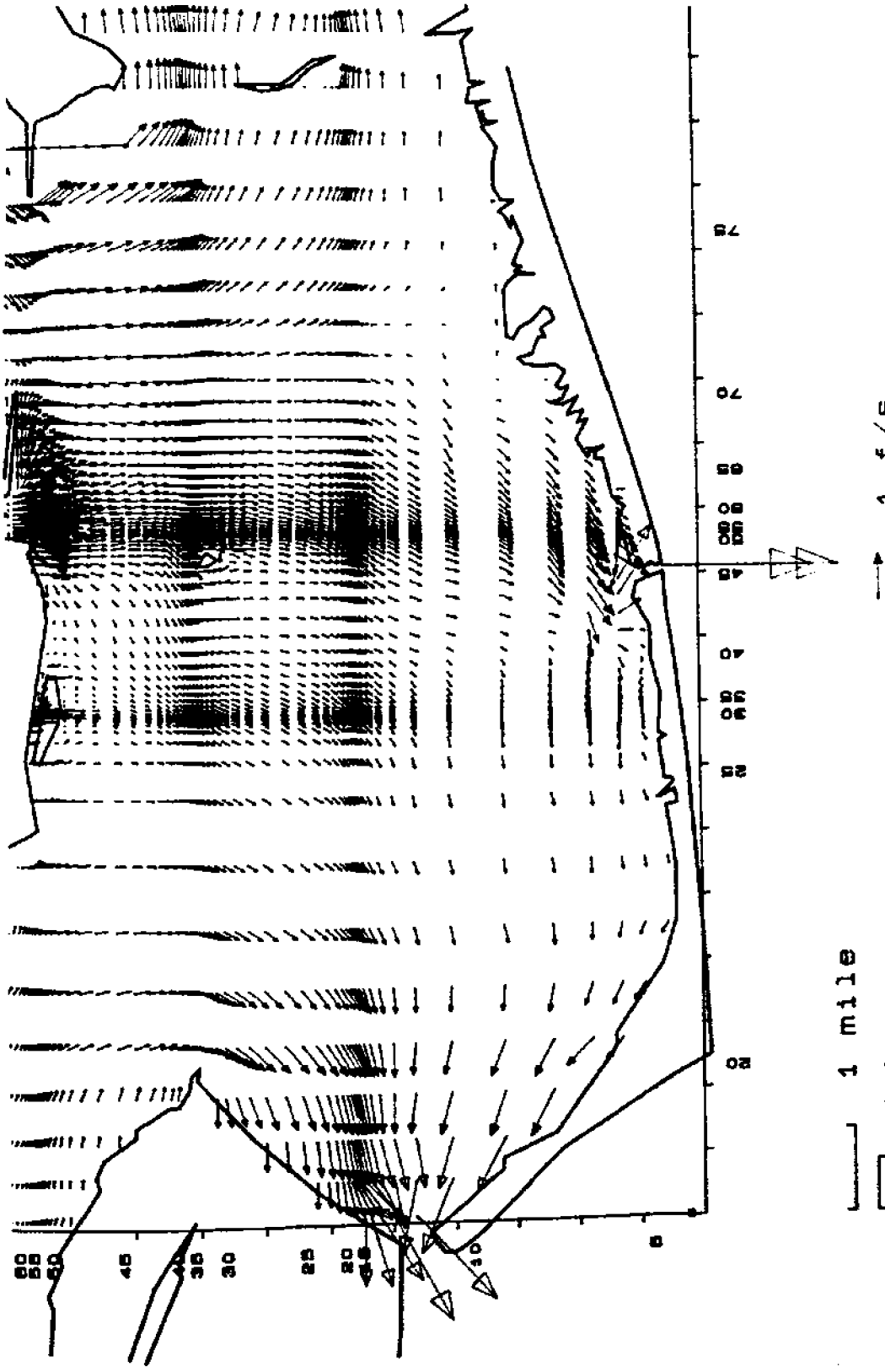

Figure A-45. Velocity Plot for Apalachicola Bay at 1300 on September 14, 1983

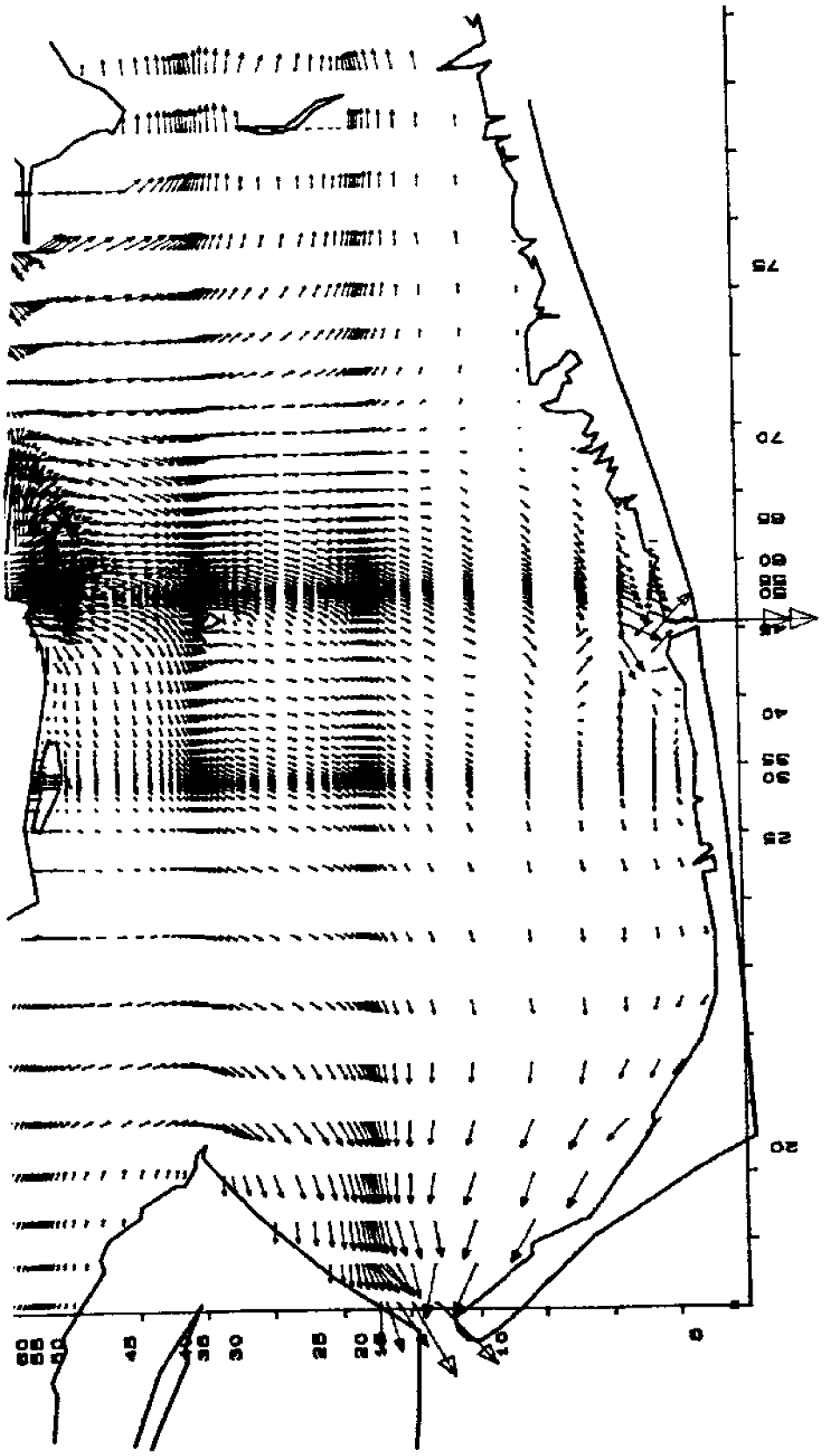

Figure A-46. Velocity Plot for Apalachicola Bay at 1700 on September 14, 1983

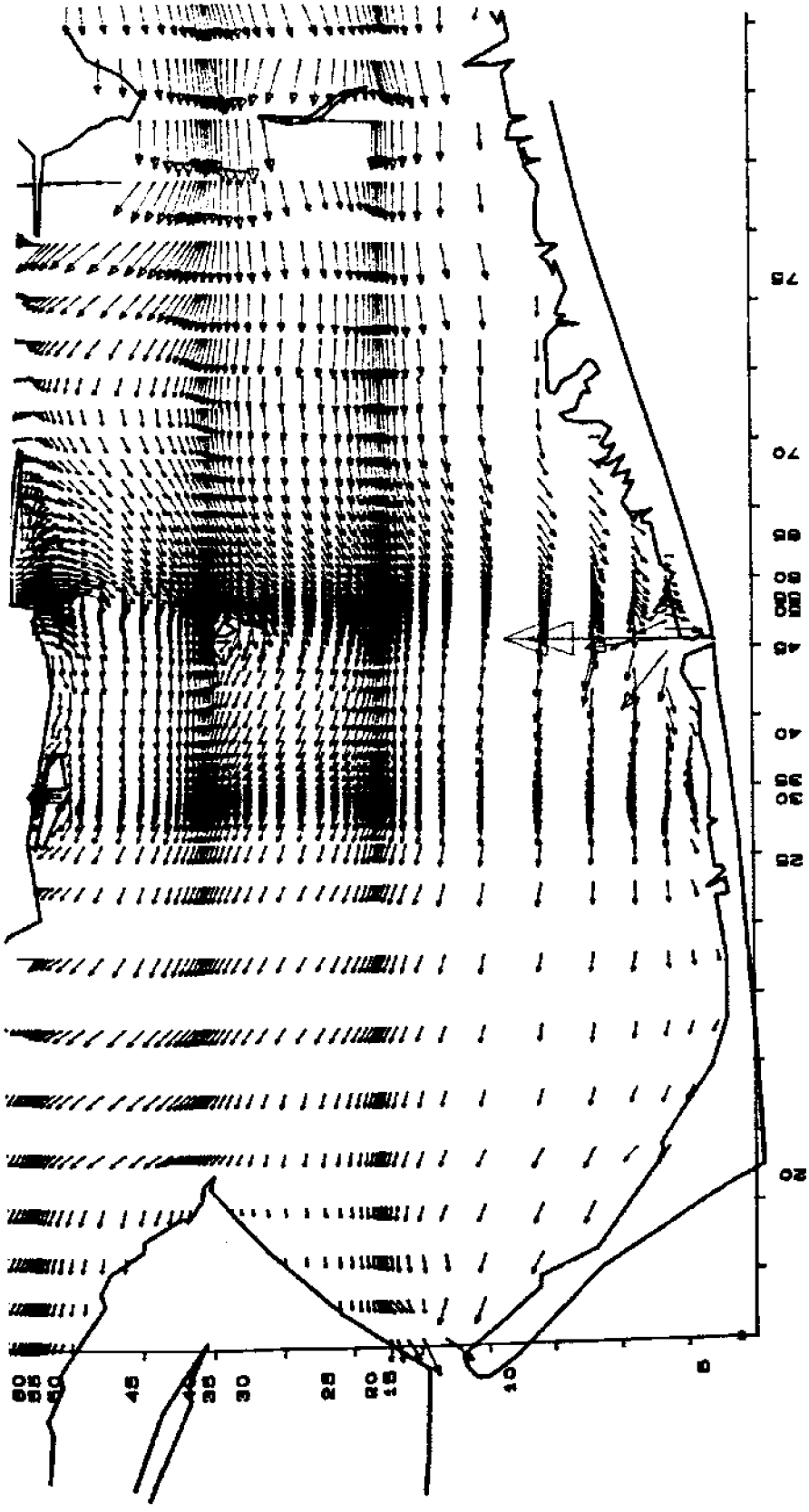

Figure A-47. Velocity Plot for Apalachicola Bay at 2100 on September 14, 1983

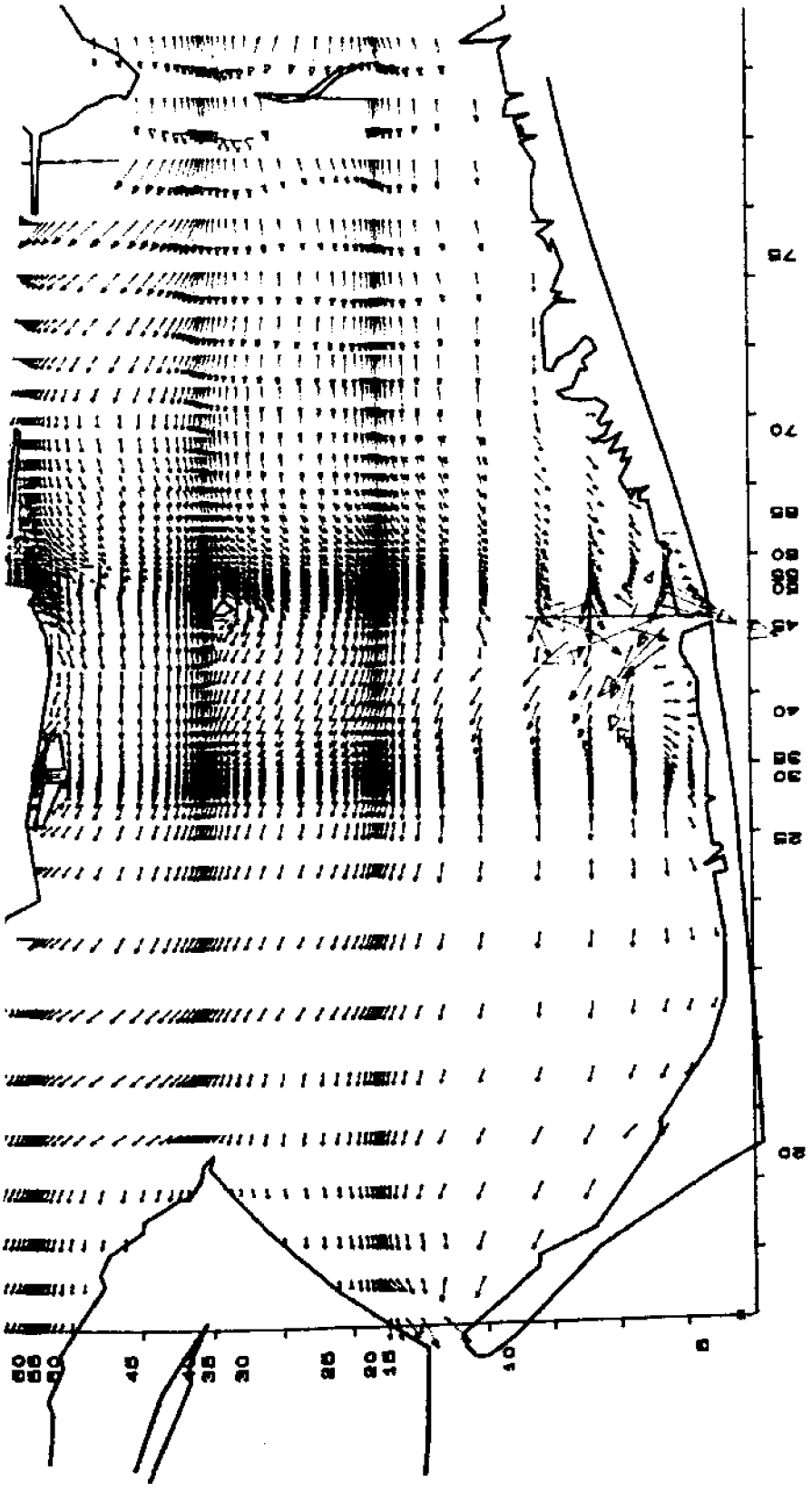

Figure A-48. Velocity Plot for Apalachicola Bay at 0100 on September 15, 1985

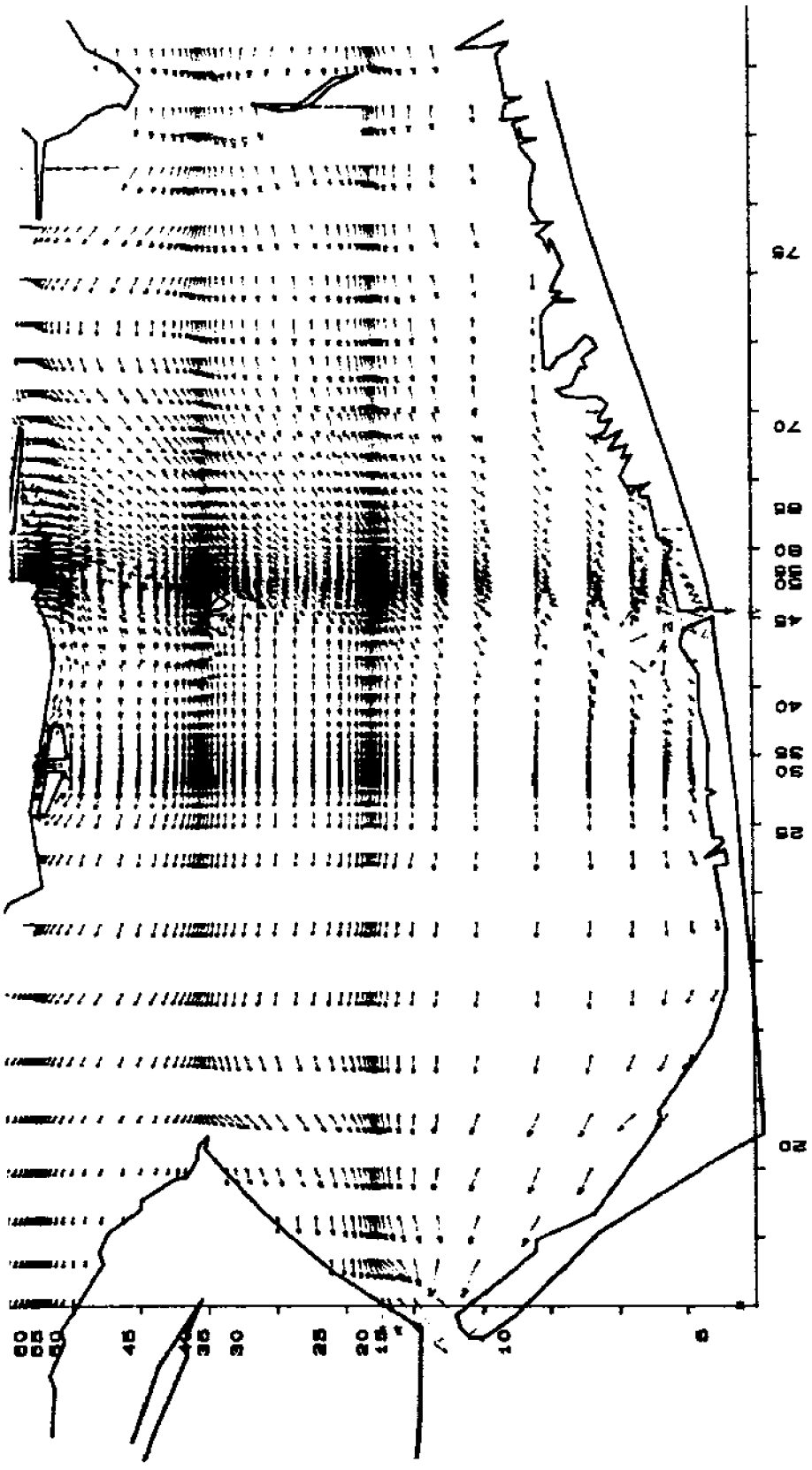

Figure A-49. Velocity Plot for Apalachicola Bay at 0500 on September 15, 1985

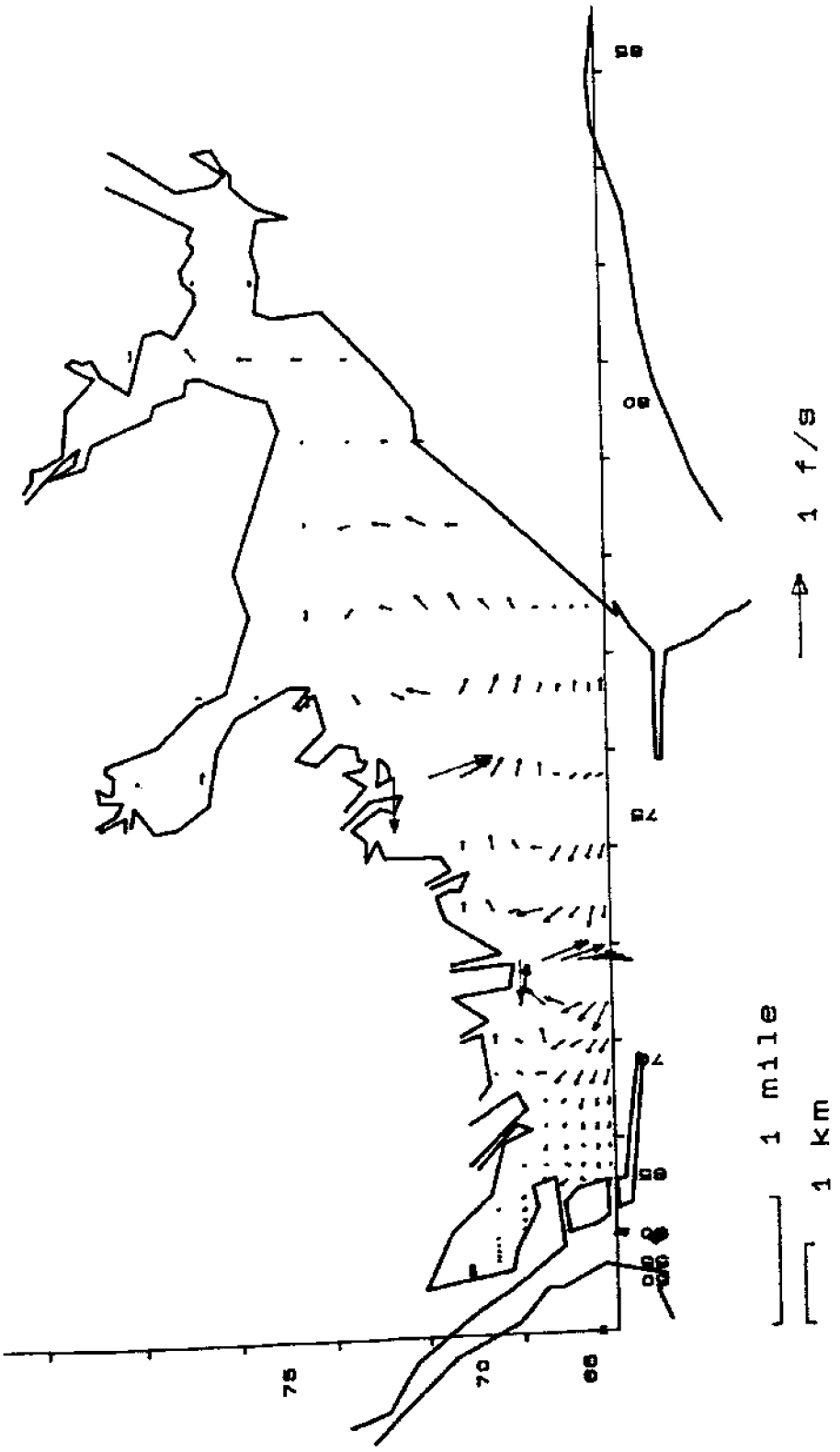
1 f/s
1 mile
1 km

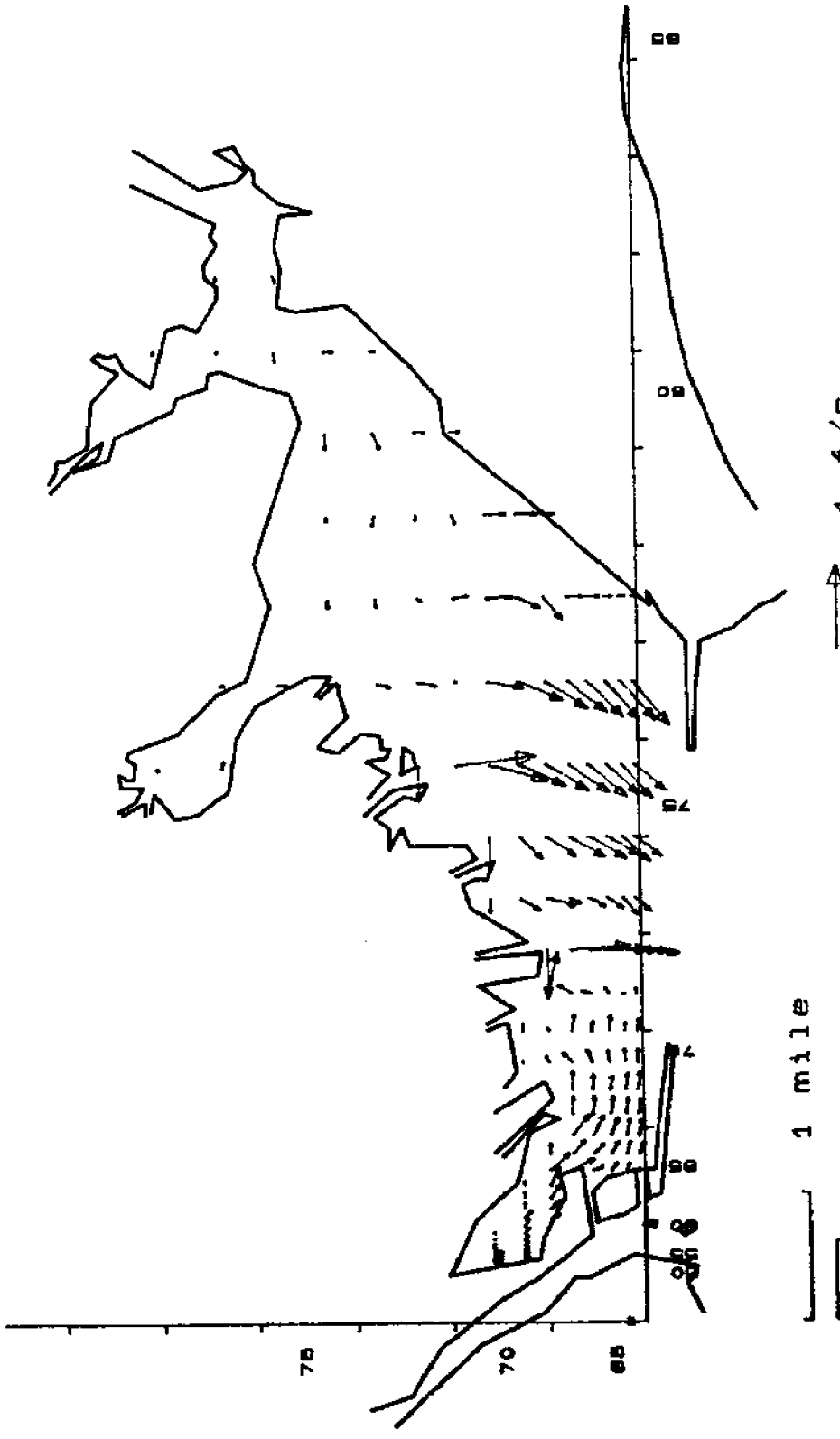

Figure A-51. Velocity Plot for East Bay at 1300 on September 14, 1983

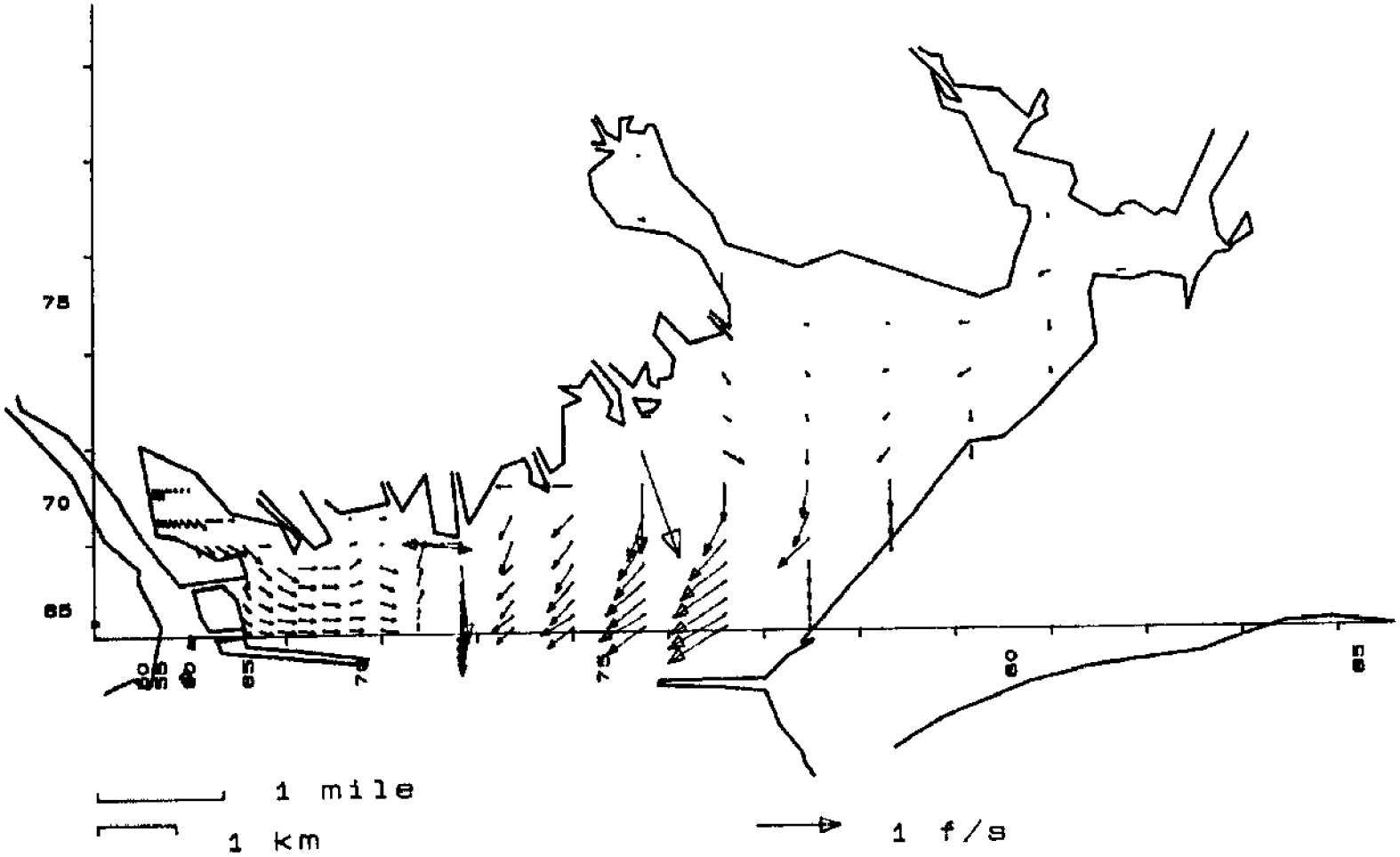

Figure A-52. Velocity Plot for East Bay at 1700 on September 14, 1983

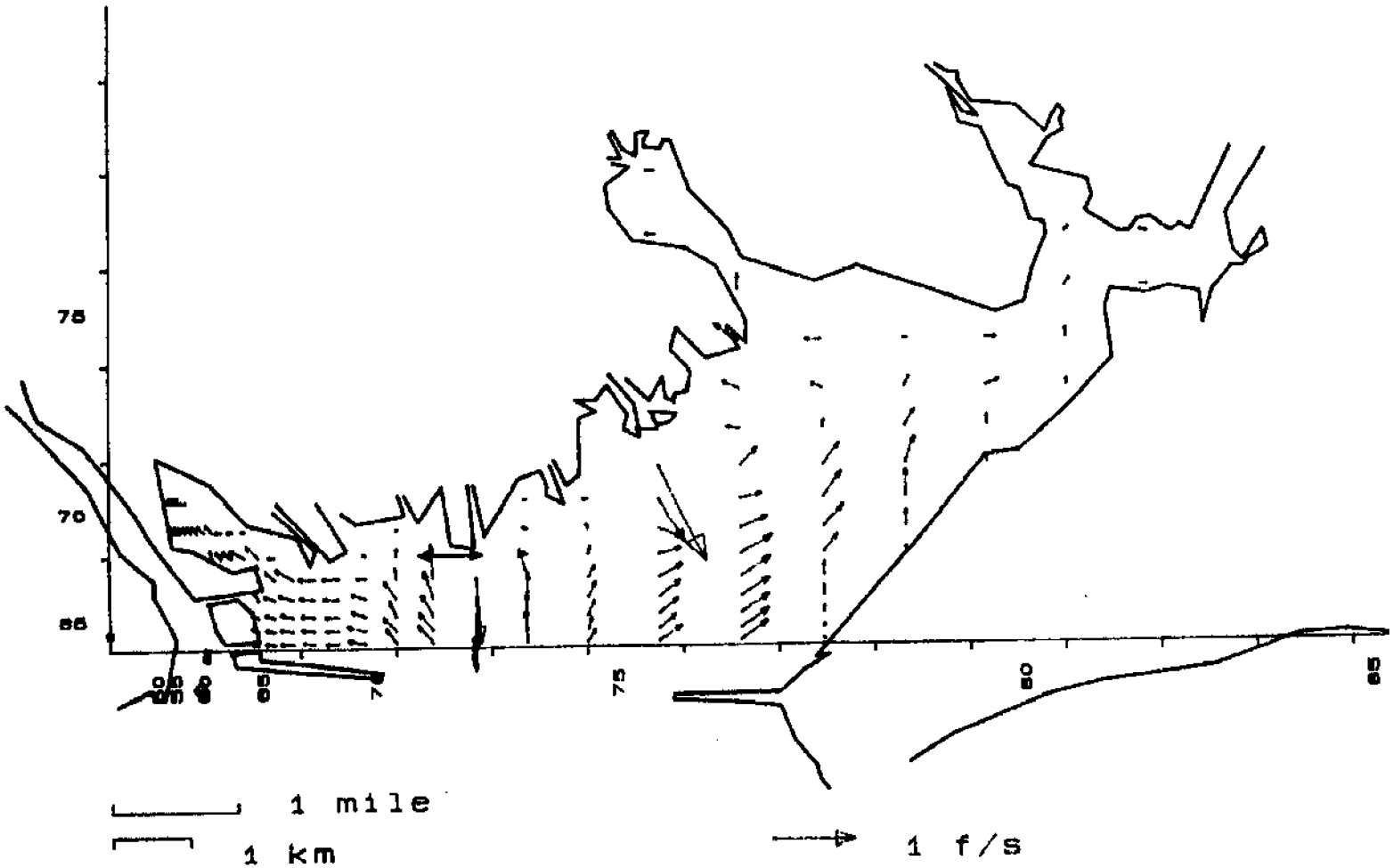

Figure A-53. Velocity Plot for East Bay at 2100 on September 14, 1983

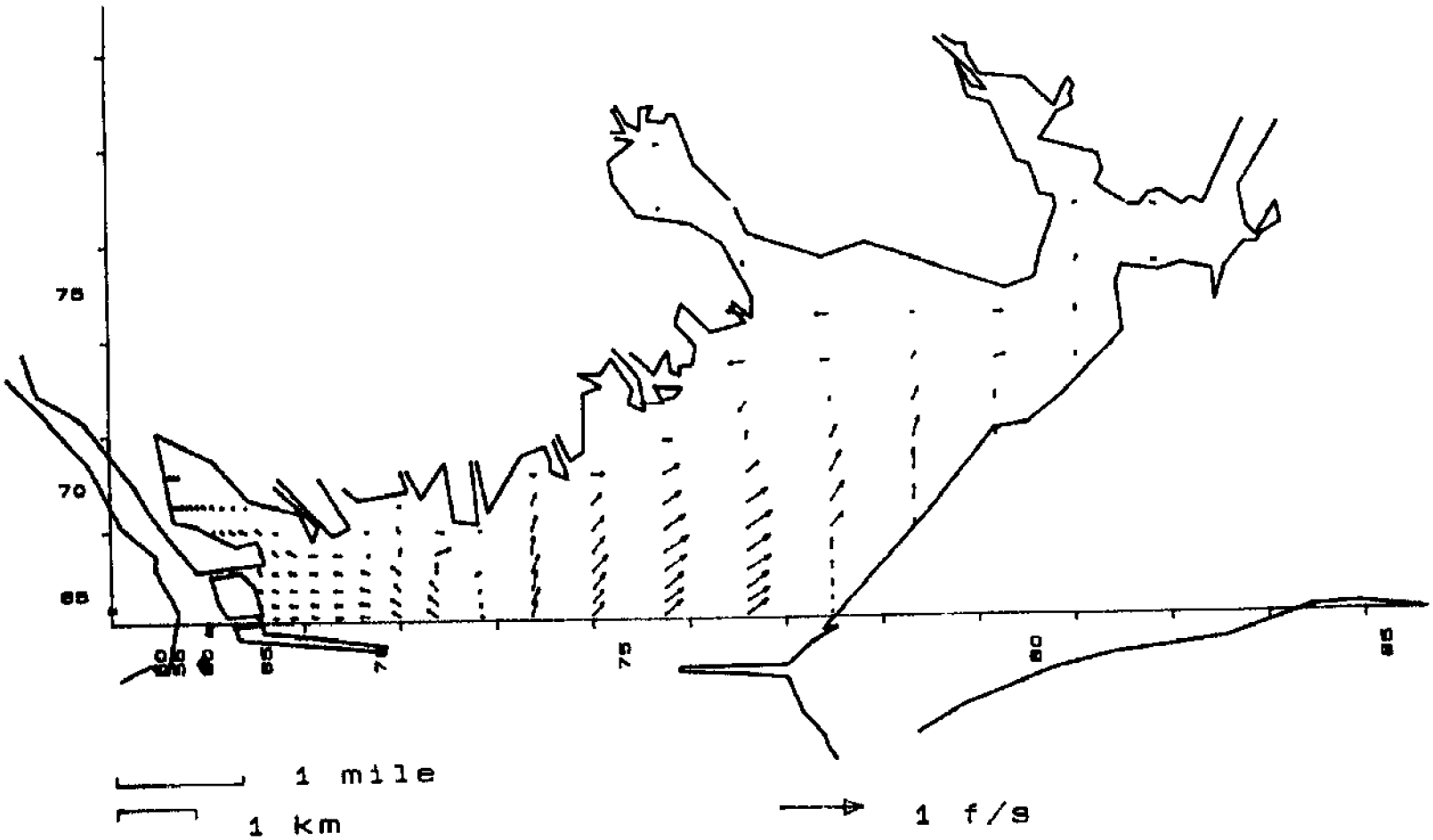

Figure A-54. Velocity Plot for East Bay at 0100 on September 15, 1983

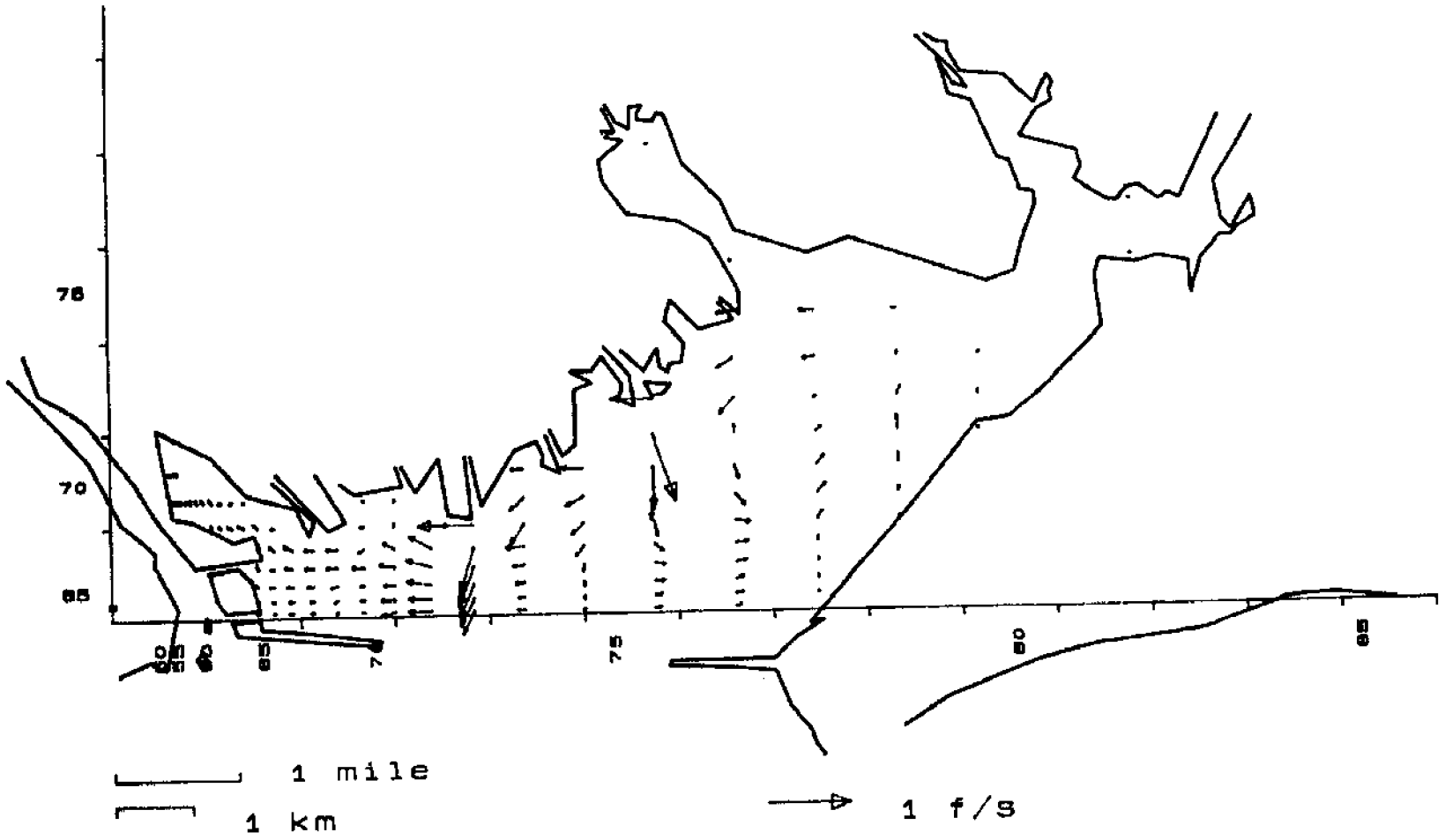

Figure A-55. Velocity Plot for East Bay at 0500 on September 15, 1983

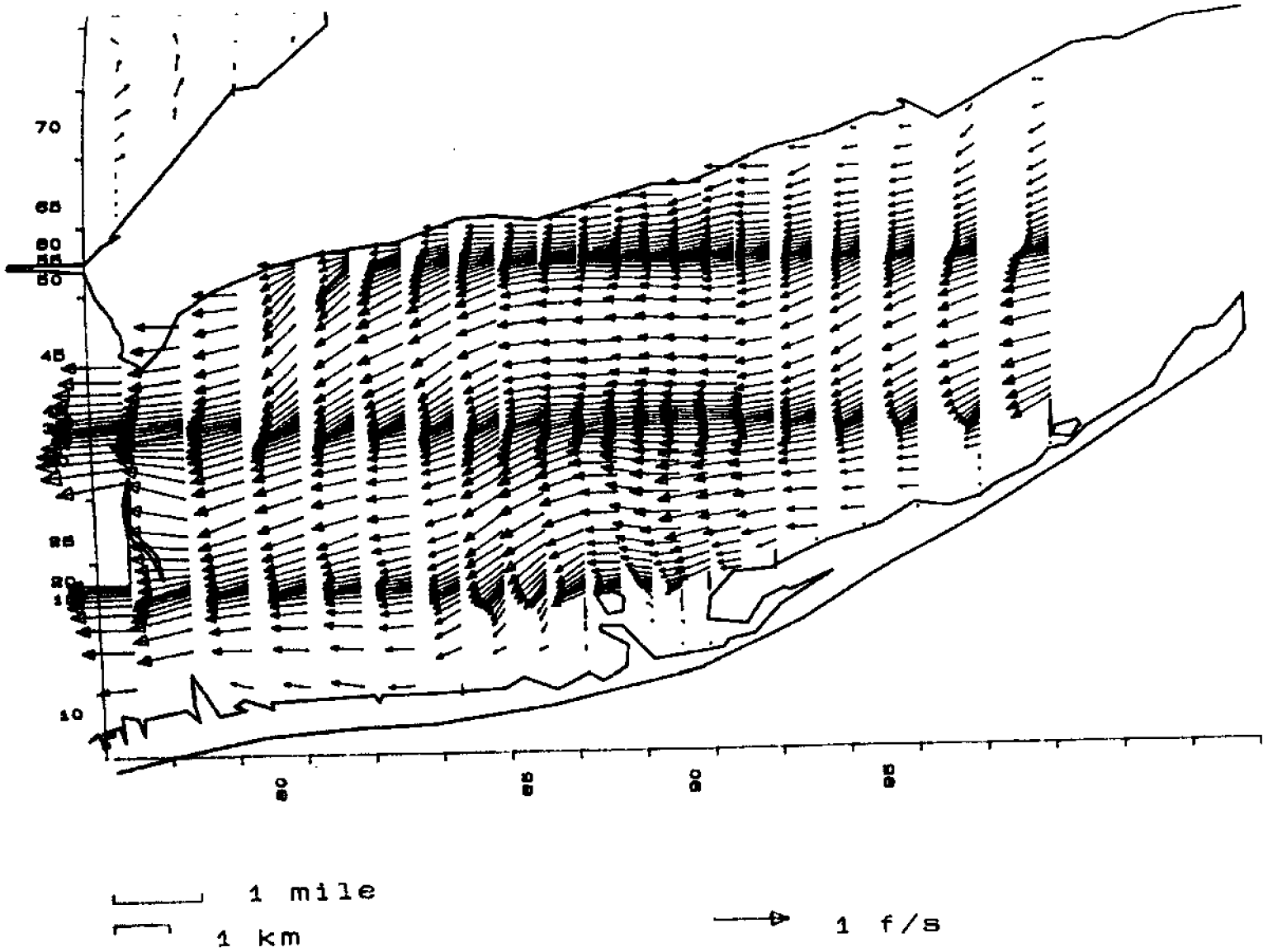

Figure A-56. Velocity Plot for St. George Sound at 0900 on September 14, 1983

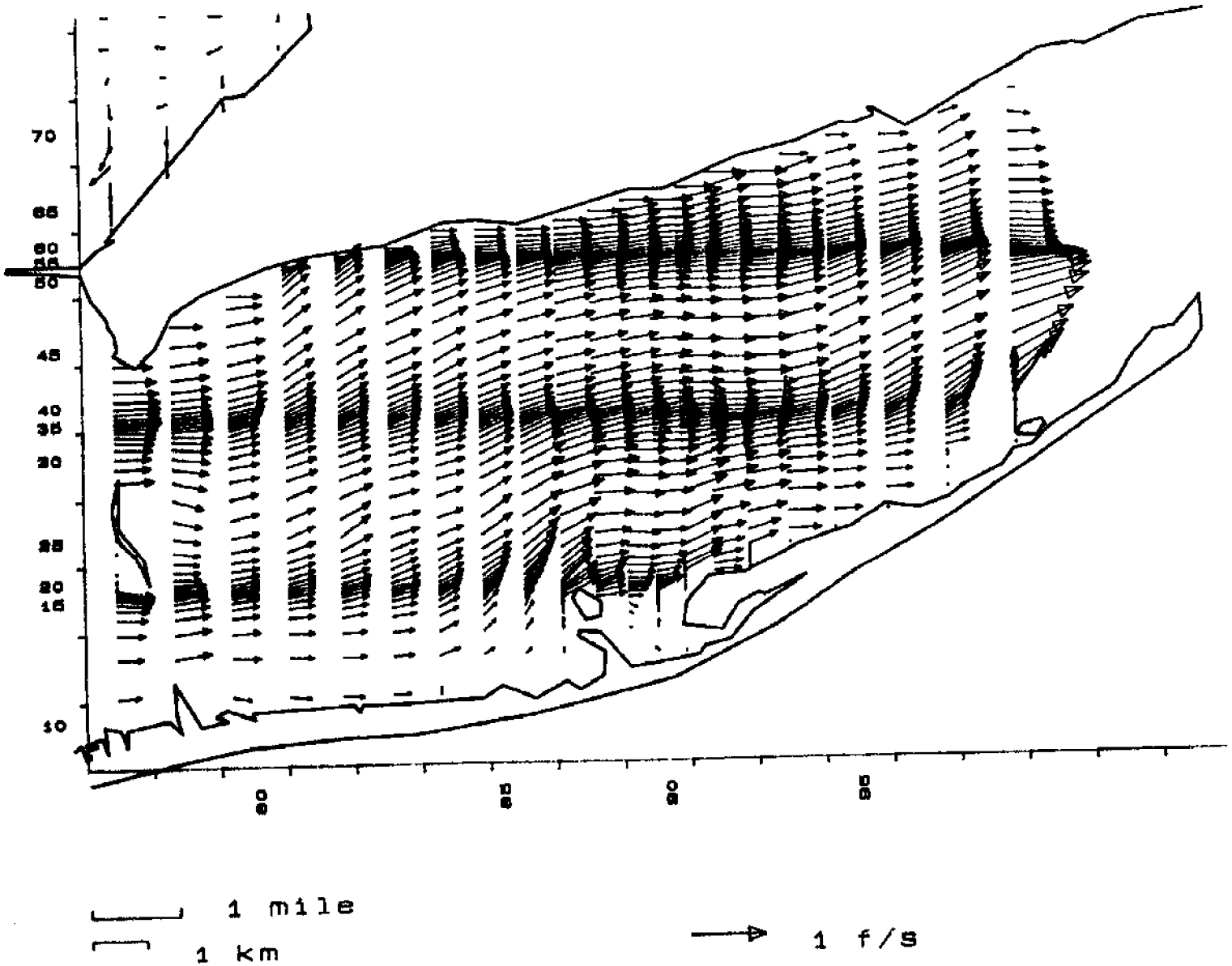

Figure A-57. Velocity Plot for St. George Sound at 1300 on September 14, 1983

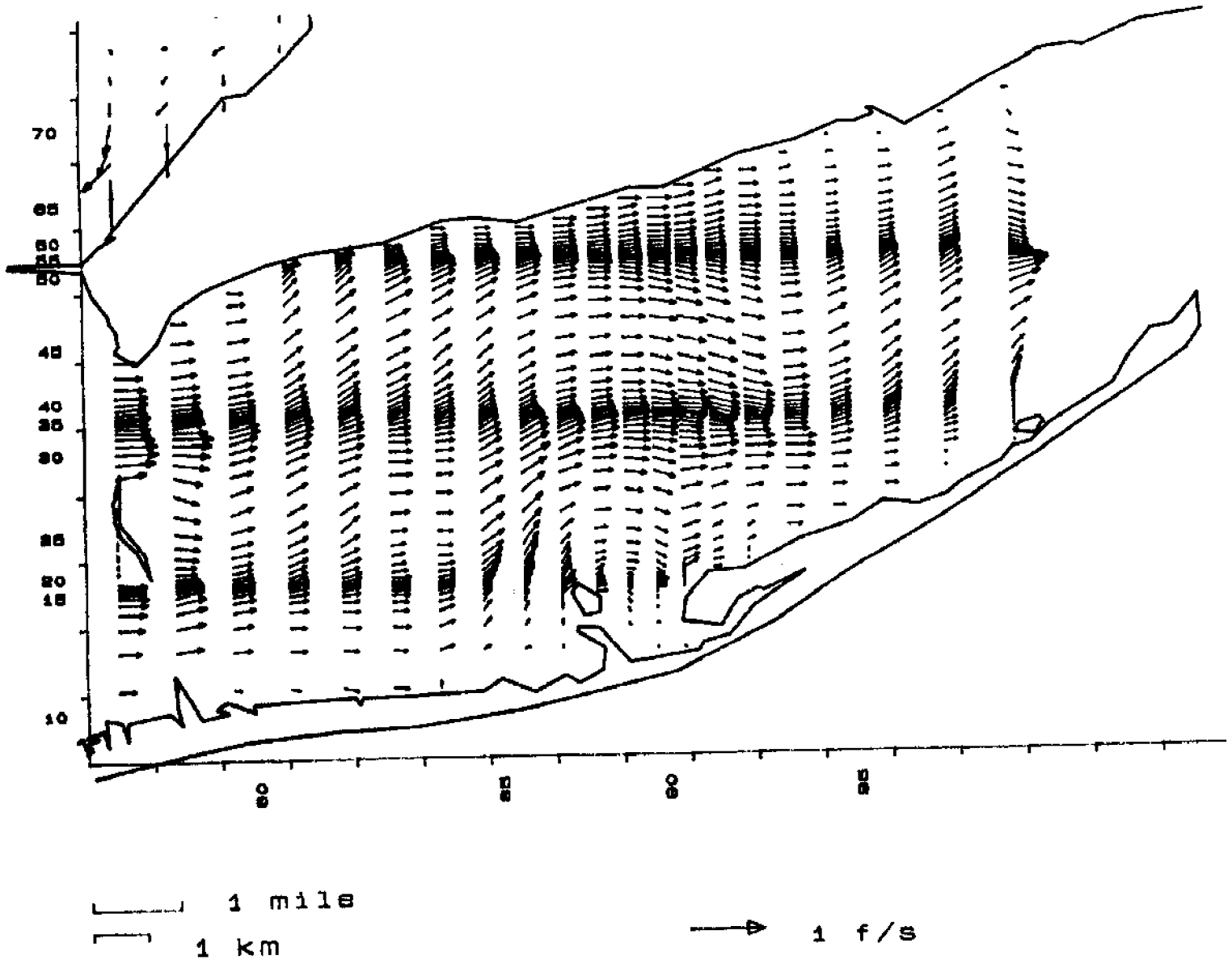

Figure A-58. Velocity Plot for St. George Sound at 1700 on September 14, 1983

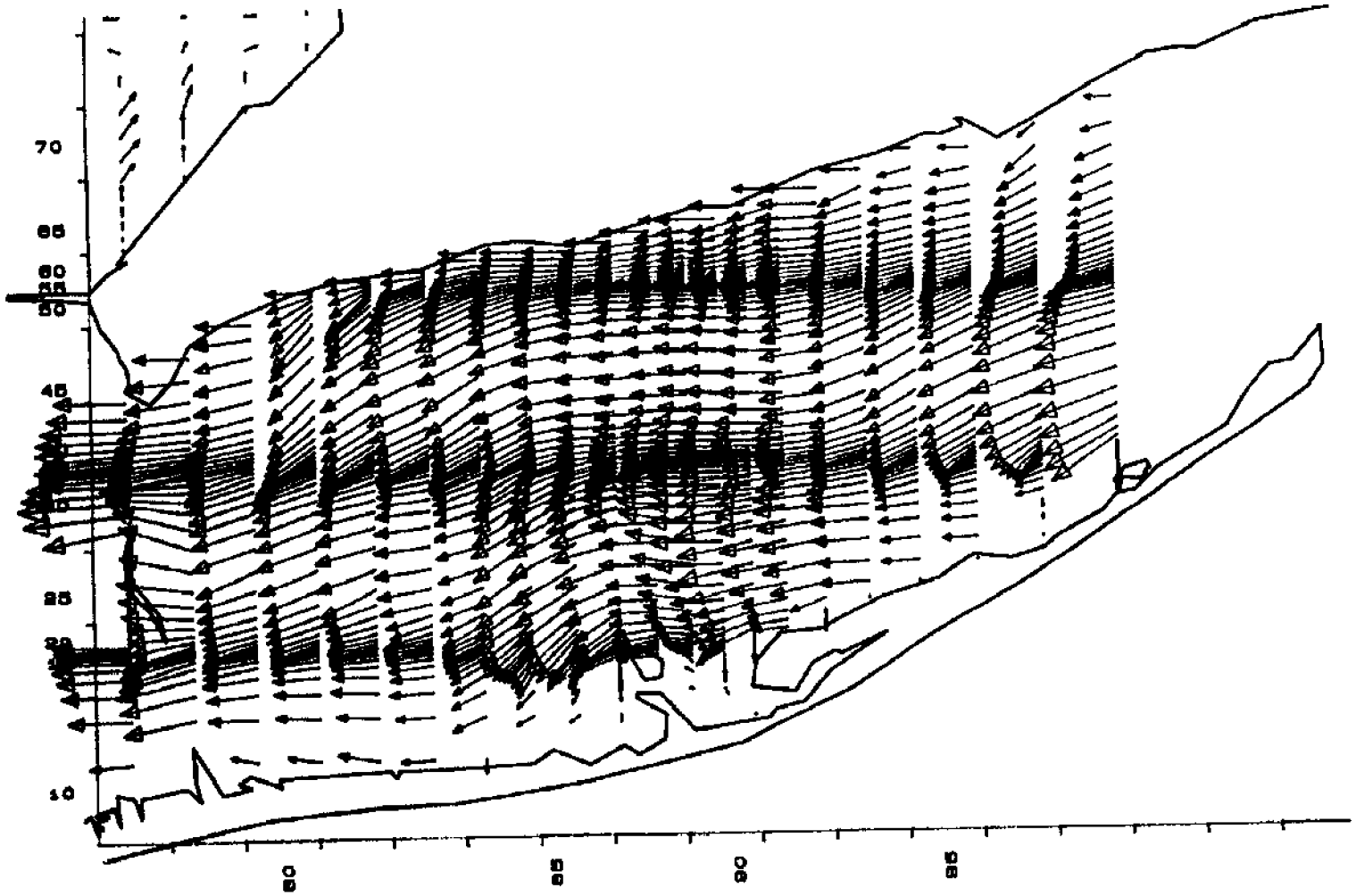

Figure A-59. Velocity Plot for St. George Sound at 2100 on September 14, 1983

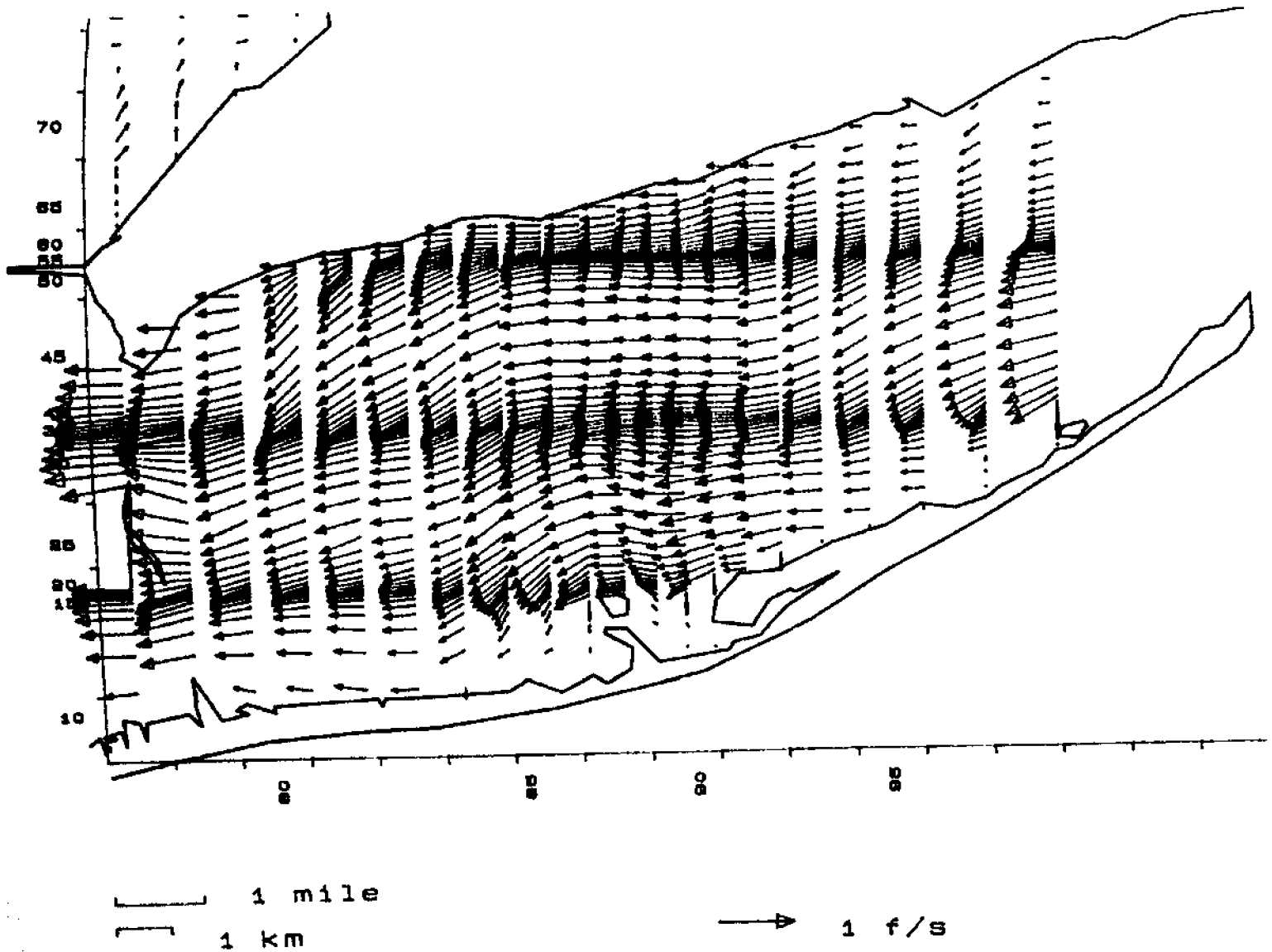

Figure A-60. Velocity Plot for St. George Sound at 0100 on September 15, 1983

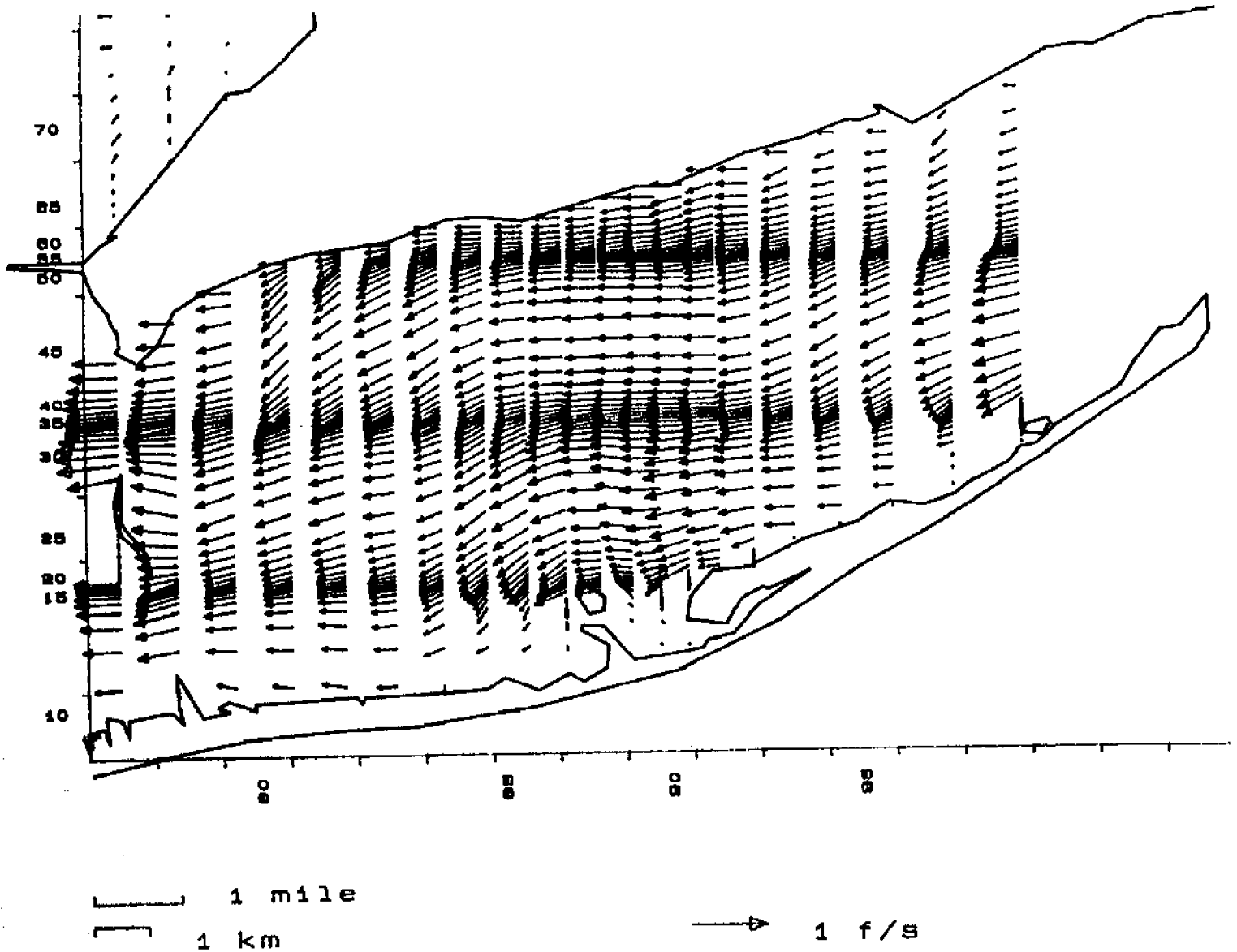

Figure A-61. Velocity Plot for St. George Sound at 0500 on September 15, 1983

APPENDIX B

Verification Results

(0900 on March 8, 1984 to 0900 on March 9, 1984)

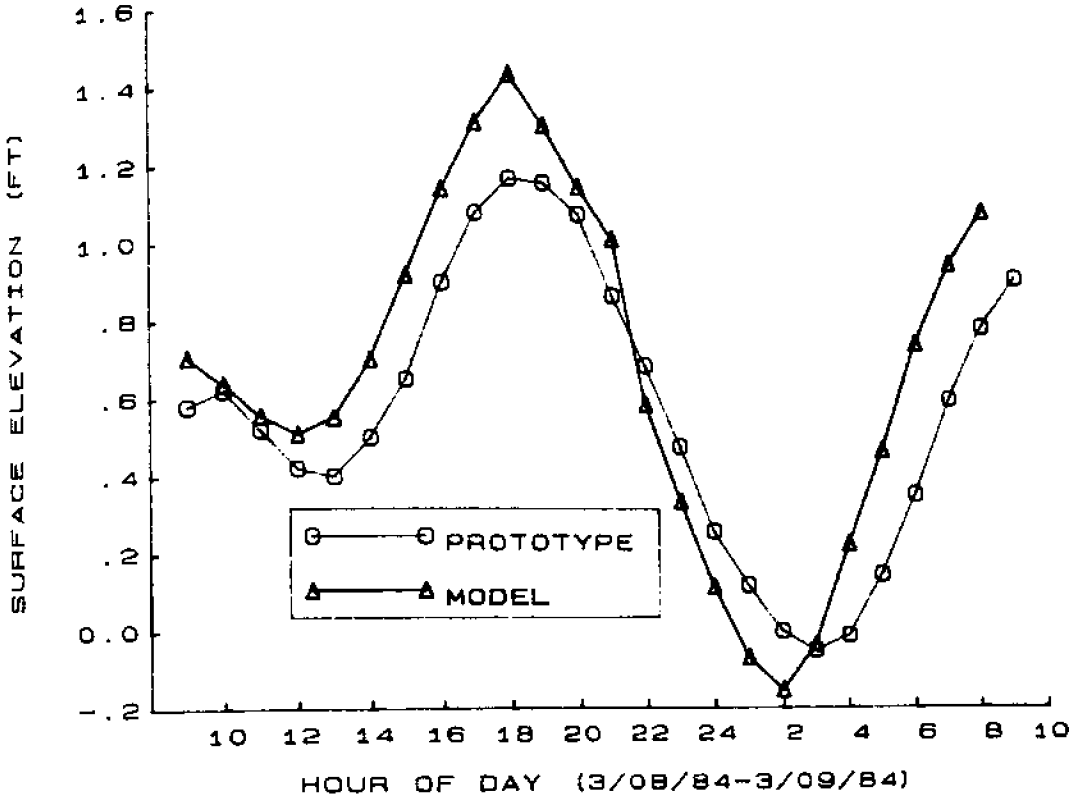

Figure B-1. Surface Elevation at Station SG3 for Verification Condition

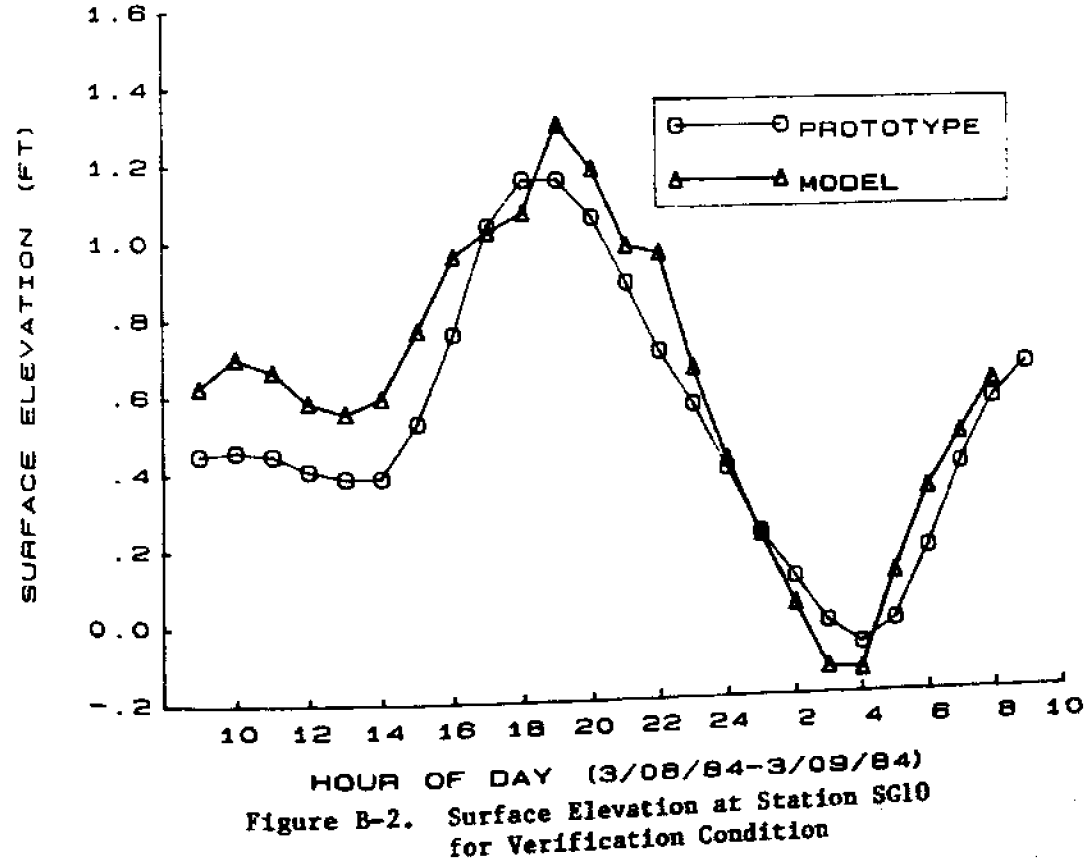

Figure B-2. Surface Elevation at Station SG10 for Verification Condition

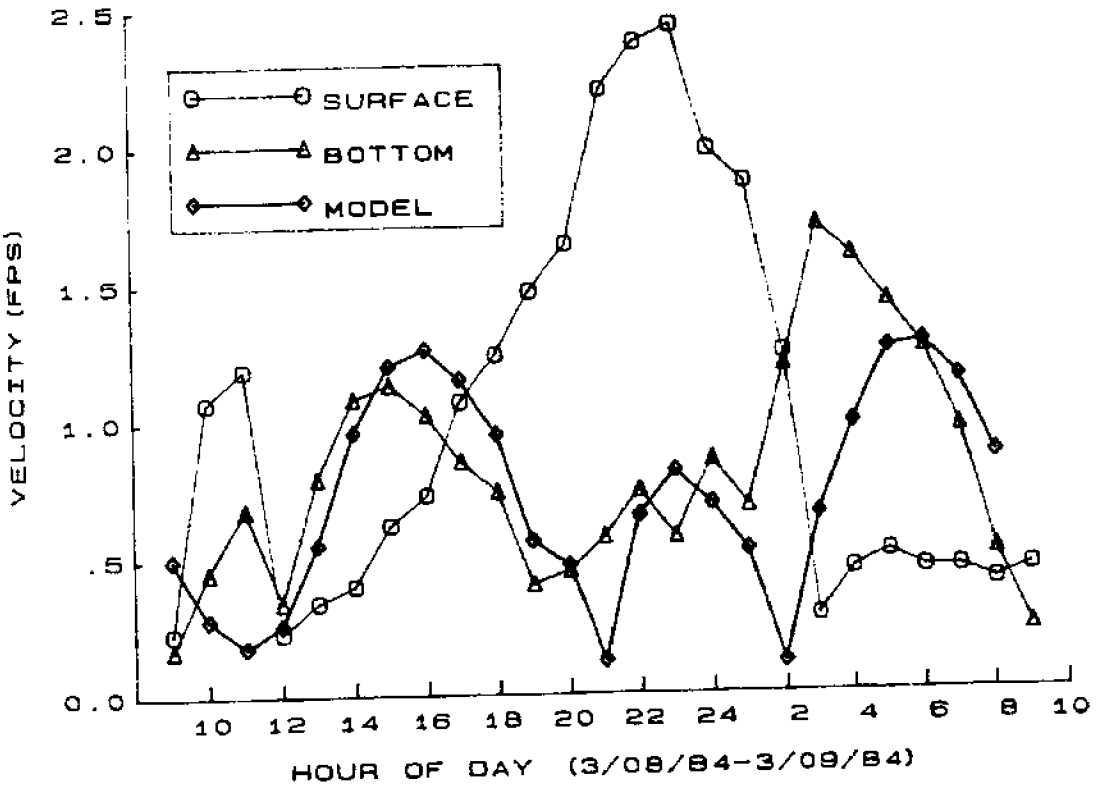

Figure B-3. Velocity at Station SG1 for Verification Condition

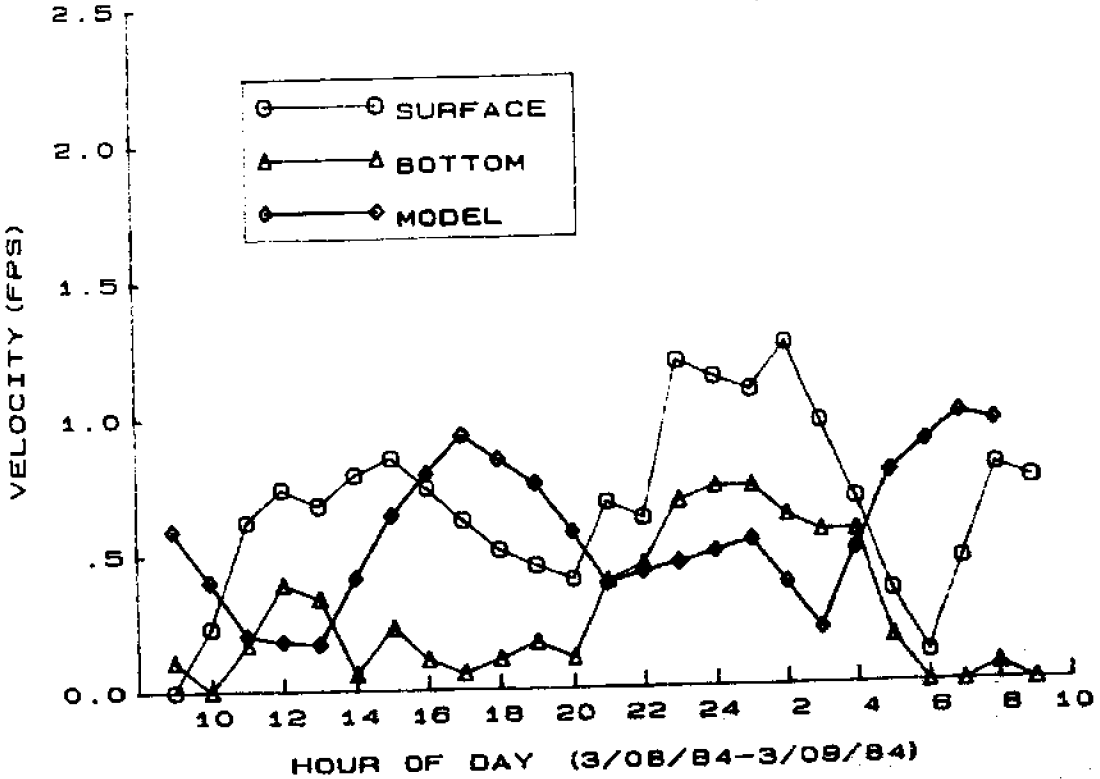

Figure B-4. Velocity at Station SG2 for Verification Condition

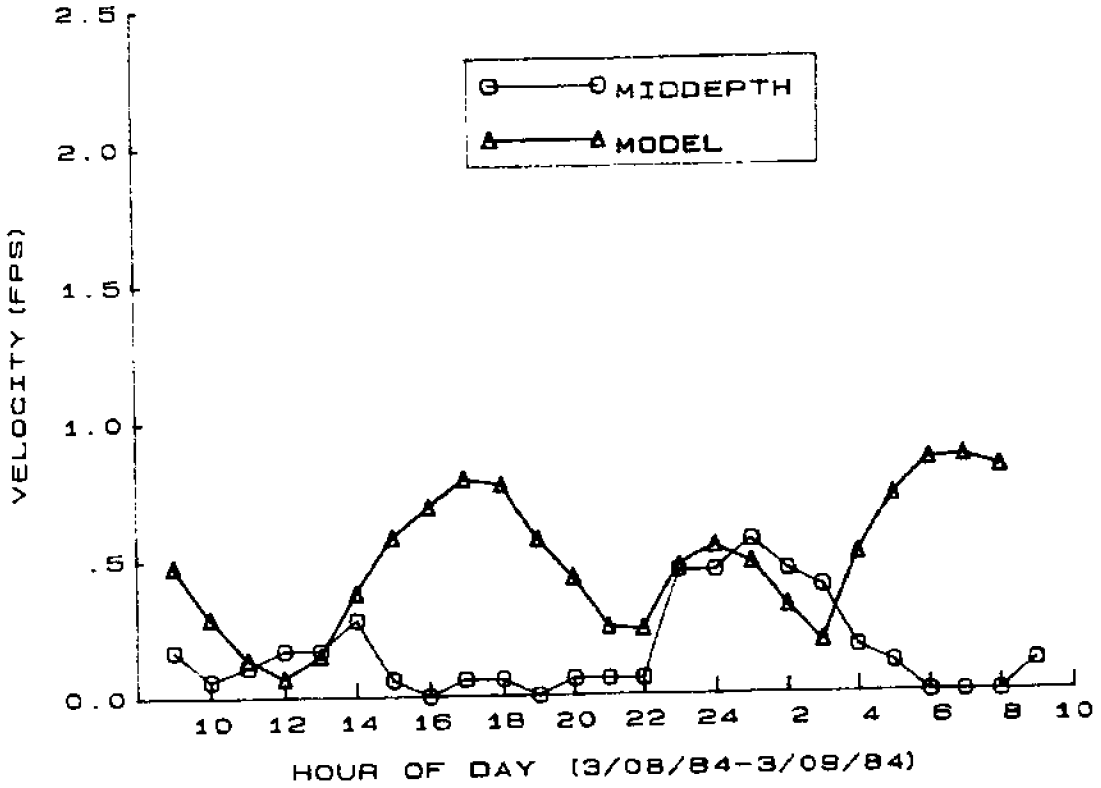

Figure B-5. Velocity at Station SG3 for Verification Condition

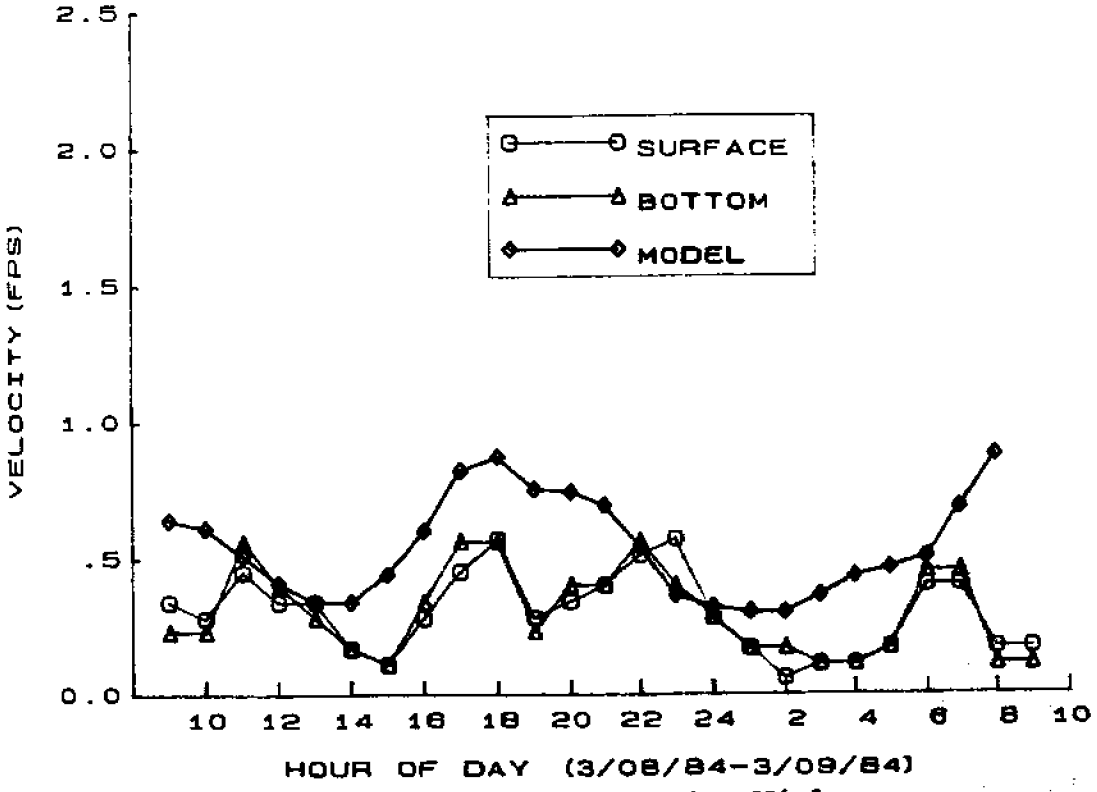

Figure B-6. Velocity at Station SG4 for Verification Condition

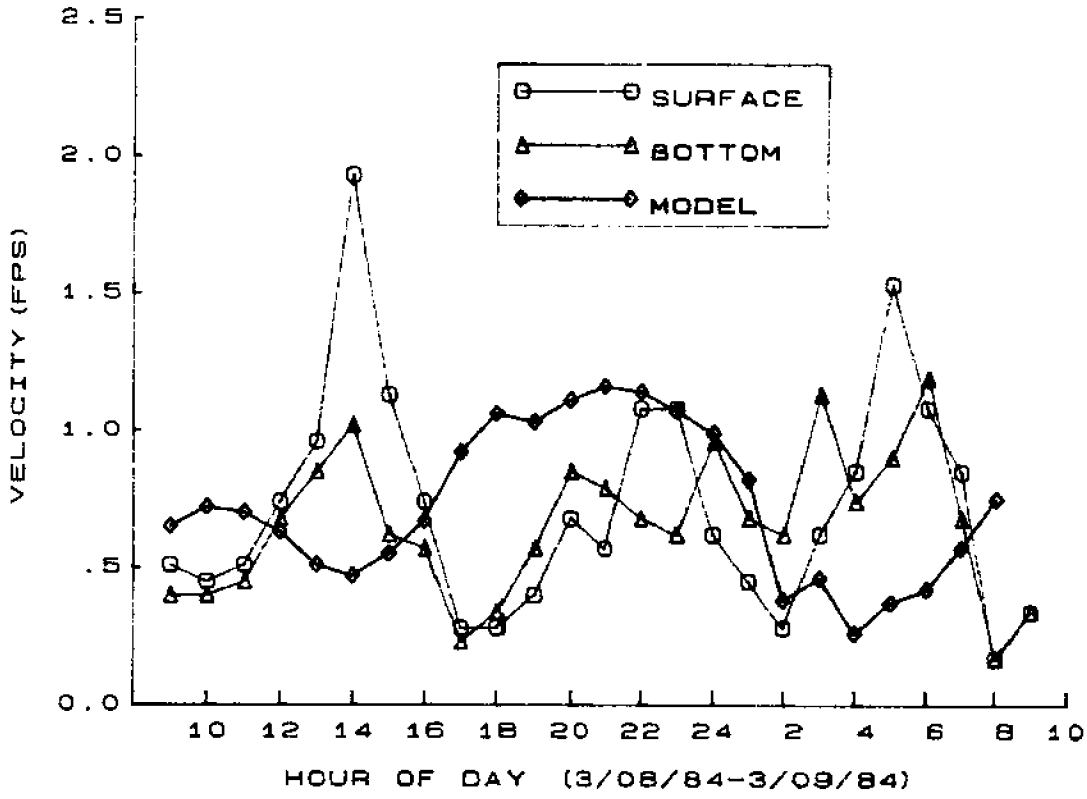

Figure B-7. Velocity at Station SG5 for Verification Condition

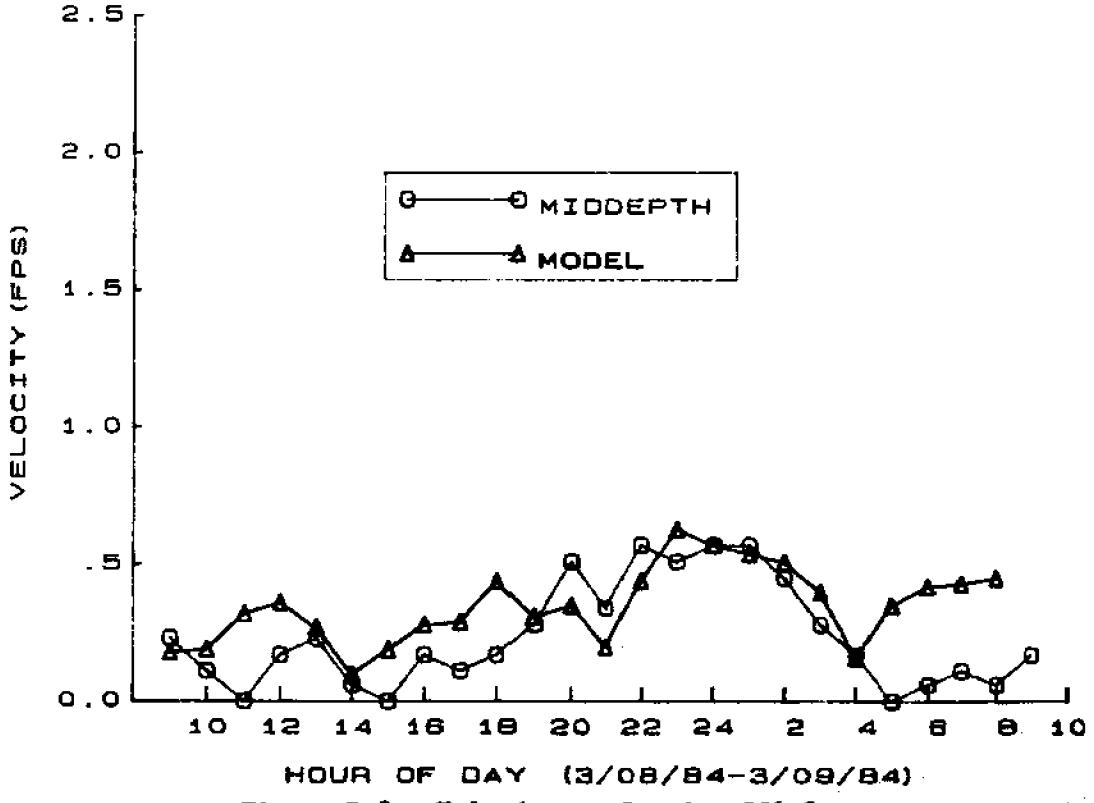

Figure B-8. Velocity at Station SG6 for Verification Condition

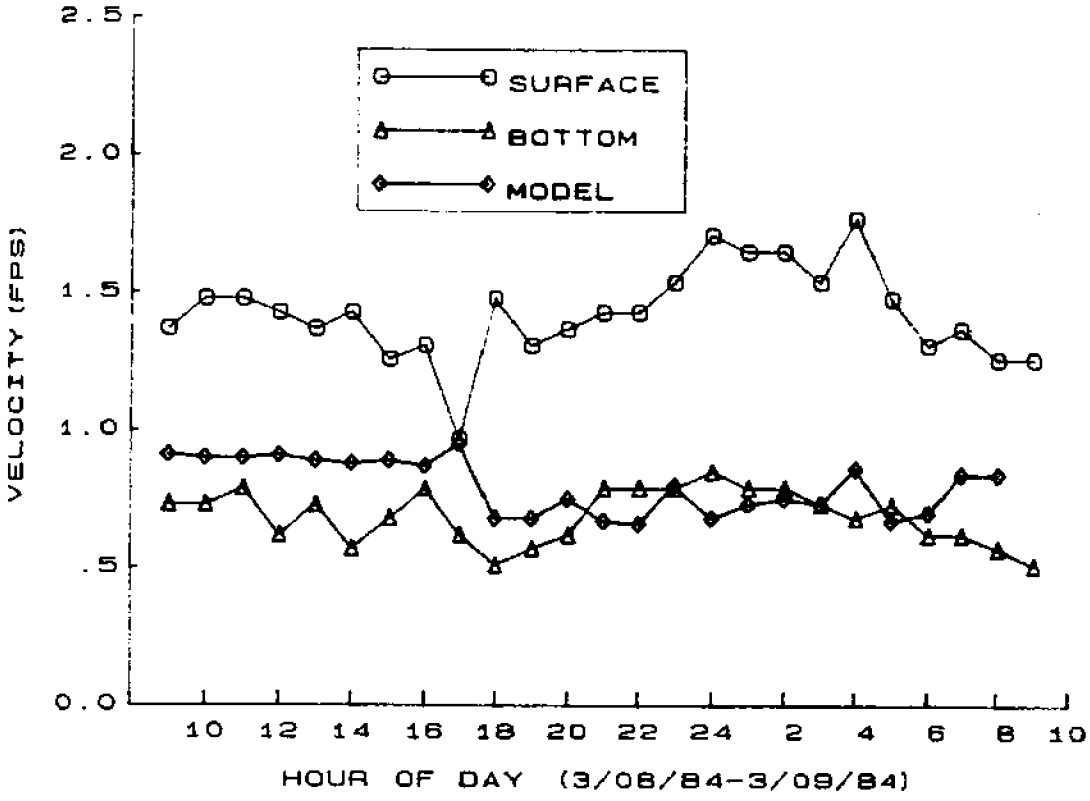

Figure B-9. Velocity at Station SG7 for Verification Condition

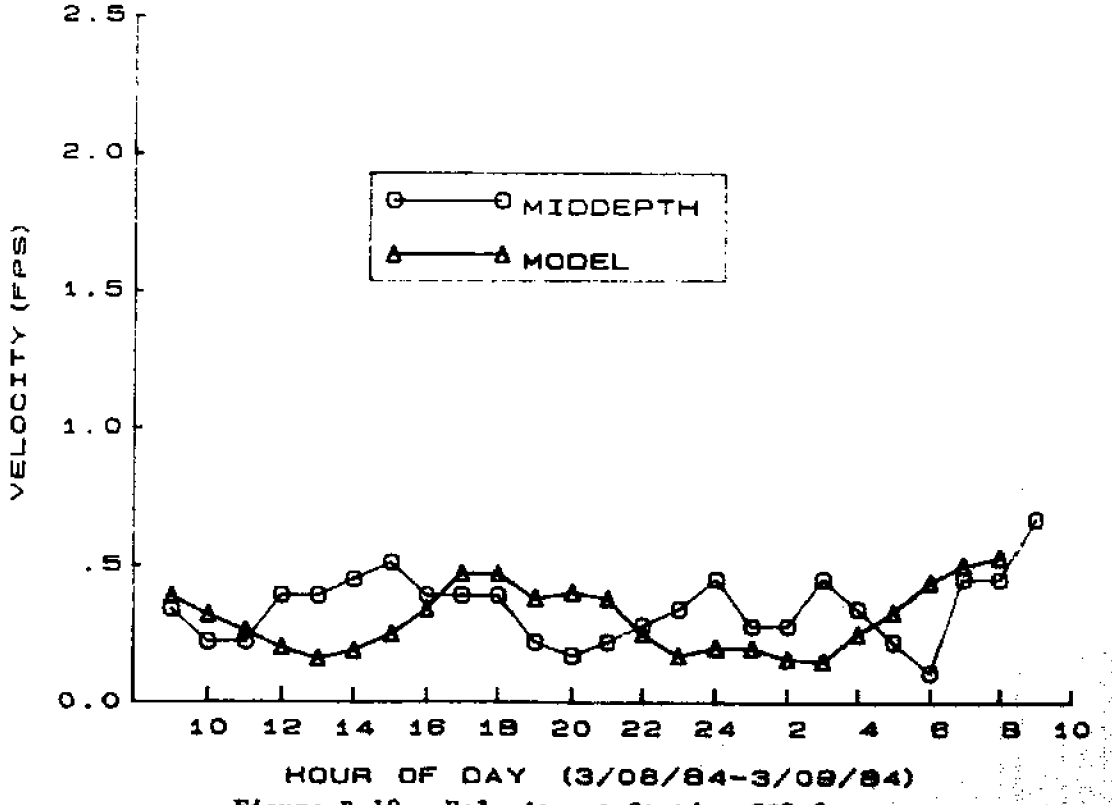

Figure B-10. Velocity at Station SG8 for Verification Condition

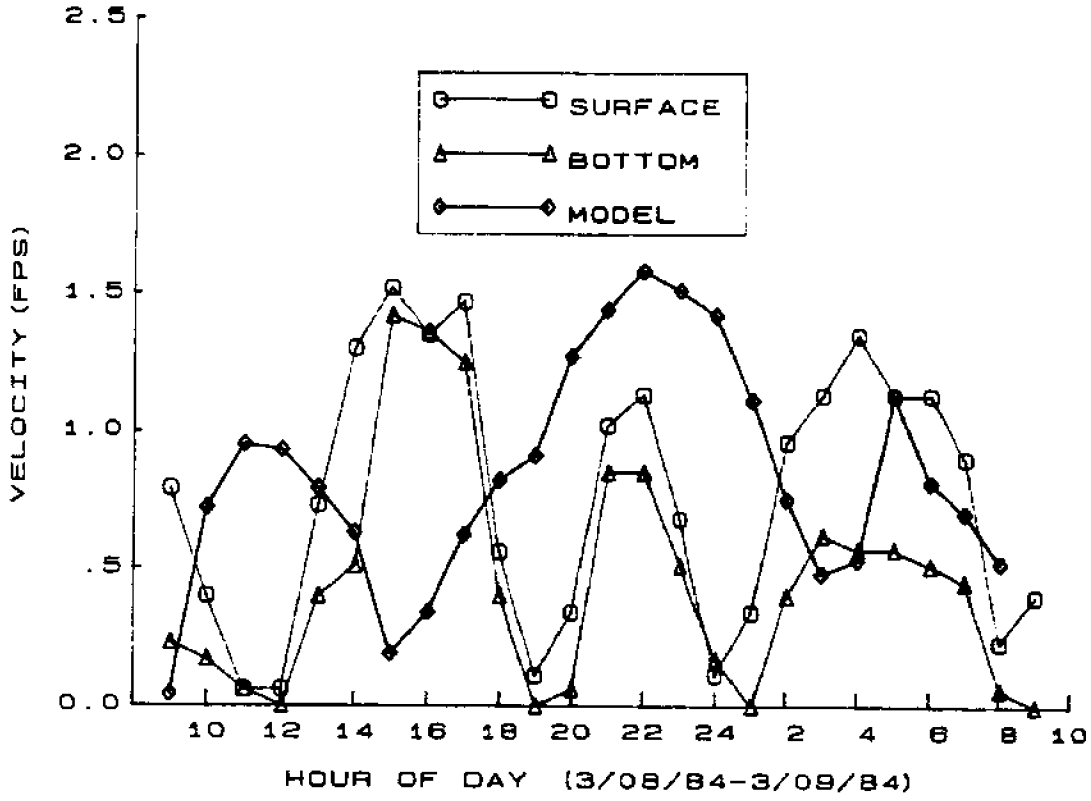

Figure B-11. Velocity at Station SG9 for Verification Condition

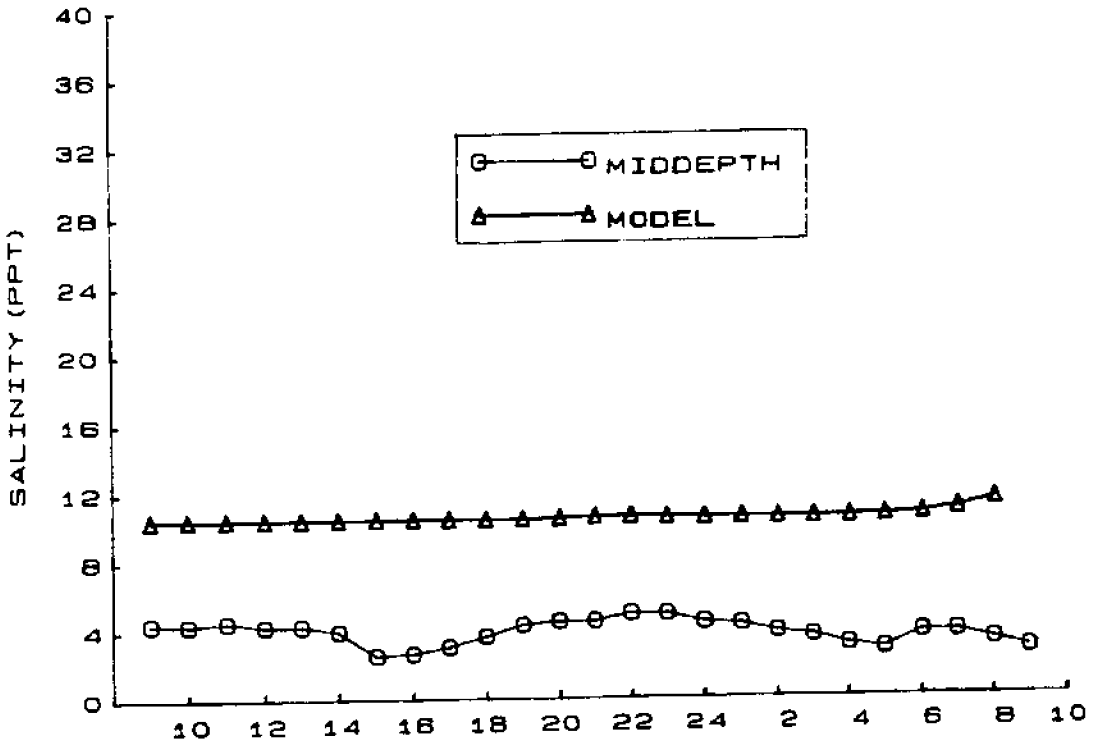

Figure B-12. Salinity at Station SG2 for Verification Condition

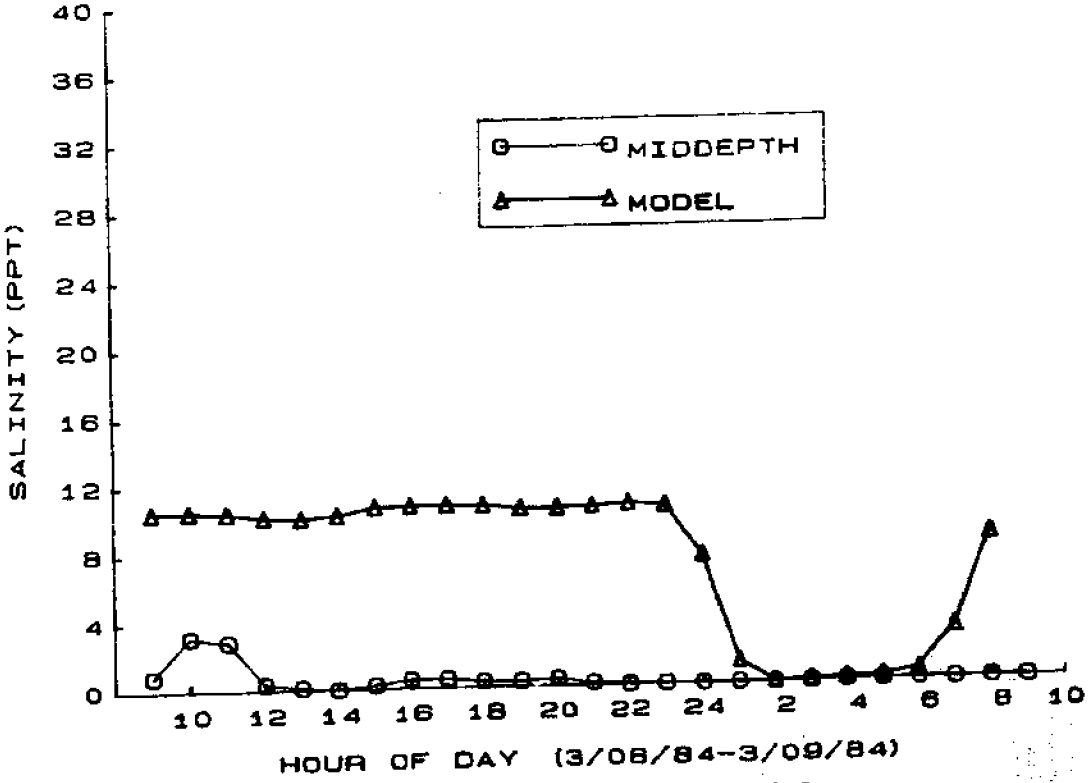

Figure B-13. Salinity at Station SG6 for Verification Condition

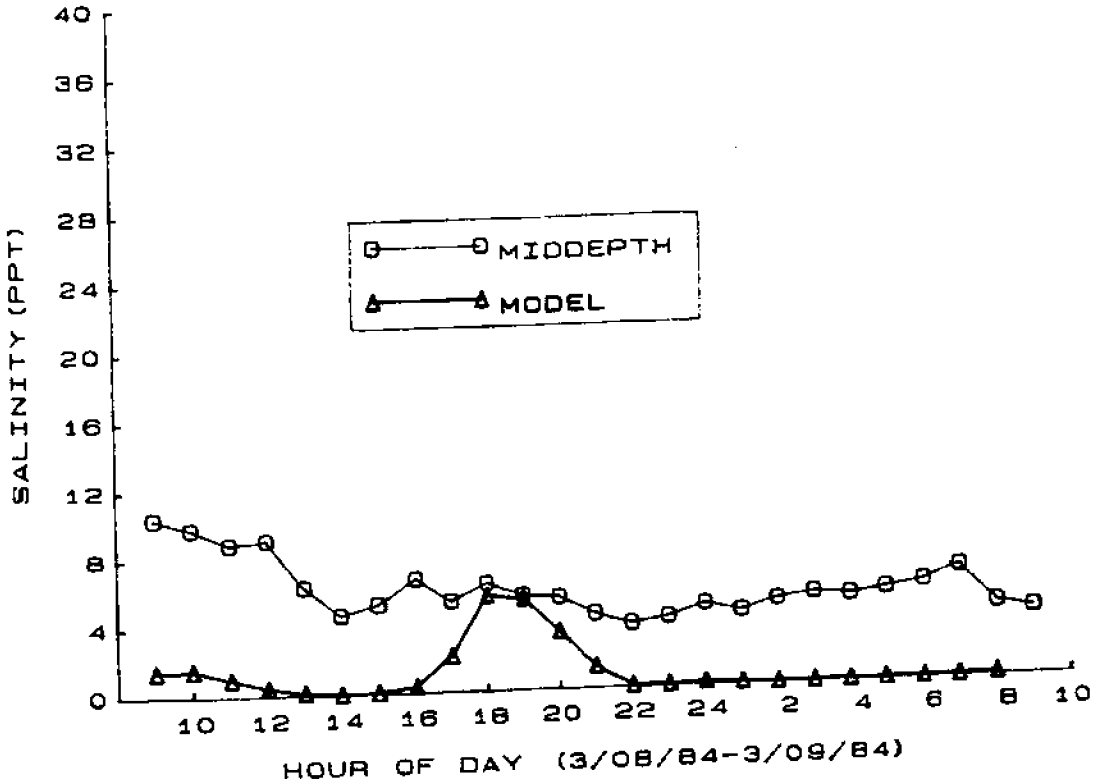

Figure B-14. Salinity at Station SG8 for Verification Condition

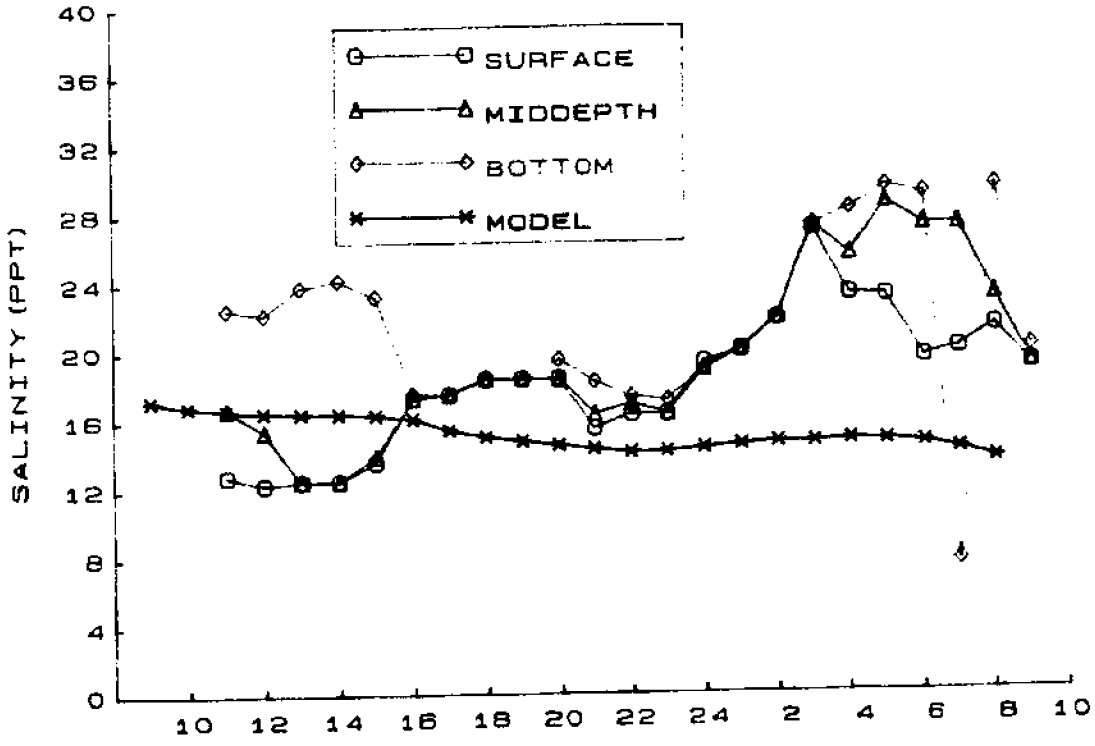

Figure B-15. Salinity at Station G2 for Verification Condition

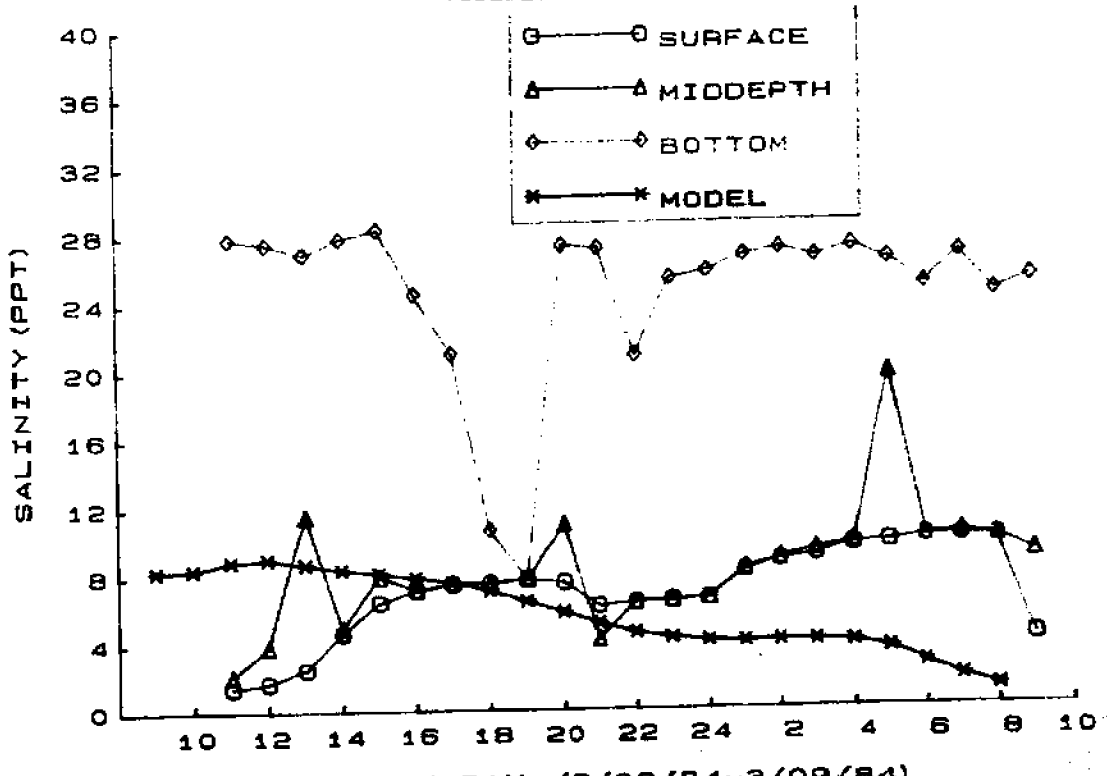

Figure B-16. Salinity at Station G3 for Verification Condition

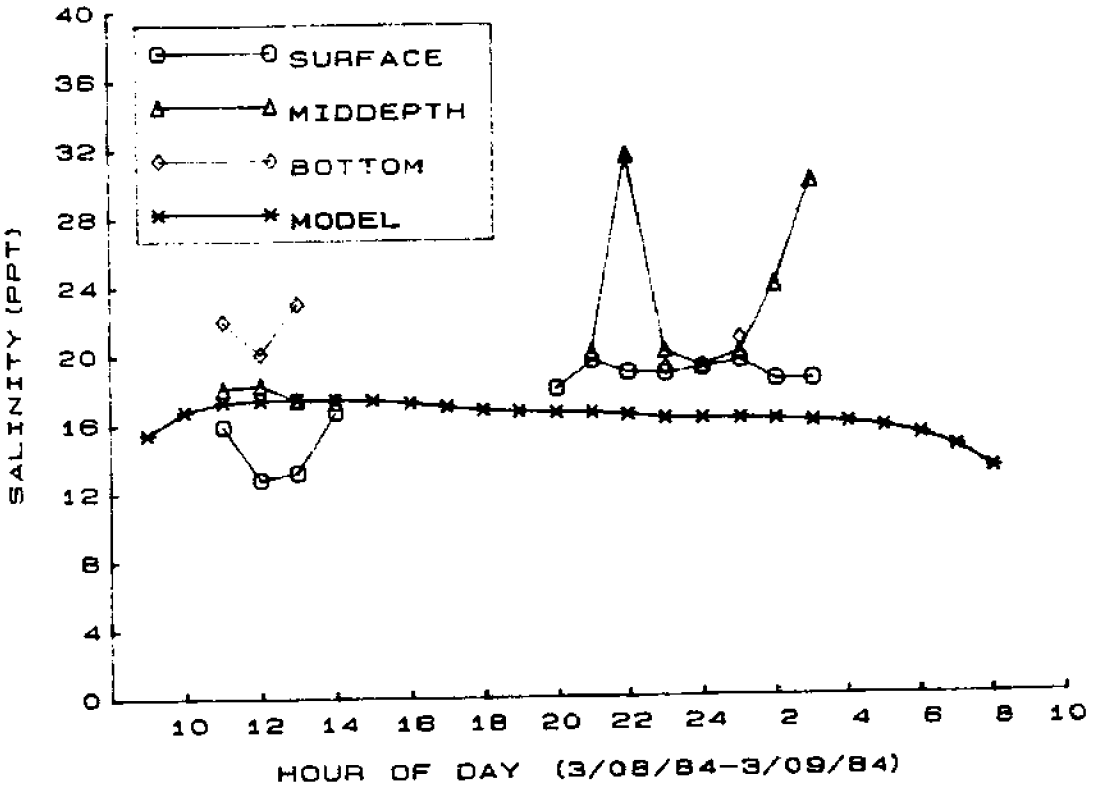

Figure B-17. Salinity at Station G4 for Verification Condition

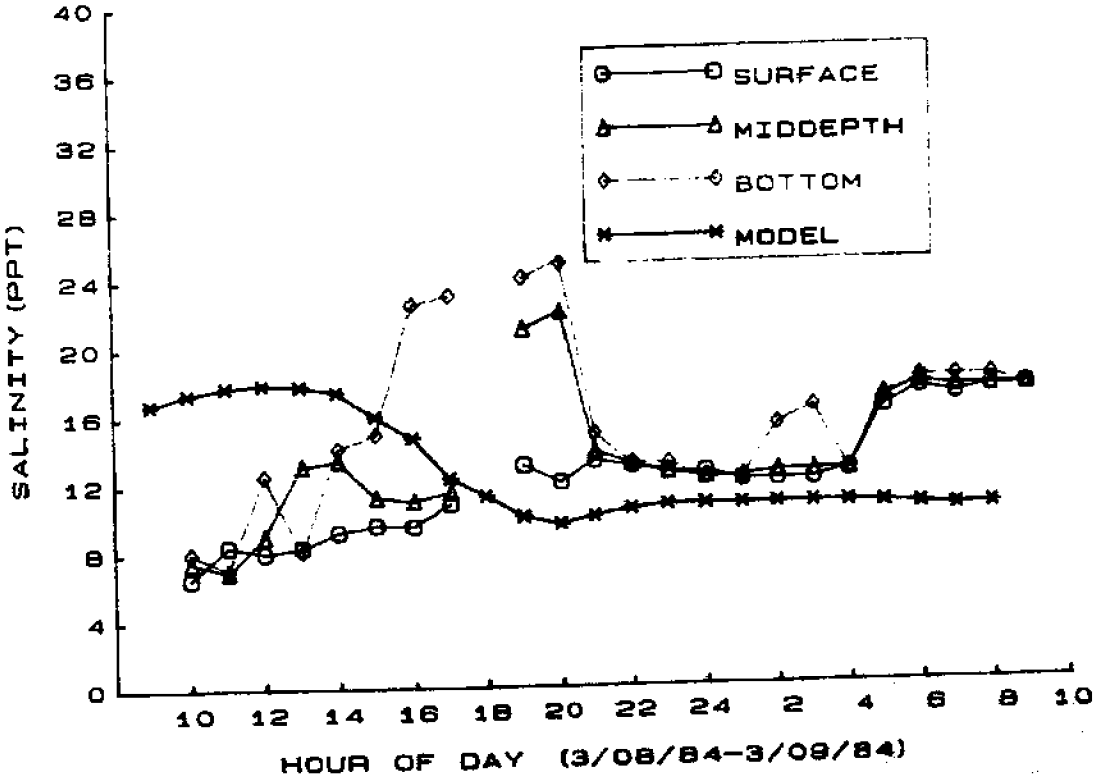

Figure B-18. Salinity at Station G5 for Verification Condition

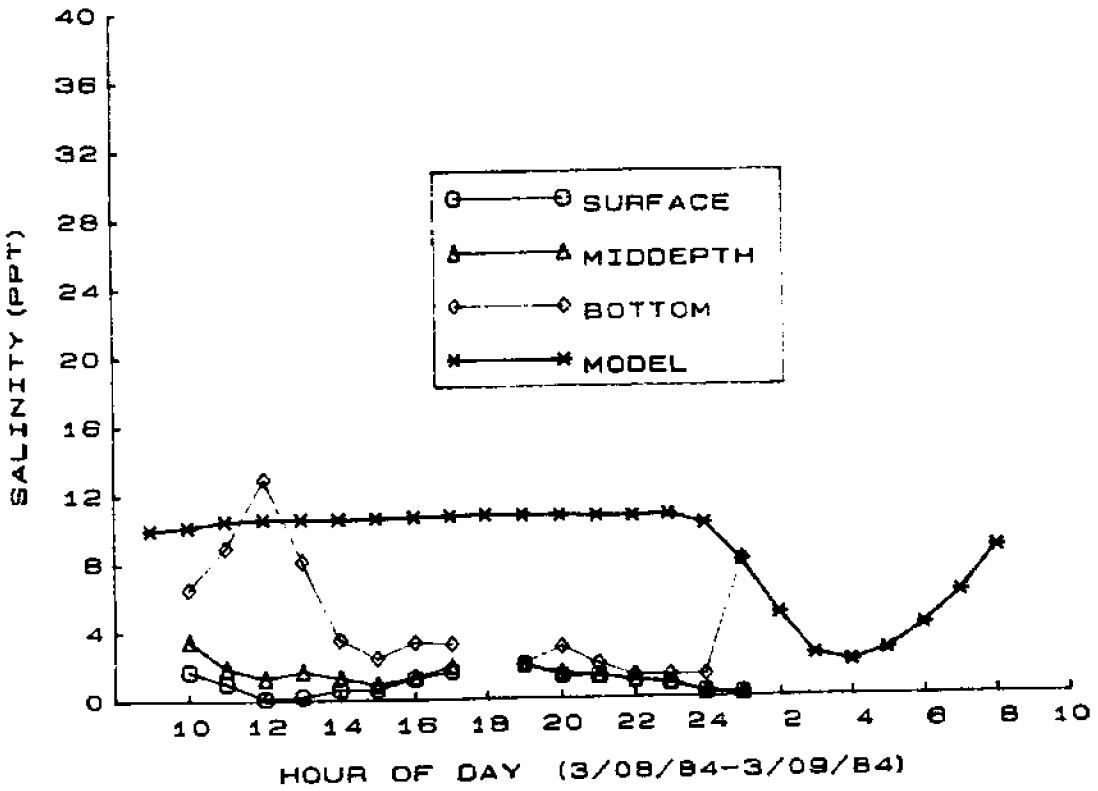

Figure B-19. Salinity at Station G6 for Verification Condition

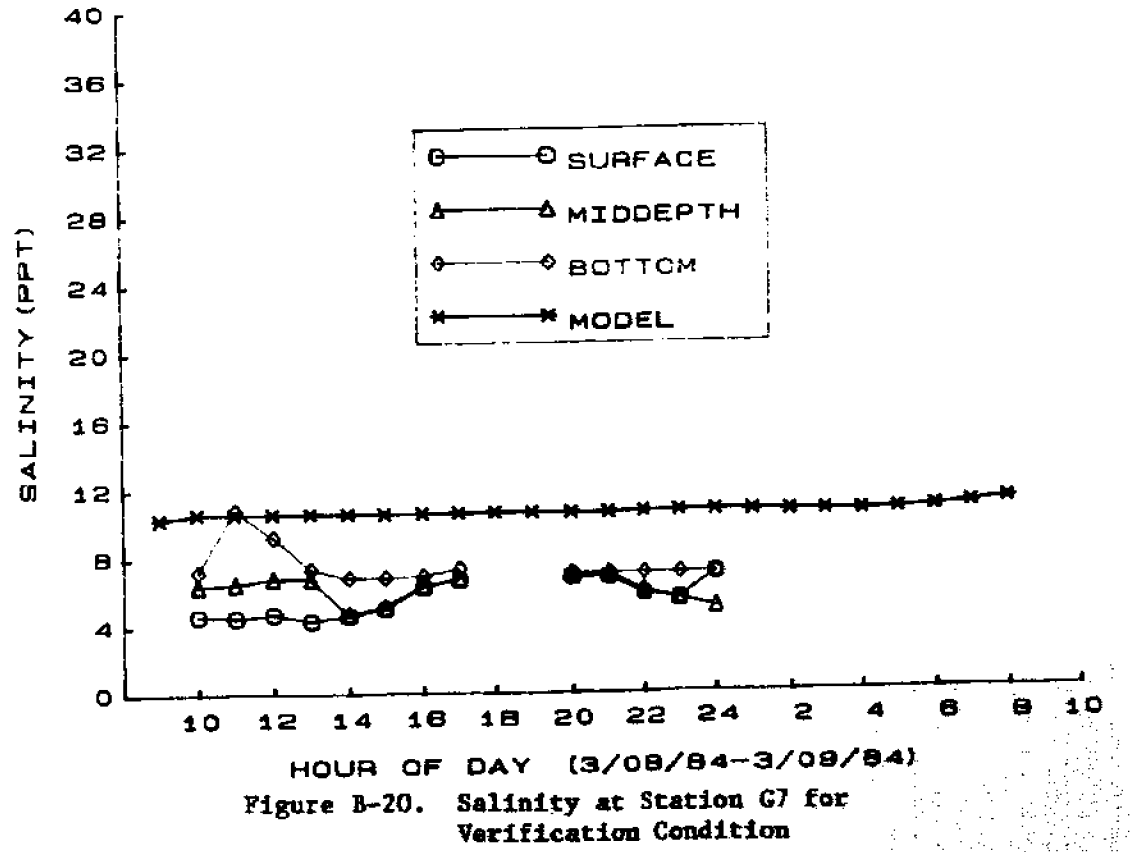

Figure B-20. Salinity at Station G7 for Verification Condition

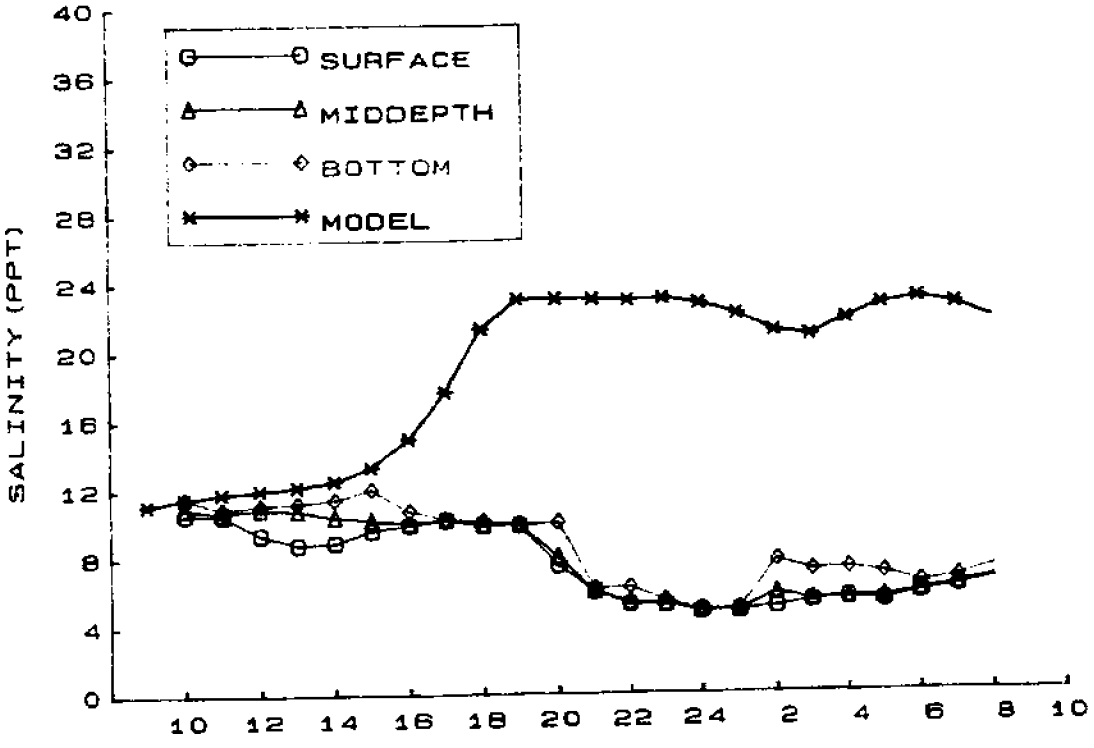

Figure B-21. Salinity at Station G8 for Verification Condition

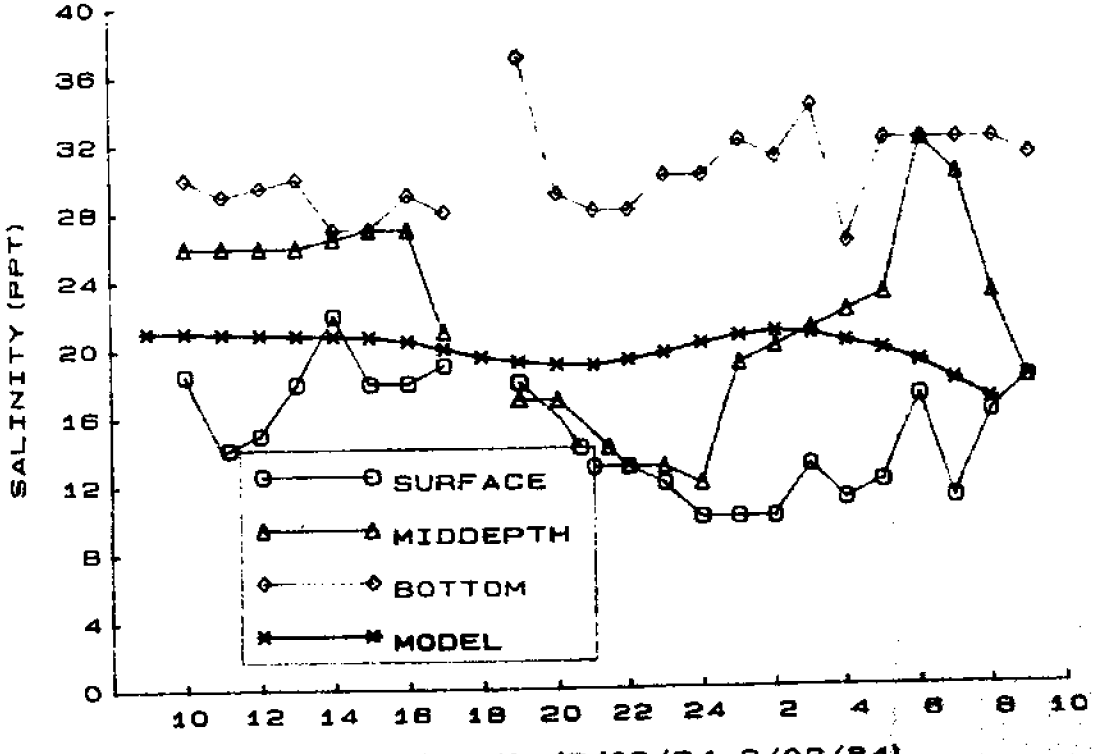

Figure B-22. Salinity at Station G9 for Verification Condition

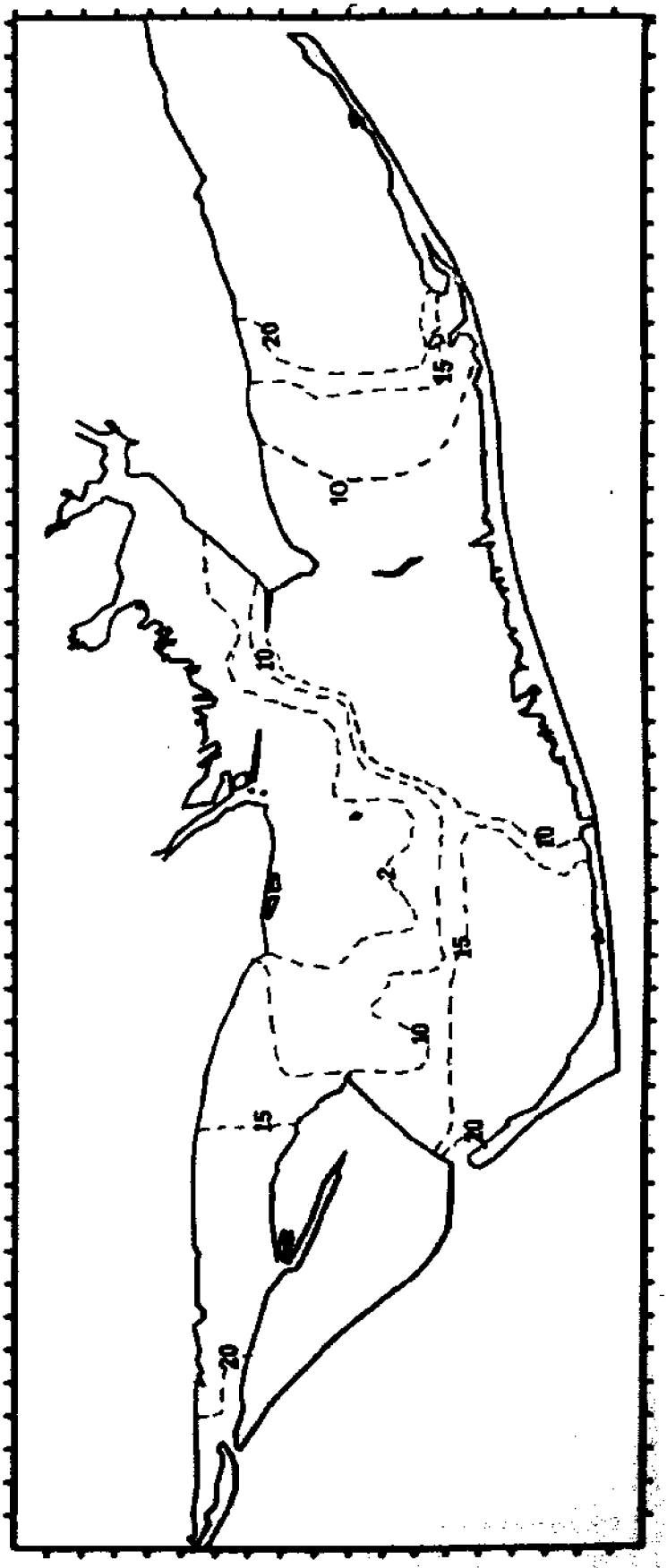

Figure B-23. Salinity Contours at 0900 on March 8, 1984

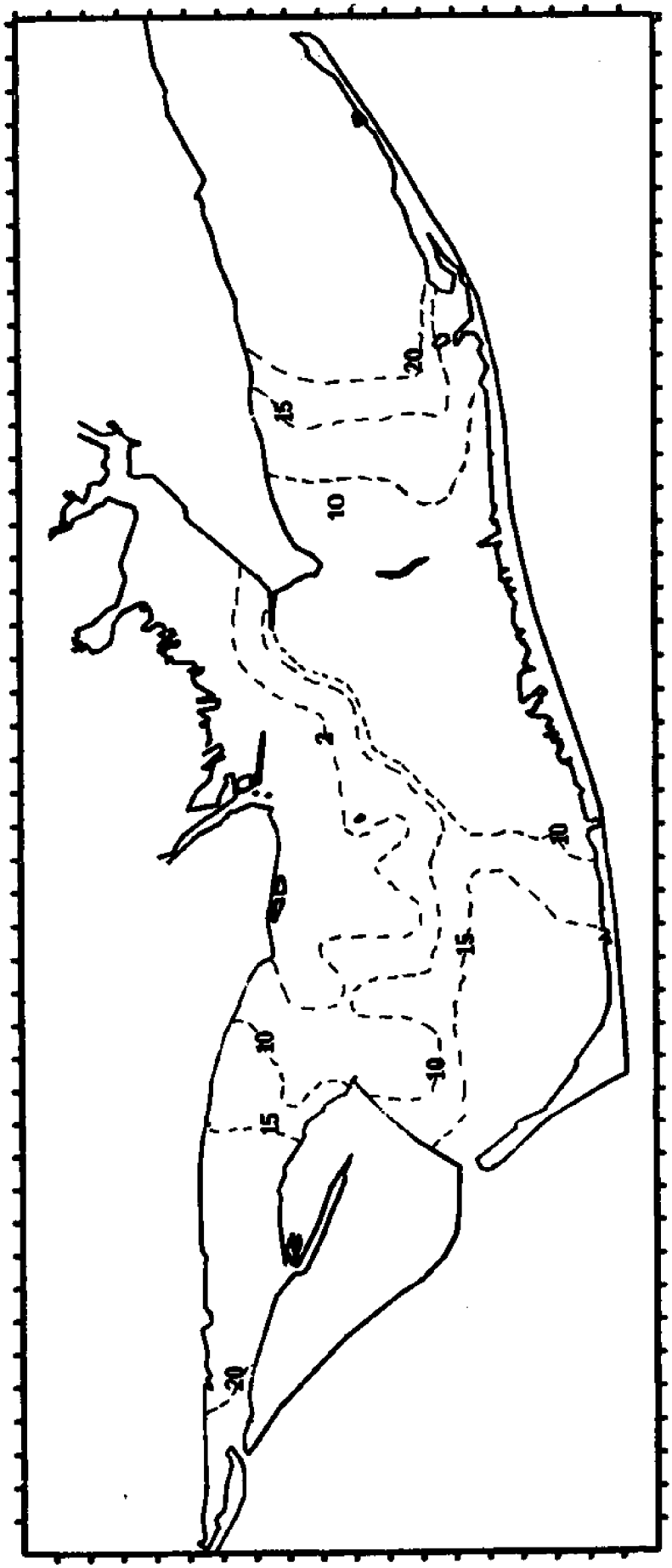

Figure B-24. Salinity Contours at 1100 on March 8, 1984

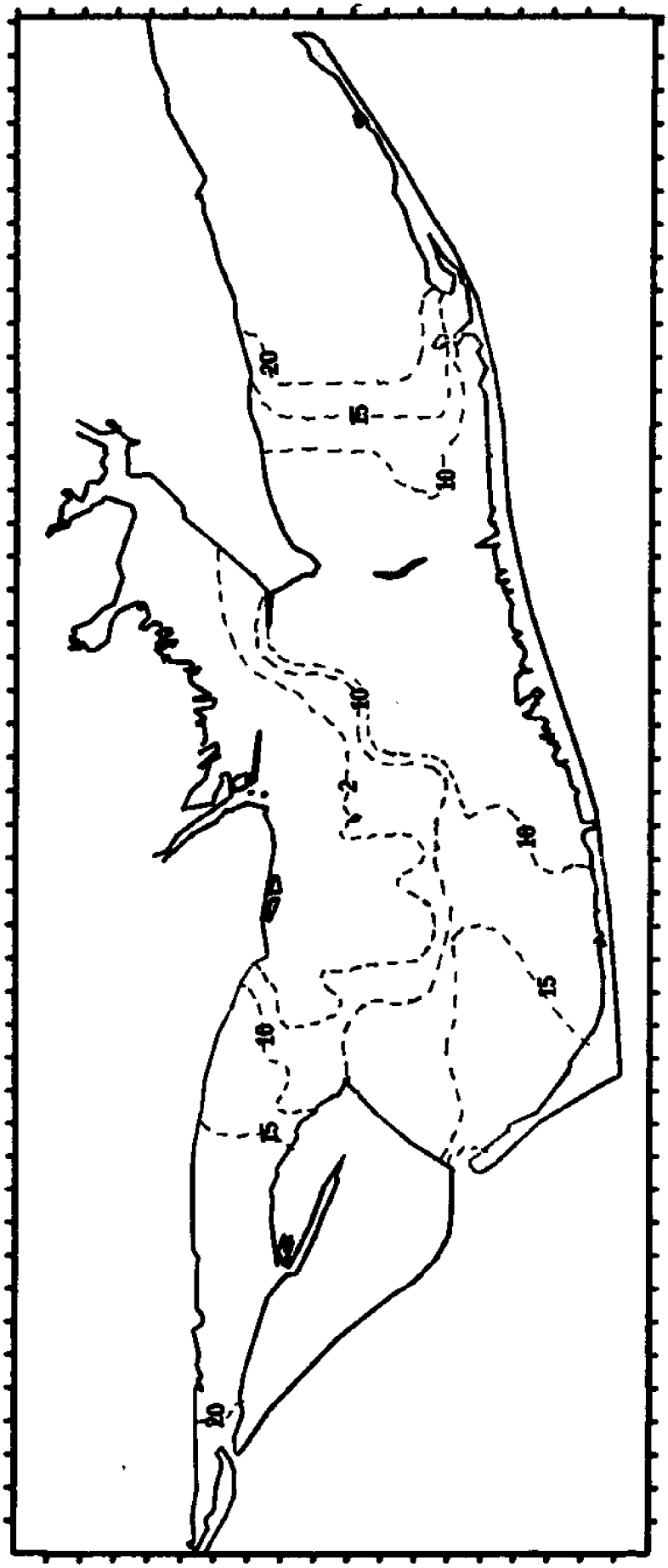

Figure B-25. Salinity Contours at 1300 on March 8, 1984

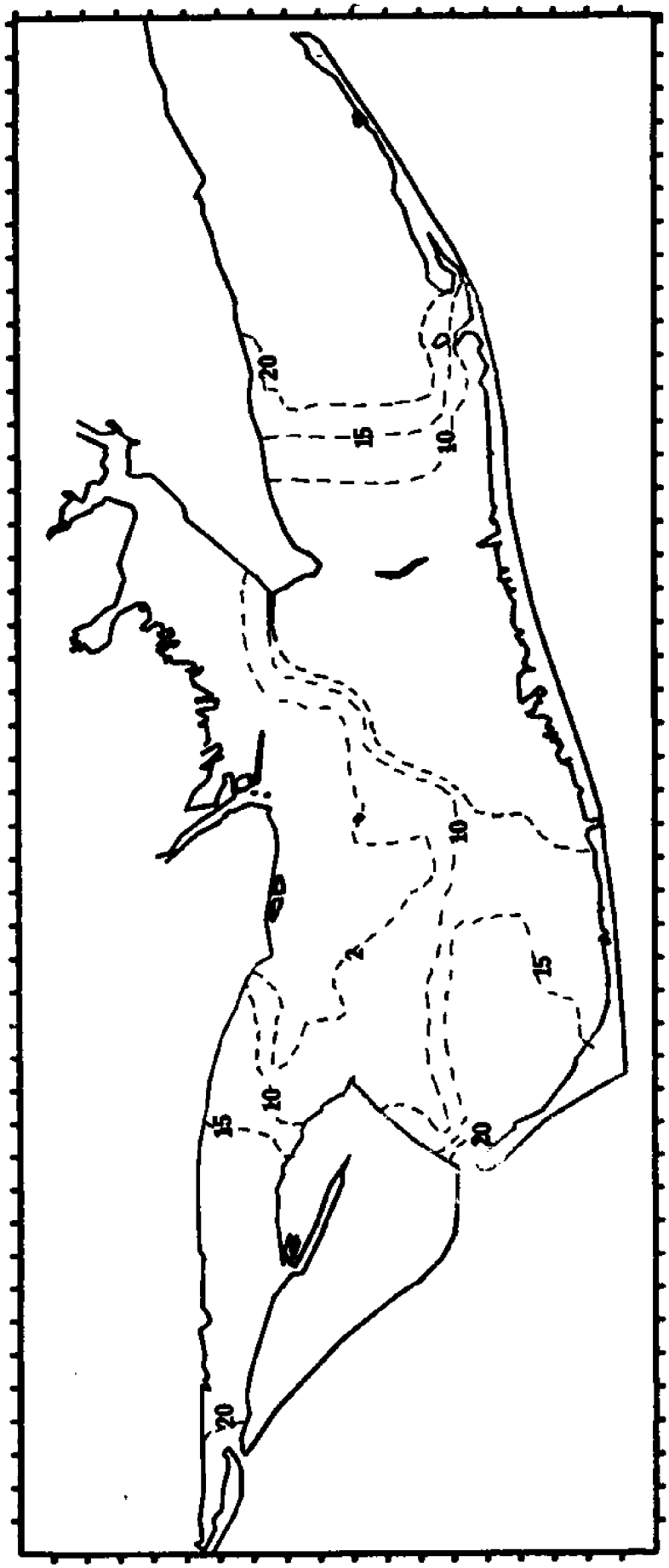

Figure B-26. Salinity Contours at 1500 on March 8, 1984

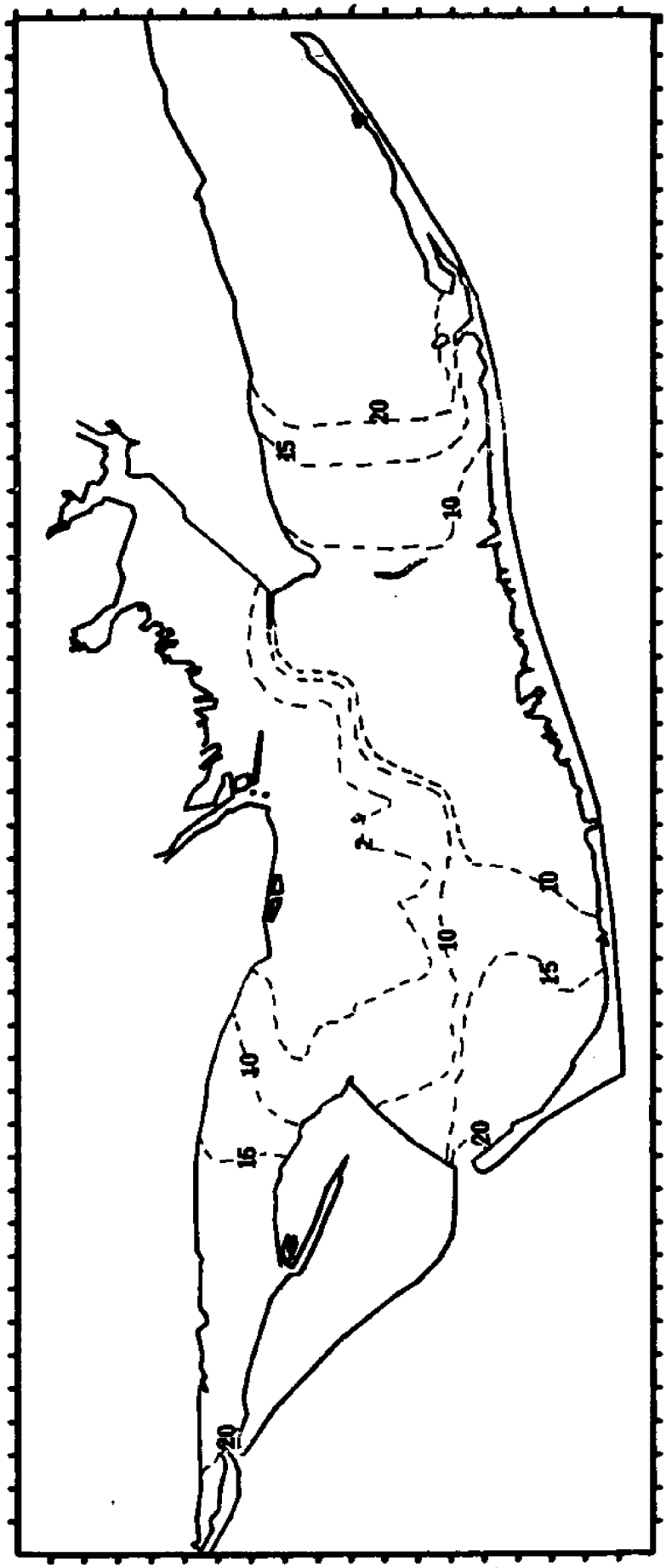

Figure B-27. Salinity Contours at 1700 on March 8, 1984

Figure B-28. Salinity Contours at 1900 on March 8, 1984

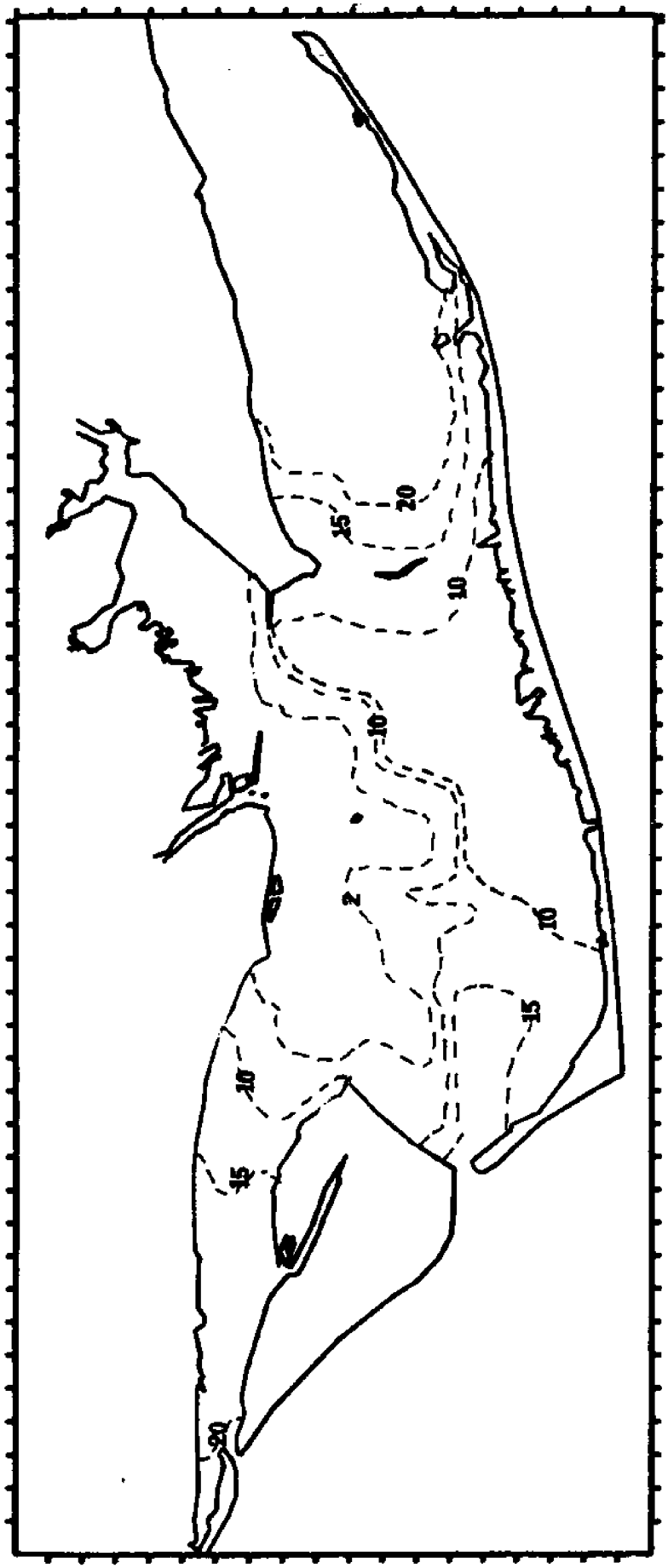

Figure B-29. Salinity Contours at 2100 on March 8, 1984

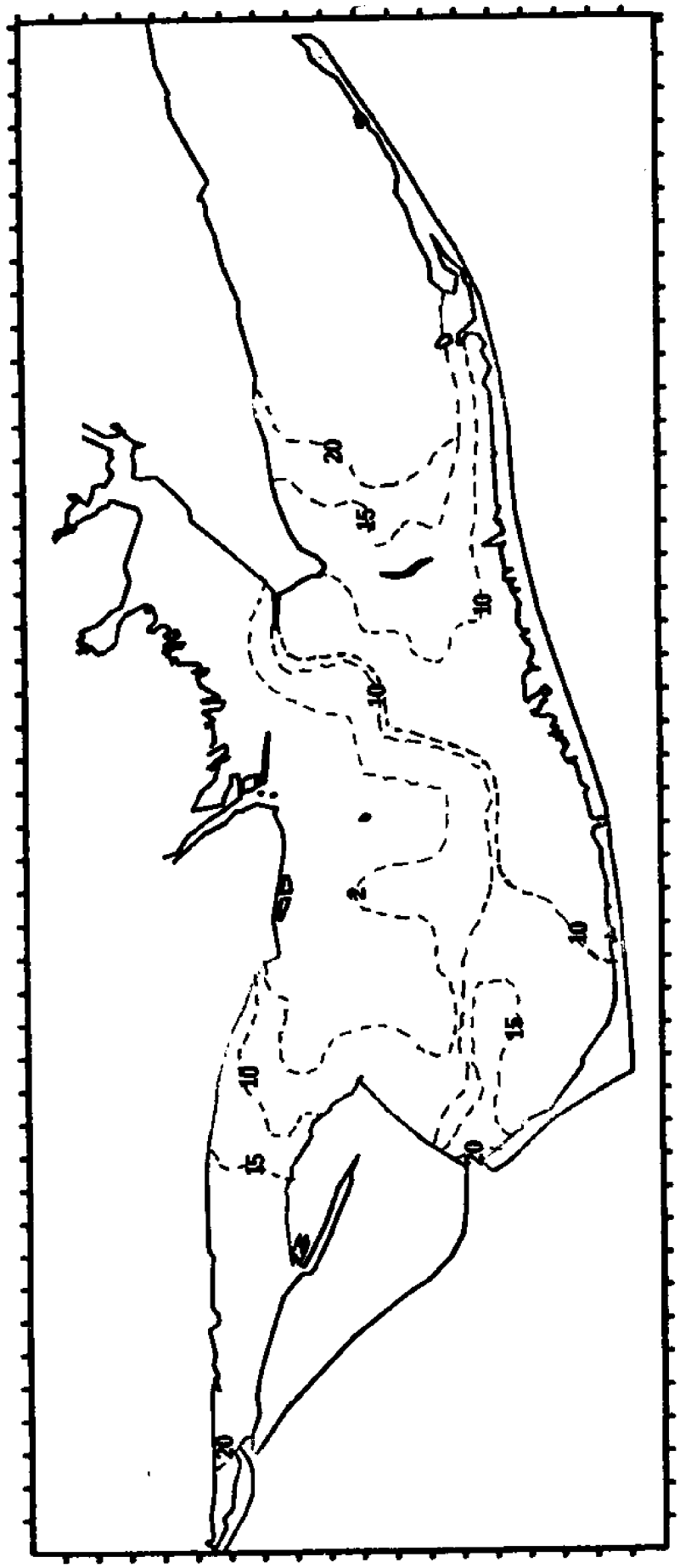

Figure B-30. Salinity Contours at 2300 on March 8, 1984

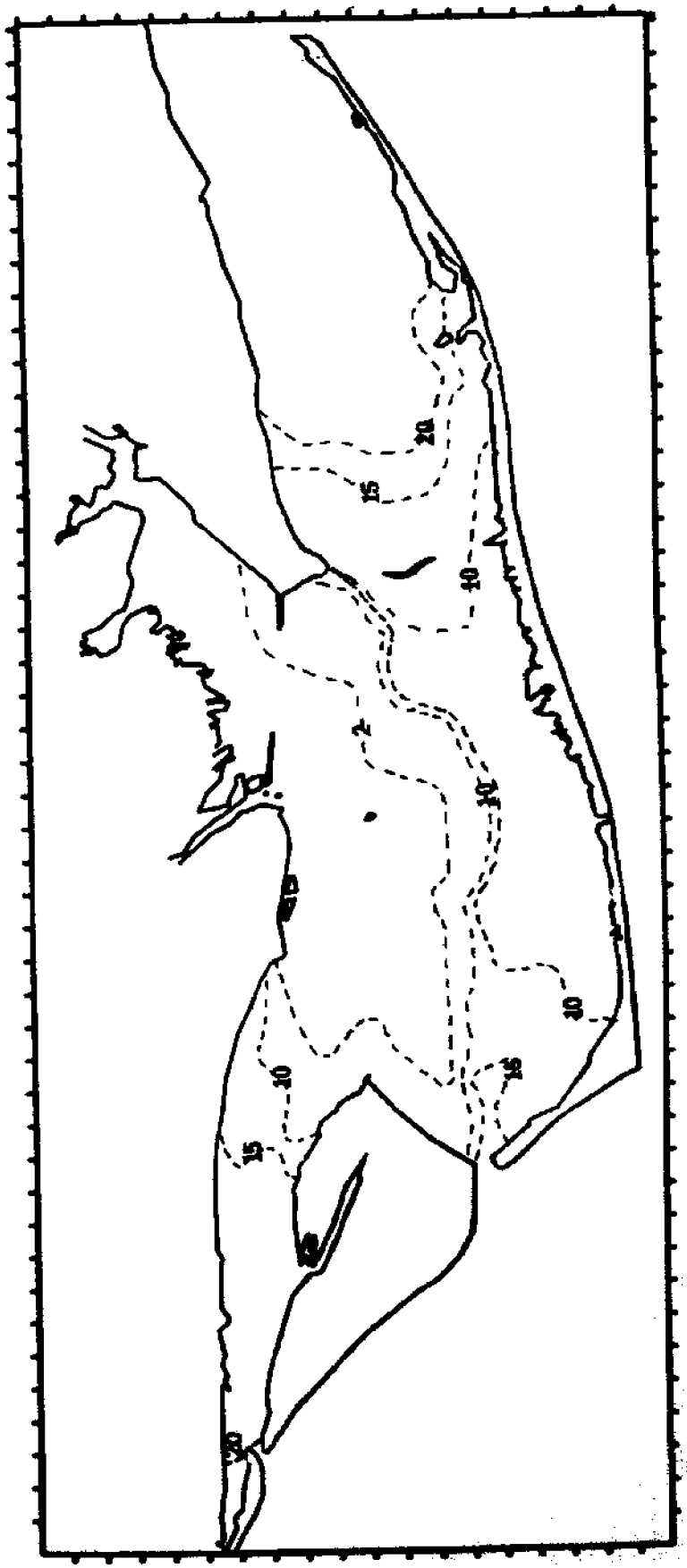

Figure B-31. Salinity Contours at 0100 on March 9, 1984

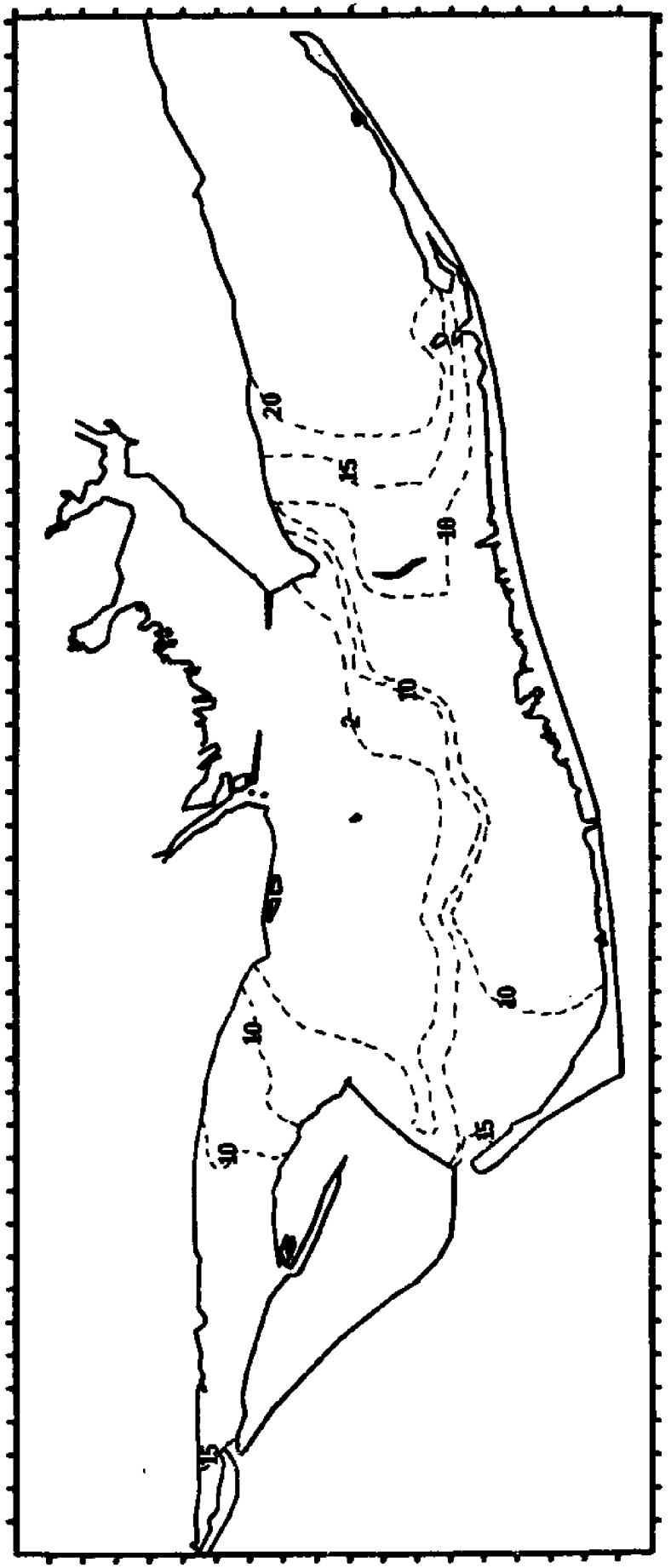

Figure B-32. Salinity Contours at 0300 on March 9, 1984

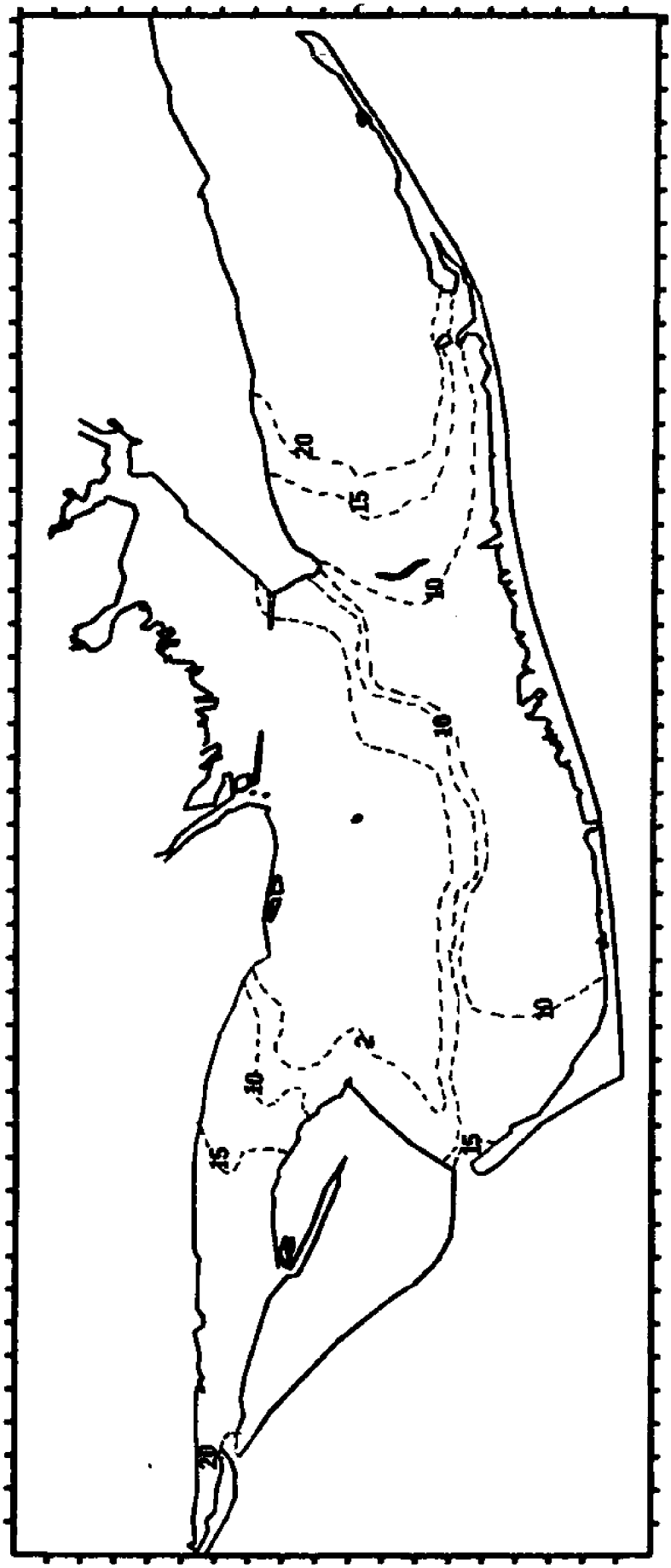

Figure B-33. Salinity Contours at 0500 on March 9, 1984

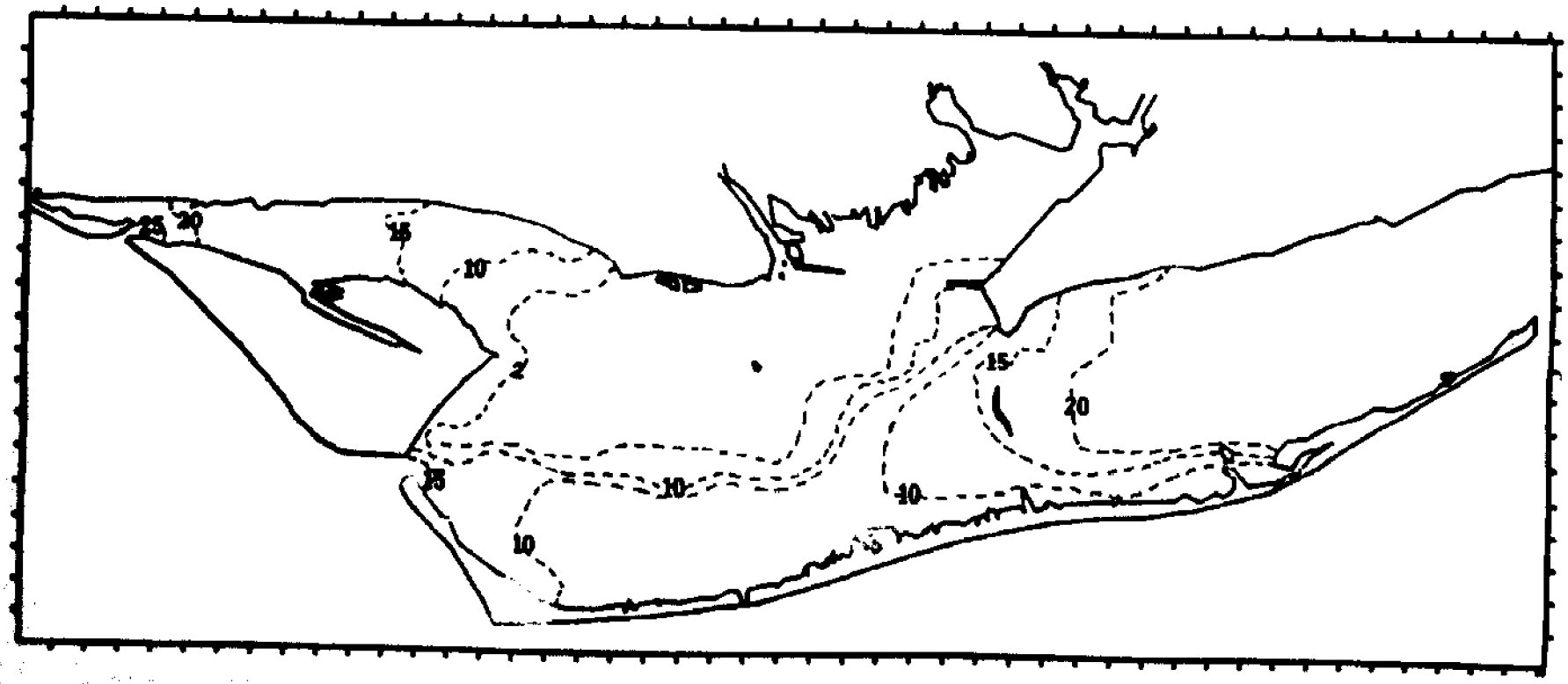

Figure B-34. Salinity Contours at 0700 on March 9, 1984

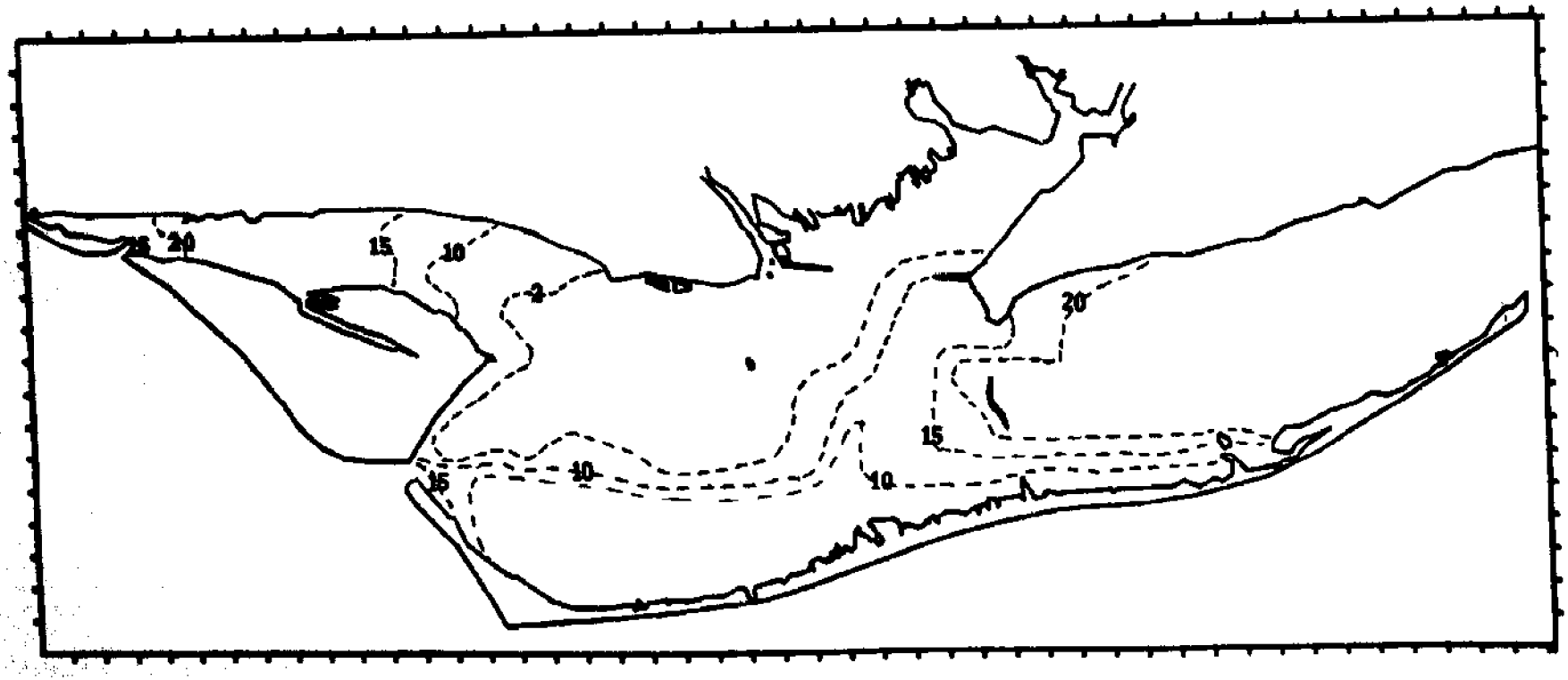

Figure B-35. Salinity Contours at 0900 on March 9, 1984

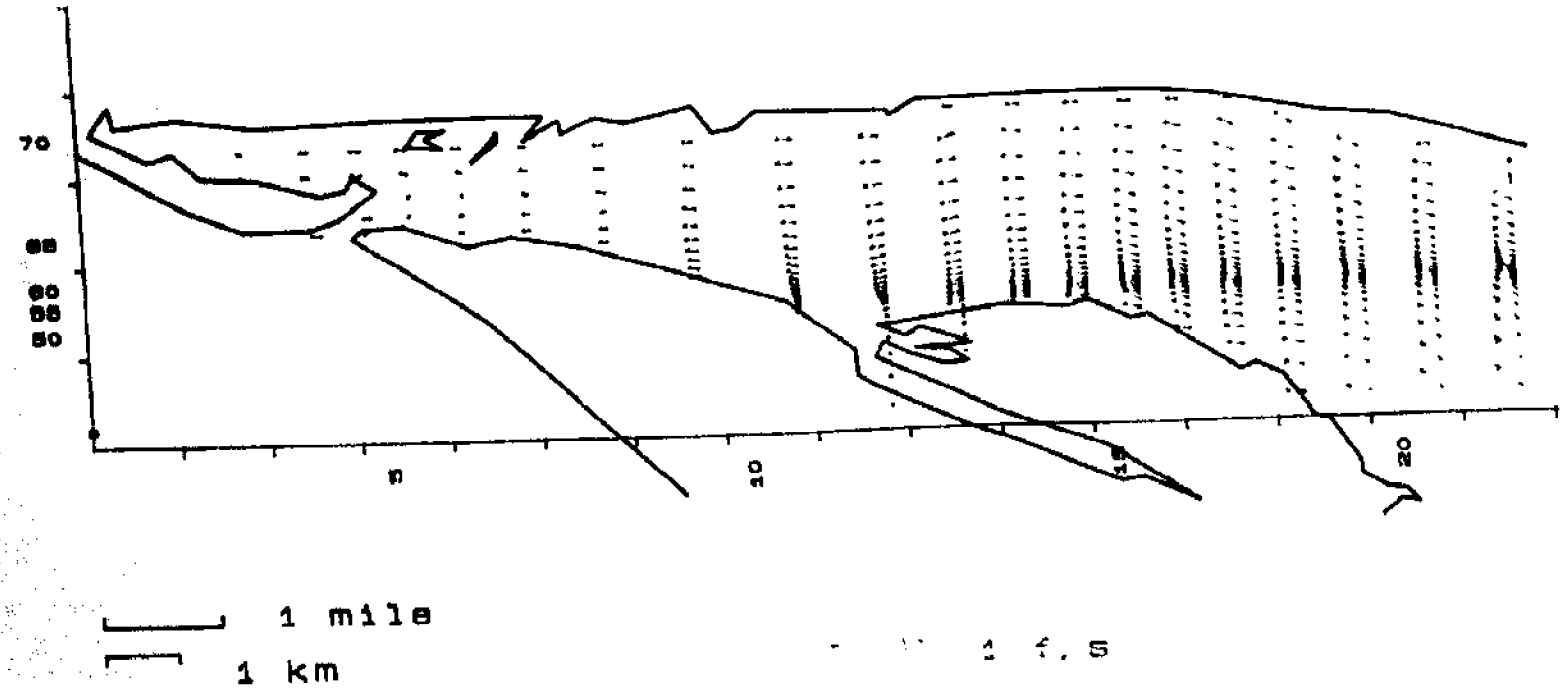

Figure B-36. Velocity Plot for St. Vincent Sound at 0900 on March 8, 1984

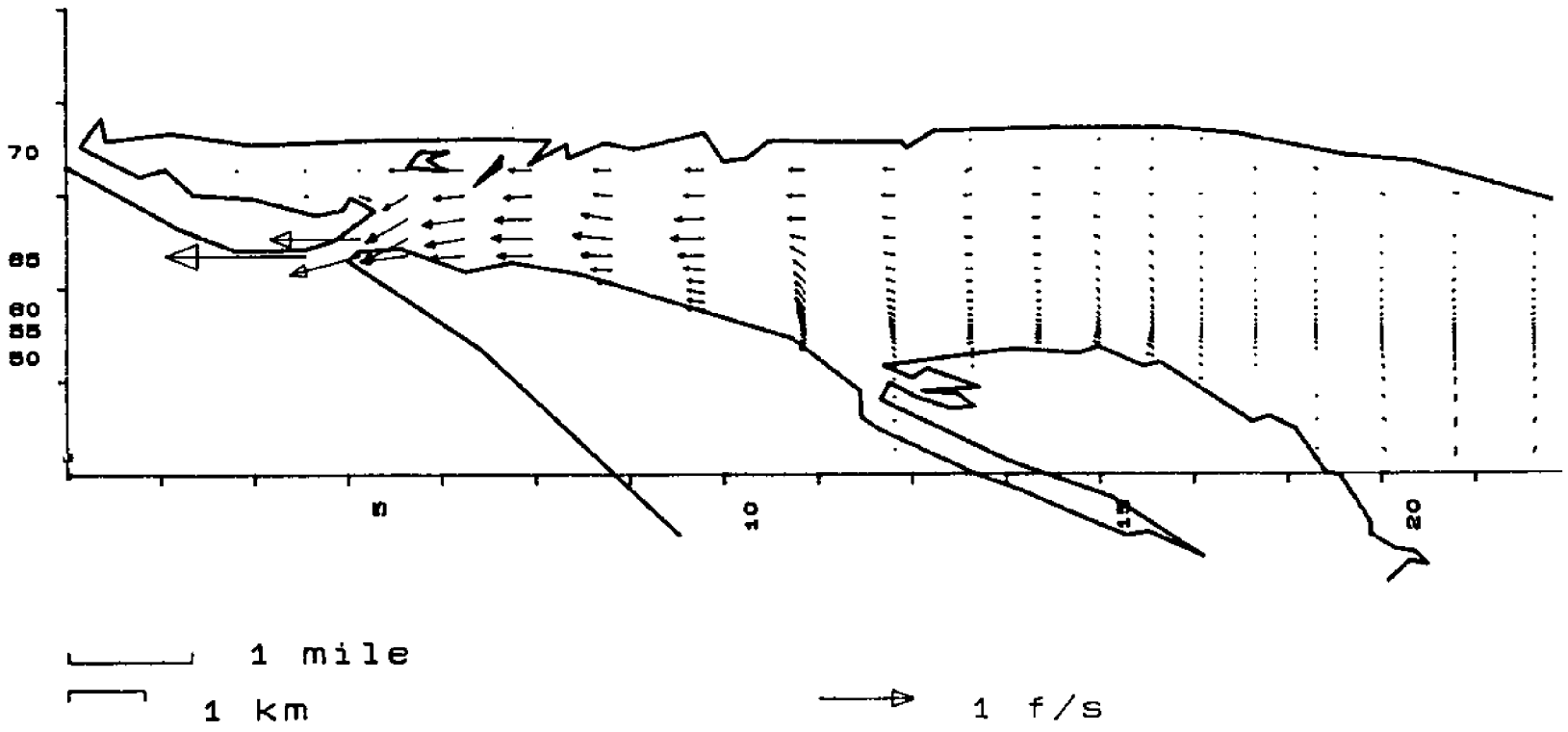

Figure B-37. Velocity Plot for St. Vincent Sound at 1300 on March 8, 1984

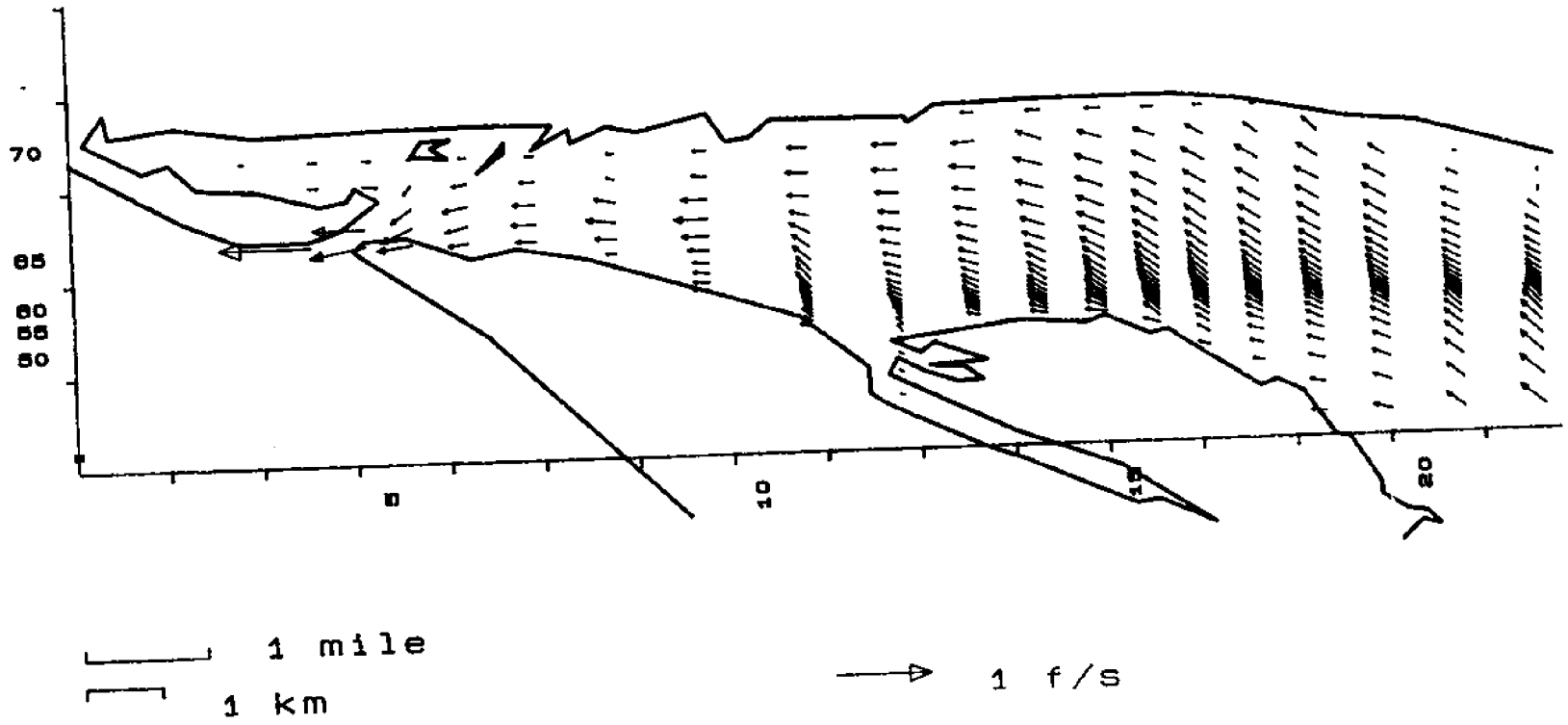

Figure B-38. Velocity Plot for St. Vincent Sound at 1700 on March 8, 1984

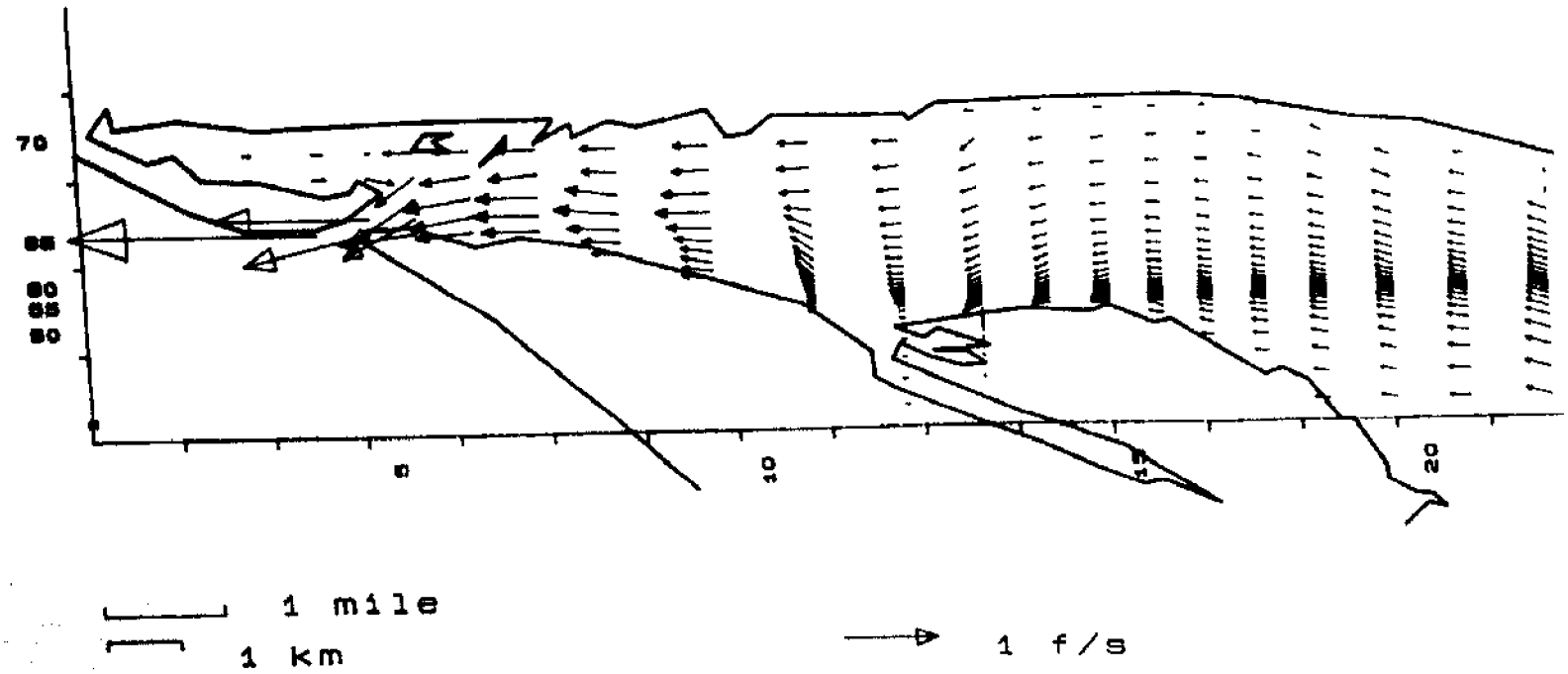

Figure B-39. Velocity Plot for St. Vincent Sound at 2100 on March 8, 1984

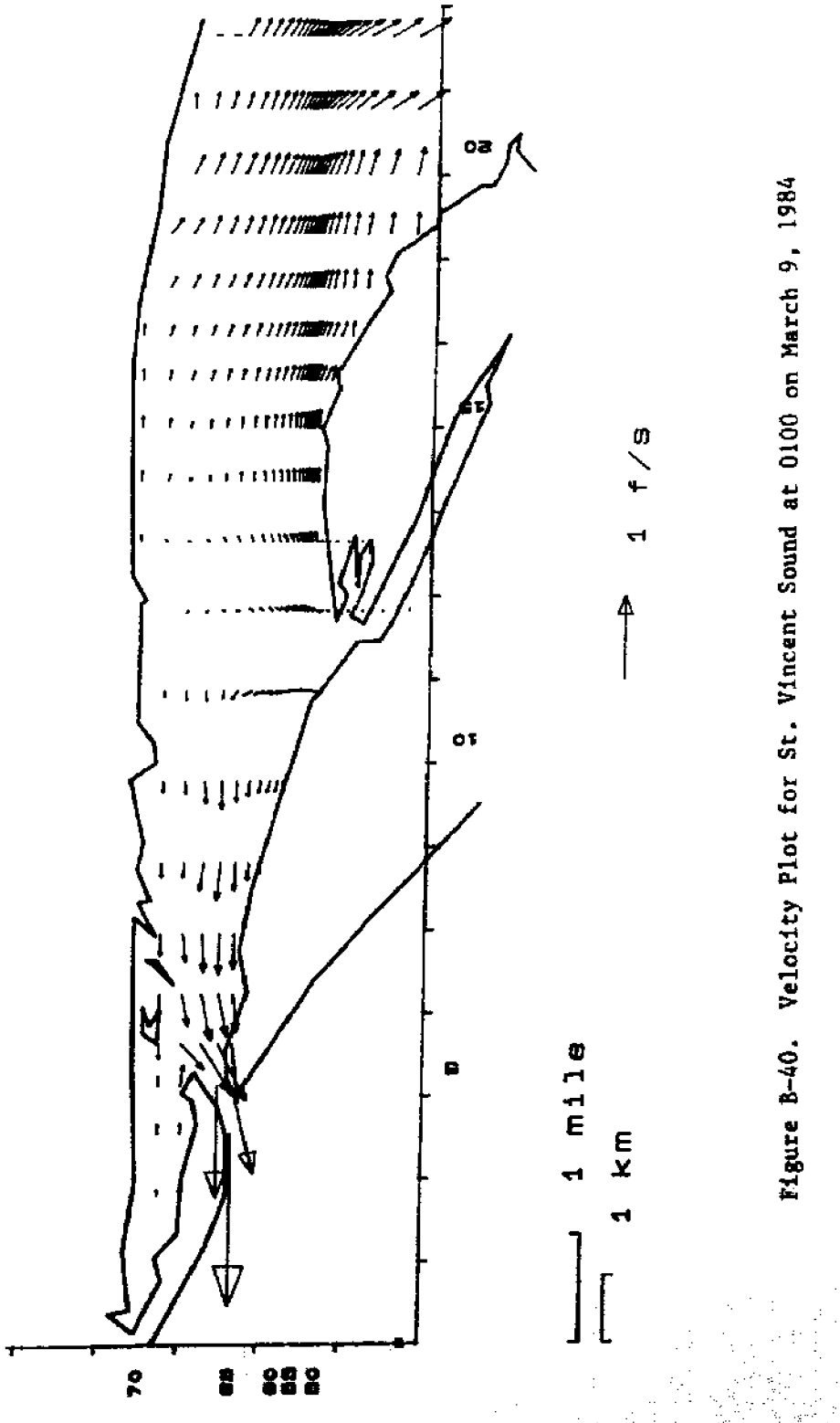

Figure B-40. Velocity Plot for St. Vincent Sound at 0100 on March 9, 1984

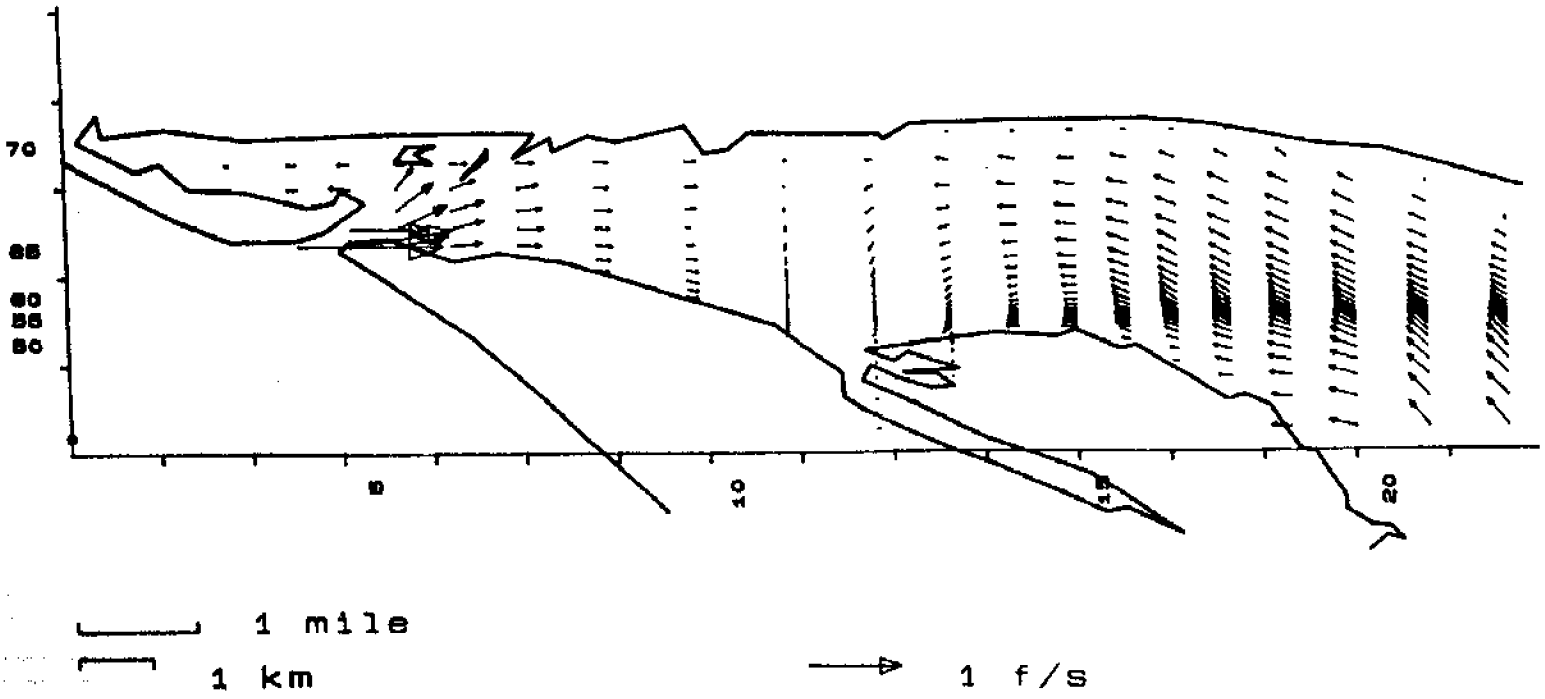

Figure B-41. Velocity Plot for St. Vincent Sound at 0500 on March 9, 1984

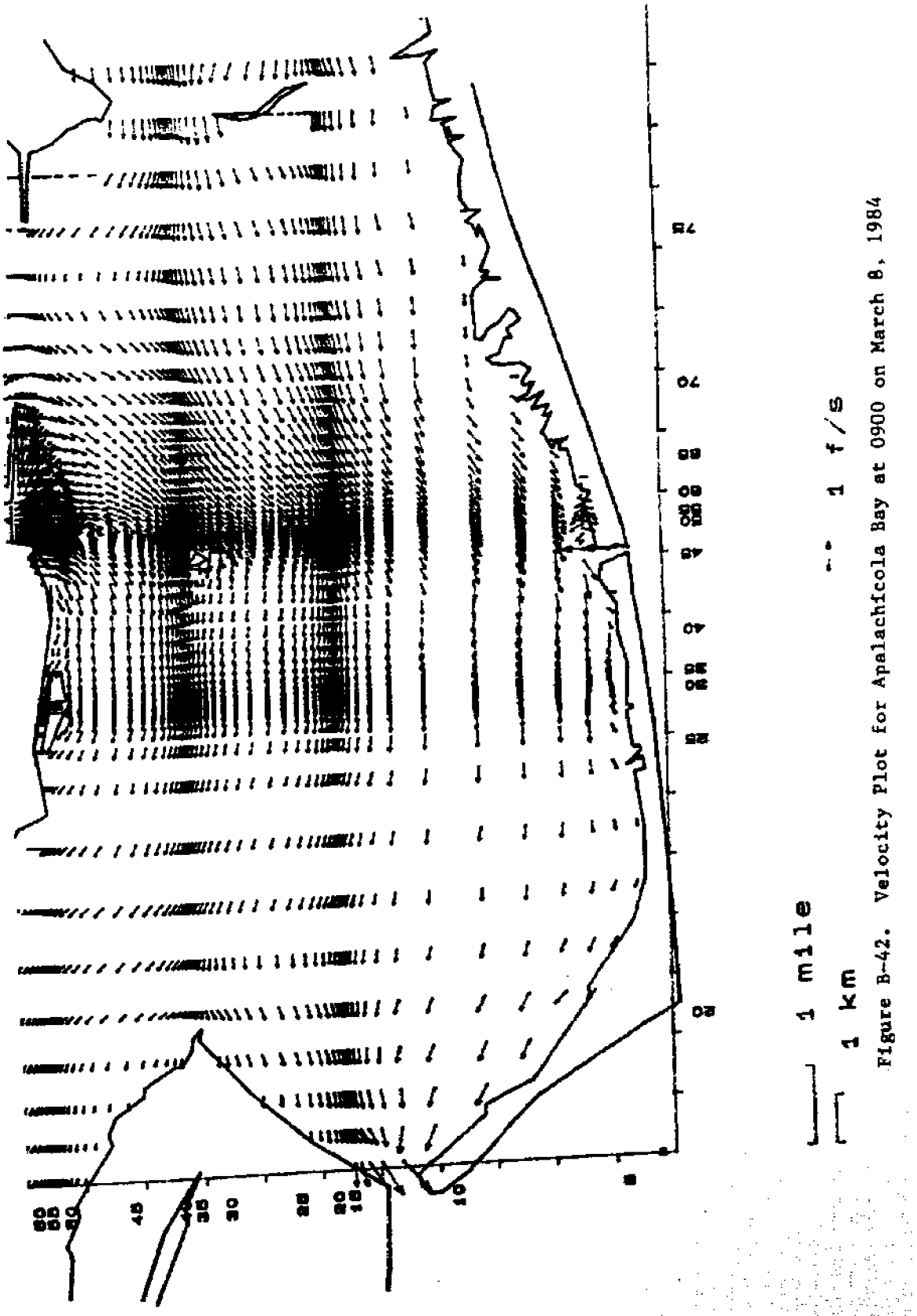

Figure B-42. Velocity Plot for Apalachicola Bay at 0900 on March 8, 1984

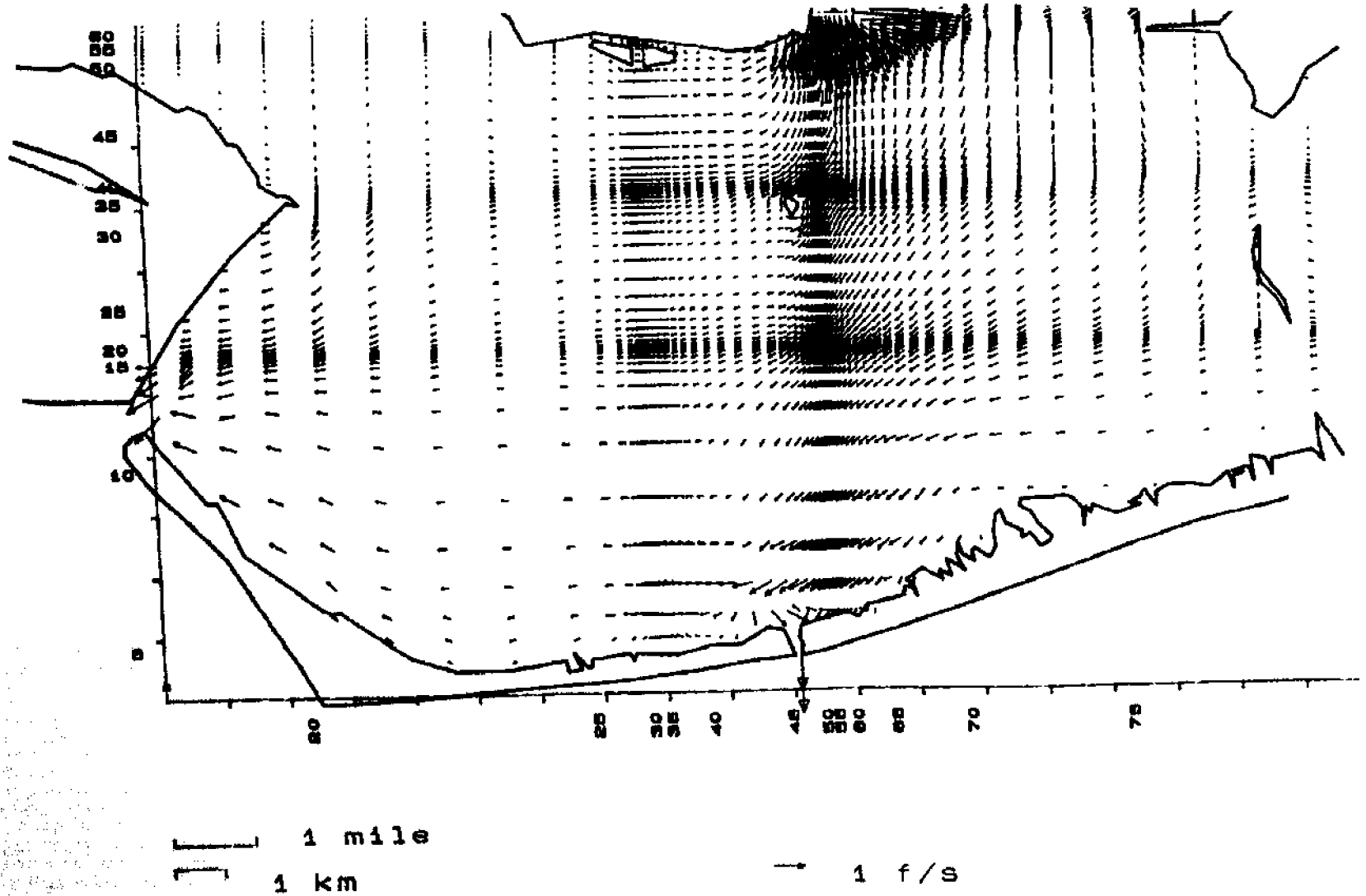

Figure B-43. Velocity Plot for Apalachicola Bay at 1300 on March 8, 1984

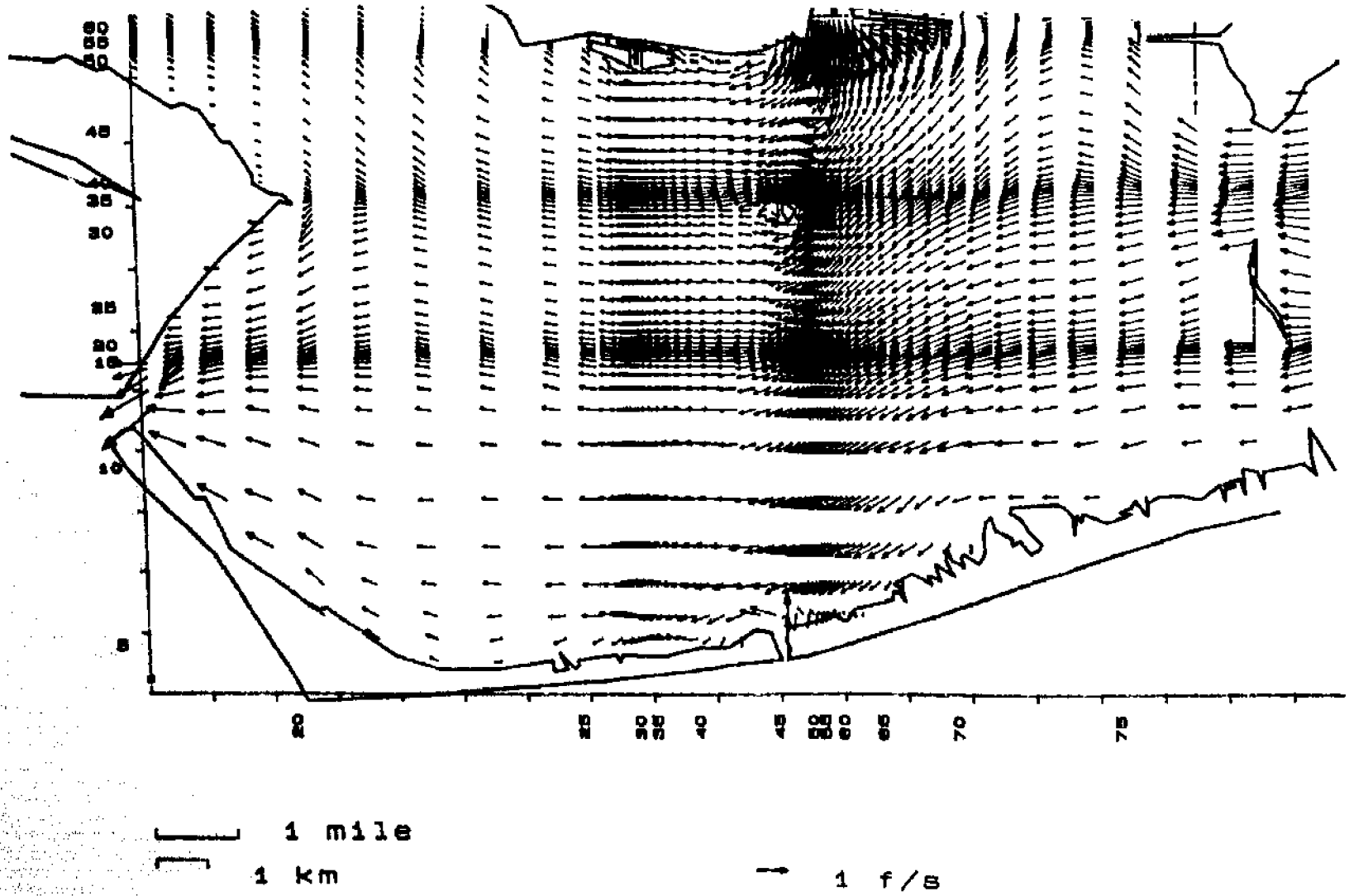

Figure B-44. Velocity Plot for Apalachicola Bay at 1700 on March 8, 1984

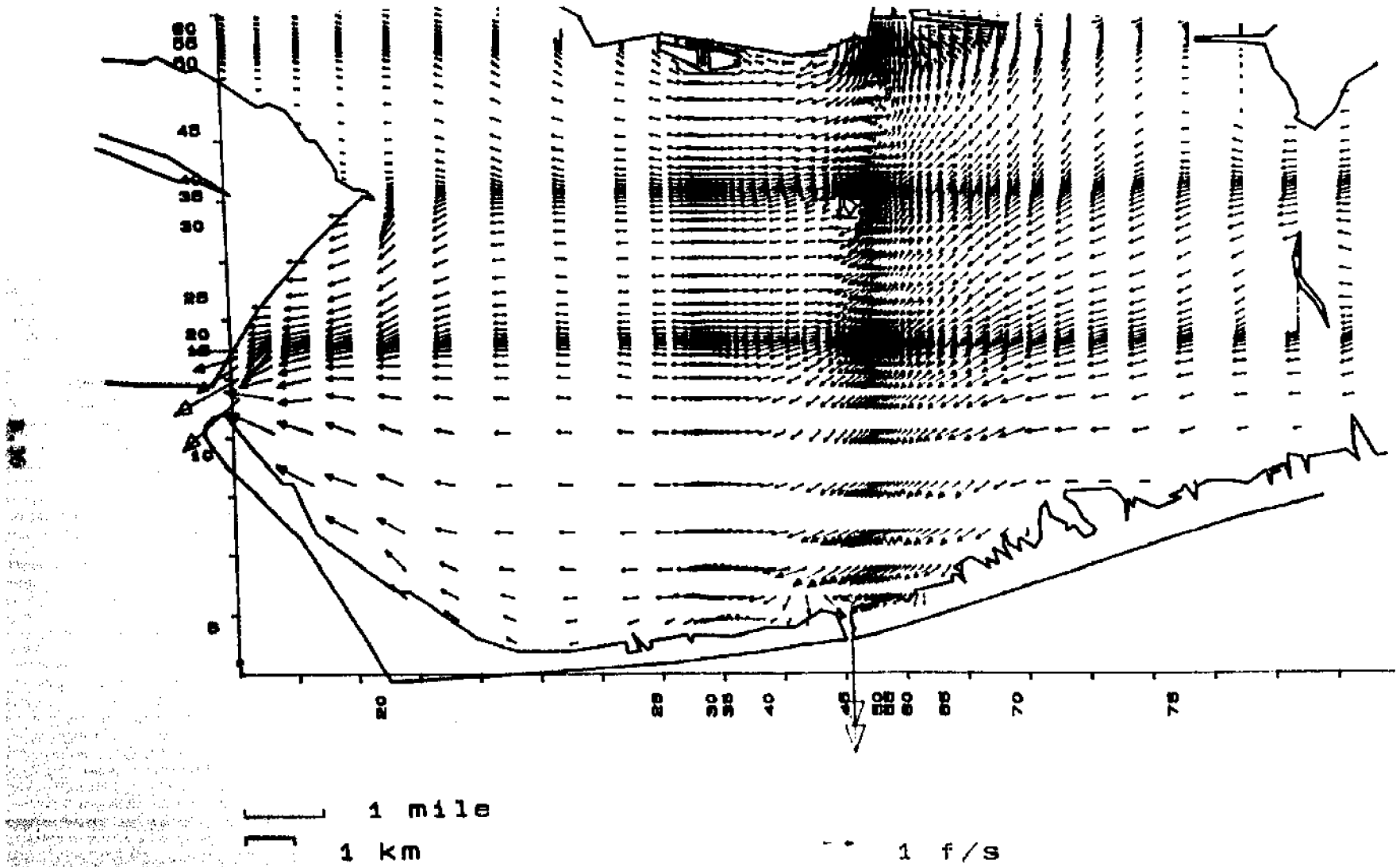

Figure B-45. Velocity Plot for Apalachicola Bay at 2100 on March 8, 1984

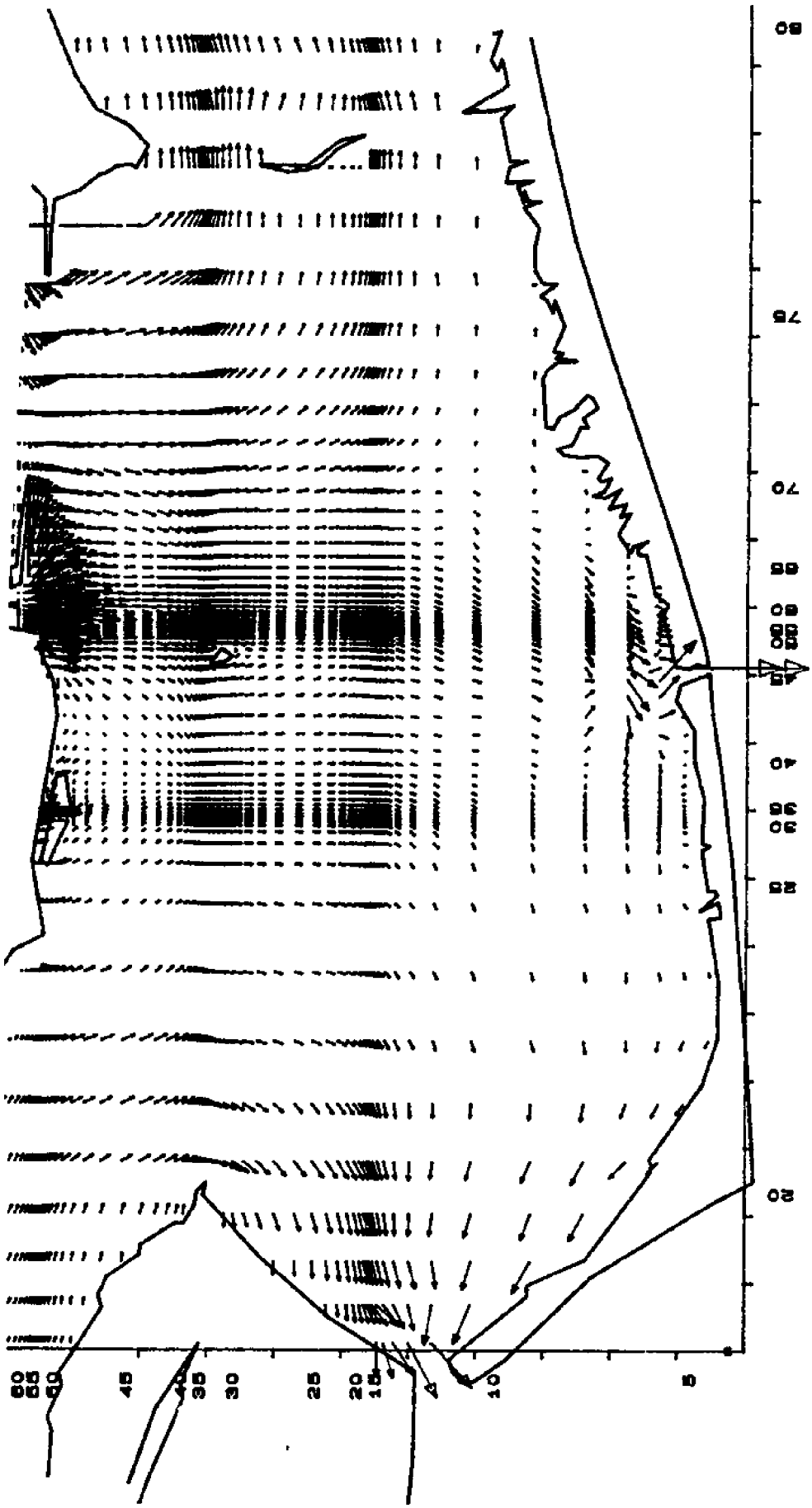

Figure B-46. Velocity Plot for Apalachicola Bay at 0100 on March 9, 1984

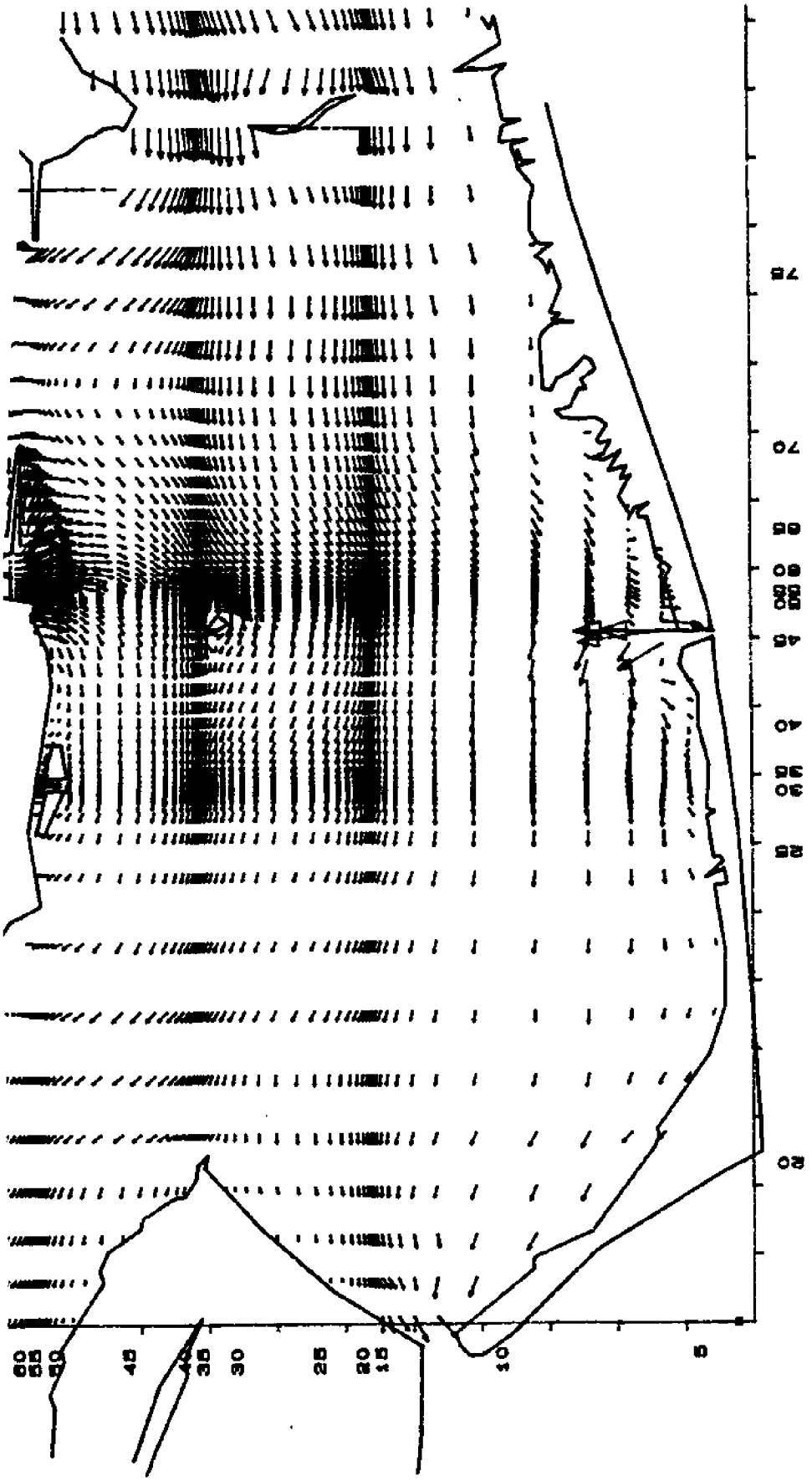

Figure B-47. Velocity Plot for Apalachicola Bay at 0500 on March 9, 1984

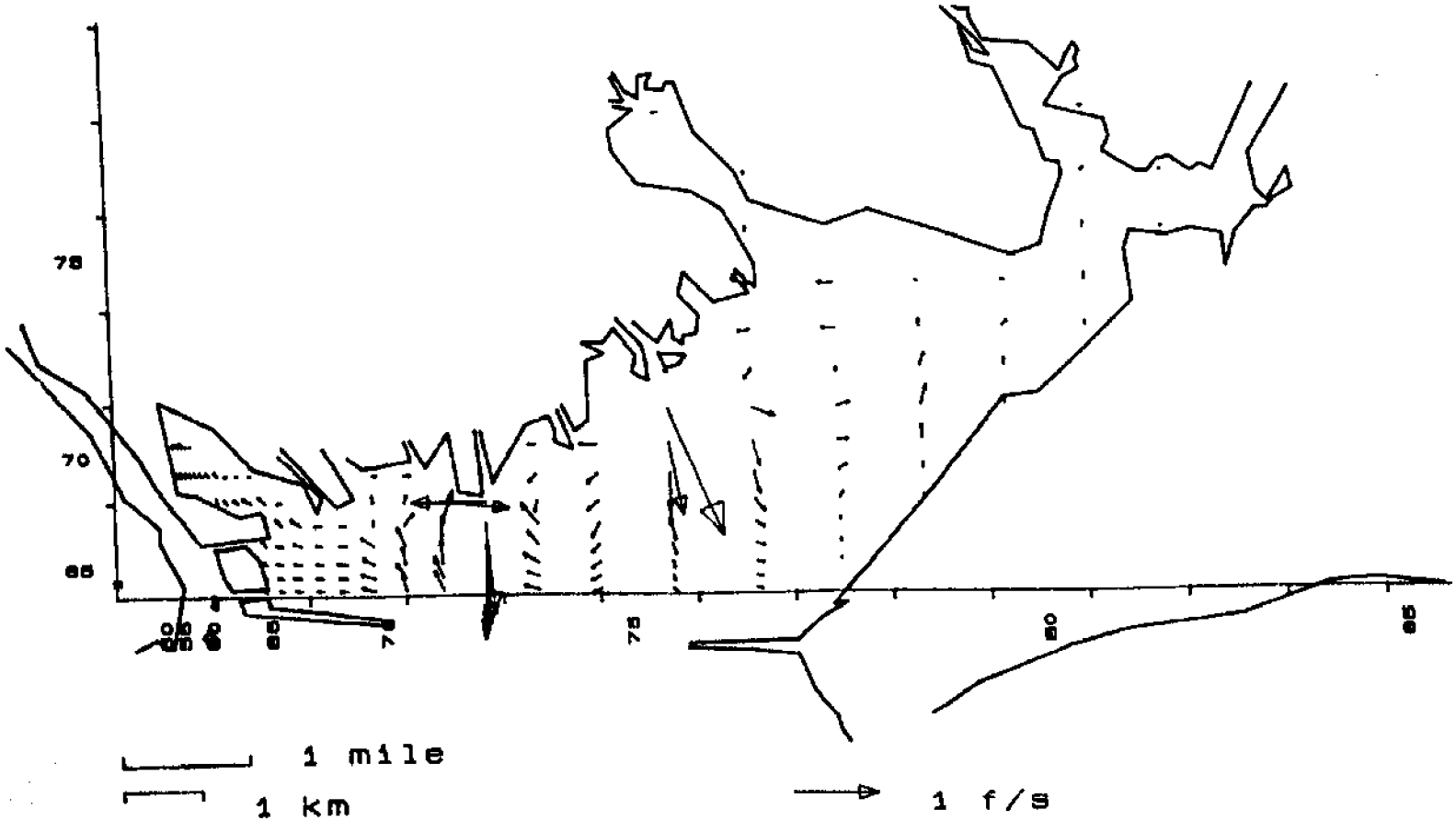

Figure B-48. Velocity Plot for East Bay at 0900 on March 8, 1984

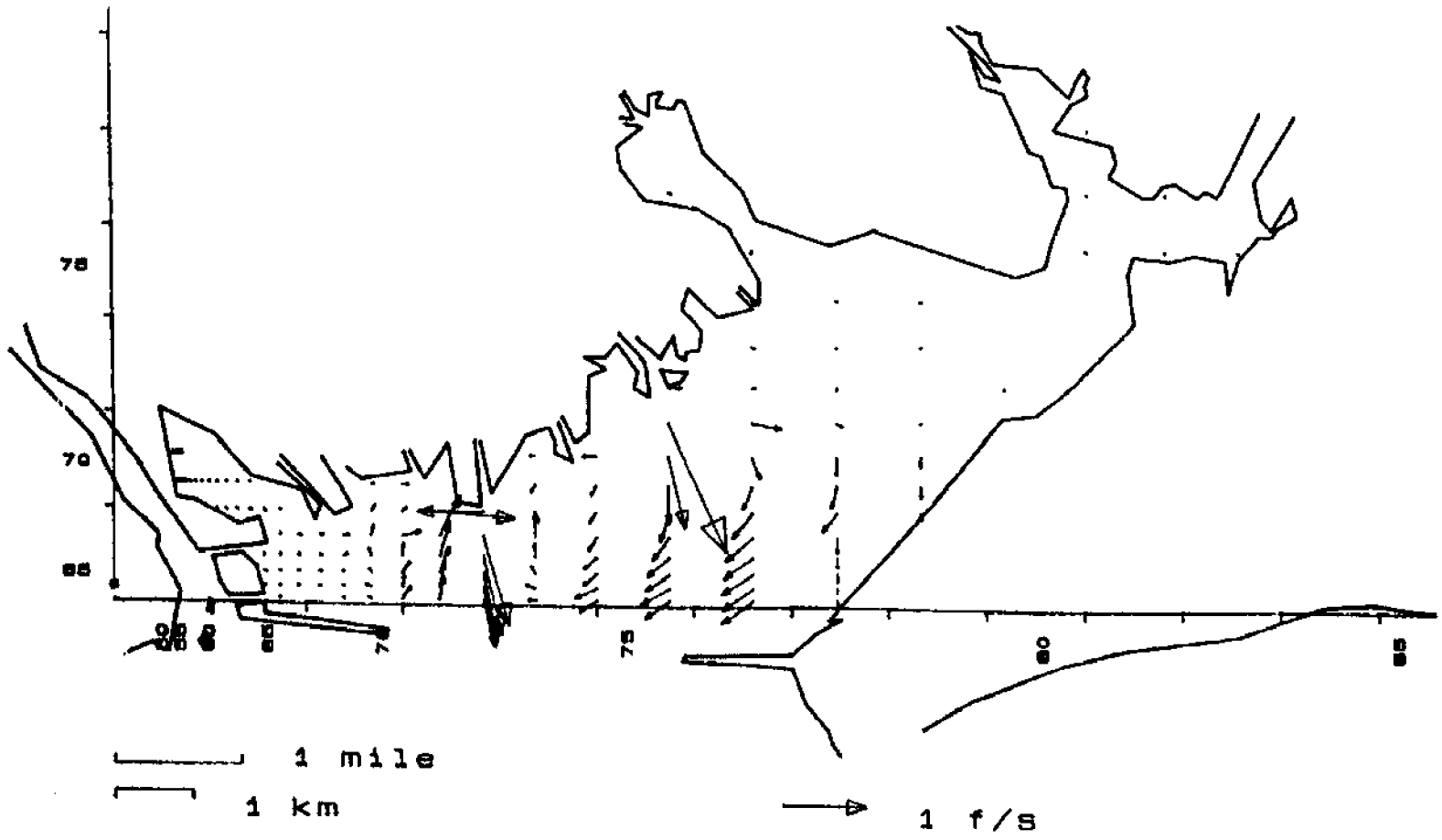

Figure B-49. Velocity Plot for East Bay at 1300 on March 8, 1984

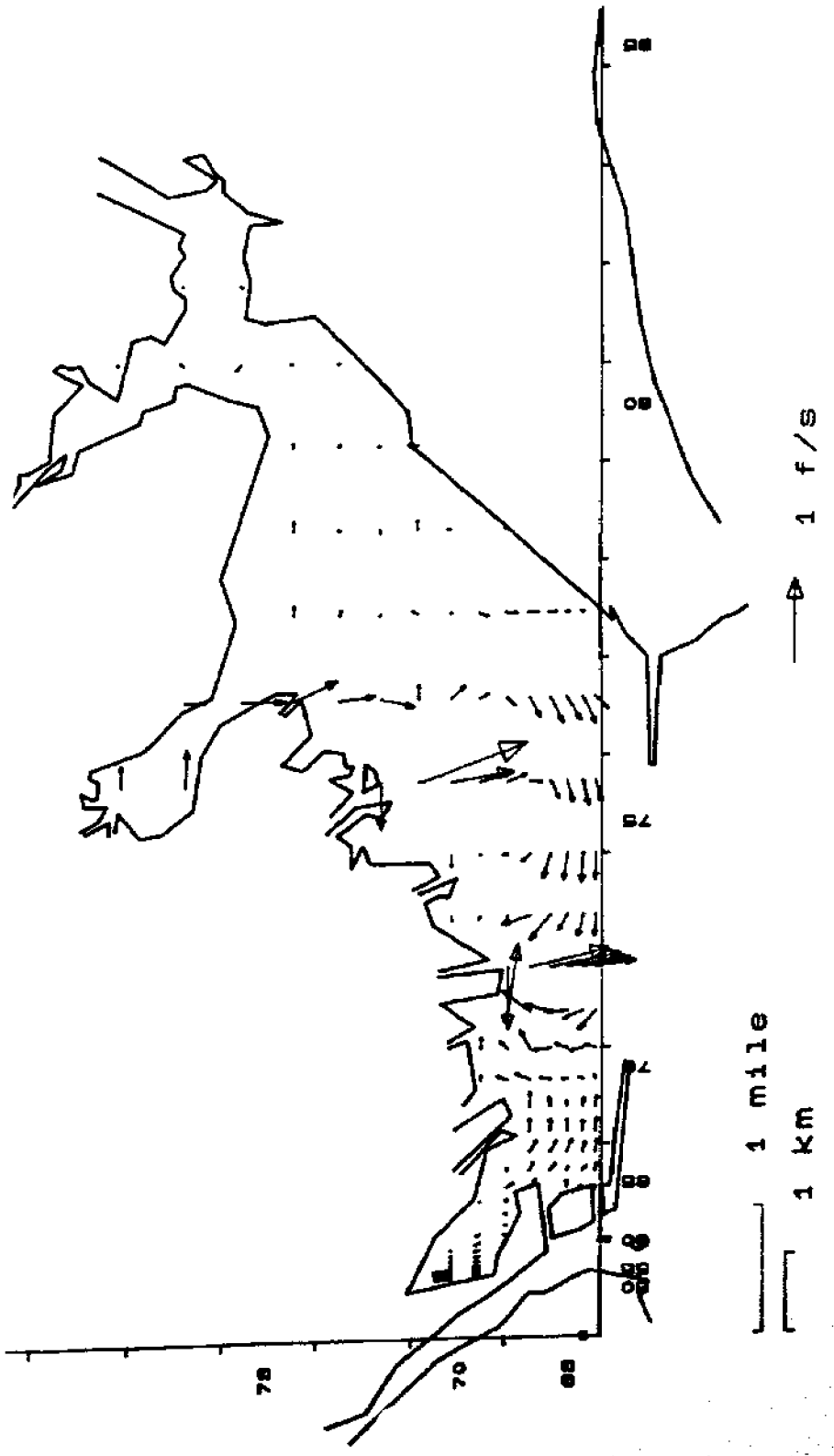

Figure B-50. Velocity Plot for East Bay at 1700 on March 8, 1984

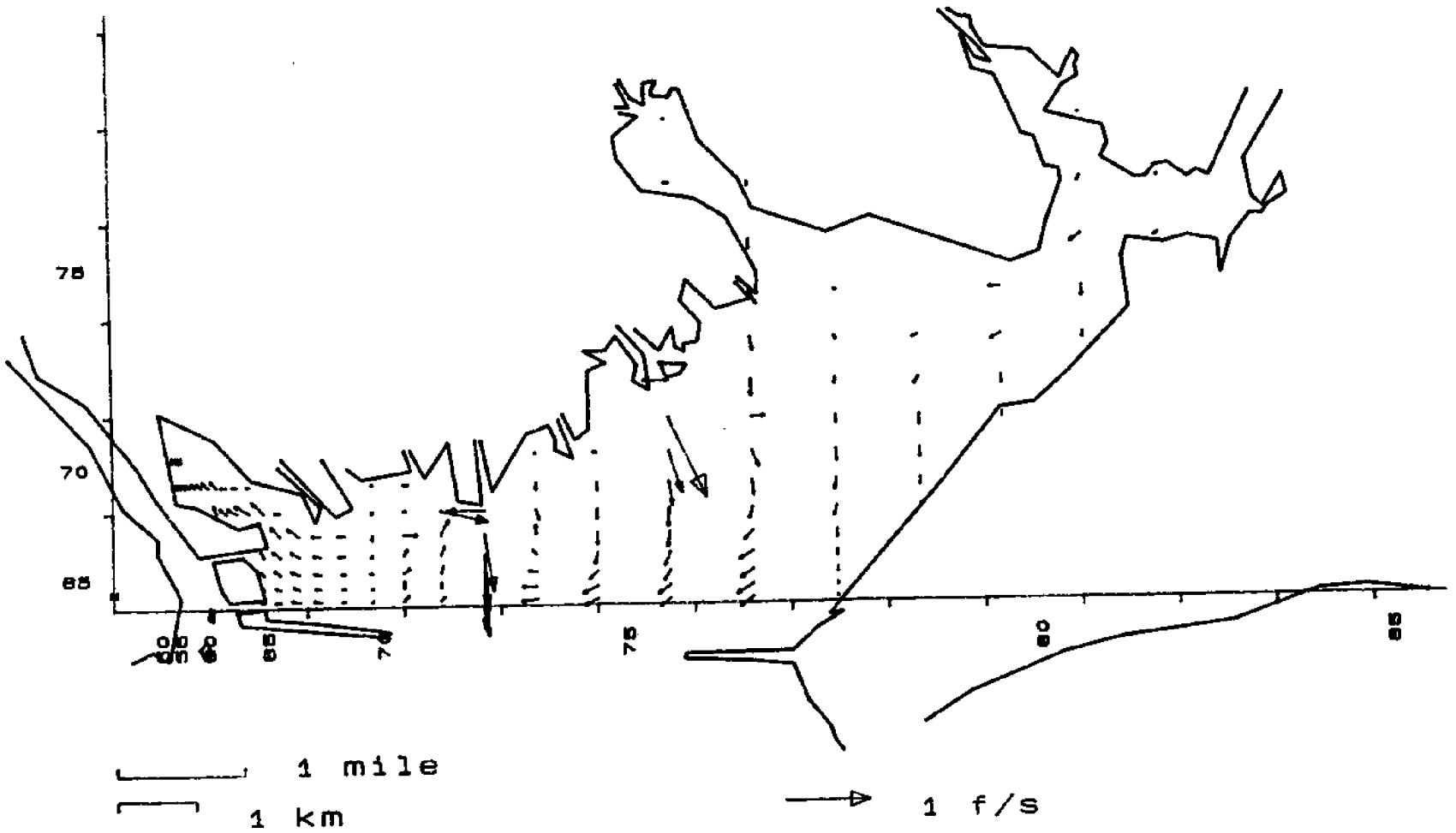

Figure B-51. Velocity Plot for East Bay at 2100 on March 8, 1984

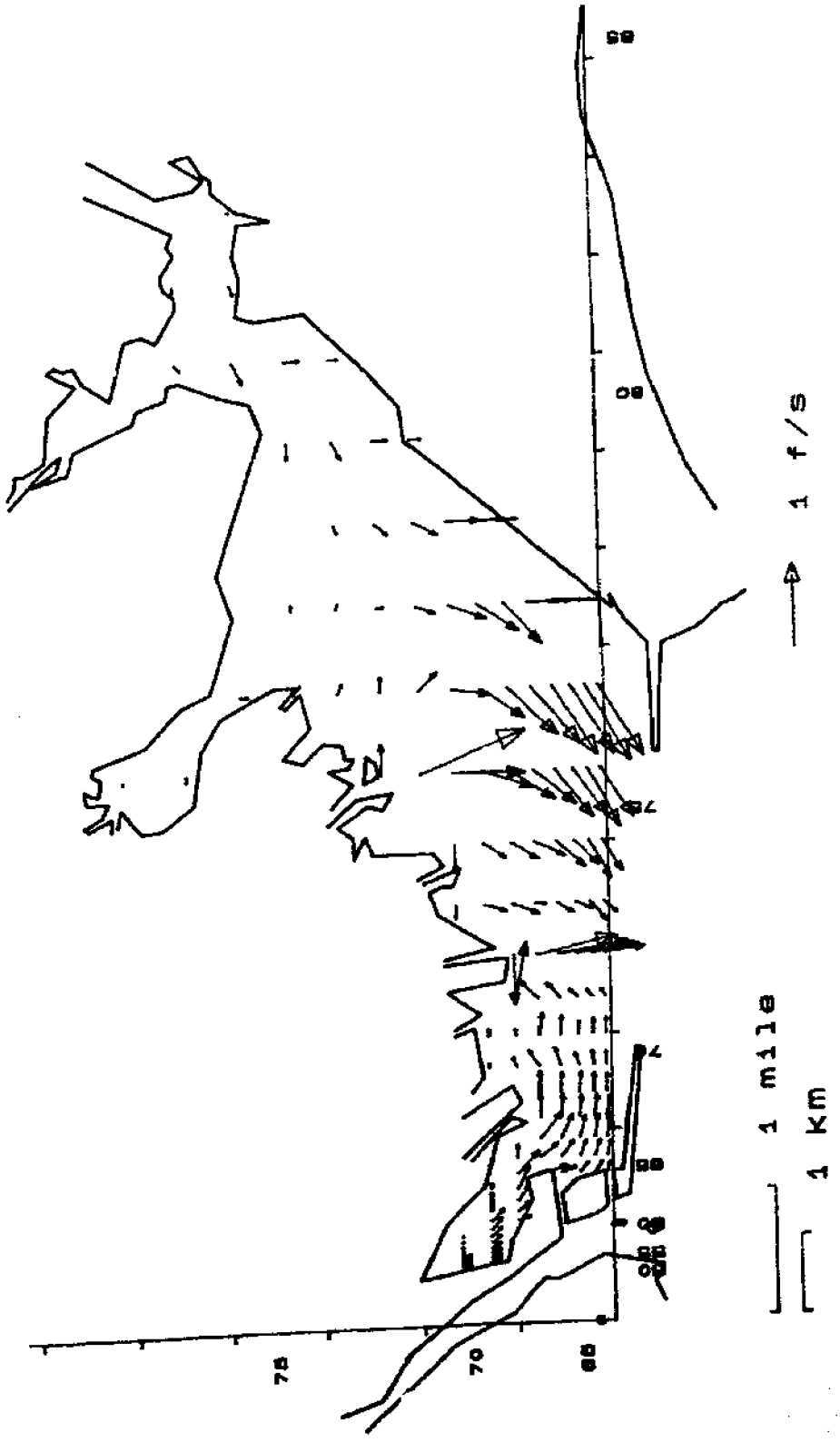

Figure B-52. Velocity Plot for East Bay at 0100 on March 9, 1984

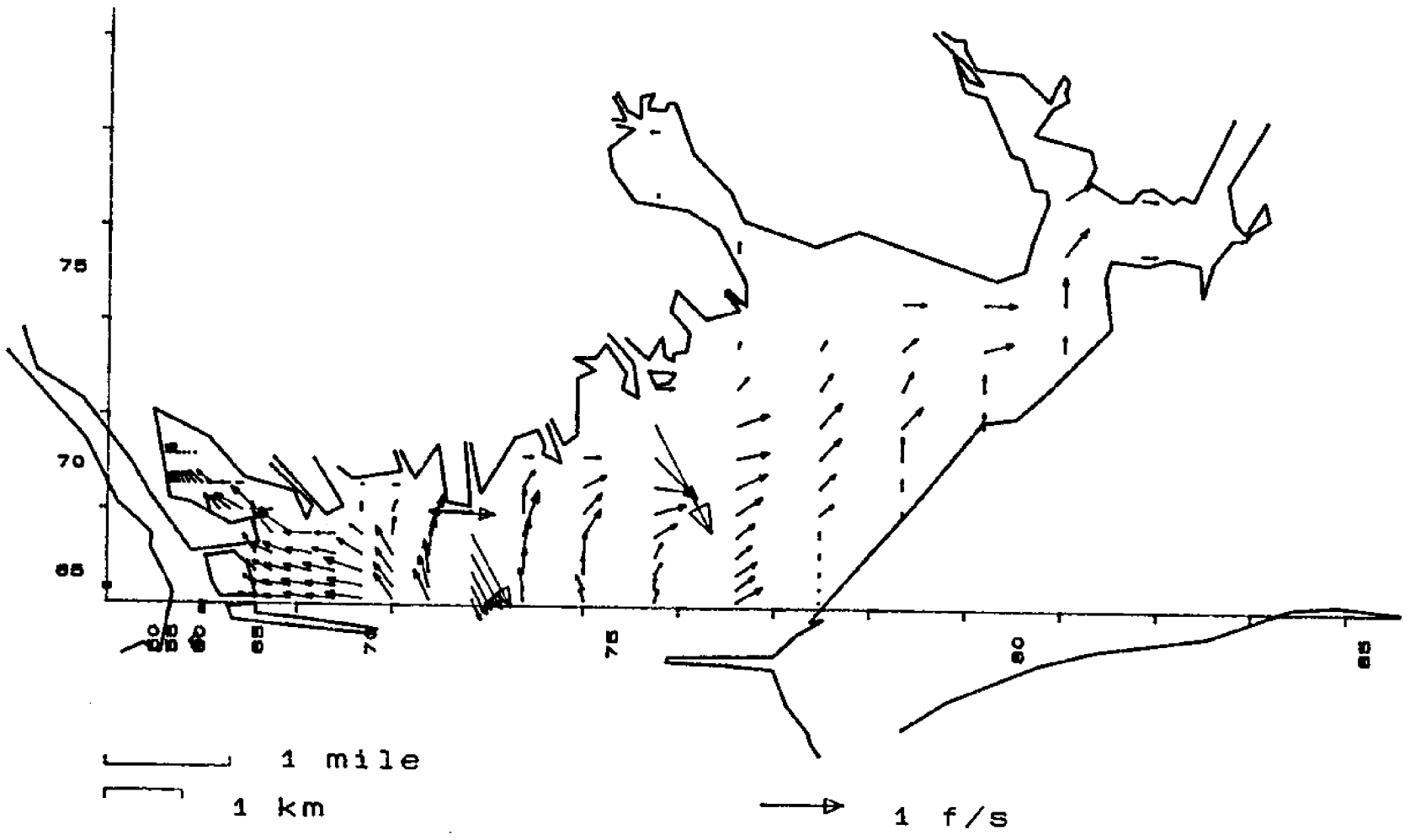

Figure B-53. Velocity Plot for East Bay at 0500 on March 9, 1984

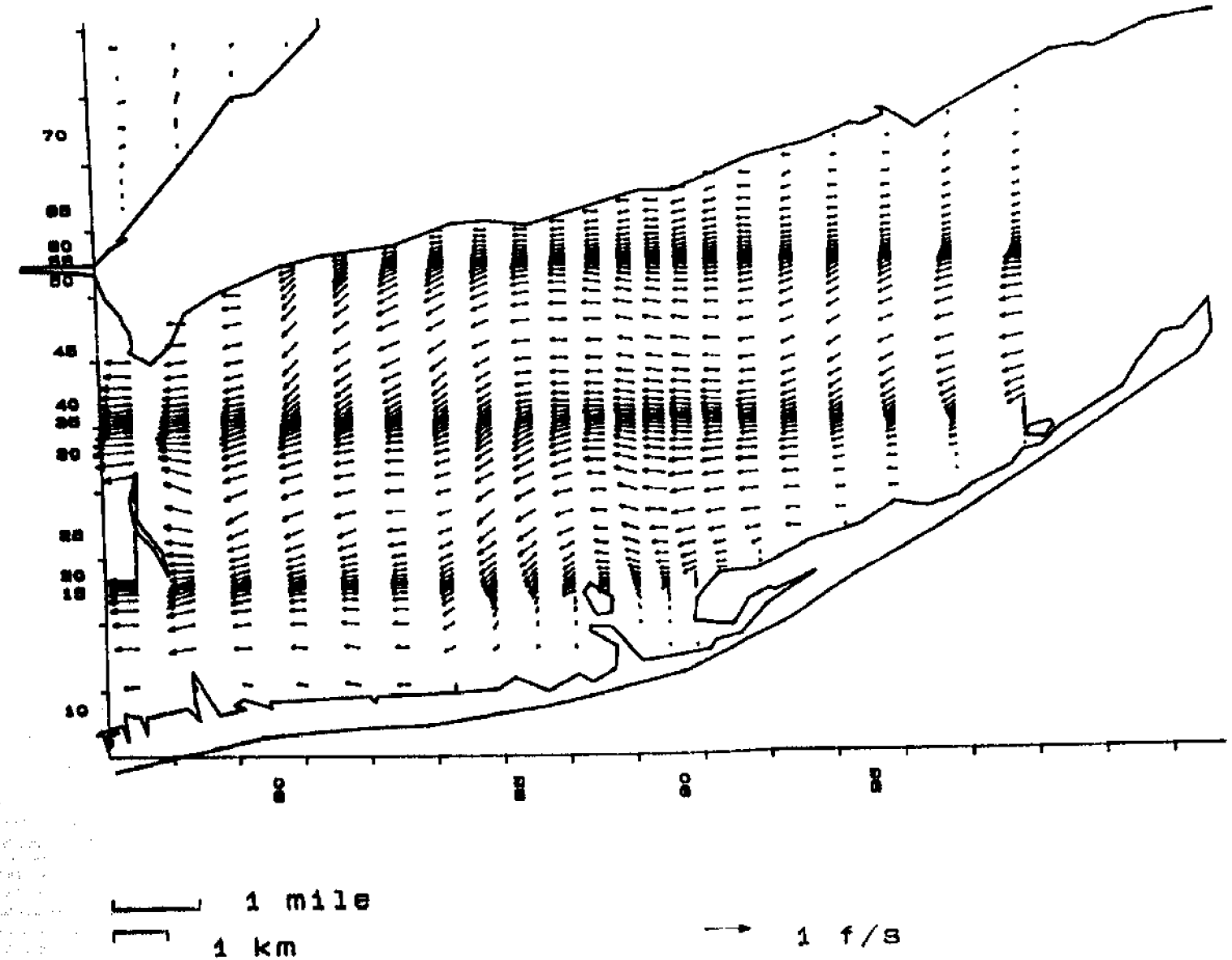

Figure B-54. Velocity Plot for St. George Sound at 0900 on March 8, 1984

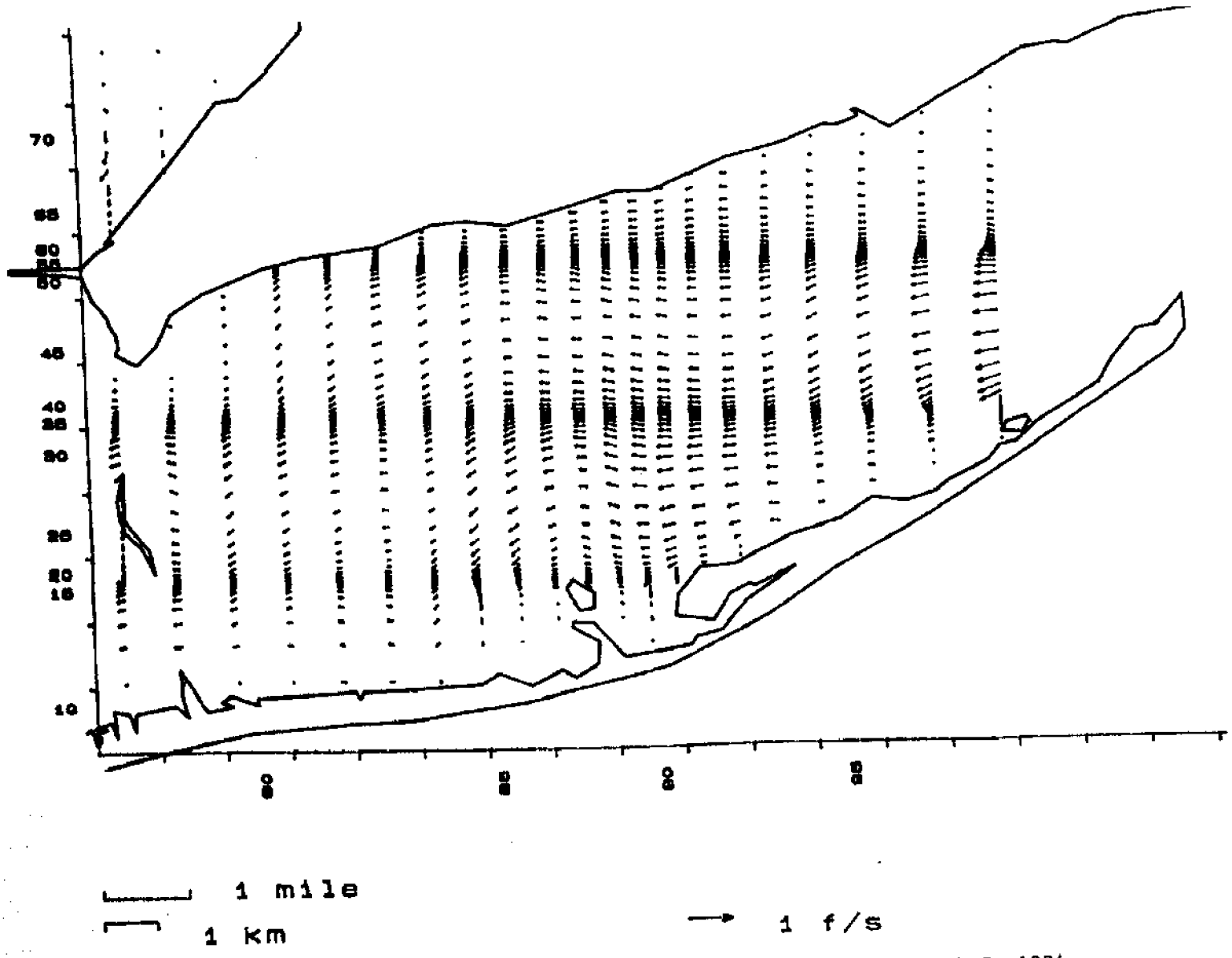

Figure B-55. Velocity Plot for St. George Sound at 1300 on March 8, 1984

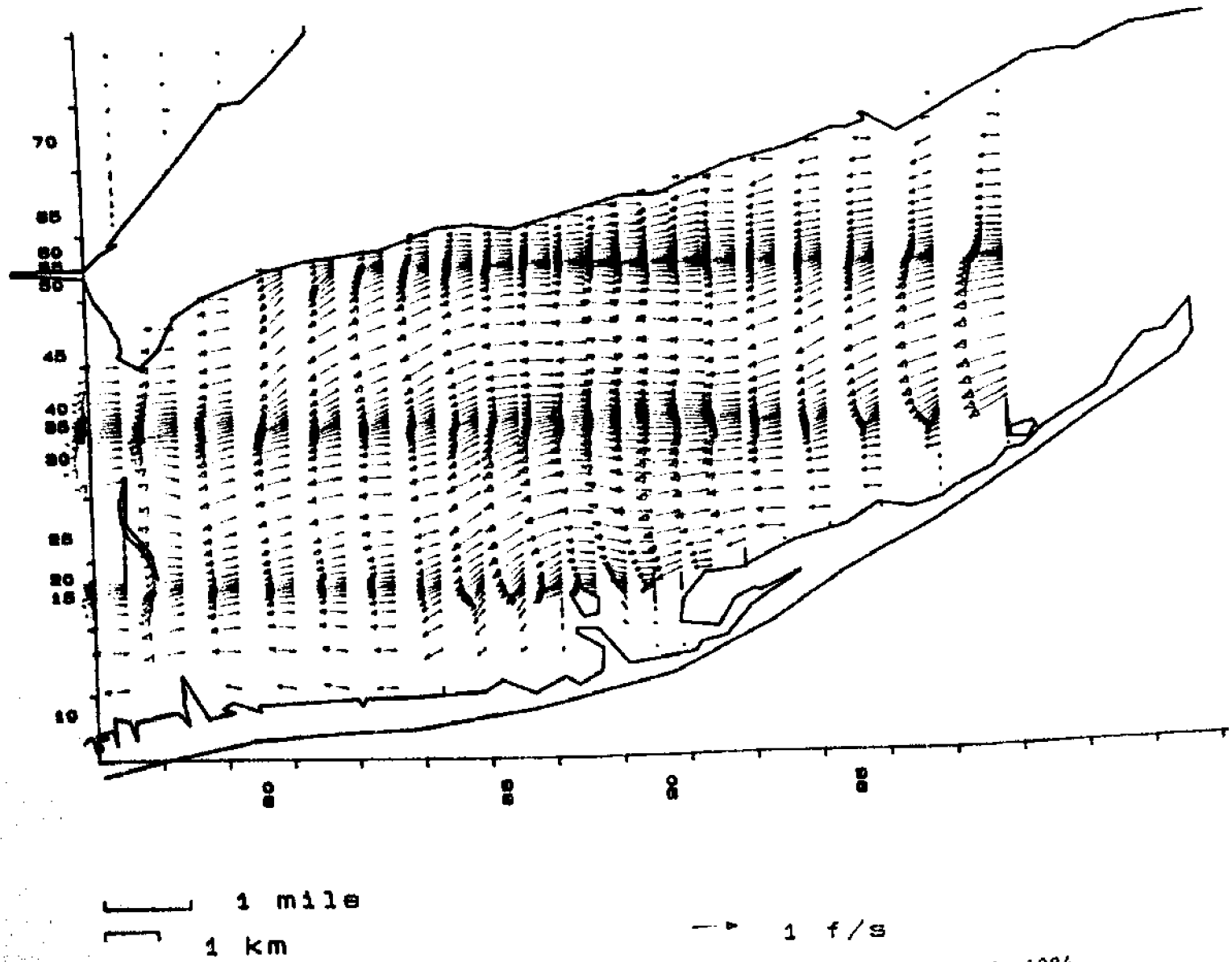

Figure B-56. Velocity Plot for St. George Sound at 1700 on March 8, 1984

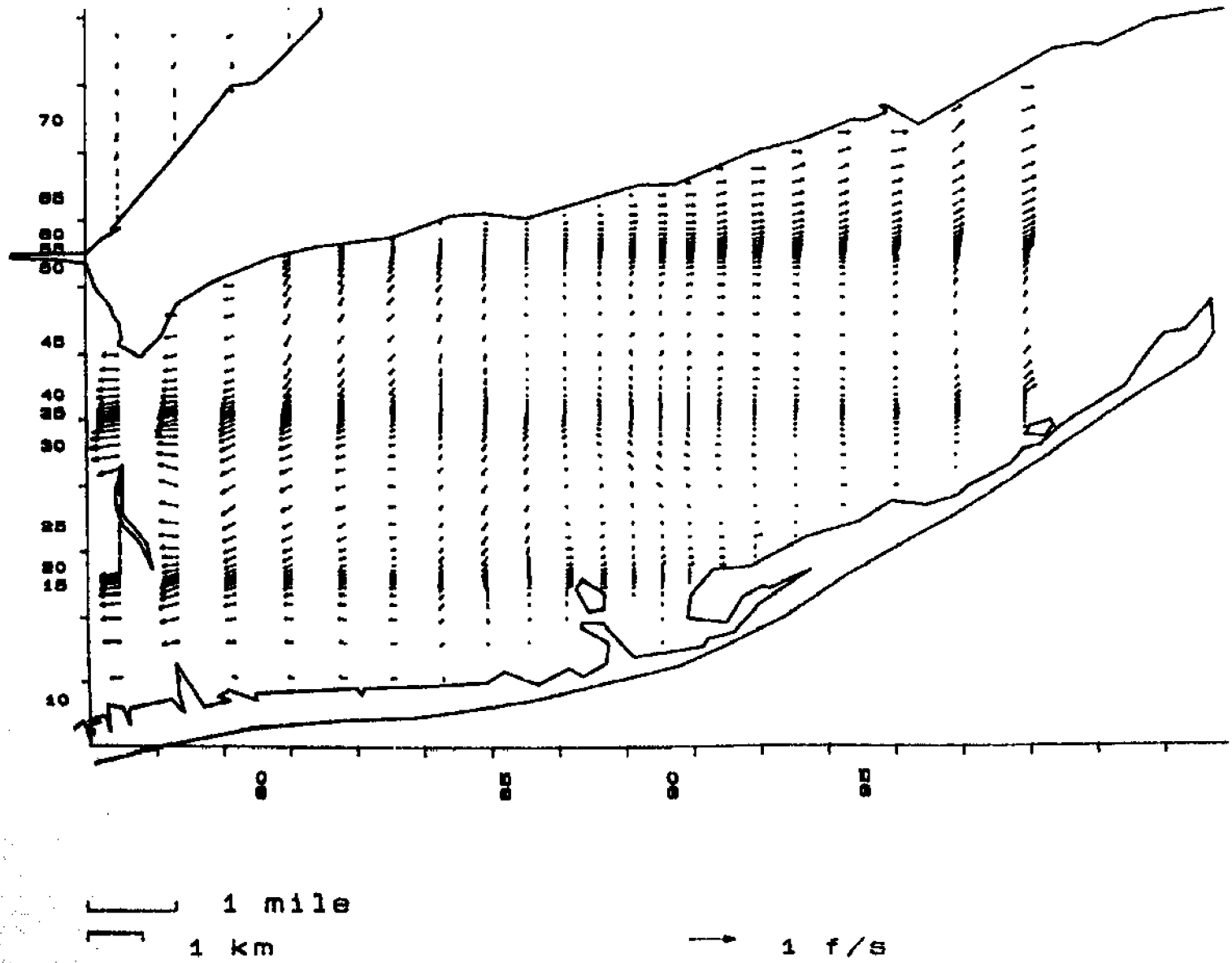

Figure B-57. Velocity Plot for St. George Sound at 2100 on March 8, 1984

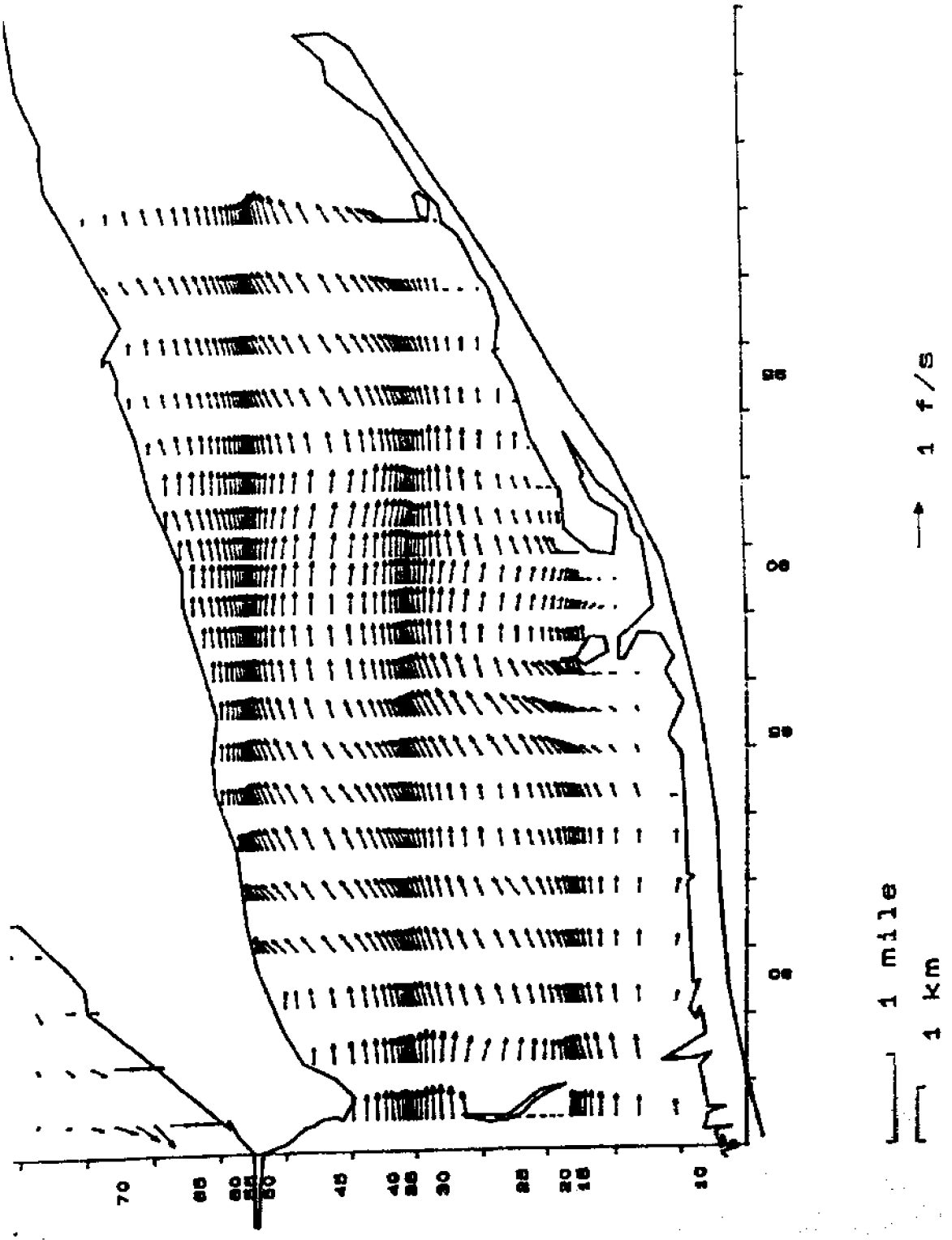
1 f/s
1 mile
1 km

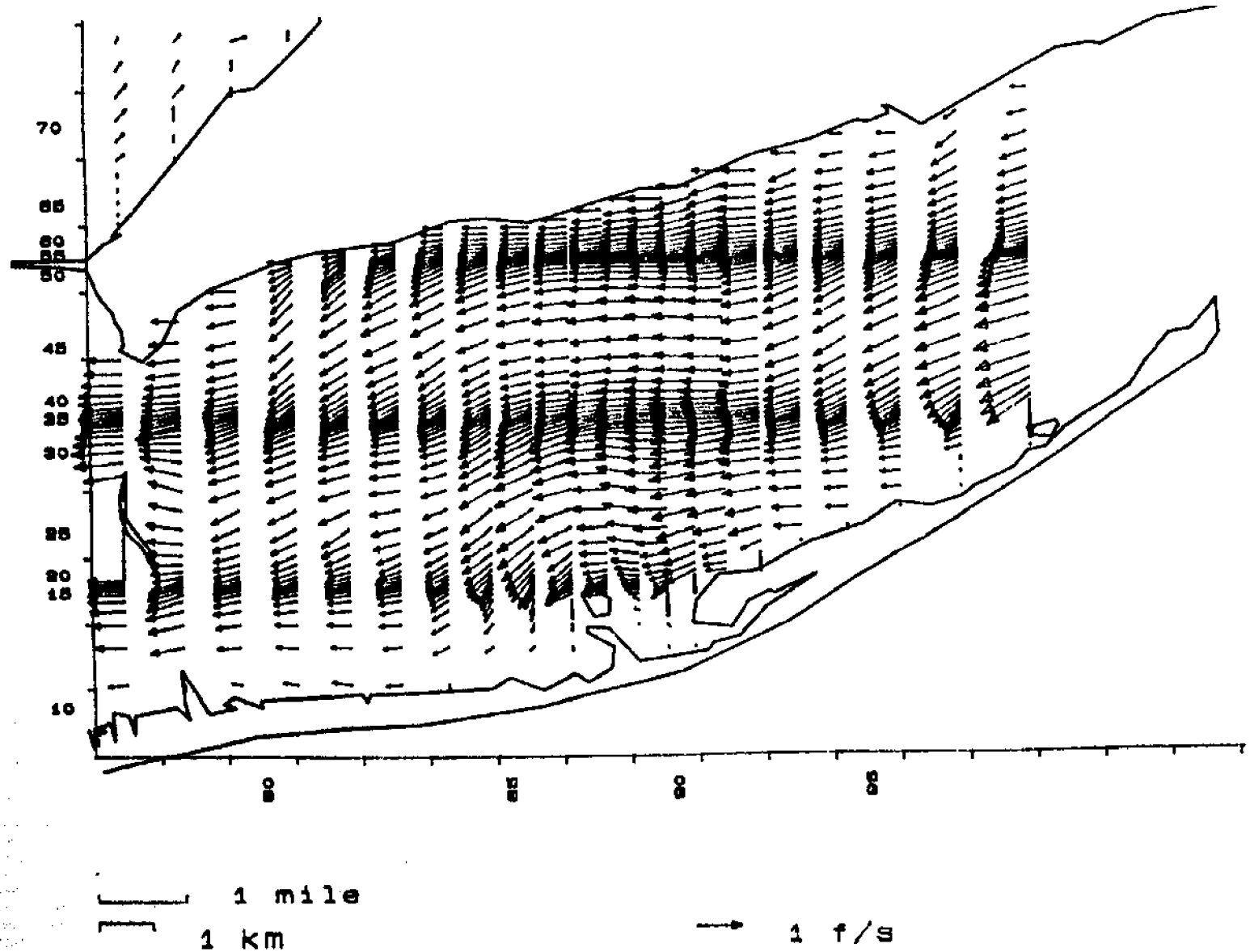

Figure B-59. Velocity Plot for St. George Sound at 0500 on March 9, 1984